

**Magnetolectric and Multiferroic Properties of
Green Phases $R_2\text{BaCuO}_5$ and Aeschynites
 $R\text{FeWO}_6$ ($R = \text{Rare earth}$)**

A Thesis

Submitted for the Degree of

Doctor of Philosophy

by

Premakumar Yanda



**Chemistry and Physics of Materials Unit
Jawaharlal Nehru Centre for Advanced Scientific Research
(A Deemed University)
Bengaluru – 560064**

August 2021

Dedicated to my parents and brother.....

DECLARATION

I hereby declare that the matter embodied in the thesis entitled “**Magnetoelectric and Multiferroic Properties of Green Phases $R_2\text{BaCuO}_5$ and Aeschynites $R\text{FeWO}_6$ ($R = \text{Rare earth}$)**” is the result of investigations carried out by me at the Chemistry and Physics of Materials Unit, Jawaharlal Nehru Centre for Advanced Scientific Research, Bangalore, India under the supervision of Prof. A. Sundaresan and it has not been submitted elsewhere for the award of any degree or diploma.

In keeping with the general practice in reporting the scientific observations, due acknowledgements have been made whenever the work described is based on the findings of other investigators. Any omission that might have occurred due to oversight or error in judgement is regretted.

Bengaluru

17/08/2021



Premakumar Yanda

CERTIFICATE

I hereby certify that the matter embodied in this thesis entitled “**Magnetoelectric and Multiferroic Properties of Green Phases $R_2\text{BaCuO}_5$ and Aeschynites $R\text{FeWO}_6$ ($R = \text{Rare earth}$)**” has been carried out by Mr. Premakumar Yanda at the Chemistry and Physics of Materials Unit, Jawaharlal Nehru Centre for Advanced Scientific Research, Bangalore, India under my supervision and it has not been submitted elsewhere for the award of any degree or diploma.



Prof. A. Sundaresan
(Research Supervisor)

ACKNOWLEDGEMENTS

I express my sincere gratitude to my research supervisor Prof. A. Sundaresan for giving me the opportunity to work under his guidance and introducing me to the field of multiferroics. I sincerely thank him for his invaluable guidance, enormous support, and constant encouragement throughout my research career. I am extremely grateful to him for providing me with good collaborations which enhanced my research experience. I am also grateful to him for giving me enough freedom to carry my research work. I thank him for his patience, belief, and positive attitude towards me in various aspects of my research work.

I would like to thank Prof. C. N. R. Rao, FRS for providing me various experimental facilities and for being a constant source of inspiration.

I would like to thank Prof. S. Balasubramanian, Prof. Chandrabhas Narayana, and Prof. A. Sundaresan, past and present chairperson, respectively, for allowing me to utilize various facilities in the unit.

I acknowledge International Centre for Materials Science (ICMS) and Sheikh Saqr Laboratory (SSL) at JNCASR for providing various experimental facilities.

I would like to thank Prof. A. Sundaresan, Prof. U V Waghmare, Prof. S M Shivaprasad, Prof. Shobhana Narasimhan, and Prof. T. N. Guru Row (IISc) for their informative course works.

It is my great pleasure to thank my collaborators. My sincere thanks to Dr. Nikita Ter-Oganessian from Southern Federal University for symmetry analysis and fruitful discussions. I specially thank Prof. Juan Rodriguez-Carvajal from Institut Laue-Langevin for providing help in solving the neutron diffraction data. I would like to thank Dr. Fabio Orlandi and Dr. Pascal Manuel from WISH, RAL, UK for neutron diffraction experiments. I also want to thank Prof. Igor Golosovsky from Konstantinov Petersburg Nuclear Physics Institute, Russia for providing neutron diffraction data.

I thank the technical staff, namely Mr. Srinath, Mr. Anil, Mr. Vasu, Mr. Mahesh, Mr. Rahul, Ms. Pavana, Ms. Radha, and Balaraju for their help in various aspects of research and academics.

I would like to thank Dr. Navneet Pandey, Quantum Design, India, whom I have learned immensely about SQUID and PPMS instruments.

I would like to thank University Grants Commission (UGC) and JNCASR for providing fellowship during my Ph.D. tenure. I would like to thank JNCASR and DST-RAL project for financial support to attend conferences and to visit RAL, UK for performing neutron diffraction experiments, respectively.

I thank Complab, Library, Academics, Administration, Dhanvantari, Housekeeping, Garden, Dining hall, and Hostel for providing and maintaining different facilities.

I must thank all my past and present lab mates, Dr. Pranab Mondal, Dr. Rana Saha, Dr. Somnath Ghara, Dr. Chandan De, Dr. Abhijit Sen, Dr. Chandriah, Dr. Madhu, Dr. Rambabu, Dr. Shivani, Dr. Anzar, Mr. Amit, Dr. Ravi, Ms. Pavitra, Ms. Swarnamayee, Mr. Debendra, Mr. Rahul, and Mr. Souvik for their various helps and useful discussions during my tenure and maintain a friendly atmosphere in the lab. My special thanks to Dr. Somnath and Dr. Chandan for fruitful discussions on various research problems.

I thank all my friends at JNCASR, especially Priyanka, Divya, Dr. Pradeep, Dr. Ravi, Shivaram, and Rajendra for their company in various activities and always being there for me. I also thank Deepak, Ganesh, Usha, Malay, Anusha, Pavitra, Shashi, and Vybhav for making my journey memorable. I would like to thank all my sports friends from cricket, badminton, and volleyball. I would like to thank my friends outside JNCASR, especially Mr. Balu.

Finally, I would like to thank my parents, Mr. Yanda Venkata Rao and Mrs. Yanda Krishnaveni and my brother, Ramesh Yanda for their unconditional love, support, and giving me this life.

Preface

The thesis aims to explore new magnetoelectric and multiferroic materials and study the underlying structure-property relationship in the green phases $R_2\text{BaCuO}_5$ and aeschynites $R\text{FeWO}_6$, where R is a rare-earth cation. It contains two parts where Part A has four chapters which deal with the findings on green phases and Part B contains one chapter which shows the results on aeschynites.

Chapter 1 gives a brief introduction to magnetodielectric, magnetoelectric and multiferroic properties, including their symmetry requirements. Also, various microscopic mechanisms responsible for magnetoelectric coupling are explained with examples.

Chapter 2 illustrates the different experimental techniques used for this work.

Chapter 3 shows the experimental discovery of the linear magnetoelectric effect in $\text{Sm}_2\text{BaCuO}_5$, which crystallizes in the centrosymmetric orthorhombic ($Pnma$) structure. Magnetization and specific heat measurements confirmed the long-range antiferromagnetic ordering of Cu^{2+} and Sm^{3+} ions moments at $T_{N1} = 23$ K and $T_{N2} = 5$ K, respectively. Furthermore, the applied magnetic field induces dielectric anomaly at T_{N1} , whose magnitude increases with the field, which results in a significant magnetodielectric effect. Interestingly, the applied magnetic field induces an electric polarization below T_{N1} , which varies linearly with the magnetic field, demonstrating a linear magnetoelectric effect. The observed linear magnetoelectricity is explained based on symmetry arguments.

Chapter 4 describes elliptical cycloidal phase and spin-induced multiferroicity in the antiferromagnetic $\text{Gd}_2\text{BaCuO}_5$. With decreasing temperature, an elliptical cycloidal ordering of both Gd^{3+} and Cu^{2+} spins at $T_N = 11.8$ K occurs with the modulation vector $\mathbf{k} = (0, 0, g)$ and a lock-in transition to a strongly noncollinear structure with $\mathbf{k}_c = (0, 0, \frac{1}{2})$ at $T_{loc} \sim 6$ K. Both spin structures induce electric polarization consistent with the polar magnetic space groups $P2_1ma1'(0,0,g)0s0s$ and $Pc2_1ca$, respectively. Based on the symmetry analysis, we suggest that the ferroelectricity in both commensurate and incommensurate phases is driven by a complex interplay of two-spins and single-spin contributions from magnetic ions located in noncentrosymmetric environments.

Chapter 5 demonstrates the linear magnetoelectric effect and field-induced ferroelectricity in $R_2\text{BaCuO}_5$ ($R = \text{Dy}$ and Ho). They undergo a long-range antiferromagnetic ordering of Cu^{2+} ($T_N^{\text{Cu}} = 18.5 \text{ K}$ and $T_N^{\text{Cu}} = 17.5 \text{ K}$) and R^{3+} ions ($T_N^{\text{Dy}} = 10.7 \text{ K}$ and $T_N^{\text{Ho}} = 8 \text{ K}$) for Dy and Ho compounds, respectively. Neutron diffraction study reveals that these compounds undergo a first-order magnetic transition from the high-temperature antiferromagnetic phase (P_b2_1/n) to the low-temperature phases, $Pnm'a$ (Dy) and $P112'_1/a$ (Ho), which allow linear magnetoelectric coupling. This observation is consistent with field-induced electric polarization below T_N^R . Above a critical field, both compounds exhibit metamagnetic transitions with nonlinear electric polarization, indicating that field-induced multiferroic behavior. We discuss the vital role of the between $4f - 3d$ coupling in determining the magnetic ground state and observation of the magnetoelectric effect.

Chapter 6 discusses the role of $4f-3d$ coupling on magnetic and magnetoelectric properties of $R_2\text{BaCuO}_5$ ($R = \text{Er}$, Eu , Y , Tm , Yb , and Lu) by means of DC magnetization, specific heat, dielectric, pyrocurrent, and neutron diffraction measurements. $\text{Er}_2\text{BaCuO}_5$ exhibits antiferromagnetic ordering of Cu^{2+} and Er^{3+} spins at $T_N^{\text{Cu}} = 19.3 \text{ K}$ and $T_N^{\text{Er}} = 5.1 \text{ K}$, respectively. Isothermal magnetization curves below T_N^{Er} confirm the metamagnetic transition at the critical field of $H_c = 0.9 \text{ T}$. Neutron diffraction study revealed the strongly noncollinear magnetic structure with P_b2_1/n . Interestingly, $\text{Er}_2\text{BaCuO}_5$ shows the field-induced multiferroic behavior only above the metamagnetic transition. $R_2\text{BaCuO}_5$ ($R = \text{Eu}$, Y , Tm , and Lu) exhibits antiferromagnetic ordering of Cu^{2+} ions in the range 15-20 K. These compounds did not show magnetoelectric coupling, which is consistent with the magnetic symmetry. Moreover, $\text{Yb}_2\text{BaCuO}_5$ shows three different magnetic phase transitions which are paramagnetic to commensurate (CM), commensurate to incommensurate (ICM), and ICM to CM. It evidences strong magnetodielectric coupling in the ICM phase indicating the possibility of multiferroicity. This study further confirms that between $4f - 3d$ coupling is necessary to achieve the magnetoelectric or multiferroic properties in the green phase compounds.

Chapter 7 deals with the synthesis, structure, and magnetism-induced multiferroic properties of the polar magnets $R\text{FeWO}_6$ ($R = \text{Tm}$, Sm , Gd , Ho , and Er). All these compounds crystallize in the orthorhombic structure with the polar symmetry $Pna2_1$. DC magnetization and specific heat measurements confirm the antiferromagnetic order of Fe^{3+} spins at $T_{N1} = 14 - 18 \text{ K}$ and magnetic ordering of R ions at low temperatures. The magnetic order of Fe^{3+} ions in these compounds accompanies a dielectric anomaly and a change in ferroelectric

polarization. Intriguingly, a second ferroelectric transition occurs at the magnetic ordering temperature ($T_{N2} = 5.5$ K) of Tm^{3+} ions in TmFeWO_6 . The magnetic field-dependent behavior of ferroelectric polarization varies with R ion, indicating the coupling between $4f - 3d$ electrons. The emergence of change in ferroelectric polarization at the magnetic ordering temperatures demonstrates the multiferroic nature of the polar magnets $R\text{FeWO}_6$ ($R = \text{Tm}, \text{Sm}, \text{Gd}, \text{Ho}, \text{and Er}$).

Publications

1. “Linear magnetoelectric effect in antiferromagnetic $\text{Sm}_2\text{BaCuO}_5$ ”. **P. Yanda**, N. V. Ter-Oganessian, and A. Sundaresan, *Phys. Rev. B* **100**, 104417 (2019).
2. “Interplay of $4f - 3d$ interactions and spin-induced ferroelectricity in the green phase $\text{Gd}_2\text{BaCuO}_5$ ”. **P. Yanda**, I. V Golosovsky, I. Mirebeau, N. V. Ter-Oganessian, J. Rodríguez-Carvajal, and A. Sundaresan, *Phys. Rev. Res.* **2**, 023271 (2020).
3. “Magnetic-order-induced ferroelectric polarization in the polar antiferromagnets $R\text{FeWO}_6$ ($R = \text{Sm}, \text{Gd}, \text{Er}, \text{and Tm}$)”. **P. Yanda**, Swarnamayee Mishra and A. Sundaresan, *Phys. Rev. Materials* **5**, 074406 (2021).
4. “Magnetic-field-induced ferroelectric states in centrosymmetric $R_2\text{BaCuO}_5$ ($R = \text{Dy}$ and Ho)”. **P. Yanda**, F. Orlandi, P. Manuel, N. Boudjada, J. Rodríguez-Carvajal and A. Sundaresan, *Phys. Rev. B* **104**, 144401 (2021).
5. “Magnetic and magnetoelectric properties of $R_2\text{BaCuO}_5$ ($R = \text{Er}, \text{Eu}, \text{Y}, \text{Lu}, \text{and Tm}$)”. **P. Yanda**, J. Rodríguez-Carvajal and A. Sundaresan, to be communicated (2021).
6. “Magnetic phase transitions and magnetodielectric effect in $\text{Yb}_2\text{BaCuO}_5$ ”. **P. Yanda**, J. Rodríguez-Carvajal and A. Sundaresan, manuscript under preparation (2021).

Other Publications

1. “Spontaneous electric polarization in the B-site magnetic spinel GeCu_2O_4 ”. **P. Yanda**, S. Ghara, and A. Sundaresan, *Solid State Commun.* **272**, 53 (2018).
2. “Magnetism, magnetocaloric and magnetodielectric properties of DyVWO_6 : a new aeschynite-type polar antiferromagnet”. **P. Yanda** and A. Sundaresan, *Mater. Res. Express* **6**, 124007 (2020).
3. Book chapter: “Linear magnetoelectrics and multiferroics”, **P. Yanda** and A. Sundaresan, in *Adv. Chem. Phys. Mater.* (WORLD SCIENTIFIC, 2019), pp. 224–248.

Miscellaneous Publications

1. “Magnetoelectric effect in the honeycomb-lattice antiferromagnet $\text{BaNi}_2(\text{PO}_4)_2$ ”. S. Mishra, **P. Yanda**, A. Sundaresan, *Phys. Rev. B* **103**, 214443 (2021).
2. “Cluster-glass behavior in the 2D-triangular lattice Ising-spin compound $\text{Li}_2\text{Mn}_3\text{O}_7$ ”. R. Kumar, **P. Yanda**, A. Sundaresan, *Phys. Rev. B* **103**, 214427 (2021).
3. “Effect of Nd substitution on magnetoelectric properties of $\text{Sm}_2\text{BaCuO}_5$ ”. S. Mishra, **P. Yanda**, A. Sundaresan, *Bull. Mater. Sci.* **43**, 1–7 (2020).
4. “Synthesis, structure, optical and magnetic properties of $\text{Nd}_{1-x}\text{A}_x\text{Mn}_{0.5}\text{Co}_{0.5}\text{O}_{3-\delta}$ ($A = \text{Ba}$, Sr and Ca ; $x = 0$ and 0.25)”. A. Hossain, **P. Yanda**, V.A. Cherepanov, K. Sakthipandi, A. Sundaresan, *Ceram. Int.* **46**, 26895–26902 (2020).
5. “Suppression of long-range ordering and multiferroicity in Sr-substituted $\text{Ba}_{3-x}\text{Sr}_x\text{MnNb}_2\text{O}_9$ ($x = 1$ and 3)”. S. Sharma, **P. Yanda**, P. Yadav, I. da Silva, A. Sundaresan, *J. Magn. Magn. Mater.* **512**, 166990 (2020).
6. “Broadband Colossal Dielectric Constant in the Superionic Halide RbAg_4I_5 : Role of Intercluster Ag^+ Diffusion”. P. Acharyya, T. Ghosh, S.M, R.K.B, **P. Yanda**, S.R. Varanasi, D. Sanyal, A. Sundaresan, S.K. Pati, K. Biswas, *J. Phys. Chem. C* **124**, 9802–9809 (2020).
7. “Evidence of a cluster spin-glass state in B-site disordered perovskite $\text{SrTi}_{0.5}\text{Mn}_{0.5}\text{O}_3$ ”. S. Sharma, P. Yadav, T. Sau, **P. Yanda**, P.J. Baker, I. da Silva, A. Sundaresan, N.P. Lalla, *J. Magn. Magn. Mater.* **492** 165671 (2019).
8. “Ground-state ferrimagnetism and magneto-caloric effects in $\text{Nd}_2\text{NiMnO}_6$ ”. R. Das, **P. Yanda**, A. Sundaresan, D.D. Sarma, *Mater. Res. Express.* **6** 116122 (2019).
9. “Average Structure, Local Structure, Photoluminescence, and NLO Properties of Scheelite Type $\text{NaCe}(\text{WO}_4)_2$ ”. A.K.M, J.C. Neuefeind, **P. Yanda**, A. Sundaresan, I. V Kityk, K. Ozga, J. Jedryka, A. Rao, N.G. Sundaram, *Cryst. Growth Des.* **19**, 6082–6091 (2019).
10. “Magnetic ground state, field-induced transitions, electronic structure, and optical bandgap of the frustrated antiferromagnet GeCo_2O_4 ”. P. Pramanik, S.G, **P. Yanda**, D.C.J, S. Pittala, A. Sundaresan, P.K. Mishra, S. Thota, M.S. Seehra, *Phys. Rev. B.* **99**, 134422 (2019).
11. “Influence of Fe substitution on structural and magnetic features of BiMn_2O_5 nanostructures”. V.M. Gaikwad, S. Goyal, **P. Yanda**, A. Sundaresan, S. Chakraverty, A.K. Ganguli, *J. Magn. Magn. Mater.* **452**, 120–128 (2018).

Contents

1. Introduction to magnetoelectrics and multiferroics

Summary	1
1.1. Historical Evolution: Magnetoelectrics and Multiferroics	3
1.2. Linear magnetoelectrics	4
1.2.1. Symmetry aspects	5
1.2.2. Microscopic theories	10
1.3. Multiferroics	11
1.3.1. Type-I multiferroics	11
1.3.1.1. Lone pair multiferroics	12
1.3.1.2. Geometrically frustrated multiferroics	13
1.3.1.3. Charge-ordered multiferroics	13
1.3.2. Type-II multiferroics	14
1.3.2.1. Exchange striction	15
1.3.2.2. Inverse DM interaction	16
1.3.2.3. <i>d-p</i> hybridization	19
1.3.3. Polar magnets as multiferroics	20
1.4. Magnetodielectric effect	22
1.5. Applications	22
1.6. Aim of the thesis	23
References	24

2. Experimental Techniques

Summary	29
2.1. Solid-state synthesis	31
2.2. Structural characterization	31
2.2.1. X-ray and neutron diffraction	31
2.2.2. Rietveld refinement	33
2.3. Physical property measurements	35
2.3.1. DC Magnetization	35
2.3.2. AC susceptibility	37

2.3.3. Heat Capacity	38
2.3.4. Dielectric study	40
2.3.5. Pyrocurrent and electric polarization	40
2.3.6. DC bias technique	42
References.....	44
PART A: Introduction to “Green Phases” – $R_2\text{BaCuO}_5$ ($R = \text{Rare Earth}$)	45
References.....	47
3. Linear magnetoelectric effect in the green phase $\text{Sm}_2\text{BaCuO}_5$	
Summary.....	49
3.1. Introduction	51
3.2. Experimental section	51
3.3. Results and discussion	52
3.3.1. Crystal structure	52
3.3.2. DC magnetic susceptibility, heat capacity, and AC susceptibility	53
3.3.3. Dielectric properties and magnetodielectric effect	56
3.3.4. Linear magnetoelectric effect	59
3.3.4.1. Pyrocurrent and electric polarization	59
3.3.4.2. Switching and DC bias measurements	61
3.3.5. Neutron diffraction and symmetry approach	62
3.4. Conclusion	65
References	66
4. Elliptical cycloidal phase and spin-driven multiferroicity in $\text{Gd}_2\text{BaCuO}_5$	
Summary.....	67
4.1. Introduction	69
4.2. Experimental section	70
4.3. Results and discussion	70
4.3.1. Crystal structure	70
4.3.2. DC magnetic susceptibility and heat capacity	72
4.3.3. Dielectric and pyrocurrent measurements	73
4.3.4. Neutron diffraction study	75
4.3.5. Theoretical approach	87
4.4. Conclusion	90

Appendix	91
References	91
5. Linear magnetoelectric effect and magnetic field-induced ferroelectricity in $R_2\text{BaCuO}_5$ ($R = \text{Dy}$, and Ho)	
Summary	93
5.1. Introduction	95
5.2. Experimental section	96
5.3. Results and discussion	96
5.3.1. Crystal structure	96
5.3.2. DC magnetic susceptibility and specific heat	99
5.3.3. Dielectric constant and electric polarization	101
5.3.4. Magnetic structure of $\text{Dy}_2\text{BaCuO}_5$	107
5.3.5. Magnetic structure of $\text{Ho}_2\text{BaCuO}_5$	111
5.4. Conclusion	120
References	122
6. Role of $4f$-$3d$ coupling on multiferroic properties of $R_2\text{BaCuO}_5$ ($R = \text{Er}$, Eu, Y, Tm, Yb, and Lu)	
Summary	125
6.1. Introduction	127
6.2. Experimental section	128
6.3. Results and discussion	128
6.3.1. Crystal structure and UV-Vis spectra	128
6.3.2. Field-induced ferroelectricity in $\text{Er}_2\text{BaCuO}_5$	132
6.3.2.1. Magnetic properties	132
6.3.2.2. Neutron diffraction	134
6.3.2.3. Electrical properties	135
6.3.3. Absence of magnetoelectric coupling in $R_2\text{BaCuO}_5$ ($R = \text{Eu}$, Y , Lu , and Tm)	137
6.3.3.1. $\text{Eu}_2\text{BaCuO}_5$	137
6.3.3.2. $R_2\text{BaCuO}_5$ ($R = \text{Y}$ and Lu)	138
6.3.3.3. $\text{Tm}_2\text{BaCuO}_5$	140
6.3.4. Magnetic transitions and magnetodielectric effect in $\text{Yb}_2\text{BaCuO}_5$	142

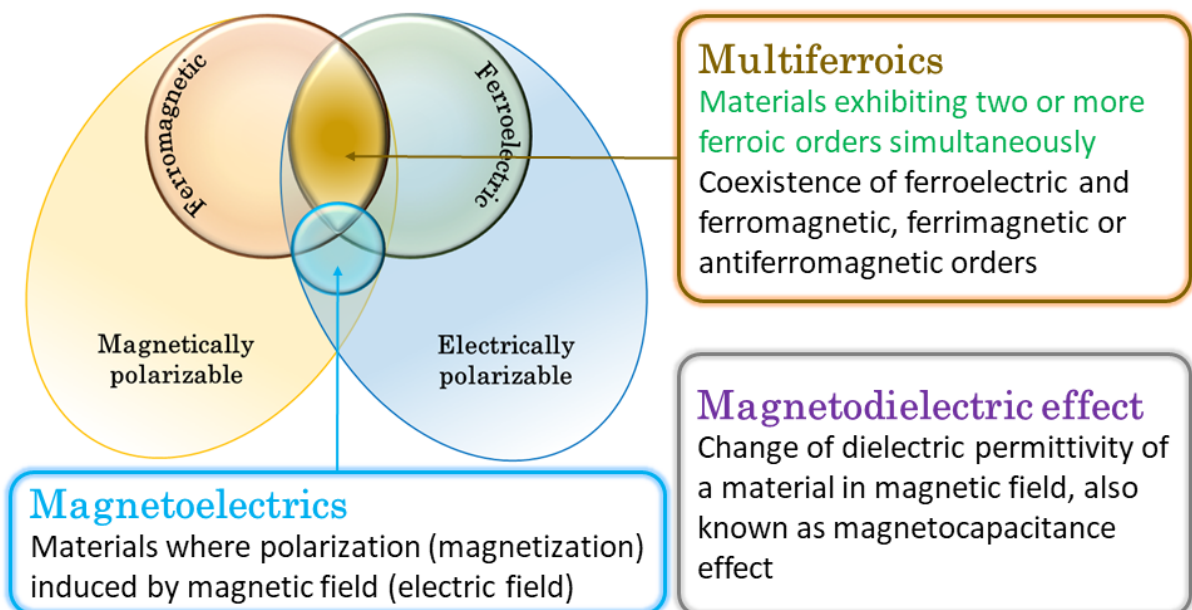
6.3.4.1. DC magnetization and heat capacity	142
6.3.4.2. Elastic neutron scattering	143
6.3.4.3. Dielectric study	144
6.4. Conclusion	147
References	148
7. PART B: Magnetic order-induced change in ferroelectric polarization in aeschynites	
<i>R</i>FeWO₆ (<i>R</i> = Sm, Gd, Ho, Er, and Tm)	
Summary	149
7.1. Introduction	151
7.2. Experimental section	152
7.3. Results and discussion	153
7.3.1. Crystal structure	153
7.3.2. TmFeWO ₆	157
7.3.3. SmFeWO ₆	160
7.3.4. GdFeWO ₆	161
7.3.5. HoFeWO ₆	163
7.3.6. ErFeWO ₆	165
7.4. Conclusion	168
References	169
Summary of thesis	172

Chapter 1

Introduction to magnetoelectrics and multiferroics

Summary

This chapter is dedicated to the introduction of magnetoelectric and multiferroic materials, where a brief history, fundamentals, and their plausible applications are presented. Firstly, magnetoelectric effect in magnetoelectrics, including symmetry requirements and microscopic origin is discussed in detail. Secondly, I have discussed different classes of multiferroics based on various mechanisms of ferroelectricity and introduced polar magnets as a different class of multiferroics. Following this, magnetodielectric effect is mentioned briefly. Finally, I have described the aim of this thesis.



1.1 Historical Evolution: Magnetolectrics and Multiferroics

Electricity and magnetism are known from ancient times, and they were considered to be two separate forces until the 17th century. The relation between them was examined by two different researchers Dr. Cookson (1735) and Gian Domenico Romagnosi (1802) for the first time. However, their findings were overlooked by the contemporary scientific community. In 1820, Ørsted observed the relation between electric and magnetic fields. His findings motivated intensive research in electrodynamics by Ampère and Faraday. Later, this view was transformed in 1873 by the famous Maxwell's equations. In 1888, the magnetoelectric effect was first discussed by Wilhelm Röntgen, who showed that a dielectric moving in electric field is magnetized. But the possibility of cross coupling between magnetic and electric fields coupling in substances was first proposed by Pierre Curie in 1894, while the name magnetoelectric is given by P. Debye in 1926 [1–4]. However, it was suggested by Piccardo, Debye, Van Vleck that magnetoelectric coupling is impossible. After 30 years of limited activity, Landau and Lifshitz in 1959 showed the probability of linear coupling between magnetic and electric fields in substances with certain magneto crystalline symmetry [5]. Soon after that, depends on symmetry grounds, Dzyaloshinskii anticipated that the antiferromagnetic Cr_2O_3 should exhibit *linear magnetoelectric (ME) effect* [6]. The prediction was confirmed experimentally in a single crystal of Cr_2O_3 by Astrov, where he found electric field-induced magnetization [7]. Simultaneously, Rado and Folen found the converse effect i.e., magnetic field induced polarization in the same material [8]. Thenceforth, several materials were found to exhibit ME effect [9–12]. Later, coexistence of ferroelectric and magnetic orders was found in magnetically diluted ferroelectric oxides, such as $\text{Pb}(\text{Fe}_{1/2}\text{Nb}_{1/2})\text{O}_3$ and $\text{Pb}(\text{Fe}_{1/2}\text{Ta}_{1/2})\text{O}_3$ [13]. Also, a clear coupling between weak ferromagnetism and ferroelectricity was demonstrated in the nickel iodine boracite $\text{Ni}_3\text{B}_7\text{O}_{13}\text{I}$ [14]. Afterward, Hans Schmid in 1994 coined a new name *multiferroic* to represent materials having two or more primary ferroic properties in the same phase [15]. However, the field of multiferroicity did not progress much until the end of the 20th century partly because ferroelectricity and magnetism have been practiced independently.

Apparently, the article *why are there so few magnetic ferroelectrics* by Hill in 2000 [16] attracted the attention of both ferroelectric and magnetic research communities towards the study of these fascinating magnetoelectric and multiferroic materials. The long-awaited period was finally over by two major breakthroughs in 2003, which were discovery of multiferroicity

in TbMnO_3 and BiFeO_3 thin films [17,18]. Now, the study of magnetoelectric coupling in materials has become one of the popular topics of modern-day interest in solid-state physics not only because of their fascinating physics and chemistry but also for their potential for applications. Subsequently, many research activities in this field resulted in various kinds of multiferroics with different coupling strengths between ferroelectricity and magnetism based on the origin of electric polarization [19–25]. This field further extended to composite and domain multiferroics; however, these two topics are out of the scope of this thesis.

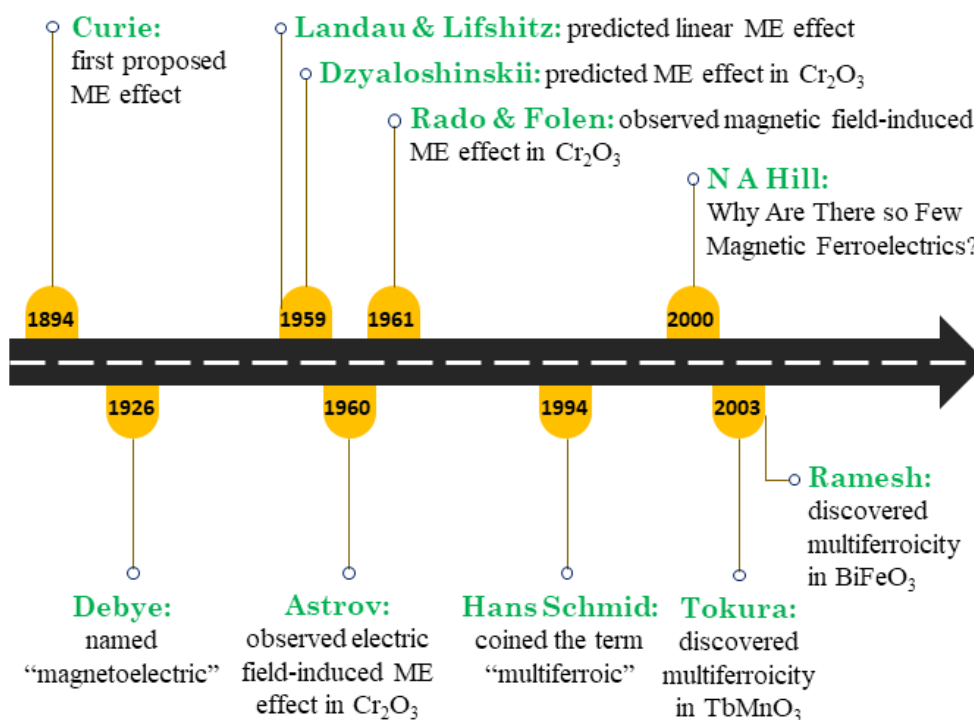


Figure 1.1 Road map of magnetoelectrics and multiferroics.

1.2 Linear magnetoelectrics

The induction of polarization by magnetic field and magnetization by electric field is known as magnetoelectric effect. Materials that exhibit magnetoelectric effect and show linear response to the applied fields are called linear magnetoelectrics, also known as magnetoelectrics. Linear magnetoelectric materials exhibit polarization at the magnetic ordering temperature only under applied magnetic fields and thereby differ from the multiferroics where a spontaneous electric polarization occurs at the magnetic ordering temperature or independently at high temperatures. Various contributions to magnetoelectric effect in materials is obtained from Taylor's expansion of free energy with electric field \vec{E} and magnetic field \vec{H} [1],

$$\begin{aligned}
F(E, H) = & F_0 - P_i^S E_i - M_i^S H_i - \frac{1}{2} \epsilon_0 \epsilon_{ij} E_i E_j - \frac{1}{2} \mu_0 \mu_{ij} H_i H_j - \alpha_{ij} E_i H_j \\
& - \frac{1}{2} \beta_{ijk} E_i H_j H_k - \frac{1}{2} \gamma_{ijk} H_i E_j E_k
\end{aligned} \quad (1)$$

From equation (1),

$$P_i(E, H) = -\frac{\partial F}{\partial E} = P_i^S - \frac{1}{2} \epsilon_0 \epsilon_{ij} E_j - \alpha_{ij} H_j - \frac{1}{2} \beta_{ijk} H_j H_k \quad (2)$$

$$M_i(E, H) = -\frac{\partial F}{\partial H} = M_i^S - \frac{1}{2} \mu_0 \mu_{ij} H_j - \alpha_{ij} E_j - \frac{1}{2} \gamma_{ijk} E_j E_k \quad (3)$$

Here, P_i^S and M_i^S are i^{th} component of the spontaneous electric polarization and spontaneous magnetization of the material. The second term in equations (2) and (3) is associated with the polarization (magnetization) induced by electric field (magnetic field), where ϵ and μ are electric and magnetic susceptibilities, respectively. The α_{ij} is a magnetoelectric tensor of rank 2, which defines the strength of coupling between electric and magnetic order parameters. From these terms, it is clear that polarization depends linearly on applied magnetic field and magnetization depends linearly on applied electric field. The coefficients β_{ijk} and γ_{ijk} are the higher-order terms which are responsible for the nonlinear magnetoelectric effect.

1.2.1 Symmetry aspects

Symmetry plays a vital role in deciding magnetoelectric and multiferroic properties of materials [1,2,26]. Spatial inversion (I) and time reversal (T) are two basic symmetry elements that govern magnetoelectrics or multiferroics. Firstly, let us consider polarization \vec{P} which is a polar vector, breaks the spatial inversion symmetry and is invariant under time reversal symmetry. In other words, polarization is odd under I and even under T , for example:

$$\vec{P}'_I = I\vec{P} = -\vec{P} \quad (4)$$

$$\vec{P}'_T = T\vec{P} = \vec{P}$$

In contrast, magnetization \vec{M} is an axial or pseudovector, breaks the time reversal symmetry but keeps the spatial inversion symmetry.

$$\vec{M}'_I = I\vec{M} = \vec{M} \quad (5)$$

$$\vec{M}'_T = T\vec{M} = -\vec{M}$$

One can understand these above rules by considering that polarization is dipole moment per unit volume. Since the dipole moment is simply $q\vec{r}$, where \vec{r} is the distance between the positive and negative charge q , the polarization switches sign under inversion which is $\vec{r} \rightarrow -\vec{r}$ but not under time reversal, $t \rightarrow -t$ (see Figure 1.2). On the other hand, magnetization is produced by the currents, invariant under spatial inversion. However, \vec{M} changes sign under time reversal which would reverse the direction of the current $\vec{J} = e\mathbf{v} = d\vec{r}/dt$ as shown in Figure 1.2 [27]. Thus, ferromagnetic material exhibits spontaneous magnetization by breaking time reversal symmetry. Likewise, antiferromagnetic (AFM) order parameter $\vec{L} = \vec{M}_1 - \vec{M}_2$ is odd under T -symmetry, which implies that AFM ordering also breaks the time reversal symmetry. Consequently, one can understand how \vec{P} and \vec{M} change under other symmetry transformations. For example, the polarization \vec{P} changes sign when it is perpendicular to the mirror plane and remains invariant when parallel to the plane [26]. In contrast, magnetization \vec{M} remains invariant under reflections when the moments are perpendicular to the mirror plane and changes sign in parallel case [26]. The action of all these symmetry operations together with spatial inversion and time reversal are very helpful in understanding the magnetoelectric properties. Therefore, from the above equations, the linear magnetoelectric effect exists in material if only I and T symmetries are simultaneously broken. However, the magnetic structure in these materials is invariant under the combined operation of IT . To simplify, for a material to exhibit linear magnetoelectric properties, the magnetic point group must break the inversion symmetry of the paramagnetic state.

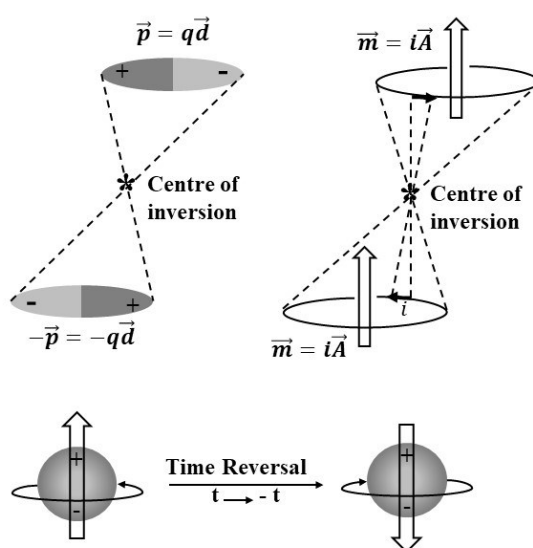


Figure 1.2 Transformation of electric and magnetic dipoles under space inversion and time reversal symmetries.

This argument can easily be understood by the classic example of linear magnetoelectric antiferromagnet Cr_2O_3 and contrasted with the antiferromagnetic Fe_2O_3 , which has the same crystal structure ($R\bar{3}c$) but different magnetic structure that does not allow magnetoelectric effect [27]. The crystal and magnetic structures of the isostructural compounds, Cr_2O_3 and Fe_2O_3 , having four cations per unit cell, are shown in Figure 1.3. Though these compounds have the same crystal structure with the magnetic point group $\bar{3}m1'$, they exhibit different antiferromagnetic spin structures corresponding to the magnetic point groups $\bar{3}m$ and $\bar{3}'m'$, respectively. As seen in Figure 1.3, the inversion symmetry is not broken in Fe_2O_3 because the spin direction remains invariant about the inversion center marked by the asterisk. On the other hand, the inversion symmetry is broken in Cr_2O_3 where the spins about the inversion center have opposite directions. Therefore, the condition of breaking of both time reversal and inversion symmetries are met in Cr_2O_3 but not in Fe_2O_3 .

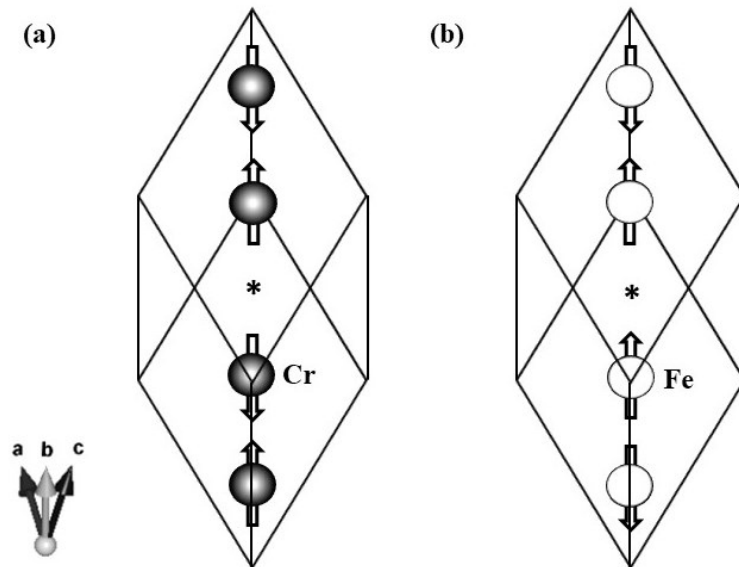


Figure 1.3 Magnetic structure in a rhombohedral unit cell of (a) Cr_2O_3 (b) Fe_2O_3 . Inversion symmetry broke in Cr_2O_3 with respect to spin arrangement whereas it is present in Fe_2O_3 .

Table 1.1 The magnetic point groups and corresponding magnetoelectric tensor forms of the linear ME effect are shown [28]. The monoclinic magnetic point groups have different settings with the 2 or 2' axis either parallel (\parallel) or perpendicular (\perp) to the \mathbf{x} , \mathbf{y} , or \mathbf{z} crystallographic axes, respectively. The most common setting for the monoclinic point groups is where the 2 or 2' axis is parallel to the \mathbf{y} -axis or perpendicular to the monoclinic plane. For orthorhombic symmetries, the recommended setting is the one with the 2 or 2' axis parallel to the \mathbf{z} -axis. Non-standard magnetic point groups are in red. Therefore, a total of 58 magnetic point groups that allow linear magnetoelectric effect are shown in black. It is important to know all possible tensors to understand magnetoelectric effect. This table is generated based on the Ref. [28].

$1, \bar{1}'$	$\begin{pmatrix} \alpha_{11} & \alpha_{12} & \alpha_{13} \\ \alpha_{21} & \alpha_{22} & \alpha_{23} \\ \alpha_{31} & \alpha_{32} & \alpha_{33} \end{pmatrix}$
$2 \quad m' \quad 2/m'$ $\parallel z \quad \perp z \quad \parallel \perp z$	$\begin{pmatrix} \alpha_{11} & \alpha_{12} & 0 \\ \alpha_{21} & \alpha_{22} & 0 \\ 0 & 0 & \alpha_{33} \end{pmatrix}$
$2' \quad m \quad 2'/m$ $\parallel z \quad \perp z \quad \parallel \perp z$	$\begin{pmatrix} 0 & 0 & \alpha_{13} \\ 0 & 0 & \alpha_{23} \\ \alpha_{31} & \alpha_{32} & 0 \end{pmatrix}$
$2 \quad m' \quad 2/m'$ $\parallel y \quad \perp y \quad \parallel \perp y$	$\begin{pmatrix} \alpha_{11} & 0 & \alpha_{13} \\ 0 & \alpha_{22} & 0 \\ \alpha_{31} & 0 & \alpha_{33} \end{pmatrix}$
$2' \quad m \quad 2'/m$ $\parallel y \quad \perp y \quad \parallel \perp y$	$\begin{pmatrix} 0 & \alpha_{12} & 0 \\ \alpha_{21} & 0 & \alpha_{23} \\ 0 & \alpha_{32} & 0 \end{pmatrix}$
$2 \quad m' \quad 2/m'$ $\parallel x \quad \perp x \quad \parallel \perp x$	$\begin{pmatrix} \alpha_{11} & 0 & 0 \\ 0 & \alpha_{22} & \alpha_{23} \\ 0 & \alpha_{32} & \alpha_{33} \end{pmatrix}$
$2' \quad m \quad 2'/m$ $\parallel x \quad \perp x \quad \parallel \perp x$	$\begin{pmatrix} 0 & \alpha_{12} & \alpha_{13} \\ \alpha_{21} & 0 & 0 \\ \alpha_{31} & 0 & 0 \end{pmatrix}$
$222 \quad 2m'm' \quad m'2m' \quad m'm'2 \quad m'm'm'$ $\parallel x \parallel y \parallel z \quad \perp x \perp y \parallel z \quad \parallel x \perp y \perp z \quad \perp x \parallel y \perp z \quad \perp x \perp y \perp z$	$\begin{pmatrix} \alpha_{11} & 0 & 0 \\ 0 & \alpha_{22} & 0 \\ 0 & 0 & \alpha_{33} \end{pmatrix}$
$2'2'2 \quad mm2 \quad 2'mm' \quad m2'm' \quad mmm'$ $\parallel x \parallel y \parallel z \quad \perp x \perp y \parallel z \quad \parallel x \perp y \perp z \quad \perp x \parallel y \perp z \quad \perp x \perp y \perp z$	$\begin{pmatrix} 0 & \alpha_{12} & 0 \\ \alpha_{21} & 0 & 0 \\ 0 & 0 & 0 \end{pmatrix}$
$2'22' \quad m2m \quad mm'2' \quad 2'm'm \quad mm'm$ $\parallel x \parallel y \parallel z \quad \perp x \parallel y \perp z \quad \perp x \perp y \parallel z \quad \parallel x \perp y \perp z \quad \perp x \perp y \perp z$	$\begin{pmatrix} 0 & 0 & \alpha_{13} \\ 0 & 0 & 0 \\ \alpha_{31} & 0 & 0 \end{pmatrix}$
$22'2' \quad 2mm \quad m'2'm \quad m'm2' \quad m'mm$ $\parallel x \parallel y \parallel z \quad \parallel x \perp y \perp z \quad \perp x \parallel y \perp z \quad \perp x \perp y \parallel z \quad \perp x \perp y \perp z$	$\begin{pmatrix} 0 & 0 & 0 \\ 0 & 0 & \alpha_{23} \\ 0 & \alpha_{32} & 0 \end{pmatrix}$
$4 \quad \bar{4}' \quad 4/m' \quad 3 \quad \bar{3}' \quad 6 \quad \bar{6}' \quad 6/m'$	$\begin{pmatrix} \alpha_{11} & \alpha_{12} & 0 \\ -\alpha_{12} & \alpha_{11} & 0 \\ 0 & 0 & \alpha_{33} \end{pmatrix}$
$4' \quad \bar{4} \quad 4'/m'$	$\begin{pmatrix} \alpha_{11} & \alpha_{12} & 0 \\ \alpha_{12} & -\alpha_{11} & 0 \\ 0 & 0 & 0 \end{pmatrix}$
$422 \quad 4m'm' \quad [\bar{4}'2m' \quad \bar{4}'m'2'] \quad 4/m'm'm'$ $32 \quad 3m' \quad \bar{3}'m'$	$\begin{pmatrix} \alpha_{11} & 0 & 0 \\ 0 & \alpha_{11} & 0 \\ 0 & 0 & \alpha_{33} \end{pmatrix}$
$622 \quad 6m'm' \quad [\bar{6}'m'2 \quad \bar{6}'2m'] \quad 6/m'm'm'$	$\begin{pmatrix} \alpha_{11} & 0 & 0 \\ 0 & \alpha_{11} & 0 \\ 0 & 0 & \alpha_{33} \end{pmatrix}$
$4'2'2 \quad 4'mm' \quad \bar{4}m2 \quad \bar{4}2'm' \quad 4'/m'mm'$ $\parallel z \parallel x \parallel d \quad \parallel z \perp x \perp d \quad \parallel z \parallel x \perp d \quad \parallel z \parallel x \perp d \quad \parallel z \perp z \perp x \perp d$	$\begin{pmatrix} \alpha_{11} & 0 & 0 \\ 0 & -\alpha_{11} & 0 \\ 0 & 0 & 0 \end{pmatrix}$
$4'2'2 \quad 4'mm' \quad \bar{4}m2 \quad \bar{4}2'm' \quad 4'/m'mm'$ $\parallel z \parallel x \parallel d \quad \parallel z \perp x \perp d \quad \parallel z \parallel x \perp d \quad \parallel z \parallel x \perp d \quad \parallel z \perp z \perp x \perp d$	$\begin{pmatrix} 0 & \alpha_{12} & 0 \\ \alpha_{12} & 0 & 0 \\ 0 & 0 & 0 \end{pmatrix}$
$42'2' \quad 4mm \quad [\bar{4}'2'm \quad \bar{4}'m'2'] \quad 4/m'mm$ $32' \quad 3m \quad \bar{3}'m$	$\begin{pmatrix} 0 & \alpha_{12} & 0 \\ -\alpha_{12} & 0 & 0 \\ 0 & 0 & 0 \end{pmatrix}$
$62'2' \quad 6mm \quad [\bar{6}'m2' \quad \bar{6}'2'm] \quad 6/m'mm$	$\begin{pmatrix} 0 & \alpha_{12} & 0 \\ -\alpha_{12} & 0 & 0 \\ 0 & 0 & 0 \end{pmatrix}$
$42 \quad m'\bar{3}' \quad 432 \quad \bar{4}'3m' \quad m'\bar{3}'m'$	$\begin{pmatrix} \alpha_{11} & 0 & 0 \\ 0 & \alpha_{11} & 0 \\ 0 & 0 & \alpha_{11} \end{pmatrix}$

As mentioned earlier, the discussion of magnetoelectric effect involves the symmetry of the arrangement of the magnetic moment rather than the symmetry of the crystallographic arrangement of atoms or ions alone. To describe the magnetic structure of the materials, combining the conventional spatial symmetry operations with the time reversal operation increases the number of crystal classes to 122 by adding 90 additional magnetic point groups. Out of this, only 58 magnetic point groups allow linear magnetoelectric effect [26]. Using Neumann's principle, one can calculate the linear magnetoelectric coefficient (α_{ij}) from the magnetic symmetry and can check the possibility of magnetoelectric effect, as shown in Table 1.1. One can show that magnetoelectric tensor α_{ij} of Cr_2O_3 in antiferromagnetic phase is of the form [27],

$$\alpha_{ij} = \begin{pmatrix} \alpha_{xx} & 0 & 0 \\ 0 & \alpha_{yy} & 0 \\ 0 & 0 & \alpha_{zz} \end{pmatrix}$$

The magnetoelectric coefficients, α_{xx} and α_{zz} become zero at $T_N = 307$ K where the long-range antiferromagnetic ordering disappears. Since antiferromagnets also have domains, it is important to pole the crystal/ceramics to make them a single domain before measuring the magnetoelectric coefficients in $E \parallel H$ or $E \perp H$ configurations based on diagonal or non-diagonal magnetoelectric tensors, respectively. Hence, symmetry plays a crucial role in choosing the material for magnetoelectric effect.

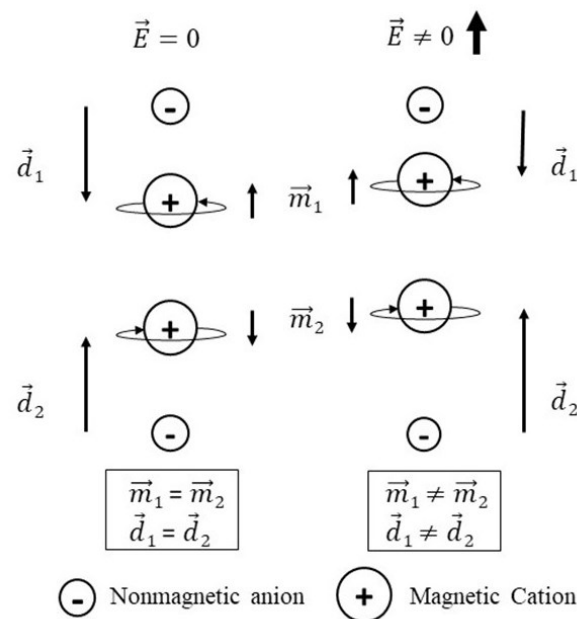


Figure 1.4 One dimensional model which explains the magnetoelectric effect.

1.2.2 Microscopic theories

One can predict the magnetoelectric materials based on the symmetry but cannot estimate the strength of the coupling by the same. To obtain the magnitude of each magnetoelectric coefficient, knowledge about the microscopic origins that induce the magnetoelectric effect is required. Several microscopic theories have been suggested for different spin structures, such as single-ion anisotropy, symmetric and antisymmetric super exchange interaction, and dipolar interactions [29]. Here, I discuss the atomic origin of magnetoelectric effect in Cr_2O_3 as illustrated in Figure 1.4 where an electrically induced magnetoelectric effect is considered [26]. In the absence of applied electric field, the dipoles cancel each other and result in zero net polarization or magnetization. When an electric field is applied along the chain direction, the cations move along the field direction and the anions move in opposite directions generating an electric polarization. The difference in the proximity of cation-anion about the inversion center results in increase or decrease in electron overlap that affects the orbital motion in the cations. This causes an imbalance in the up and down spins, causing a net magnetic moment. Thus, the applied electric field induces a magnetic moment proportional to the electric field. Theoretical understanding of these microscopic origins suggests a weak magnetoelectric coupling. It was shown that the magnetoelectric response is limited by the relation [30],

$$\alpha_{ij} \leq \sqrt{\chi_{ii}^e \chi_{jj}^m}$$

where χ^e and χ^m are the electric and magnetic susceptibilities. This equation suggests that the materials with coexisting ferroelectric and ferromagnetic properties can have large magnetoelectric effect.

Table 1.2 Some examples of linear magnetoelectrics.

Compound	Mag. Symm.	Ref.	Compound	Mag. Symm.	Ref.
Cr_2O_3	$\bar{3}'m'$	[31]	$\text{Fe}_4\text{Nb}_2\text{O}_9$	$\bar{1}'$	[32]
RAIO_3 ($R = \text{Dy, Gd, \& Tb}$)	$m'm'm'$		MnTiO_3	$\bar{3}'$	[33]
TbPO_4	mmm'		NdCrTiO_5	mmm'	[34]
TbCoO_3	$m'm'm'$		Co_3O_4	$\bar{3}'m'$	[35]
LiAPO_4 ($A = \text{Fe, Co, \& Ni}$)	mmm'		MnGa_2O_4	$\bar{3}'m'$	[35]
LiMnPO_4	$m'm'm'$		CoAl_2O_4	$\bar{3}'m'$	[36]
Fe_2TeO_6	$4/m'm'm'$		$\alpha\text{-FeOOH}$	$m'mm$	[37]
Cr_2WO_6	$m'mm$		DyCrO_4	$2'/m$	[38]
$\text{A}_4\text{Nb}_2\text{O}_9$ ($A = \text{Mn \& Co}$)	$\bar{3}'m'$		$\text{BaNi}_2(\text{PO}_4)_2$	$\bar{1}'$	[39]

1.3 Multiferroics

Multiferroics are the materials where ferroelectricity and ferromagnetism coexist and are coupled to each other. Since ferroelectricity and ferromagnetism have large electric and magnetic susceptibilities, multiferroics can be good candidates to exhibit strong magnetoelectric effects. However, designing new multiferroics is challenging for the following reasons:

Symmetry restrictions: Broken spatial inversion and time reversal symmetries are prerequisites for ferroelectricity and magnetism. It turns out that only 13-point groups out of 233 Shubnikov magnetic point groups that are 1, 2, 2', m , m' , 3, 3 m' , 4, 4 $m'm'$, $m'm2'$, $m'm'2'$, 6 and 6 $m'm'$ allow the coupling between electric polarization and magnetization.

Electronic constraints: Most of the perovskite oxides, such as BaTiO₃, exhibit ferroelectricity where the transition metal ion with d^0 electronic states, such as Ti⁴⁺, Zr⁴⁺, and Nb⁵⁺, is responsible for ferroelectric polarization. In contrast, magnetism requires a partially filled d (or f) shell.

Electrical limitation: In general, ferroelectrics are insulators. Otherwise, an applied electric field produces a flow of electric current instead of electric polarization. On the other hand, most ferromagnetic materials are metallic. Materials that can exhibit both insulating and magnetic behavior are antiferromagnets, ferrimagnets, or weak ferromagnets.

Structural constraints: Incorporation of magnetism in conventional ferroelectrics is not allowed due to the second order Jahn-Teller distortion or covalency of transition metal ions with the surrounding oxygen ions.

However, extensive studies on multiferroics produced various ways to combine ferroelectricity with magnetism in single material [19]. Further, multiferroics are classified into type-I and type-II multiferroics depending on the origin of ferroelectricity [22,27].

1.3.1 Type-I multiferroics (Split-order-parameter)

Type-I multiferroics have a polar crystal structure, which exhibits ferroelectric and magnetic ordering at different temperatures due to their independent origin [22]. Since the polar structure is stabilized at high temperatures, the spatial inversion symmetry (I) is already broken, and magnetic ordering breaks the time reversal (T) symmetry at low temperatures.

Therefore, the condition of symmetry is met in these multiferroics. Unfortunately, the polar distortion relates to the off-center shift of nonmagnetic ions and thus, results in weak coupling between magnetism and ferroelectricity. However, there have been a lot of studies on type-I multiferroics in the recent past. Based on the mechanism of origin of ferroelectricity, these multiferroics are further classified; some are discussed below.

1.3.1.1 Lone pair multiferroics

Most of the lone pair ferroelectrics are perovskite oxides where ferroelectricity arises from lone-pair active A -site cations (Bi^{3+} or Pb^{2+}) and magnetism stems from B -site cations [22]. The $6s$ electrons sometimes do not participate in the bonding; rather, they form stereochemically active lone pairs. Since the lone pair state is unstable, the $6s$ orbitals hybridize with their own p orbitals or with the p orbitals of oxygen ions and thus resulting in lobe-shaped as shown in Figure 1.5(a). The uniform alignment of these lobes can break the inversion center and stabilizes the polar structure. For example, perovskite oxide PbVO_3 exhibits ferroelectricity, originating from the combined effect from covalency of d^0 transition metals with their surrounding oxygens and stereochemical active $6s$ lone pair electrons of Pb^{2+} ion, and the magnetism stems from V^{4+} ions [40]. In the same way, famous BiFeO_3 shows ferroelectric transition at $T_C = 1103$ K due to lone pairs of Bi^{3+} as described in Figure 1.5(a). It exhibits large ferroelectric polarization of $60 \mu\text{C}/\text{cm}^2$ at room temperature. In this compound, the Fe^{3+} spins undergo spiral antiferromagnetic ordering at $T_N = 643$ K [18]. Other examples of this type are BiMnO_3 , PbMnO_3 , $\text{Bi}_2\text{FeAlO}_6$, etc [22,41].

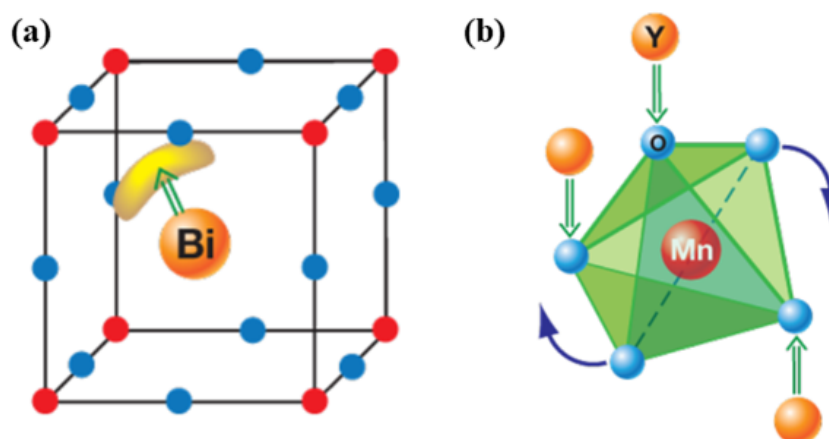


Figure 1.5 Microscopic mechanisms for lone pair and geometrically frustrated multiferroics (adapted from Ref. [22]). (a) The ordering of lone pairs (lobe – yellow) in BiFeO_3 stabilizes the polar structure. (b) Tilting of MnO_5 polyhedra in YMnO_3 , resulting in net polarization.

1.3.1.2 Geometrically frustrated multiferroics

The geometric frustration drives the ferroelectricity in hexagonal manganites $RMnO_3$ ($R = \text{Ho-Lu}$ and Y) with space group $P6_3cm$. As mentioned before, ferroelectricity in perovskite oxides originates from polar structural instability, known as *proper* ferroelectrics. In contrast, hexagonal manganites are *improper* ferroelectrics where the polarization is a by-product of complex lattice distortion. For example, $YMnO_3$ undergoes paraelectric to ferroelectric transition occurs $T_C = 950$ K and the Mn^{3+} ions order antiferromagnetically at $T_N = 77$ K [42]. The structure of hexagonal manganites is distinct from the perovskite, where the Mn^{3+} ions are coordinated by five oxygens in trigonal bipyramidal configuration. Also, $Mn-3d$ levels are split into two lower energy doublets and a high-energy singlet. Moreover, the buckled MnO_5 polyhedrons displace Y ions, as seen in Figure 1.5(b), promoting a net electric polarization. Though $YMnO_3$ exhibits ferroelectricity and magnetism, the magnetoelectric coupling remains weak due to their different origins.

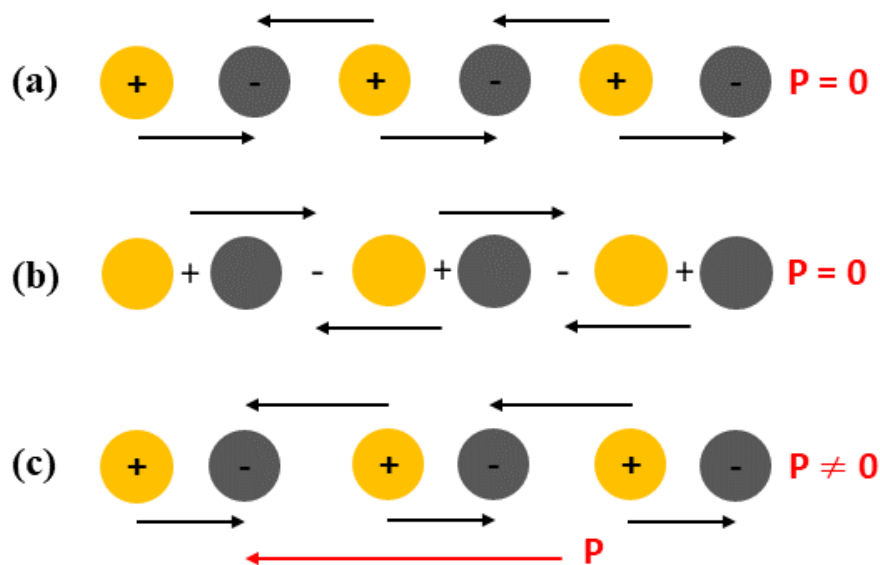


Figure 1.6 Mechanism for ferroelectricity induced due to charge ordering. (a) Site centered (b) Bond centered and (c) Site and bond centered charge ordering.

1.3.1.3 Charge-ordered multiferroics

Another group of improper ferroelectrics is charge-ordered insulators. Charge ordering can occur when cations with different valence are present at same structural site. As shown in Figure 1.6, the combination of site-centered and bond-centered charge ordering can result in ferroelectric polarization [43]. Examples for charge-ordered multiferroics are $(Pr,Ca)MnO_3$,

LuFe_2O_4 , RNiO_3 , and RMn_2O_5 [22,43]. However, the strength of the magnetoelectric coupling in this type is still an open question.

1.3.2 Type-II multiferroics (Joint-order-parameter)

In contrast to multiferroics mentioned above, type-II multiferroics possess centrosymmetric crystal structures and certain types of magnetic structures break the inversion center and induce spontaneous electric polarization at magnetic ordering [20,22,44,45]. As the polarization originates at the magnetic ordering temperature, the coupling between ferroelectricity and magnetism is inherently strong and they can be described by a single or joint order parameter. Such magnetically driven multiferroics are found in materials with competing magnetic interactions and frustration, where the magnetic ordering favors the complex magnetic structures. Unfortunately, polarization obtained in these multiferroics is several orders of magnitude smaller than the type-I multiferroics. Further, the condition of breaking spatial inversion (I) and time reversal (T) symmetries is achieved by magnetic ordering. However, in contrast to magnetoelectrics, the magnetic structure of these multiferroics is odd under combined operation (IT). As of today, three well-known microscopic mechanisms describe the formation of ferroelectricity by magnetism in the literature [44,46,47]. These mechanisms can be addressed by a simple cluster model consisting of two magnetic ions, carrying spins \vec{S}_i and \vec{S}_j , which are connected through the vector \vec{e} and hybridized through the ligand ion as illustrated in Figure 1.7 [48],

$$\mathbf{P} = \mathbf{P}^{ES}\vec{e} \cdot (\vec{S}_i \cdot \vec{S}_j) + \mathbf{P}^{DMI}\vec{e} \times (\vec{S}_i \times \vec{S}_j) + \mathbf{P}^{d-p} \left((\vec{e} \cdot \vec{S}_i) \cdot \vec{S}_i - (\vec{e} \cdot \vec{S}_j) \cdot \vec{S}_j \right) \quad (6)$$

Here, the three terms represent the ferroelectric polarization due to the exchange striction (\mathbf{P}^{ES}), inverse Dzyaloshinskii-Moriya (DM) interaction (\mathbf{P}^{DMI}), and d - p hybridization (\mathbf{P}^{d-p}), respectively. These mechanisms are discussed briefly below.

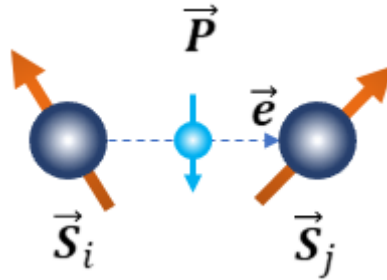


Figure 1.7 A simple two-spin cluster model.

1.3.2.1 Exchange striction or symmetric exchange

This mechanism involves the crystal structure deformation due to the change in bond length by the magnetic ordering which results in breaking of inversion symmetry and thus, allows macroscopic polarization [20,44]. The magnetic structure which induces ferroelectricity by this mechanism is generally commensurate with crystal periodicity. For example, a collinear up-up-down-down (UUDD) spin structure can induce electric polarization according to the exchange striction mechanism [20,44]. This type of UUDD spin structure occurs due to the presence of competing nearest-neighbor ferromagnetic (J_F) and next nearest-neighbor antiferromagnetic (J_{AF}) interactions when the ratio is $J_F/J_{AF} > 1/2$. Whereas the ratio between $1/2$ and $1/4$ favors the spiral magnetic ground state [20]. The occurrence of electric polarization due to ionic displacements in the UUDD spin structure can be understood by Goodenough-Kanamori-Anderson (GKA) rules as described in Figure 1.8 [49–51]. As seen from Figure 1.8(a), the GKA rules predict the antiferromagnetic alignment with bond angles close to 180° and ferromagnetic with bond angles approximately 90° . A simple antiferromagnetic UDUD spin chain is centrosymmetric and does not allow the polarization as seen from Figure 1.8(b). Furthermore, the UUDD structure induces polarization due to the difference between UU and UD bonds [see Figure 1.8(c)] [20,44,46]. The polarization for this case is represented by the first term in equation (6).

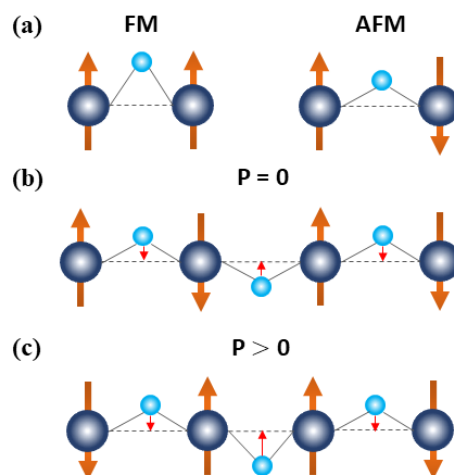


Figure 1.8 Illustration of exchange striction mechanism. (a) Goodenough-Kanamori-Anderson rules. (b) Centrosymmetric spin chain with no polarization. (c) Noncentrosymmetric spin chain with finite polarization.

As an example, I discuss the multiferroicity induced by the exchange striction mechanism in $\text{Ca}_3\text{CoMnO}_6$ [52]. This compound crystallizes in centrosymmetric $R\bar{3}c$ structure

with alternately ordered Co^{2+} and Mn^{4+} ions forming one-dimensional chains. Below $T_N = 16.5$ K, it exhibits commensurate antiferromagnetic ordering with up-up-down-down spin fashion as displayed in Figure 1.9(a) [52]. This spin structure allows electric polarization along the chain direction by breaking the inversion center of paramagnetic crystal structure as shown in Figure 1.9(b). Another interesting example of same kind is orthorhombic RMnO_3 with ($R = \text{Ho}, \text{Er}, \text{Tm}, \text{Yb}, \text{and Lu}$) which are stabilized by the high pressures [45,46]. Unlike $\text{Ca}_3\text{CoMnO}_6$, the magnetic ions in these materials are identical but with a zig-zag fashion of Mn^{3+} -O- Mn^{3+} bonds and exhibits E -type antiferromagnetic ordering. It has been shown that the exchange striction shifts oxygen ions perpendicular to the Mn-Mn bonds, resulting in polarization along the same direction. This mechanism is applicable for other materials such as RMn_2O_5 ($R = \text{Tb}, \text{Ho}, \text{Er}, \text{Tm}, \text{and Y}$) and RFeO_3 ($R = \text{Gd and Dy}$) [53–55]. The electric polarization in this type of materials results from the ionic displacements and therefore having higher polarization than that induced by inverse DM interaction, which will be discussed in the next section.

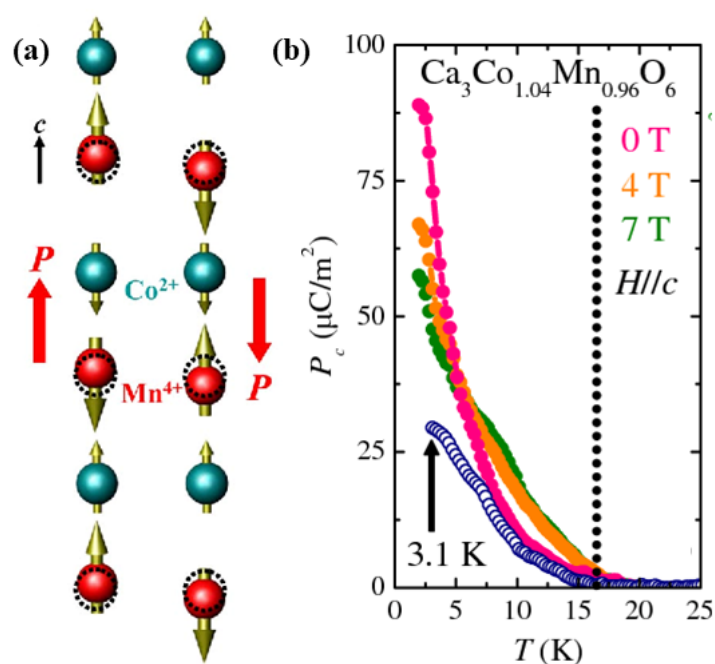


Figure 1.9 (a) Collinear UUDD spin structure of Ising magnet $\text{Ca}_3\text{CoMnO}_6$ and (b) electric polarization below magnetic ordering temperature (adapted with permission from Ref. [52], © (2008) by the American Physical Society).

1.3.2.2 Spin-current mechanism or inverse DM interaction

Magnetic frustration in materials due to competing interactions more often results in spiral magnetic orders [44]. Some of these spiral spin structures break the inversion symmetry

and induces ferroelectricity. The microscopic mechanism which induces the polarization in spiral magnets is described by the famous inverse DM interaction, also known as antisymmetric exchange interaction [20,44]. This interaction is a relativistic correction to the super exchange between two noncollinear spins \vec{S}_i and \vec{S}_j with the microscopic origin of spin orbit coupling. According to this mechanism, if spins are canted like in spiral magnets, then the ligand ion would shift in order to gain the DM interaction energy. In some cases, this shift can result in finite electric polarization of the form $\vec{P} \propto \vec{e}_{ij} \times (\vec{S}_i \times \vec{S}_j)$ as described in the Figure 1.10.

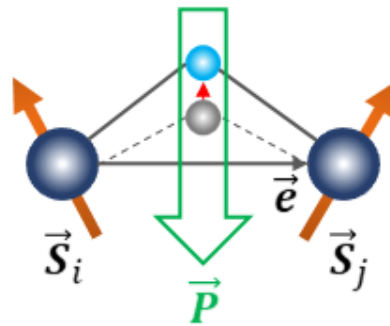


Figure 1.10 Mechanism of inverse DM interaction which shifts the ligand ion.

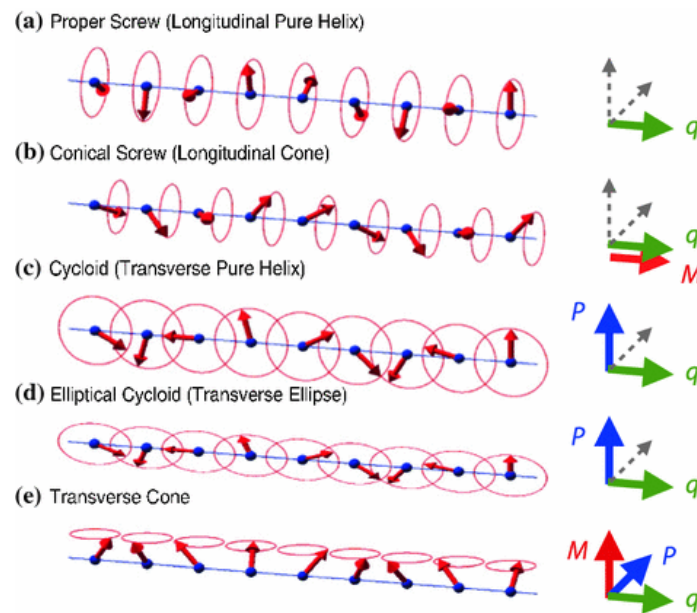


Figure 1.11 Various types of spiral spin structures. q , M , and P denote the propagation vector, magnetization, and electric polarization along with their direction expected from the inverse DM interaction (adapted with permission from Ref. [56], © (2012) by the Springer Nature).

I have shown the different spiral magnetic structures in Figure 1.11. According to inverse DM interaction, proper screw spin structure does not allow electric polarization [44]. The circular and elliptical cycloidal structures are shown in Figures 1.11(c and d), break the

inversion symmetry and allows the polarization direction perpendicular to the propagation vector [20,22,44]. The longitudinal and transverse conical spiral orders are displayed in Figures 1.11 (b and e), respectively. The antiferromagnetic components of the spins in the longitudinal cone form the screw structure and forbids the polarization. On the other hand, antiferromagnetic components in the transverse conical spin structure form a cycloid that allows electric polarization. Moreover, it can be noted that cycloidal magnetic structure does not have spontaneous magnetization but the transverse conical has both antiferromagnetic and ferromagnetic components. In other words, materials with transverse conical spin structure can induce the coupling between ferromagnetism and ferroelectricity. Below, I will briefly discuss two examples TbMnO_3 and CoCr_2O_4 , representing the cycloidal and transverse conical spin order induced ferroelectrics.

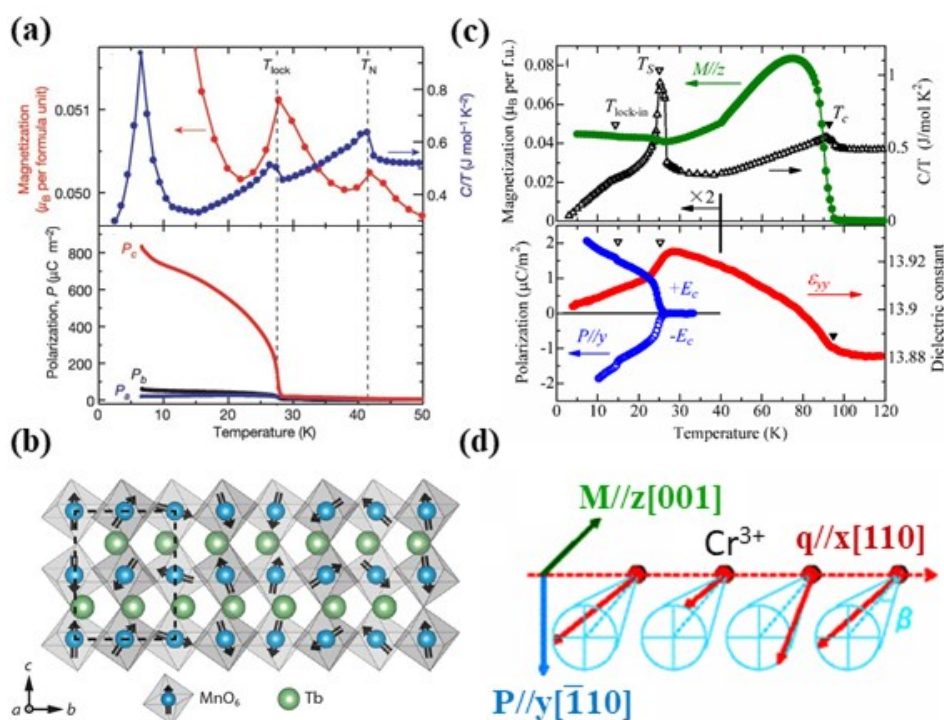


Figure 1.12 (a) Different magnetic transitions and electric polarization (adapted with permission from Ref. [17], © (2003) by the Nature Publishing Group) and (b) Cycloidal magnetic structure (adapted with permission from Ref. [57], © (2014) by the AAAS); for TbMnO_3 . (c) Electric polarization below magnetic ordering and (d) Transverse conical spin structure; for CoCr_2O_4 (adapted with permission from Ref. [58], © (2006) by the American Physical Society).

TbMnO_3 is the first and best-known example for cycloidal magnetic structure induced ferroelectricity, showing strong magnetoelectric coupling [17]. It crystallizes in orthorhombic structure with space group $Pbnm$ and exhibits a collinear sinusoidal antiferromagnetic ordering

at $T_{N1} \sim 42$ K. More importantly, it undergoes a cycloidal magnetic ordering at $T_{N2} \sim 28$ K as shown in Figure 1.12(a). In this structure, spins rotate in the **bc**-plane while the propagation direction is along the **b**-axis [see Figure 1.12(b)]. As explained before, cycloidal spin ordering breaks the inversion center by inverse DM interaction and induces electric polarization along the **c**-axis ($P_c \sim 600\text{--}800 \mu\text{C}/\text{m}^2$) as shown in Figure 1.12(a) [17]. Cycloidal spin order driven ferroelectricity has been observed in well-known materials such as $\text{Ni}_3\text{V}_2\text{O}_8$, MnWO_4 , LiCu_2O_2 , LiCuVO_4 , BaYFeO_4 , and CuO , etc [59–64].

The classic material that exhibits a transverse conical magnetic structure is the normal spinel CoCr_2O_4 [58]. This compound crystallizes in cubic $Fd\bar{3}m$ structure and shows a ferrimagnetic transition at $T_C = 93$ K as shown in Figure 1.12(c). At $T_S = 26$ K, it transforms to the incommensurate transverse conical spin state, where the ferromagnetic component of spins pointed along z-direction and other components form cycloid in plane perpendicular to z-direction as illustrated in Figure 1.12(d) [58]. This magnetic structure induces polarization which is successfully explained by the spin current mechanism. Further, it undergoes to a lock-in phase transition at $T = 15$ K below which the spin structure is commensurate. The other example that belongs to this category is the Y-type hexaferrite $\text{Ba}_2\text{Mg}_2\text{Fe}_{12}\text{O}_{22}$. However, this compound exhibits the longitudinal spin structure and transforms to a transverse conical structure under low magnetic fields, thus inducing polarization [48].

1.3.2.3 *d-p* hybridization

Another member of spiral magnets is an incommensurate proper screw spin structure where spins rotate in the plane perpendicular to the propagation direction. The delafossite oxides AMO_2 ($A = \text{Cu}, \text{Ag}$ and $M = \text{Cr}, \text{Fe}$) where the magnetic MO_2 units form a layered triangular lattice known to exhibit the proper screw spin structure [65,66]. According to the spin current model, this structure does not allow spontaneous electric polarization. Therefore, spin-dependent *p-d* hybridization was proposed to explain the proper screw-induced electric polarization in these compounds [67]. The main difference is that this mechanism deals with a single magnetic site, while the spin current model involves two magnetic sites. The underlying mechanism in this model involves hybridization of *d*-orbitals of transition metal with ligand's *p*-orbitals depending on the direction of local spin moment through relativistic spin-orbit coupling which results in net polarization. A typical example is the rhombohedral CuFeO_2 where a proper screw magnetic structure with a 120° spin rotation angle allows electric

polarization along the bond direction, which is governed by this mechanism [66]. The other examples of this type are MI_2 ($M = \text{Mn, Ni}$) with CdI_2 structure [67]. Later, a careful symmetry analysis has demonstrated that this model cannot induce electric polarization if the magnetic ions are located at the local centrosymmetric site since all the dipoles will cancel each other [68]. However, this model is applied to noncentrosymmetric $\text{Ba}_2\text{CoGe}_2\text{O}_7$ with a tetragonal structure ($P\bar{4}2_1m$) and $R\text{Fe}_3(\text{BO}_3)_4$ having $R32$ structure, which evidences the proper screw induced ferroelectricity [69,70].

1.3.3 Polar magnets as multiferroics

In type-I multiferroics, the ferroelectricity originating from the polar structural distortion occurs at high temperatures and the magnetism appears at low temperatures and thus, there is a weak coupling between the ferroelectricity and magnetism [22]. On the other hand, type-II multiferroics possess centrosymmetric crystal structures, and inversion symmetry is broken by the magnetic ordering with complex spin structures, inducing electric polarization with strong magnetoelectric coupling [20,44]. In this section, a new class of multiferroics which are mostly pyroelectric at all temperatures and the magnetic ordering induces a change in polarization (ΔP) are discussed [25,71]. The fact that the polarization is enhanced at the magnetic ordering temperature and is influenced positively or negatively by the external magnetic field evidence the magnetoelectric effect. Though this class of materials may appear to have commonalities with type-I and type-II materials, these materials can form a separate class for the following reasons. First of all, the common feature of all the known polar magnets is the chemical or charge ordering of same or different cations, which seems to be responsible for stabilizing the polar structure right at the formation temperature of the compounds [71]. Thus, they differ from type-I multiferroics which exhibit polar - nonpolar transition. Since the inversion symmetry is broken at the melting point or the decomposition temperature, the magnetic ordering of any kind should induce some form of magnetoelectric coupling in these compounds. However, the extent of magnetoelectric effect depends on the underlying mechanisms that couple the magnetism with electric polarization. More importantly, they also contrast with type-II multiferroics where the inversion symmetry is broken only at the magnetic ordering temperature by complex magnetic structures. Considering these facts, one can categorize the polar magnets as different class of multiferroics [25,71].

These materials are promising for room temperature magnetoelectric effect because they do not necessarily involve complex spin structures resulted from magnetic frustration.

Furthermore, the appearance of electric polarization without poling electric field making them interesting from the application point of view [25,71,72]. The microscopic mechanism responsible for the ferroelectricity in these materials might be associated with magnetostriction (magnetoelastic coupling) [73]. However, the possibility of exchange striction or inverse DM interaction cannot be neglected [72]. There are considerable number of polar magnets that exhibit multiferroicity are reported in the literature.

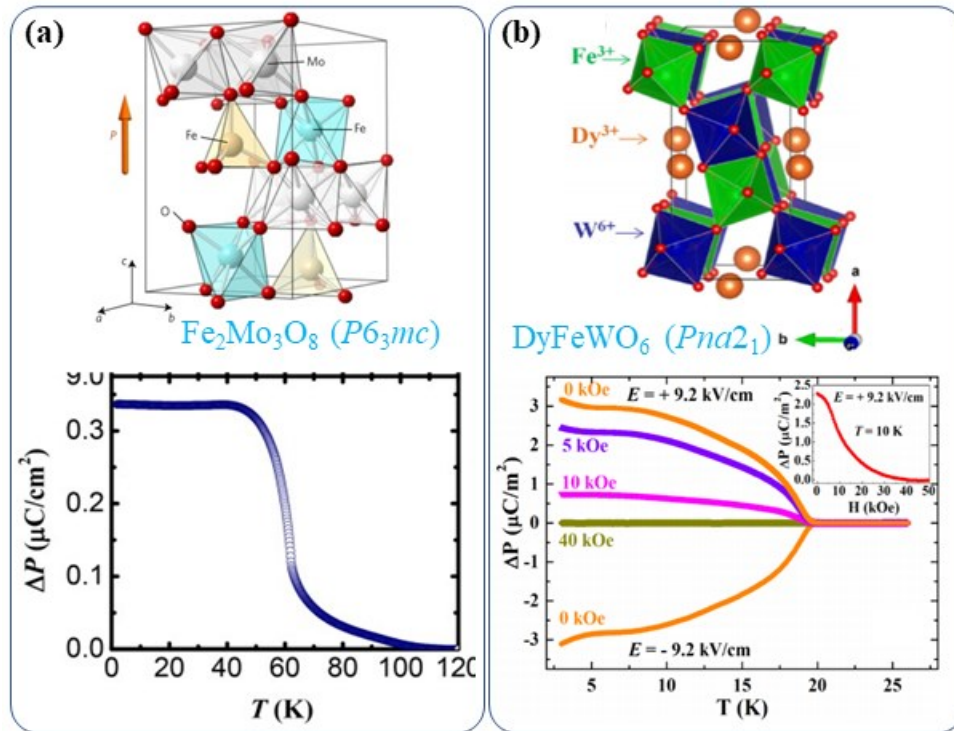


Figure 1.13 (a) Crystal structure (adapted from Ref. [74], © (2017) by the Nature Publishing Group) and polarization (adapted from Ref. [72]) of mineral kamiokite $\text{Fe}_2\text{Mo}_3\text{O}_8$. (b) Ordered aeschynite structure and T - H dependent polarization for DyFeWO_6 (adapted with permission from Ref. [75], © (2017) by the American Physical Society).

For example, mineral kamiokite $\text{Fe}_2\text{Mo}_3\text{O}_8$ is a polar magnet and exhibits a large linear magnetoelectric effect [72]. This compound crystallizes in the hexagonal crystal structure with polar space group $P6_3mc$ where Fe^{2+} ions occupy two different crystallographic sites with FeO_4 tetrahedra and FeO_6 octahedra [see Figure 1.13(a)], which share corners to form a honeycomb-like arrangement in the \mathbf{ab} -plane. These Fe-O layers are separated by sheets of Mo^{4+} ions and stacked along the \mathbf{c} -axis. Moreover, this compound demonstrates change in electric polarization ($\Delta P = 0.3 \mu\text{C}/\text{m}^2$) below collinear antiferromagnetic ordering of Fe^{2+} spins, $T_N = 60 \text{ K}$ as shown in Figure 1.13(a). Another interesting example to consider is aeschynite family compounds with chemical formula $R\text{FeWO}_6$ ($R = \text{Dy}, \text{Eu}, \text{Tb}, \text{and Y}$) which are ordered derivatives of centrosymmetric parent compound CaTa_2O_6 (Space group: $Pnma$) [75]. The chemical ordering

of Fe^{3+} and W^{6+} ions occur in RFeWO_6 due to significant charge and size difference of these ions, which stabilizes the polar $Pna2_1$ structure. The ordered aeschynite structure of DyFeWO_6 is shown in Figure 1.13(b) where the structure consists of alternate ordering of Fe^{3+} and W^{6+} ions. All the compounds exhibit multiferroic properties below antiferromagnetic ordering temperature of Fe^{3+} moments; for example, Figure 1.13(b) shows the change in polarization at T_N for DyFeWO_6 . Some other materials of this type are corundum-type Ni_3TeO_6 , brownmillerites, $M_2\text{Mo}_3\text{O}_8$ ($M = \text{Co}$ and Mn), $\text{CaBaCo}_4\text{O}_7$, and doubly ordered perovskites [71,76–79].

1.4 Magnetodielectric effect

Apart from magnetoelectric effect in linear magnetoelectrics and multiferroics, another term is introduced to classify certain materials that possess neither linear magnetoelectric effect nor multiferroicity but show some coupling between magnetism and dielectric properties. Magnetodielectric effect is nothing but change in dielectric constant with respect to the external magnetic fields, also known as magnetocapacitance effect is given by the relation,

$$MD(\%) = \frac{\epsilon_r(H) - \epsilon_r(0)}{\epsilon_r(0)}$$

This was first introduced by Lawes *et al.* for more general couplings, which can, in principle, be observed in any insulating magnet, unlike the magnetoelectric effect is reserved for special symmetries [80]. This terminology is widely used for many systems, especially magnetocapacitance measurements on systems that are magnetoelectric. The materials that exhibit magnetodielectric effect are called magnetodielectrics. It is known that all magnetoelectrics are magnetodielectrics, but the reverse is not true [81]. For example, most magnetoelectrics exhibit magnetodielectric effect but some materials are only magnetodielectric such as $\text{Dy}_2\text{Ti}_2\text{O}_7$, ZnFe_2O_4 , SeCuO_3 , and TeCuO_3 [80,81].

1.5 Possible applications

Magnetoelectric multiferroic materials are very promising for many applications in modern technology [1,82–84]. However, there are some desired requirements for multiferroics to use in applications: high transition temperatures, considerable polarization, and magnetization, and more importantly, strong cross-coupling between magnetization and polarization. The materials available as on today do not satisfy all these requirements. Despite

these, there have been many efforts in the past and presently, research on multiferroic moving towards practical applications. One of the most promising uses of magnetoelectric multiferroics would be four state magnetoelectric random access memory (MeRAM), a next-generation memory that can replace the current storage devices such as DRAM, external hard drive, solid-state drive, and flash memory [82,85]. Other possible applications include magnetic field sensors, microwave generators, spin-wave generators, phase shifters, domain wall devices, energy harvesters, etc [1,86,87].

1.6 Aim of the thesis

There has been a surge of research on magnetoelectrics and multiferroics in the past two decades due to their underlying physics and application potential in future memory devices. Despite tremendous development, it is still very challenging to design new magnetoelectric or multiferroic material. This thesis aims to find new magnetoelectric and multiferroic materials and understand the structure and property relations, which will help achieve new materials with the phenomena mentioned earlier for the multiferroic research community. Mainly, we have worked on well-known green phase compounds with the chemical formula $R_2\text{BaCuO}_5$, where R is rare-earth. These compounds exhibit a wide variety of magnetic structures depends on $4f$ - $3d$ coupling associated with each R ion. We have discovered that these compounds exhibit interesting magnetoelectric and multiferroic properties. Based on our findings, we argue that the whole family of green phase compounds serves as a rich playground for studying the magnetoelectric and multiferroic phenomena. The importance of $4f$ - $3d$ interactions in determining the ground state magnetic structure suggests that the richness of such phenomena in this class of compounds will arguably become as famous as orthorhombic rare-earth manganites RMnO_3 and manganates RMn_2O_5 including the diversity in electric polarization directions and its magnetic field induced reorientations. Further, the multiferroics materials should exhibit a strong magnetoelectric coupling at accessible temperatures to have practical applications. Though magnetism-induced multiferroics (type-II) exhibit a strong coupling, the involvement of complex magnetic structures makes the transition temperatures are not accessible. To enhance the magnetic ordering temperature, polar magnets can be good candidates. Along this line, we have extended study on the aeschynite family of compounds where RFeWO_6 ($R = \text{Sm, Gd, Er, and Tm}$) exhibit multiferroic properties below their antiferromagnetic ordering temperature.

References

- [1] M. Fiebig, *J. Phys. D. Appl. Phys.* **38**, R123 (2005).
- [2] W. Eerenstein, N. D. Mathur, and J. F. Scott, *Nature* **442**, 759 (2006).
- [3] P. Curie, *J. Phys.* **3**, 401 (1894).
- [4] P. Debye, *Zeitschrift Für Phys.* **36**, 300 (1926).
- [5] L. D. Landau, J. S. Bell, M. J. Kearsley, L. P. Pitaevskii, E. M. Lifshitz, and J. B. Sykes, *Electrodynamics of Continuous Media* (elsevier, 2013).
- [6] I. E. Dzyaloshinskii, *Sov. Phys. JETP* **10**, 628 (1960).
- [7] D. N. Astrov, *Sov. Phys. JETP* **11**, 708 (1960).
- [8] G. T. Rado, *Phys. Rev. Lett.* **13**, 335 (1964).
- [9] M. Mercier, *CR Seances Acad. Sci., Ser. B* **264**, 979 (1967).
- [10] R. M. Hornreich, *Solid State Commun.* **7**, 1081 (1969).
- [11] E. Fischer, G. Gorodetsky, and R. M. Hornreich, *Solid State Commun.* **10**, 1127 (1972).
- [12] G. T. Rado, J. M. Ferrari, and W. G. Maisch, *Phys. Rev. B* **29**, 4041 (1984).
- [13] G. A. Smolenskiï and I. E. Chupis, *Sov. Phys. Uspekhi* **25**, 475 (1982).
- [14] E. Ascher, H. Rieder, H. Schmid, and H. Stössel, *J. Appl. Phys.* **37**, 1404 (1966).
- [15] H. Schmid, *Ferroelectrics* **162**, 317 (1994).
- [16] N. A. Hill, *J. Phys. Chem. B* **104**, 6694 (2000).
- [17] T. Kimura, T. Goto, H. Shintani, K. Ishizaka, T. Arima, and Y. Tokura, *Nature* **426**, 55 (2003).
- [18] J. Wang, J. B. Neaton, H. Zheng, V. Nagarajan, S. B. Ogale, B. Liu, D. Viehland, V. Vaithyanathan, D. G. Schlom, and U. V Waghmare, *Science* (80-.). **299**, 1719 (2003).
- [19] D. I. Khomskii, *J. Magn. Magn. Mater.* **306**, 1 (2006).
- [20] S. W. Cheong and M. Mostovoy, *Nat. Mater.* **6**, 13 (2007).
- [21] K. F. Wang, J. M. Liu, and Z. F. Ren, *Adv. Phys.* **58**, 321 (2009).
- [22] D. Khomskii, *Physics (College. Park. Md.)* **2**, 20 (2009).
- [23] C. N. R. Rao, A. Sundaresan, and R. Saha, *J. Phys. Chem. Lett.* **3**, 2237 (2012).
- [24] J. Wang, *Multiferroic Materials: Properties, Techniques, and Applications* (CRC Press, 2016).
- [25] P. Yanda and A. Sundaresan, in *Adv. Chem. Phys. Mater. Overv. Sel. Top.* (World Scientific, 2020), pp. 224–248.
- [26] R. E. Newnham, *Properties of Materials: Anisotropy, Symmetry, Structure* (Oxford University Press on Demand, 2005).

- [27] D. I. Khomskii, editor, in *Transit. Met. Compd.* (Cambridge University Press, Cambridge, 2014), pp. 269–309.
- [28] J. P. Rivera, *Eur. Phys. J. B* **71**, 299 (2009).
- [29] G. A. Gehring, *Ferroelectrics* **161**, 275 (1994).
- [30] W. F. Brown Jr, R. M. Hornreich, and S. Shtrikman, *Phys. Rev.* **168**, 574 (1968).
- [31] A. K. Agyei and J. L. Birman, *J. Phys. Condens. Matter* **2**, 3007 (1990).
- [32] J. Zhang, N. Su, X. Mi, M. Pi, H. Zhou, J. Cheng, and Y. Chai, *Phys. Rev. B* **103**, L140401 (2021).
- [33] N. Mufti, G. R. Blake, M. Mostovoy, S. Riyadi, A. A. Nugroho, and T. T. M. Palstra, *Phys. Rev. B - Condens. Mater. Phys.* **83**, 104416 (2011).
- [34] J. Hwang, E. S. Choi, H. D. Zhou, J. Lu, and P. Schlottmann, *Phys. Rev. B* **85**, 024415 (2012).
- [35] R. Saha, S. Ghara, E. Suard, D. H. Jang, K. H. Kim, N. V Ter-Oganessian, and A. Sundaresan, *Phys. Rev. B* **94**, 014428 (2016).
- [36] S. Ghara, N. V. Ter-Oganessian, and A. Sundaresan, *Phys. Rev. B* **95**, 094404 (2017).
- [37] N. V Ter-Oganessian, A. A. Guda, and V. P. Sakhnenko, *Sci. Rep.* **7**, 16410 (2017).
- [38] X. Shen, L. Zhou, Y. Chai, Y. Wu, Z. Liu, Y. Yin, H. Cao, C. Dela Cruz, Y. Sun, and C. Jin, *NPG Asia Mater.* **11**, 50 (2019).
- [39] S. Mishra, P. Yanda, and A. Sundaresan, *Phys. Rev. B* **103**, 214443 (2021).
- [40] R. V Shpanchenko, V. V Chernaya, A. A. Tsirlin, P. S. Chizhov, D. E. Sklovsky, E. V Antipov, E. P. Khlybov, V. Pomjakushin, A. M. Balagurov, and J. E. Medvedeva, *Chem. Mater.* **16**, 3267 (2004).
- [41] C. De, Á. M. Arévalo-López, F. Orlandi, P. Manuel, J. P. Attfield, and A. Sundaresan, *Angew. Chemie Int. Ed.* **57**, 16099 (2018).
- [42] B. B. Van Aken, T. T. M. Palstra, A. Filippetti, and N. A. Spaldin, *Nat. Mater.* **3**, 164 (2004).
- [43] J. van den Brink and D. I. Khomskii, *J. Phys. Condens. Matter* **20**, 434217 (2008).
- [44] Y. Tokura and S. Seki, *Adv. Mater.* **22**, 1554 (2010).
- [45] Y. Tokura, S. Seki, and N. Nagaosa, *Rep. Prog. Phys.* **77**, 076501 (2014).
- [46] I. A. Sergienko, C. Şen, and E. Dagotto, *Phys. Rev. Lett.* **97**, 227204 (2006).
- [47] H. Katsura, N. Nagaosa, and A. V Balatsky, *Phys. Rev. Lett.* **95**, 057205 (2005).
- [48] T. Kimura, *Annu. Rev. Condens. Matter Phys.* **3**, 93 (2012).
- [49] J. B. Goodenough, *Phys. Rev.* **100**, 564 (1955).
- [50] J. B. Goodenough, *J. Phys. Chem. Solids* **6**, 287 (1958).
- [51] J. Kanamori, *J. Phys. Chem. Solids* **10**, 87 (1959).

- [52] Y. J. Choi, H. T. Yi, S. Lee, Q. Huang, V. Kiryukhin, and S.-W. Cheong, *Phys. Rev. Lett.* **100**, 047601 (2008).
- [53] N. Hur, S. Park, P. A. Sharma, J. S. Ahn, S. Guha, and S. W. Cheong, *Nature* **429**, 392 (2004).
- [54] Y. Tokunaga, N. Furukawa, H. Sakai, Y. Taguchi, T. Arima, and Y. Tokura, *Nat. Mater.* **8**, 558 (2009).
- [55] Y. Tokunaga, S. Iguchi, T. Arima, and Y. Tokura, *Phys. Rev. Lett.* **101**, 097205 (2008).
- [56] S. Seki, in edited by S. Seki (Springer Japan, Tokyo, 2012), pp. 1–13.
- [57] T. Kubacka, J. A. Johnson, M. C. Hoffmann, C. Vicario, S. De Jong, P. Beaud, S. Grübel, S.-W. Huang, L. Huber, and L. Patthey, *Science* (80-.). **343**, 1333 (2014).
- [58] Y. Yamasaki, S. Miyasaka, Y. Kaneko, J.-P. He, T. Arima, and Y. Tokura, *Phys. Rev. Lett.* **96**, 207204 (2006).
- [59] G. Lawes, A. B. Harris, T. Kimura, N. Rogado, R. J. Cava, A. Aharony, O. Entin-Wohlman, T. Yildirim, M. Kenzelmann, C. Broholm, and A. P. Ramirez, *Phys. Rev. Lett.* **95**, 087205 (2005).
- [60] O. Heyer, N. Hollmann, I. Klassen, S. Jodlauk, L. Bohaty, P. Becker, J. A. Mydosh, T. Lorenz, and D. Khomskii, *J. Phys. C Solid State Phys.* **18**, L471 (2006).
- [61] S. Park, Y. J. Choi, C. L. Zhang, and S. W. Cheong, *Phys. Rev. Lett.* **98**, 057601 (2007).
- [62] Y. Naito, K. Sato, Y. Yasui, Y. Kobayashi, Y. Kobayashi, and M. Sato, *J. Phys. Soc. Japan* **76**, 23708 (2007).
- [63] J. Z. Cong, S. P. Shen, Y. S. Chai, L. Q. Yan, D. S. Shang, S. G. Wang, and Y. Sun, *J. Appl. Phys.* **117**, 174102 (2015).
- [64] T. Kimura, Y. Sekio, H. Nakamura, T. Siegrist, and A. P. Ramirez, *Nat. Mater.* **7**, 291 (2008).
- [65] S. Seki, Y. Onose, and Y. Tokura, *Phys. Rev. Lett.* **101**, 067204 (2008).
- [66] T. Kimura, J. C. Lashley, and A. P. Ramirez, *Phys. Rev. B* **73**, 220401 (2006).
- [67] T. Kurumaji, S. Seki, S. Ishiwata, H. Murakawa, Y. Tokunaga, Y. Kaneko, and Y. Tokura, *Phys. Rev. Lett.* **106**, 167206 (2011).
- [68] M. Matsumoto, K. Chimata, and M. Koga, *J. Phys. Soc. Japan* **86**, 34704 (2017).
- [69] V. Hutanu, A. Sazonov, H. Murakawa, Y. Tokura, B. Náfrádi, and D. Chernyshov, *Phys. Rev. B - Condens. Mater. Phys.* **84**, 212101 (2011).
- [70] A. K. Zvezdin, S. S. Krotov, A. M. Kadomtseva, G. P. Vorob'ev, Y. F. Popov, A. P. Pyatakov, L. N. Bezmaternykh, and E. A. Popova, *J. Exp. Theor. Phys. Lett.* **81**, 272 (2005).
- [71] R. Shankar P N, S. Mishra, and S. Athinarayanan, *APL Mater.* **8**, 40906 (2020).
- [72] Y. Wang, G. L. Pascut, B. Gao, T. A. Tyson, K. Haule, V. Kiryukhin, and S.-W. Cheong, *Sci. Rep.* **5**, 12268 (2015).
- [73] M.-R. Li, E. E. McCabe, P. W. Stephens, M. Croft, L. Collins, S. V. Kalinin, Z. Deng,

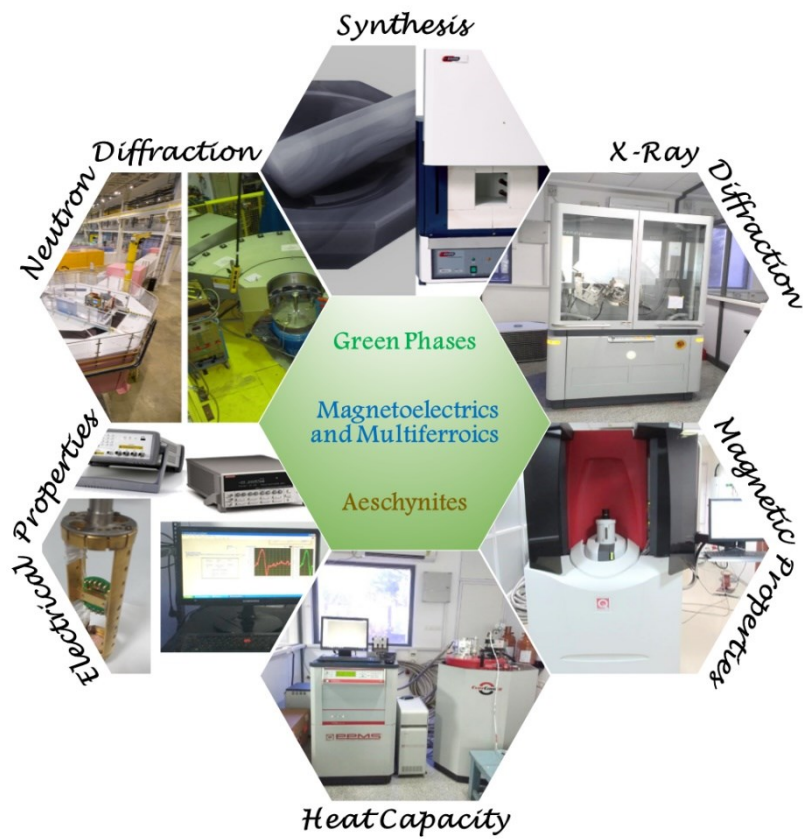
- M. Retuerto, A. Sen Gupta, H. Padmanabhan, V. Gopalan, C. P. Grams, J. Hemberger, F. Orlandi, P. Manuel, W.-M. Li, C.-Q. Jin, D. Walker, and M. Greenblatt, *Nat. Commun.* **8**, 2037 (2017).
- [74] T. Ideue, T. Kurumaji, S. Ishiwata, and Y. Tokura, *Nat. Mater.* **16**, 797 (2017).
- [75] S. Ghara, E. Suard, F. Fauth, T. T. Tran, P. S. Halasyamani, A. Iyo, J. Rodríguez-Carvajal, and A. Sundaresan, *Phys. Rev. B* **95**, 224416 (2017).
- [76] Y. S. Oh, S. Artyukhin, J. J. Yang, V. Zapf, J. W. Kim, D. Vanderbilt, and S. W. Cheong, *Nat. Commun.* **5**, 3201 (2014).
- [77] K. Singh, V. Caignaert, L. C. Chapon, V. Pralong, B. Raveau, and A. Maignan, *Phys. Rev. B* **86**, 024410 (2012).
- [78] C. De and A. Sundaresan, *Phys. Rev. B* **97**, 214418 (2018).
- [79] R. Shankar P N, F. Orlandi, P. Manuel, W. Zhang, P. S. Halasyamani, and A. Sundaresan, *Chem. Mater.* **32**, 5641-5649 (2020).
- [80] G. Lawes, T. Kimura, C. M. Varma, M. A. Subramanian, N. Rogado, R. J. Cava, and A. P. Ramirez, *Prog. Solid State Chem.* **37**, 40 (2009).
- [81] G. Catalan, *Appl. Phys. Lett.* **88**, 18 (2006).
- [82] J. F. Scott, *Nat. Mater.* **6**, 256 (2007).
- [83] J. F. Scott, *J. Mater. Chem.* **22**, 4567 (2012).
- [84] M. M. Vopson, *Crit. Rev. Solid State Mater. Sci.* **40**, 223 (2015).
- [85] J. F. Scott, *ChemPhysChem* **10**, 1761 (2009).
- [86] J. F. Scott, *J. Mater. Chem.* **22**, 4567 (2012).
- [87] C. W. Nan, M. I. Bichurin, S. Dong, D. Viehland, and G. Srinivasan, *J. Appl. Phys.* **103**, (2008).

Chapter 2

Experimental techniques

Summary

This chapter briefly discusses sample preparation, characterization techniques, and physical property measurements used in the present thesis.



2.1 Solid-state synthesis

Conventional solid-state synthesis or ceramic method is a well-known technique in condensed matter research for its versatility for preparing various bulk materials, including various oxides [1]. In this method, the chemical reaction between starting materials at moderate to high temperatures results in a new solid with a well-defined structure. Mainly, it depends on the inter-diffusion between the ions and therefore using fine reactant powders is the main prerequisite. As a result, the products obtained are polycrystalline. The principal reaction mechanism is the diffusion coefficient (D), which is given by Fick's law [1],

$$J = -D \frac{d\phi}{dx}$$

where J is the flux of the diffusion elements and $\frac{d\phi}{dx}$ is the concentration gradient. The diffusion coefficient (D) depends on the temperature of the reaction. To obtain a good reaction product, D should be greater than 10^{-12} cm²/s. According to Tamman's rule, the reaction temperature is at least 2/3 of the melting point of one or more starting materials for a proper reaction. The reaction temperatures are usually kept as high as 500 °C to 1500 °C to maximize the diffusion length, and the reaction would occur at an appreciable rate. The thermodynamic factor, which is the change in free energy involved during the reaction, is also an important parameter for the success of a solid-state reaction [1]. All samples which are used in thesis work are polycrystalline and synthesized by using this method. The synthesis was carried in commercial muffle furnaces which are available at our lab. A detailed description of the procedures is present in the subsequent chapters for each sample.

2.2 Structural characterizations

2.2.1 X-ray and neutron diffraction

X-ray diffraction is one of the most widely used techniques and regarded as fundamental in structural analysis since its discovery in 1925 by W. L Bragg [2]. For all the samples synthesized, X-ray diffraction was performed using a laboratory Bruker D8 Advance X-ray diffractometer and PANalytical Empyrean alpha-1 diffractometer with monochromatic Cu K α_1 radiation. The data obtained in the latter were used for crystal structure analysis. The X-ray diffractometer setup usually consists of an X-ray tube, a sample mounting stage, and a

detector. When X-rays incident on the powder sample, there are various levels at which the scattering occurs. Some of the radiation will be scattered by the atoms of the first layer or plane as shown in Figure 2.1 and the rest will pass through the first layer and subsequently scattered by the succeeding layers. It is mainly because the sample consists of grains arranged in all possible random orientations. For X-ray scattering to occur, the spacing between crystallographic planes must be of the order of the wavelength of the incident beam. A peak in the X-ray diffraction pattern is obtained only when constructive interference, the phase of the scattering rays arising from two different planes are same, occurs. According to Bragg's condition, interference occurs constructively if it follows [1],

$$2d \sin\theta = \lambda$$

where d is the spacing between the consecutive layers, λ is the incident wavelength, and θ is the incident angle of the X-ray, as illustrated in Figure 2.1. When Bragg's law is satisfied by sets of planes in any sample, peaks will appear at only certain 2θ positions. Consequently, the X-ray diffraction pattern obtained of intensity versus 2θ will be characteristic for different materials. Now, the 2θ values depend on the distance between the planes d , which in turn is function of the lattice parameters. Thus, by indexing the obtained diffraction parameter, one can determine the lattice parameters of the samples. Likewise, the powder X-ray diffraction data can be analysed using different tools to obtain different information resulting in a complete crystal structure. The phase purity of a known compound can also be checked by comparing its X-ray diffraction data with the pattern available in various databases such as Inorganic Crystal Structure Database (ICSD). Additionally, the impurity phases can also be identified in a similar manner.

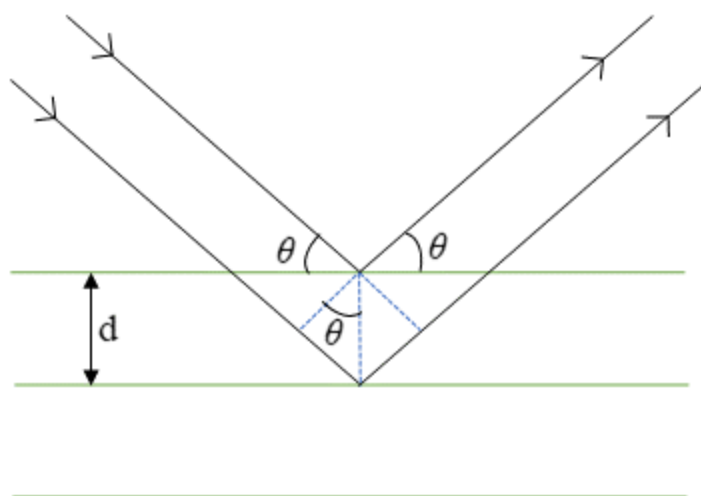


Figure 2.1 Illustration of X-ray diffraction and Bragg's law [1].

In most cases, compounds contain light elements such as oxygen, carbon, and hydrogens, and since X-rays are insensitive to these lighter elements, making neutron diffraction experiments become necessary for crystal structure determination and to obtain accurate positional parameters. Because neutrons interact with the nucleus of the atom, they can determine the position of the lighter elements more accurately. More importantly, neutron possesses an intrinsic magnetic moment that can interact with the moment of an atom in the compound and hence one can obtain the magnetic structure of the compounds. Neutron diffraction experiments on my samples were performed in WISH diffractometer at RAL, Didcot, UK [3] and D1B beamline at the Institut Laue-Langevin (ILL), Grenoble, France.

2.2.2 Rietveld refinement

Rietveld refinement is the most applicable technique for the complete structural analysis of materials obtained from the X-ray and neutron diffraction data [2]. This method uses the least-squares approach to calculate the theoretical profile until it matches to experimental diffraction pattern. In this refinement process, the intensity at each point of the experimental data (y_{io}) and the corresponding calculated point (y_{ic}) in the model are compared. For this comparison, a residual function S is minimized through the least square process, which is given by [2],

$$S = \sum_i w_i |y_{io} - y_{ic}|^2$$

where w_i is a weight factor that depends on the standard deviation in peak and background intensity. The theoretical intensity at a point can be given by,

$$y_{ic} = s \sum_k m_k L_k |F_k|^2 G(\Delta\theta_{ik}) + y_{ib}$$

where s is a scale factor, m_k is the multiplicity factor, L_k is the Lorentz polarization factor for reflection k , and F_k is the structure factor. In the equation, $G(\Delta\theta_{ik})$ is the reflection profile function where $\Delta\theta_{ik} = 2\theta_i - 2\theta_k$ and $2\theta_k$ is the calculated position of the Bragg peak, and y_{ib} being the background intensity.

Structure factor (F_k) and the reflection profile function $G(\Delta\theta_{ik})$ are important parameters. The structure factor F_{hkl} ($= F_k$ for k^{th} reflection) is given by,

$$F_{hkl} = \sum_{j=1}^m N_j f_j e^{2\pi(hx_j + ky_j + lz_j)}$$

$$|f|^2 = e^{-\frac{B \sin^2 \theta}{\lambda^2}}$$

where f is the atomic form factor and B is the Debye-Waller temperature factor.

The peak profile (reflection profile function) depends on several parameters, such as the radiation source, detector, and wavelength distribution. Various functional forms can be used for the peak shape function, with the pseudo-Voigt (pV) function being the most widely used. The functional form is as follows:

$$pV = \eta L + (1 - \eta)G; \text{ with } 0 \leq \eta \leq 1$$

where L and G are Lorentzian and Gaussian functions, respectively. The functional forms can be written as the following,

$$L = \frac{C_1^{\frac{1}{2}}}{\pi H_k} \left\{ 1 + C_1 \left(\frac{\Delta \theta_{ik}}{H_k} \right)^2 \right\}^{-1}$$

$$G = \frac{C_0^{\frac{1}{2}}}{\sqrt{\pi H_k}} e^{-C_0 \left(\frac{\Delta \theta_{ik}}{H_k} \right)^2}$$

where C_0 and C_1 are constants and H_k is the full width at half maxima (FWHM) of the k^{th} reflection. Further, FWHM (H_k) for Gaussian and Lorentzian peak functions are given by,

$$(H_k)_G = (U \tan^2 \theta + V \tan \theta - W)^{1/2}$$

$$(H_k)_L = X \tan \theta + \frac{Y}{\cos \theta}$$

Here, the parameters U , V , W , X , and Y can be refined during pattern matching of the diffraction data. It is also noteworthy that the background can be selected manually or as a polynomial function of 2θ , which is given by

$$y_{ib} = \sum_n a_n (2\theta_i)^n$$

This background must be refined while pattern matching by refining the coefficient a_n .

At the last cycle of the refinement, the quality of the refinement is evaluated by the R parameters given below [2],

$$R_p(\text{profile}) = \frac{\sum |y_{io} - y_{ic}|}{\sum y_{io}}$$

$$R_{wp}(\text{Weighted profile}) = \left(\frac{\sum w_i (y_{io} - y_{ic})^2}{\sum w_i y_{io}^2} \right)^{1/2}$$

$$R_{pE}(\text{expected}) = \left\{ \frac{N-P}{\sum w_i y_{io}^2} \right\}^{1/2}$$

$$\chi^2(\text{Goodness of fit}) = \left(\frac{R_{wp}}{R_E} \right)^2 = \frac{\sum w_i (y_{io} - y_{ic})^2}{(N-P)}$$

where N is the number of profile points, and P is the number of refined parameters. It is the χ^2 parameter which determines how good or accurate the fit is obtained. For a good refinement, χ^2 should approach 1. However, one should completely rely on these parameters to validate the refinement. In addition to these, one must check the fit between observed and calculated patterns and the chemical sense of the structural model.

Precisely, Rietveld refinement is carried out in three steps using a software package. Firstly, the lattice parameters and FWHM parameters (U , V , W , and/or X , Y , and asymmetry parameters) are refined for pattern matching, followed by background refinement. Secondly, a probable structural model is added to refine atomic positions and scale factor in good agreement with the experimental data. And finally, the bond lengths and bond angles are obtained from the crystal structure. The crystal and magnetic structure refinements were performed using the Fullprof software package and JANA crystallographic software [4,5]. The crystal and magnetic structures were then visualized using VESTA software [6]. Symmetry analysis for refining and understanding the magnetic structures, I have used ISODISTORT and Bilbao Crystallographic Server [7,8]. Since VESTA software cannot treat the incommensurate magnetic structures, I have used MVISUALIZE or Jmol available at Bilbao Crystallographic Server to visualize the incommensurate and commensurate magnetic structures [8,9].

2.3 Physical property measurements

2.3.1 DC magnetization

DC magnetization measurements presented in this thesis were carried using Superconducting Quantum Interference Device (SQUID) equipped in Magnetic Property Measurement System (MPMS3) which is shown in Figure 2.2(a) [10]. The fundamental

principle of these measurements is explained by Faraday's law of induction stating that the induced voltage in a closed circuit is proportional to the rate of change of magnetic flux through the circuit. The magnetic flux (ϕ) through a coil of n turns with cross-sectional area A is given by the equation $\phi = AB$, where B is the magnetic field. The induced voltage (V) in the coil is thus given by,

$$V = -n \frac{d\phi}{dt} = -nA \frac{dB}{dt}$$

where oscillating sample inside a coil induces B .

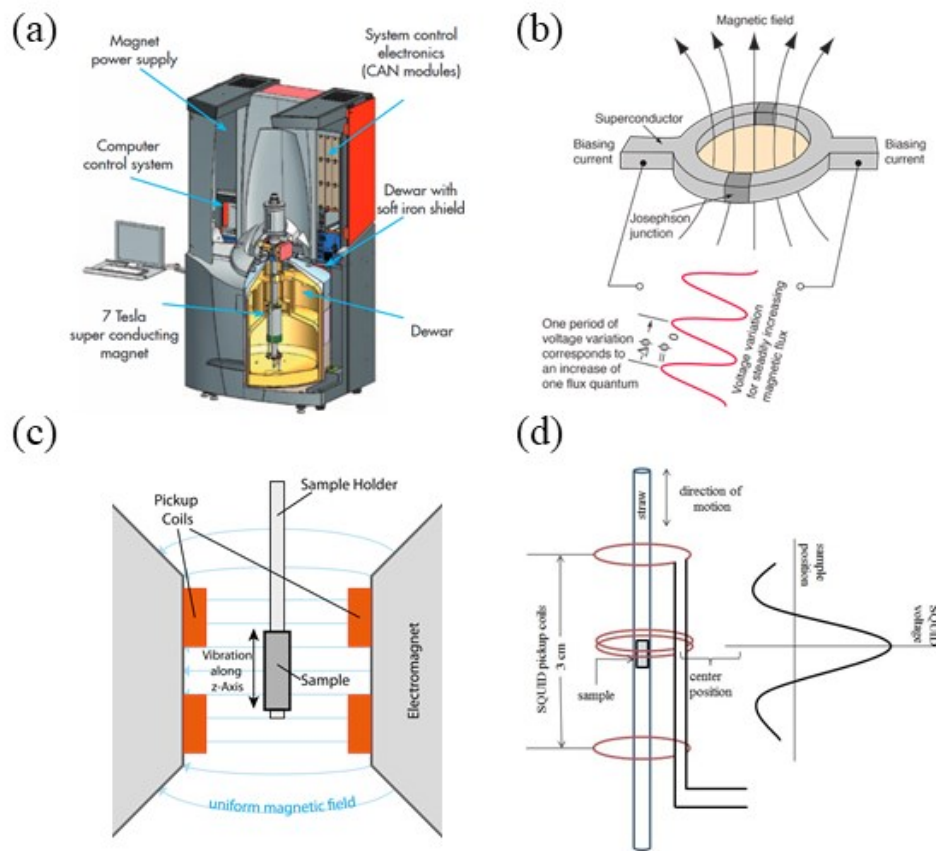


Figure 2.2 (a) Schematic diagram of SQUID MPMS3, Quantum Design. (b) Scheme of two Josephson junctions of SQUID device. (c) Illustration of second-order gradiometer superconducting pick-up coils. (d) Schematic diagram of VSM. (adapted from Ref. [10])

SQUID magnetometer

It is a very sensitive magnetometer used for measuring extremely subtle magnetic fields. The SQUID consists of two superconductors separated by thin insulating layers to form two parallel Josephson junctions [see Figure 2.2(b)]. For the measurement, a constant biasing current is maintained in the device with simultaneous oscillation of measured voltage with changes in phase at the two junctions. The change in phase depends on the change in magnetic

flux due to sample oscillation. This allows the sample magnetic moment to be measured from which DC magnetization and magnetic susceptibility can be obtained. Two different modes exist for the magnetization measurements: Vibrating sample magnetometer (VSM) mode and dc mode [10]. In VSM mode shown in Figure 2.2(c), the sample vibrates sinusoidally up and down with a large frequency, whereas in the dc scan mode, instead of oscillating the sample, it is moved up and down uniformly. Therefore, dc scan mode is preferred to measure high-quality data. The temperature range used for measurements is 1.8 K to 400 K with an applied field varying between 0 and 7 T. A superconducting magnet, made of a solenoid of superconducting wires, is used to generate the required magnetic fields. Both superconducting magnet and sample chamber are contained in a Dewar and cooled with liquid He [10]. The superconducting detection coil is a single piece of superconducting wire that acts as a two-level gradiometer as shown in Figure 2.2(d). This coil is placed in a uniform magnetic field of the superconducting magnet. This coil together with the SQUID circuit, which contains signal to flux convertor, flux to voltage converter, and the other electronics, measures the magnetic moment.

2.3.2 AC susceptibility

For studying the dynamics of magnetization, the AC susceptibility measurements are performed. Since DC magnetization remains constant with time, it cannot provide the magnetization dynamics in many cases, such as studies on spin glasses, etc. In this scenario where below spin-glass transition magnetization decays over time, the ac susceptibility measurements provide useful insights. In ac susceptibility measurements, the sample does not oscillate and remains static, then a small ac magnetic field ($H = H_{ac} \sin(\omega t)$) is applied to the sample in the presence or absence of a dc magnetic field where H_{ac} and ω are the amplitude and frequency of the applied ac magnetic field, respectively. In a small AC field, the susceptibility is defined as [11],

$$M_{AC} = \frac{dM}{dH} H_{AC} \sin(\omega t)$$

where $\chi = \frac{dM}{dH}$ is the slope of the magnetization (M) vs magnetic field (H) data. In the case of a large AC magnetic field, the AC magnetization of the sample does not follow the driving frequency and lags behind the applied AC field. Consequently, two quantities are yielded, the magnitude of the susceptibility and the phase shift of the induced signal with respect to the driving signal. Therefore, the susceptibility is obtained as a complex quantity with an in-phase

component χ' (real part) and an out-of-phase component χ'' (the imaginary part indicating the dissipative processes in the sample).

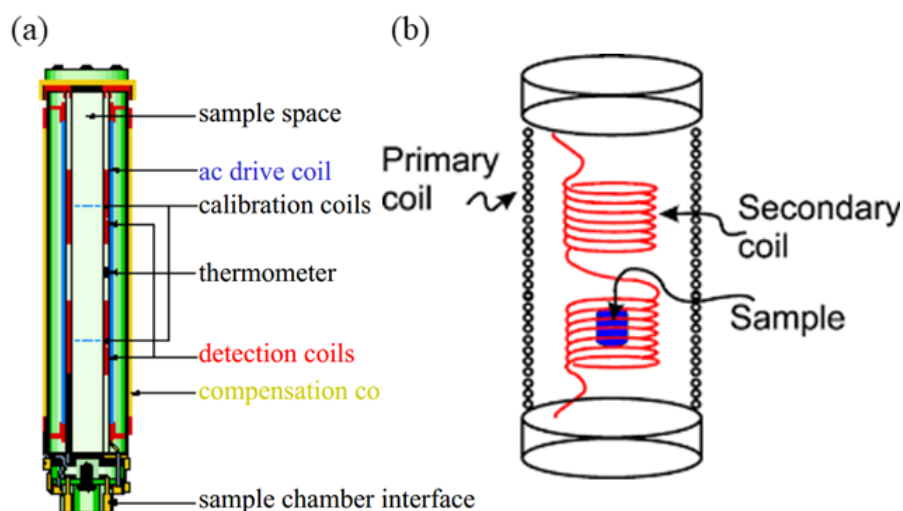


Figure 2.3 Schematic diagram of the different components of ACMS coil in PPMS [12].

AC susceptibility measurements presented in the thesis were carried in the ACMS option of Physical Property Measurement System (PPMS) [12]. The basic susceptometer consists of one long primary and two secondary coils as shown in Figure 2.3. The primary coil (AC drive coil), which induces magnetic flux inside one secondary coil (AC Drive Compensation Coil), generates AC magnetic field. The secondary coil is wound in the opposite direction to cancel out the voltage induced from the primary coil. But the total magnetic flux obtained has contributions from the primary coil and the magnetization induced in the sample. Hence, to detect signals only from the sample, another secondary coil (pick-up coil) consisting of a combination of two coils (top and bottom) is tuned [see Figure 2.3(b)]. The measurements are performed by five-point BTBCC (bottom-top-bottom-center-center) measurement process in the PPMS [12]. From the first three readings, the signals from the detection coil are amplified and visualized by an analog to digital (A/D) converter which is saved as a response waveform. Following this, the real and imaginary components of each response waveform are calculated by fitting the data and comparing it with the driving signal. In the end, the calibration readings are used to get the real and imaginary part of the AC susceptibility of the sample.

2.3.3 Heat capacity

The measurement was carried on the PPMS using the constant pressure relaxation method. Heat capacity is the first-order derivative with respect to the temperature of the

enthalpy at constant pressure, governed by two contributing factors from conduction electrons and lattice. During the measurement, a cycle of heating and cooling is performed on the sample under high vacuum. The vacuum intercepts heat dissipation in the chamber. A known amount of heat is provided to the sample for a fixed period. Following this, sample is allowed to cool for the same period and the temperature response is visualized during each cycle in the MultiVu software. The program in the software fits and plots the temperature response for the full cycle using a model, which is further used to calculate the heat capacity of the sample.

The sample holder shown in Figure 2.4 consists of a heating resistor and thermal sensor connected between the holder (goes into PPMS) and platform using Cu wires [13]. The sample is placed on the platform with a thin layer of Apiezon grease, which ensures good thermalization. Before performing the heat capacity measurement on the sample, addenda measurement needs to be carried where just Apiezon grease in minimal quantity is applied to the sample platform, and heat capacity is measured as a reference. The sample pellet is placed on the stage, where the grease holds the sample, and the total heat capacity is measured. The MultiVu software in PPMS automatically subtracts the reference heat capacity to obtain the heat capacity of the material [13]. Generally, a peak is obtained at long-range magnetic ordering in the heat capacity data. The change in magnetic entropy related to the long-range ordering is obtained by subtracting lattice contribution from the total heat capacity observed. The lattice contribution is generally calculated using a combined Debye-Einstein model or experimentally can be obtained by measuring the heat capacity of an isostructural non-magnetic sample. PPMS provides the temperature range of 1.8-400 K and the magnetic field of 0-9 T, allowing for wide range of studies [13].

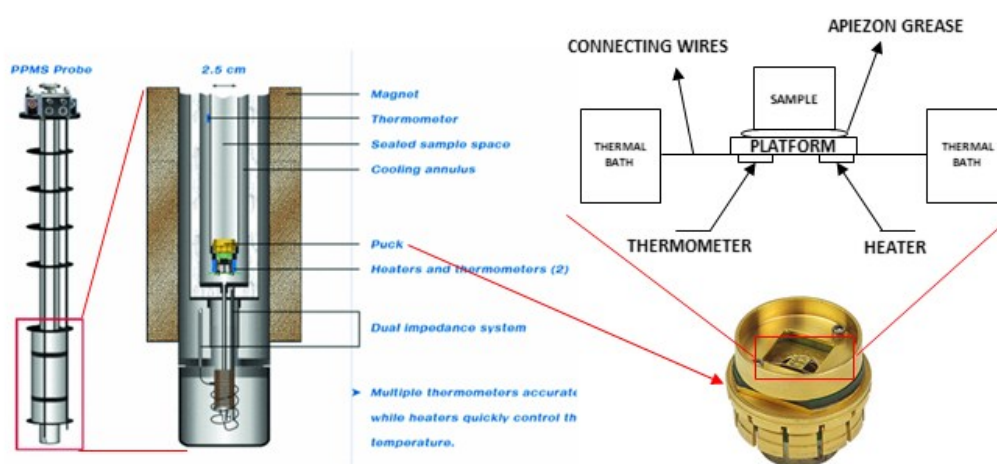


Figure 2.4 Left. Detailed view of the sample chamber of PPMS probe. Right. Heat capacity puck along with the schematic diagram of the sample stage. (adapted from Ref. [12,13])

2.3.4 Dielectric study

The dielectric constant is an important electrical property of the materials used to characterize the magnetoelectric and multiferroic materials. The dielectric constant can be measured by using two electrodes on opposite sides of the sample pellet as in a parallel plate capacitor. Electrical contacts are made using copper wires attached with silver paste on either side of the sample. I have used PELCO high-performance silver paste which has less dielectric noise and is effective at wide range of temperatures. Then this sample will be connected to the multifunction probe which is inserted into PPMS's sample chamber. PPMS will provide the temperature and magnetic field control. Further, these two electrodes are connected to an external LCR (model E4980A) meter to measure the capacitance. Then the capacitance data were collected with the help of the LabVIEW program while ramping the temperature with a rate of 2 K/min and the magnetic field with a sweep rate of 100 Oe/sec. The obtained dielectric constant is a complex quantity and is given by,

$$\begin{aligned}\epsilon_r &= \epsilon_r' - i\epsilon_r'' \\ \text{loss} &= \tan\delta = \epsilon_r''/\epsilon_r'\end{aligned}$$

here ϵ_r' and ϵ_r'' are the real and imaginary parts of the dielectric constant, respectively. The dielectric loss is also known as dissipation factor. From the capacitance data, the dielectric constant is obtained by using the relation,

$$\epsilon_r' = Cd/\epsilon_0 A$$

where, ϵ_0 is the permittivity of free space (8.854×10^{-12} F.m⁻¹), A is the area of the parallel electrodes, and d is the distance between the electrodes or thickness of the sample. For probing magnetodielectric effect, capacitance is recorded by varying the magnetic field between ± 9 T and temperature constant. Further, the magnetodielectric (*MD*) effect is obtained by the following equation,

$$MD (\%) = \frac{\epsilon_r(H) - \epsilon_r(0)}{\epsilon_r(0)}$$

here the ϵ_r is real part of the dielectric constant.

2.3.5 Pyrocurrent and electric polarization

Since the electric polarization in spin-induced multiferroics is small ($\sim 10^{-2}$ $\mu\text{C}/\text{cm}^2$), pyroelectric measurements have been widely used to measure electric polarization [14]. The pyrocurrent measurement procedure is displayed in Figure 2.5. In this measurement, the sample

is first poled with an electric field while cooling the sample across the ferroelectric transition temperature. After that, the external electric field is switched off and the electrode wires are shorted for sufficient time in order to remove all the stray charges accumulated at sample electrode interfaces. Then the electrode wires are connected to the Keithley 6517A electrometer and recorded the current while warming the sample with a constant rate. The pyrocurrent peak amplitude depends on the warming rate. In ferroelectrics, an asymmetric pyrocurrent anomaly will be observed at transition temperature as shown in Figure 2.6. This pyrocurrent is integrated with respect to time to obtain the electric polarization (see Figure 2.6). Since the sample is poled across the transition temperature in this measurement, the material can be polarized even with a lower electric field, and a very small polarization signature can also be detected in this process, which may not be possible in the normal $P(E)$ measurement described before. Thus, in multiferroic materials, where the polarization is comparatively low and the transition temperature is low, pyrocurrent measurement has become a standard protocol for polarization measurements. The switching of polarization can also be checked by reversing the poling field sign, which is an intrinsic property of ferroelectricity.

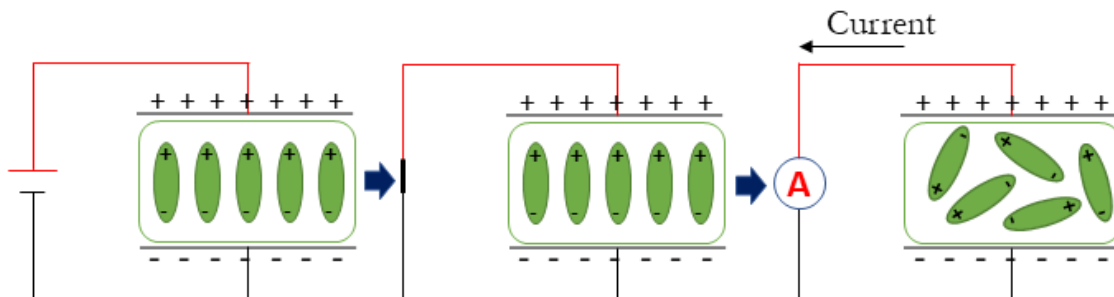


Figure 2.5 Procedure of pyrocurrent technique.

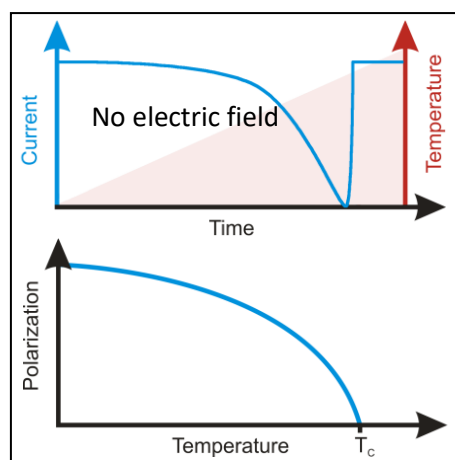


Figure 2.6 Top. Pyrocurrent as a function of temperature and time. Bottom. Corresponding polarization.

In this thesis, this technique is used the most to characterize the magnetoelectric and multiferroics. I have followed the warming rate of 10 K/min and magnetic field sweep rate of 100 Oe/sec. This rate is constant throughout the thesis unless it is mentioned. Another point to note here is that we must pole the sample in the presence of both magnetic and electric fields in the case of magnetoelectrics – magnetoelectric poling. Also, depends on the magnetic symmetry, one may have to carry the measurements in either $E \parallel H$ or $E \perp H$ configurations [15].

2.3.6 DC bias technique

Unlike magnetic measurements, the measurement of electric polarization suffers from many artifacts. In general, the ferroelectric properties are studied by P - E hysteresis loop measurement using the Sawyer-Tower circuit. In an ideal ferroelectric like BaTiO_3 , we get a proper hysteresis loop. In many materials, particularly in multiferroics where the leak current and trapped charged carriers can dominate the displacement current and change the shape of the hysteresis loop [14,16]. While most researchers working on ferroelectrics are aware of these artifacts, perhaps the magnetism community involved in exploring multiferroics is not aware of such problems and often cigar-shaped loops that manifest the lossy nature of the sample are mistaken for ferroelectricity. Scott pointed this out in an interesting way in the skin of a banana [17]. Further, the ferroelectric characterization in the polycrystalline samples is determined by the density and thickness of the sample. Many times, the researchers perform the P - E loop measurements in thick samples and, therefore, are limited to the voltage that is lower than the coercive field.

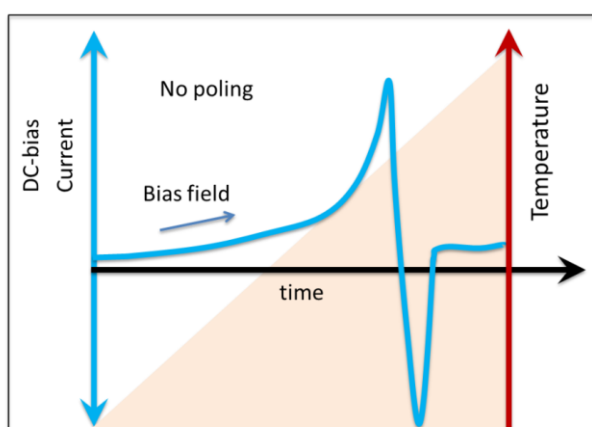


Figure 2.7 Output of the DC bias measurement.

As seen in the previous section, pyrocurrent is used to measure the electric polarization in magnetoelectrics and multiferroics. However, a broad and symmetric pyrocurrent peak

appears in the vicinity of magnetic ordering in many cases due to leakage current and thermally stimulated free charge carriers (TSFC), but it is not associated with the intrinsic polarization. These pyrocurrent anomalies are also switchable and many researchers more often think it is due to intrinsic polarization. In many cases, the heating rate-dependent pyroelectric current is useful to differentiate the intrinsic polarization from the extrinsic effects discussed above. However, it is not helpful in all cases. Therefore, our group invented the DC bias technique to differentiate the true intrinsic electric polarization from the artifacts [14].

In this DC bias technique, we apply an electric field while warming the sample and record the pyroelectric current, unlike conventional pyrocurrent measurement where we apply the electric field while cooling the sample, then we record the pyrocurrent without the electric field. In the DC bias process, the applied electric field below the transition temperature acts as a poling field and thus polarizes the dipoles. This change in polarization appears as a positive current peak in dc bias signal. As we cross the transition temperature and move towards paraelectric region, the dipoles start to depolarize which appears as a negative dc bias signal. The outcome of the DC bias measurement for the case of magnetoelectrics or multiferroics is shown in Figure 2.7. In extrinsic cases like leakage currents or thermally stimulated free charge carriers, the dc bias current increases monotonously across the transition.

References

- [1] A. R. West, *Solid State Chemistry and Its Applications* (John Wiley & Sons, 2014).
- [2] H. M. Rietveld, *J. Appl. Crystallogr.* **2**, 65 (1969).
- [3] L. C. Chapon, P. Manuel, P. G. Radaelli, C. Benson, L. Perrott, S. Ansell, N. J. Rhodes, D. Raspino, D. Duxbury, and E. Spill, *Neutron News* **22**, 22 (2011).
- [4] J. Rodriguez-Carvajal, in *Satell. Meet. Powder Diffr. XV Congr. IUCr* (Toulouse, France:[sn], 1990).
- [5] V. Petříček, M. Dušek, and L. Palatinus, *Zeitschrift Für Krist. Cryst. Mater.* **229**, 345 (2014).
- [6] K. Momma and F. Izumi, *J. Appl. Crystallogr.* **41**, 653 (2008).
- [7] H. T. Stokes, D. M. Hatch, B. J. Campbell, and D. E. Tanner, *J. Appl. Crystallogr.* **39**, 607 (2006).
- [8] Bilbao Crystallographic Server, <http://www.cryst.ehu.es>.
- [9] J. M. Perez-Mato, S. V Gallego, E. S. Tasci, and L. Elcoro, *Annu. Rev. Mater. Res* **45**, 217 (2015).
- [10] *Magnetic Property Measurement System - MPMS 3 User's Manual (Quantum Design)*.
- [11] D. Martien, *Introduction to AC susceptibility (Quantum Design)* (2002).
- [12] *Physical Property Measurement System - AC Measurement System (ACMS) Option - User's Manual (Quantum Design)*.
- [13] *Physical Property Measurement System - Heat Capacity Option - User's Manual (Quantum Design)*.
- [14] C. De, S. Ghara, and A. Sundaresan, *Solid State Commun.* **205**, 61 (2015).
- [15] S. Shtrikman and D. Treves, *Phys. Rev.* **130**, 986 (1963).
- [16] S. W. S. McKeever and D. M. Hughes, *J. Phys. D. Appl. Phys.* **8**, 1520 (1975).
- [17] J. F. Scott, **021001**, (2008).


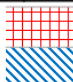


PART A

Introduction to “Green Phases” – R_2BaCuO_5 ($R = \text{Rare Earth}$)

Ternary inorganic oxides with the general formula R_2BaMO_5 , where R is rare-earth and M is transition metal, form a plethora of compounds with riveting structural and magnetic properties. These compounds were synthesized and characterized in detail during the 1980s by Muller Buschbaum’s group, C. Michel and Raveau, and few other researchers [1–6]. They are classified into four different structural types, mainly characterized by the different oxygen coordination geometry around the divalent transition metal, as seen in Table I. The known coordinations are square planar, square pyramidal, and octahedral. Among these types, the first and well-known Sm_2BaCuO_5 -type shows the complex orthorhombic structure with space group $Pnma$ ($Z = 4$) [1]. The second type, Nd_2BaMO_5 ($M = \text{Pt, Pd, and Cu}$) exhibit a tetragonal structure with $P4/mbm$ where the M^{2+} ions found in isolated square planar coordinated MO_4 connected to NdO_8 polyhedra. The third type, Nd_2BaZnO_5 crystallizes in tetragonal $I4/mcm$ with Zn^{2+} -ions in tetrahedral (ZnO_4) coordination. Finally, the so-called Nd_2BaMO_5 ($M = \text{Ni and Co}$)-type has the orthorhombic structure with space group $Immm$ ($Z = 2$). This structure is composed of isolated chains of corner shared NiO_6 octahedra running parallel to \mathbf{a} -axis resulting in one-dimensional character. However, R_2BaMO_5 ($M = \text{Ni, and Co}$) with smaller size R -ion show dimorphism, which crystallize in both $Immm$ and $Pnma$ structures.

Table I. Different structure types of R_2BaMO_5 compounds.

$R \backslash M$	La	Ce	Pr	Nd	Sm	Eu	Gd	Tb	Dy	Y	Ho	Er	Tm	Yb	Lu
Co			Blue diagonal	Blue diagonal	Blue diagonal	Blue diagonal	Blue diagonal	Blue diagonal	Blue diagonal	Blue diagonal	Blue diagonal	Blue diagonal	Blue diagonal	Blue diagonal	Blue diagonal
Ni			Blue diagonal	Blue diagonal	Blue diagonal	Blue diagonal	Blue diagonal	Blue diagonal	Blue diagonal	Blue diagonal	Blue diagonal	Blue diagonal	Blue diagonal	Blue diagonal	Blue diagonal
Cu	Green diagonal		Green diagonal	Green diagonal	Green diagonal	Green diagonal	Green diagonal	Green diagonal	Green diagonal	Green diagonal	Green diagonal	Green diagonal	Green diagonal	Green diagonal	Green diagonal
Zn	Red cross		Red cross	Red cross	Red cross	Red cross	Red cross	Red cross	Red cross	Red cross	Red cross	Red cross	Red cross	Red cross	Red cross
Pd	Green diagonal		Green diagonal	Green diagonal	Green diagonal	Green diagonal	Green diagonal	Green diagonal	Green diagonal	Green diagonal	Green diagonal	Green diagonal	Green diagonal	Green diagonal	Green diagonal
Pt	Green diagonal		Green diagonal	Green diagonal	Green diagonal	Green diagonal	Green diagonal	Green diagonal	Green diagonal	Green diagonal	Green diagonal	Green diagonal	Green diagonal	Green diagonal	Green diagonal

 Sm_2BaCuO_5 -type; S.G: $Pnma$	 Nd_2BaZnO_5 -type; S.G: $I4/mcm$
 Nd_2BaPtO_5 -type; S.G: $P4/mbm$	 Nd_2BaNiO_5 -type; S.G: $Immm$

Most of the $R_2\text{BaCuO}_5$ compounds crystallize in $\text{Sm}_2\text{BaCuO}_5$ -type, which are popularly known as “green phases”. These compounds have been found more often as secondary phases in the early synthesis of well-known $123\text{-}R\text{Ba}_2\text{Cu}_3\text{O}_7$ superconductors [1,4]. Later, small particles of these compounds were used as flux pinning centers in high- T_c superconductors to increase the critical current density. As mentioned earlier, the structure of these compounds was first solved by C. Michel and Raveau [1]. In this crystal structure, the copper ions are situated in distorted square pyramids (CuO_5) and Ba^{2+} ions are eleven coordinated, which are in the cavities formed by edge shared $R_2\text{O}_{11}$ groups. These groups are made up of the common triangular face shared monocapped trigonal prisms RO_7 . The structure of these compounds will be discussed more in detail later in the thesis. Afterward, the structure was confirmed by single-crystal X-ray diffraction and neutron diffraction studies [4,7–9]. Raman and infrared spectroscopic studies were consistent with the orthorhombic structure with space group $Pnma$ [10].

Later, their magnetic properties were extensively investigated by different experiments like heat capacity, magnetic measurements, electron paramagnetic resonance (EPR), Mossbauer, optical absorption, and neutron diffraction [11–20]. They exhibit a wide range of magnetism and ground state spin structures due to strong $4f\text{-}3d$ coupling. These compounds show two magnetic transitions corresponding to antiferromagnetic ordering of Cu^{2+} and R^{3+} ions. Also, it is suggested that some of these compounds show a considerable magnetocaloric effect [21]. Since the $4f\text{-}3d$ interaction associated with each R ion is different due to their different magnetism, crystal field effects, and magnetic anisotropy, these compounds evidence interesting magnetic ground states. For example, ground state magnetic structures possess different propagation vectors for each compound, such as $\mathbf{k}_C = (0, 0, 0)$ for $R = \text{Dy}$, $\mathbf{k}_{C1} = (0, \frac{1}{2}, 0) + \mathbf{k}_{C2} = (0, 0, 0)$ for Ho , $\mathbf{k}_C = (0, \frac{1}{2}, \frac{1}{2})$ for $R = \text{Y}$, $\mathbf{k}_C = (0, \frac{1}{2}, 0)$ for $R = \text{Er}$ and Tm and $\mathbf{k}_C = (0, 0, \frac{1}{2})$ for $R = \text{Gd}$ [18–20]. However, the magnetic structures of these compounds were not well studied. From the viewpoint of magnetic symmetry, these compounds might be good candidates to show magnetoelectric or multiferroic properties. Therefore, we have extensively investigated the magnetoelectric and multiferroic properties of $R_2\text{BaCuO}_5$ ($R = \text{Sm-Lu, Y}$) family of compounds. Indeed, they exhibit linear magnetoelectric effect and multiferroicity along with intriguing magnetic structures.

Part A has four chapters that deal with the structural, magnetic, magnetoelectric, and multiferroic properties of green phase compounds in detail.

References

- [1] C. Michel and B. Raveau, *J. Solid State Chem.* **43**, 73 (1982).
- [2] C. Michel and B. Raveau, *J. Solid State Chem.* **49**, 150 (1983).
- [3] S. Schiffler and H. Mueller-Buschbaum, *Monatsh. Chem.:(Austria)* **117**, (1986).
- [4] A. Salinas-Sanchez, J. L. Garcia-Muñoz, J. Rodriguez-Carvajal, R. Saez-Puche, and J. L. Martinez, *J. Solid State Chem.* **100**, 201 (1992).
- [5] E. Garcia-Matres, J. L. Martinez, J. Rodriguez-Carvajal, J. A. Alonso, A. Salinas-Sánchez, and R. Saez-Puche, *J. Solid State Chem.* **103**, 322 (1993).
- [6] R. Saez-Puche and J. Hernandez-Velasco, in *Adv. Mater. Res.* (Trans Tech Publ, 1994), pp. 65–82.
- [7] J. A. Campá, J. M. G. de Salazar, E. Gutiérrez-Puebla, M. A. Monge, I. Rasines, and C. Ruíz-Valero, *Phys. Rev. B* **37**, 529 (1988).
- [8] S. Sato and I. Nakada, *Acta Crystallogr. Sect. C Cryst. Struct. Commun.* **45**, 523 (1989).
- [9] B. A. Hunter, S. L. Town, R. L. Davis, G. J. Russell, and K. N. R. Taylor, *Phys. C Supercond.* **161**, 594 (1989).
- [10] H. C. Gupta and V. Sharma, *J. Raman Spectrosc. An Int. J. Orig. Work All Asp. Raman Spectrosc. Incl. High. Order Process. Also, Brillouin Rayleigh Scatt.* **36**, 83 (2005).
- [11] R. Z. Levitin, B. V Mill, V. V Moshchalkov, N. A. Samarin, V. V Snegirev, and J. Zoubkova, *J. Magn. Magn. Mater.* **90**, 536 (1990).
- [12] V. V Moshchalkov, N. A. Samarin, I. O. Grishchenko, B. V Mill, and Z. J., *Solid State Commun.* **78**, 879 (1991).
- [13] K. Kanoda, T. Takahashi, T. Kawagoe, T. Mizoguchi, S. Kagoshima, and M. Hasumi, *Jpn. J. Appl. Phys.* **26**, L2018 (1987).
- [14] Y. A. Koksharov, V. V Moshchalkov, A. A. Gippius, B. V Mill, Y. Zoubkova, S. V Gudenko, and A. N. Mezhuev, *Phys. C Supercond.* **185**, 1151 (1991).
- [15] M. Strecker, P. Hettkamp, G. Wortmann, and G. Stewart, *J. Magn. Magn. Mater.* **177–181**, 1095 (1998).
- [16] I. V Paukov, M. N. Popova, and B. V Mill, *Phys. Lett. A* **169**, 301 (1992).
- [17] M. Baran, H. Szymczak, S. A. Klimin, M. N. Popova, and R. Z. Levitin, *J. Exp. Theor. Phys.* **84**, 175 (1997).
- [18] I. V Golosovsky, V. P. Plakhtii, V. P. Kharchenkov, J. Zoubkova, B. V Mill, M. Bonnet, and E. Roudeau, *Fiz. Tve. Tela.* **34**, 1483 (1992).
- [19] I. V Golosovsky, P. Böni, and P. Fischer, *Solid State Commun.* **87**, 1035 (1993).
- [20] A. K. Ovsyanikov, I. V Golosovsky, I. A. Zobkalo, and I. Mirebeau, *J. Magn. Magn. Mater.* **353**, 71 (2014).
- [21] L. Li, K. Su, and D. Huo, *J. Alloys Compd.* **735**, 773 (2018).

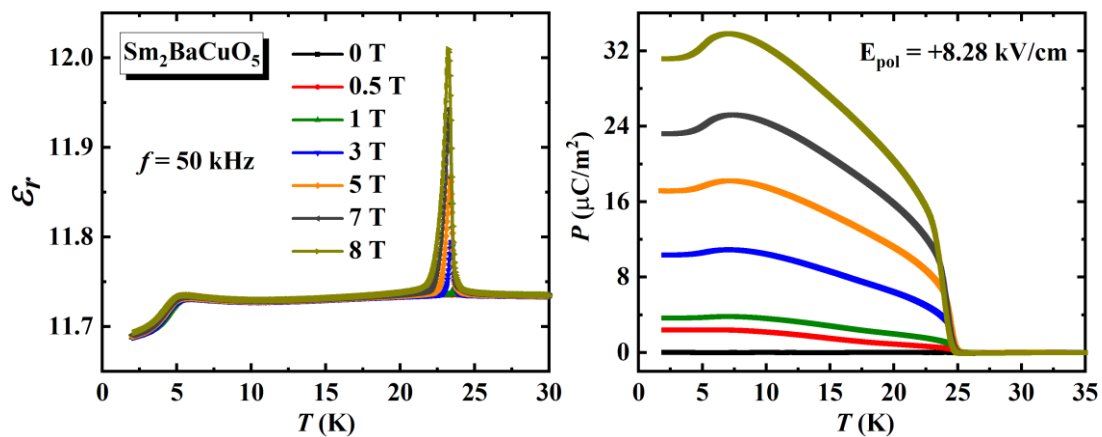
Chapter 3

Linear magnetoelectric effect in the green phase

$\text{Sm}_2\text{BaCuO}_5^*$

Summary

The present chapter deals with the discovery of linear magnetoelectric effect in the well-known green phase compound, $\text{Sm}_2\text{BaCuO}_5$, which crystallizes in the centrosymmetric orthorhombic ($Pnma$) structure. Magnetization and specific heat measurements revealed the long-range antiferromagnetic ordering of Cu^{2+} and Sm^{3+} ions at $T_{N1} = 23$ K and $T_{N2} = 5$ K, respectively. Applied magnetic field induces dielectric anomaly at T_{N1} whose magnitude increases with field, which results in a significant (1.7 %) magnetocapacitance effect. On the other hand, the dielectric anomaly observed in the absence of magnetic field at T_{N2} shows a small (0.4 %) magnetocapacitance effect. Interestingly, applied magnetic field induces an electric polarization below T_{N1} and the polarization varies linearly up to the maximum applied field of 9 T with the magnetoelectric coefficient $\alpha \sim 4.4$ ps/m, demonstrating magnetoelectric coupling. Below T_{N2} , the electric polarization decreases from 35 to 29 $\mu\text{C}/\text{m}^2$ at 2 K and 9 T due to the ordering of Sm sublattice. The observed linear magnetoelectricity in $\text{Sm}_2\text{BaCuO}_5$ is explained using symmetry analysis.



*This work is published in Phys. Rev. B, **100**, 104417 (2019), © 2019 by the American Physical Society.

3.1 Introduction

Magnetoelectric effect allows the control of electric polarization by magnetic field or magnetization by an electric field, which is promising for applications in spintronic devices, magnetic field sensors, non-volatile memories, etc., as discussed earlier in Chapter 1. In the linear magnetoelectric materials, the induced electric polarization or magnetization is linearly proportional to the applied magnetic or electric field, respectively, is shown in the form $P = \alpha H$ or $M = \alpha E$, where α is the magnetoelectric coefficient. However, these materials are restricted by symmetry requirements, involving simultaneous breaking of time reversal and spatial inversion symmetries. However, it is still very challenging to find new materials within different structural types which show magnetoelectric effect with strong coupling between magnetic and electric orders.

$\text{Sm}_2\text{BaCuO}_5$ belongs to the green phase $R_2\text{BaCuO}_5$ family of compounds, where R stands for rare earth, which crystallizes in the orthorhombic structure with space group $Pnma$ as mentioned earlier [1,2]. Previously, it is reported that this compound exhibits two magnetic transitions at 22 and 5 K from specific heat and magnetic measurements [3,4]. It is known that compounds with magnetic ions located at the local noncentrosymmetric sites, which have spin-dependent electric dipoles, can cause the magnetoelectric effect depending on single-ion contributions [5]. Considering that magnetic ions are placed at the local noncentrosymmetric site ($4c$), $\text{Sm}_2\text{BaCuO}_5$ might show magnetoelectric coupling. Therefore, we have investigated the magnetoelectrical properties of $\text{Sm}_2\text{BaCuO}_5$.

In this chapter, we present the observation of linear magnetoelectric effect in the green phase oxide $\text{Sm}_2\text{BaCuO}_5$. In this compound, Cu^{2+} ions order antiferromagnetically at $T_{N1} = 23$ K, where electric polarization appears under applied magnetic fields and varies linearly with the field. The origin of linear magnetoelectric effect has been discussed based on symmetry analysis.

3.2 Experimental section

Polycrystalline samples of $\text{Sm}_2\text{BaCuO}_5$ were prepared by heating the stoichiometric mixture of high purity Sm_2O_3 (preheated), BaCO_3 , and CuO at 950°C for 12 hrs in the air. After this, we have made the pellets and sintered at same temperature for 12 hrs. X-ray powder diffraction data was recorded using a PANalytical Empyrean diffractometer with Cu

$K\alpha_1$ radiation. The crystal structure refinement was performed by using Fullprof program [6]. Magnetic measurements, such as DC magnetic susceptibility and isothermal magnetization, were performed by a Superconducting Quantum Interference Device (SQUID, Quantum Design) magnetometer. The specific heat (C_p) and AC susceptibility were measured in the Physical Property Measurement System (PPMS, Quantum Design). To measure the dielectric properties and pyrocurrent (electric polarization), silver paste was coated on both sides of the disk-shaped sample of dimension $5\text{ mm} \times 5\text{ mm}$ area and 0.362 mm thickness, while the temperature and magnetic fields were controlled by PPMS. The dielectric constant as a function of temperature under different magnetic fields was recorded using an Agilent E4980A LCR meter. The temperature dependence of pyrocurrent was measured with a Keithley 6517A electrometer and electric polarization was obtained by integrating the pyrocurrent with respect to time. We have followed warming rate of 2 K/min for dielectric and 10 K/min for pyrocurrent measurements. This rate is consistent throughout the thesis unless it is mentioned. The details of all experimental techniques were discussed in Chapter 2.

3.3 Results and discussion

3.3.1 Crystal structure

The Rietveld refinement of room temperature X-ray powder diffraction data of $\text{Sm}_2\text{BaCuO}_5$ confirms the orthorhombic structure with the space group $Pnma$. Trace amount ($\sim 1\%$) of Sm_2CuO_4 phase was present as a minor phase which was included in the refinement. The refined XRD pattern is shown in Figure 3.1. The detailed structural parameters are listed in Table 3.1. The crystal structure can be considered as built up from distorted monocapped trigonal prisms SmO_7 , which share one triangular face forming Sm_2O_{11} blocks. These Sm_2O_{11} blocks then share edges to form a three-dimensional network which demarcates the cavities where Ba^{2+} and Cu^{2+} are located. Each barium ion is coordinated by 11 oxygen atoms, while unusual CuO_5 forms an isolated distorted square pyramid as reported earlier [2].

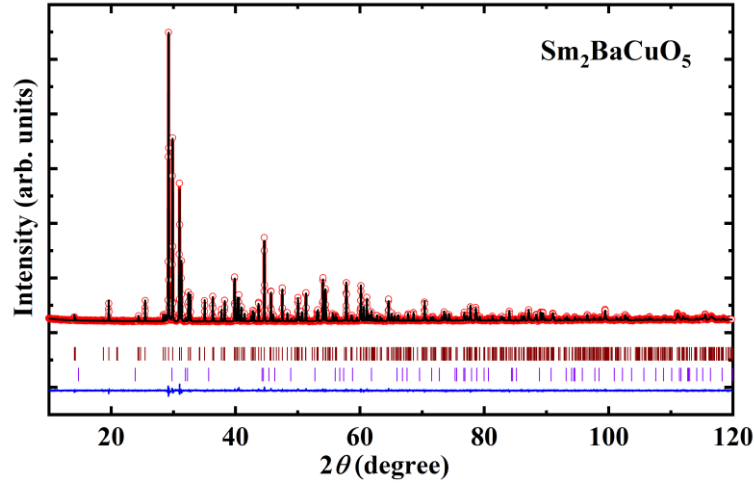


Figure 3.1 Rietveld refined room temperature X-ray diffraction pattern of $\text{Sm}_2\text{BaCuO}_5$. The second row of vertical tick marks indicates the secondary phase Sm_2CuO_4 (<1 %).

Table 3.1 Structural parameters of $\text{Sm}_2\text{BaCuO}_5$ obtained from Rietveld refinement. Space group: $Pnma$; $a = 12.4140$ (1) Å, $b = 5.7647$ (1) Å, $c = 7.2798$ (2) Å, $V = 520.968$ (6) Å³; $\chi^2 = 1.53$; Bragg R -factor = 3.98 (%), R_f -factor = 4.15 (%).

Atom	Wyckoff position	Symmetry	x	y	z	B_{iso} (Å ²)	Occu.
Sm1	4c	. m .	0.2886 (1)	0.2500	0.1142 (2)	0.033 (22)	0.50
Sm2	4c	. m .	0.0737 (1)	0.2500	0.3938 (2)	0.033 (22)	0.50
Ba	4c	. m .	0.9062 (1)	0.2500	0.9301 (2)	0.253 (36)	0.50
Cu	4c	. m .	0.6584 (3)	0.2500	0.7132 (5)	0.082 (81)	0.50
O1	8d	1	0.4342 (10)	-0.0124 (18)	0.1746 (11)	1.000	1.00
O2	8d	1	0.2271 (8)	0.5120 (19)	0.3505 (16)	1.000	1.00
O3	4c	. m .	0.0951(12)	0.250	0.0694 (19)	1.000	0.50

3.3.2 DC magnetic susceptibility, heat capacity and ac susceptibility

Figure 3.2(a) shows temperature dependence of dc magnetic susceptibility data $\chi(T)$ measured with an applied field of 0.1 kOe under the field cooled condition. These data show two clear anomalies in $\chi(T)$ at $T_N^{\text{Cu}} = 23$ K and $T_N^{\text{Sm}} = 5$ K corresponding to antiferromagnetic ordering of Cu and Sm-moments, respectively. The long-range magnetic order is confirmed by the λ -type anomalies in specific heat $C_p(T)$ data as seen in Figure 3.2(b). Overall, these results are similar to those reported earlier [3,4]. The presence of two anomalies at 23 and 5 K in $C_p(T)$ data suggests the independent ordering of Cu and Sm moments, respectively. However, it is possible that the local field created by Cu ordering may induce partial ordering

of Sm moments at T_N^{Cu} but it requires neutron diffraction studies to confirm this possibility. A broad hump around 65 K is seen in the magnetization data but there is no corresponding anomaly in $C_p(T)$. The origin of this hump is due to the presence of superconducting impurity phase Sm123, which was previously observed in some of the green phase compounds [7]. We did not observe this impurity phase in our laboratory X-ray powder diffraction data. However, this anomaly cannot influence the main results of this compound. The magnetic field-dependent magnetization $M(H)$ at different temperatures is shown in the inset of Figure 3.2(a). The curves at low temperatures are linear and in good agreement with the antiferromagnetic ordering of Cu and Sm ions and room temperature data resembling the paramagnetic behavior.

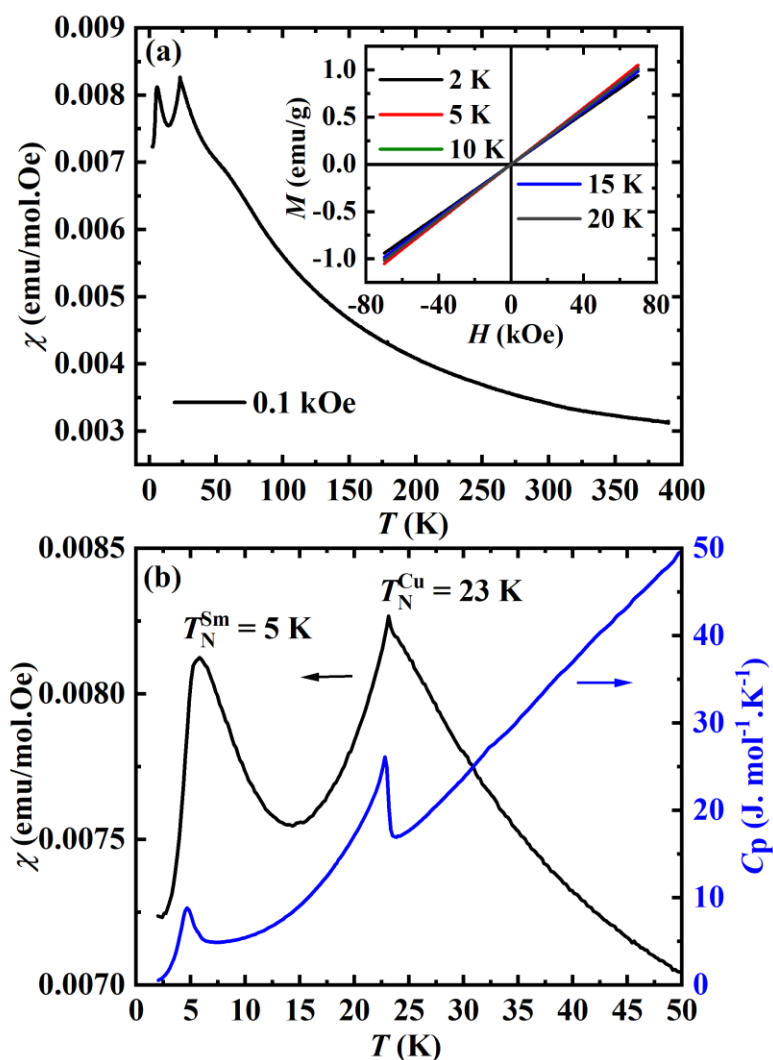


Figure 3.2 (a) Magnetic susceptibility as a function of temperature measured with magnetic field of 0.1 kOe under field cooled sequence. Inset shows the magnetization curves against magnetic field at different temperatures. (b) Magnetic susceptibility and specific heat in the low temperature region.

We have performed the ac susceptibility measurements to confirm the long-range magnetic ordering. Figure 3.3 shows the real and imaginary parts of ac magnetization measured at different frequencies of applied ac magnetic field. There are two anomalies in the real part at 23 and 5 K associated with the Cu^{2+} and Sm^{3+} ions ordering, respectively. These anomalies are insensitive to the applied ac magnetic field frequency and confirm the long-range magnetic ordering. However, we did not observe any features in the imaginary component. This can be due to the low moment of both copper and samarium.

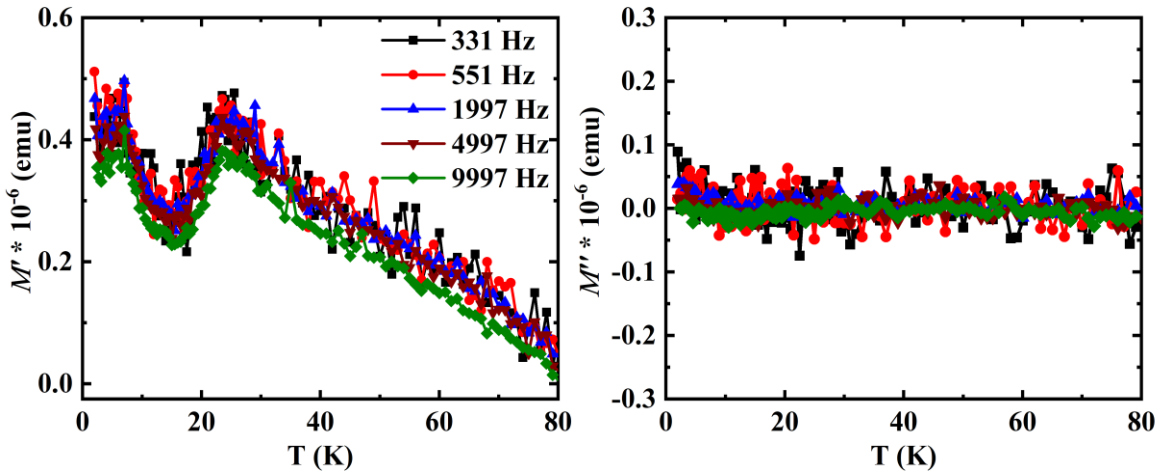


Figure 3.3 ac susceptibility data of $\text{Sm}_2\text{BaCuO}_5$ measured under different frequencies at an ac field 10 Oe.

To estimate the magnetic contribution $C_{\text{Mag}}(T)$ to the heat capacity, phonon contribution (C_{ph}) is calculated by fitting the total heat capacity using combined Debye-Einstein model, as given by,

$$C_{\text{Phonon}} = C_{\text{Debye}} + C_{\text{Einstein}} = \frac{9Ra_1}{x_D^3} \int_0^{x_D} \frac{x^4 e^x}{(e^x - 1)^2} dx + 3R \sum_{n=1}^2 b_n \frac{x_{E,n}^2 e^{x_{E,n}}}{(e^{x_{E,n}} - 1)^2}$$

where R is the universal gas constant, $x_{D,E} = \theta_{D,E}/T$ where $\theta_{D,E}$ are the Debye and Einstein temperatures, respectively. We have fitted the heat capacity data in the temperature range 30 to 100 K, which is shown in Figure 3.4(a). Debye (a_1) and Einstein coefficients (b_1 and b_2) are 1, 3, and 5, respectively, are used since the total number of modes in the Debye-Einstein equation are equal to the number of atoms in the formula unit. The obtained values of the θ_D , θ_{E1} , and θ_{E2} are 84, 181, and 506, respectively. The lattice contribution is extrapolated down to 2 K, as shown by the solid line in Figure 3.4(a). By subtracting this lattice contribution $C_{\text{ph}}(T)$ from total heat capacity, magnetic contribution $C_{\text{Mag}}(T)$ obtained is shown in Figure

3.4(b). The change in magnetic entropy $\Delta S_{\text{Mag}}(T)$ associated with the magnetic transitions is calculated by using the equation,

$$\Delta S_{\text{Mag}}(T) = \int_0^T \frac{C_{\text{Mag}}(T)}{T} dT$$

The $\Delta S_{\text{Mag}}(T)$ for $\text{Sm}_2\text{BaCuO}_5$ is shown in the inset of Figure 3.4(b). The expected value of change in entropy due to magnetic ordering of $\text{Cu}^{2+}(S = 1/2)$ and $\text{Sm}^{3+}(S = 5/2)$ spins is $\Delta S_{\text{Mag}} = R \ln(2S + 1) = 9.13 \text{ J/mol-K}$ at high temperatures. The observed value $\Delta S_{\text{Mag}} \sim 7.57 \text{ J/mol-K}$ at 100 K, which is almost $\sim 83 \%$ of the expected change in entropy.

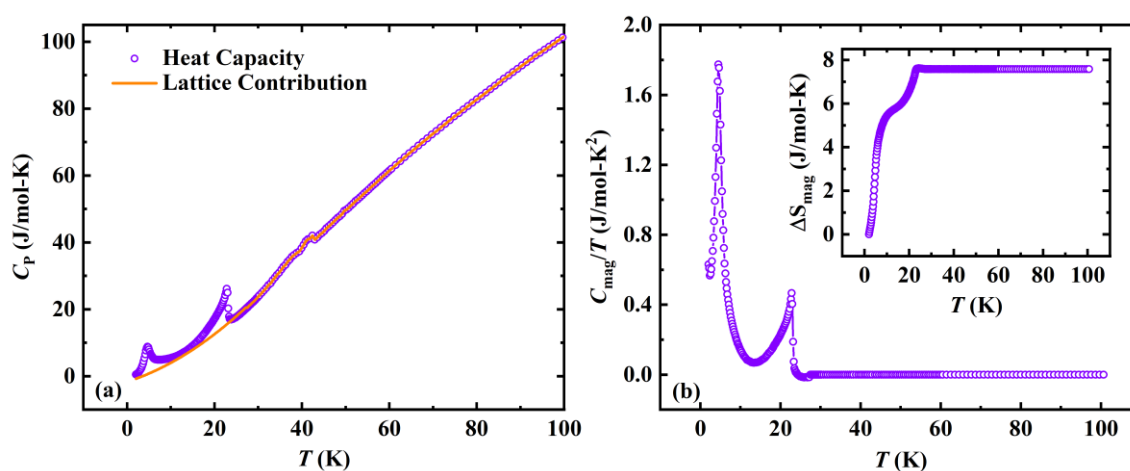


Figure 3.4 (a) Temperature-dependent heat capacity measured under 0 T and the solid line is phonon contribution obtained using the combined Debye-Einstein model. (b) Magnetic contribution to the heat capacity (C_{Mag}/T) and the inset shows the magnetic change in entropy.

3.3.3 Dielectric properties and magnetodielectric effect

Temperature dependence of the dielectric constant measured for different fields and the corresponding dissipation factor are shown in Figure 3.5(a & b). We did not observe any dielectric anomaly at the magnetic ordering temperature of Cu^{2+} ions under zero applied magnetic field. However, applied magnetic field induces a dielectric anomaly whose magnitude increases with the field as shown in Figure 3.5(a). Correspondingly, the loss data also displays a peak at T_{N}^{Cu} under applied magnetic field. This behavior is typical of linear magnetoelectric effect. Hence, the dielectric behavior at $T_{\text{N}}^{\text{Cu}} = 23 \text{ K}$ signifies the role of Cu spin structure and strong coupling between the magnetic and electric properties of $\text{Sm}_2\text{BaCuO}_5$ and the possible magnetoelectric effect. On the other hand, we observed a broad

dielectric anomaly at the Sm-ordering temperature (T_{N2}) in the absence of magnetic field, which is almost insensitive to the applied magnetic field.

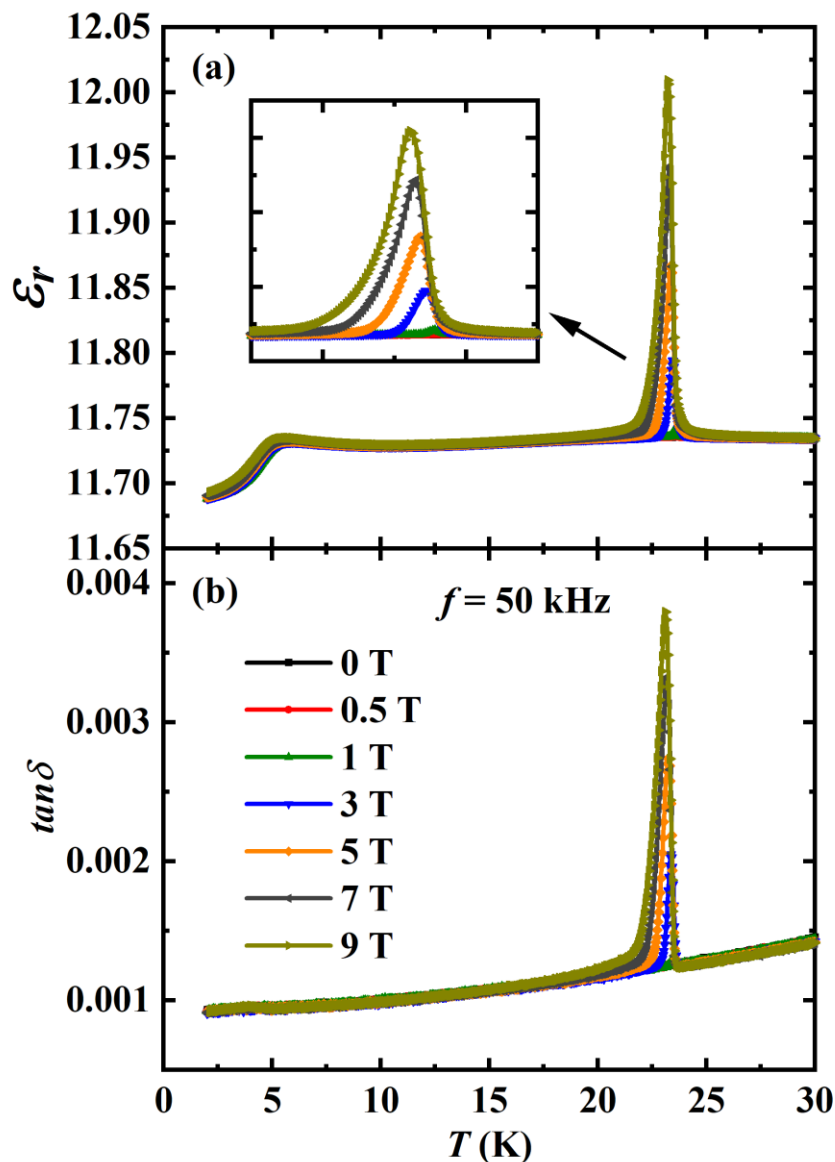


Figure 3.5 (a) Temperature-dependent dielectric constant and (b) corresponding loss factor measured under different magnetic fields with frequency $f = 50$ kHz.

Figure 3.6(a & b) shows the dielectric constant variation with temperature at different frequencies and the corresponding loss, respectively. The dielectric constant and loss values increased with temperature and decreased with increasing frequency. It shows an anomaly at 5 K which did not shift with frequency indicating the magnetic origin. Further, there are two broad anomalies at high temperatures in both dielectric and loss data, and they shift with frequency. This kind of behavior is generally a signature of dielectric relaxation (DR). In this compound, the observed relaxation (DR1 and DR2) can be of Maxwell-Wagner type which arises due to charge separation at the grain boundaries or sample and electrode interface.

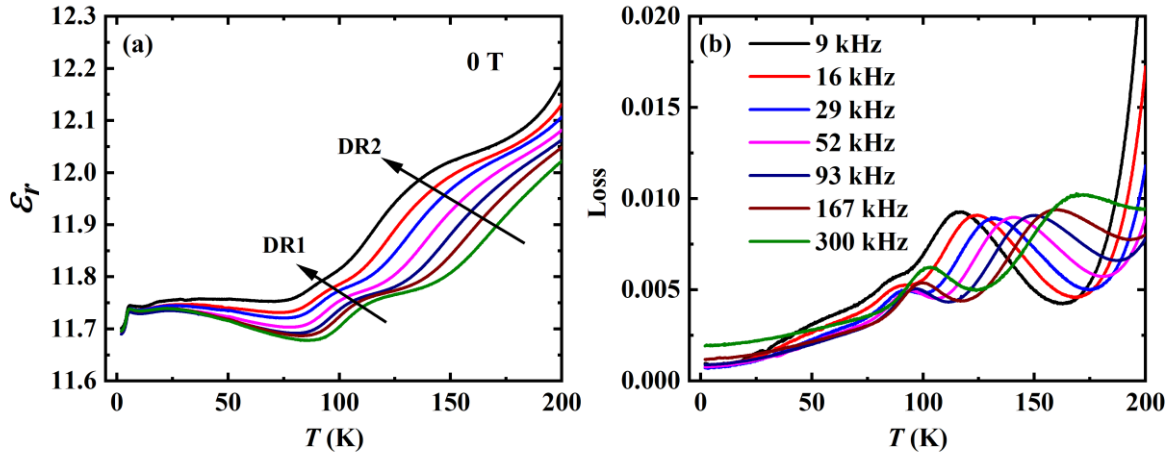


Figure 3.6 (a) Temperature-dependent dielectric constant and (b) corresponding loss factor measured under different frequencies measured at 0 T. It shows relaxation behavior at high temperatures.

Further, this compound exhibits the significant magnetodielectric effect (MD) – the change of dielectric constant with applied magnetic field, which is shown in Figure 3.7(a). This is obtained from the following equation,

$$MD (\%) = \frac{\epsilon_r(H) - \epsilon_r(0)}{\epsilon_r(0)}$$

The maximum change of 1.7 % is observed at $T_N^{\text{Cu}} = 23$ K and 7 T. There is a very small change below T_N^{Sm} and constant above the copper magnetic ordering temperature. This shows the presence of coupling between magnetic and electric orders below T_N^{Cu} .

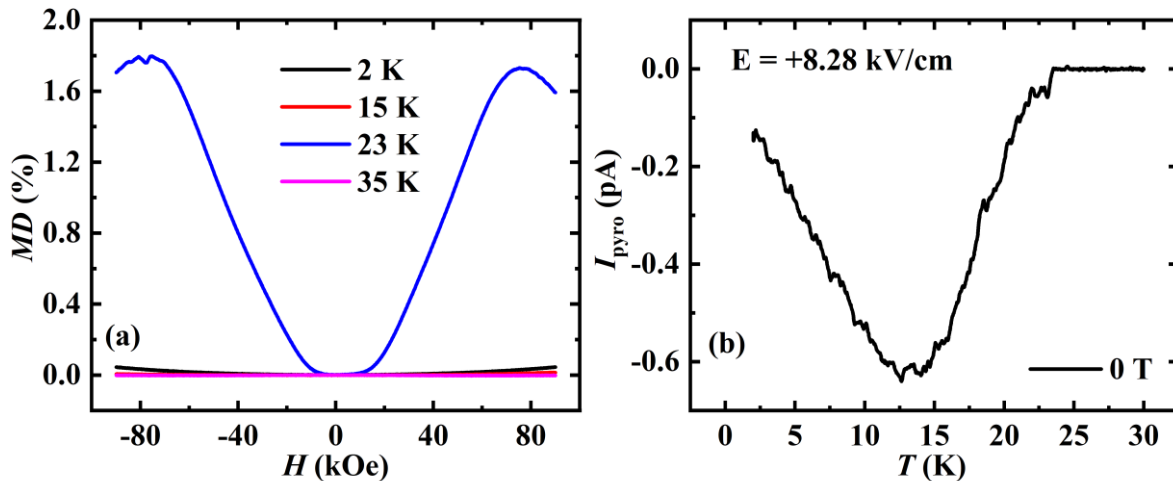


Figure 3.7 (a) Magnetic field change in dielectric constant at 2, 15, 23, and 35 K measured under frequency of 50 kHz. (b) Pyrocurrent recorded while warming under 0 T after poling with an electric field of $E = 8.28$ kV/cm.

3.3.4 Linear magnetoelectric effect

3.3.4.1 Pyrocurrent and electric polarization

To verify whether these dielectric anomalies are associated with field-induced electric polarization, which is a requirement for linear magnetoelectric effect, we have performed pyrocurrent measurements at various applied magnetic fields and a poling electric field $E_{\text{pol}} = +8.28$ kV/cm. After magnetoelectric poling, the current was measured in the presence of magnetic field. In zero magnetic field, we did not observe any pyrocurrent peak (no polarization) at the magnetic ordering temperatures but there is a broad peak due to leakage current of 0.6 pA centered around 15 K as shown in Figure 3.7(b). The intrinsic pyrocurrent peak appears only under magnetic field at T_{N1} and its magnitude increases with increasing magnetic field. In contrast, the leakage contribution remains almost constant with applied magnetic fields. To find the actual magnetoelectric current, we have subtracted the pyrocurrent measured under zero magnetic field from those measured under different magnetic fields as shown in Figure 3.8(a). The appearance of pyrocurrent under the magnetic fields demonstrate the strong magnetoelectric effect in $\text{Sm}_2\text{BaCuO}_5$.

The electric polarization obtained by integrating the pyrocurrent with respect to time is shown in Figure 3.8(b). With increasing magnetic field, the polarization increases monotonously to a value of $32 \mu\text{C}/\text{m}^2$ at 7 K for $H = 9$ T. It is worth pointing out the behavior of pyrocurrent at the independent Sm ordering temperature. A pyrocurrent peak appears at T_{N2} but opposite to the direction of the peak at Cu ordering temperature, indicating the suppression of polarization at 5 K as seen in Figure 3.8(b). This is due to the effect of independent ordering of Sm magnetic sublattice. There are few possibilities for the decrease of polarization below T_{N2} . It is possible that there is an additional contribution to the polarization from Sm moments in the temperature range $T_{N2} < T < T_{N1}$, due to its induced ordering at T_{N1} , which changes below T_{N2} . Alternatively, the independent Sm-ordering is strong enough to alter the copper magnetic structure decreasing electric polarization induced by it or which induces its contribution to polarization opposite to that due to the copper sublattice. However, neutron diffraction studies are required in order to determine the exact nature of magnetic phase transitions at T_{N1} and T_{N2} and the resulting magnetic structures of Sm and Cu sublattices as a function of temperature.

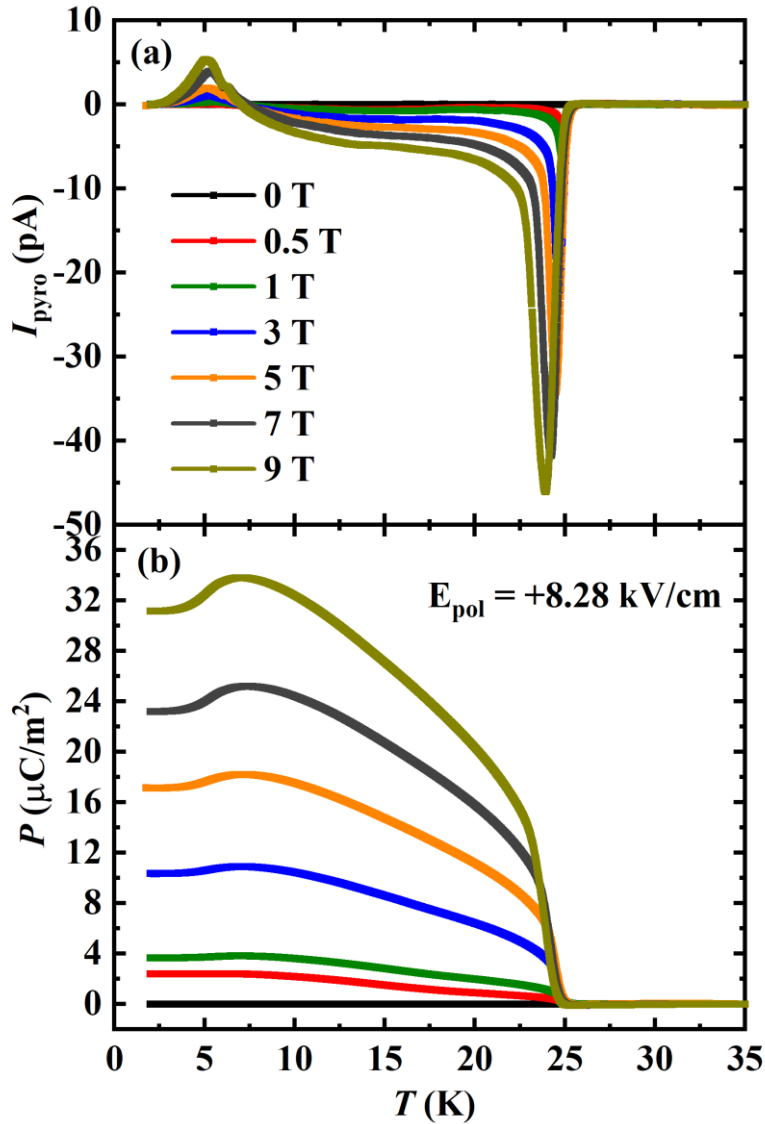


Figure 3.8 (a) Leakage current subtracted pyroelectric current as a function of temperature under different magnetic fields and poling electric field $E = +8.28 \text{ kV}/\text{cm}$ and (b) corresponding polarization obtained by integrating pyrocurrent with respect to time.

At 10 K, the polarization increases linearly with the magnetic field (see Figure 3.9), demonstrating the linear magnetoelectric effect in $\text{Sm}_2\text{BaCuO}_5$. The calculated magnetoelectric coefficient α of $\text{Sm}_2\text{BaCuO}_5$ is $\sim 4.4 \text{ ps}/\text{m}$ which is larger than that reported for the conventional linear magnetoelectric material Cr_2O_3 . In fact, this value is higher than many of the known magnetoelectrics for example, NdCrTiO_5 (0.51 ps/m), MnTiO_3 (2.6 ps/m), Co_3O_4 (2.6 ps/m), MnGa_2O_4 (0.17 ps/m), indicating the strong magnetoelectric coupling in $\text{Sm}_2\text{BaCuO}_5$ [8–11]. The observed value is relatively high even though our sample is polycrystalline, and a bigger value is expected for the single crystal. As of today, the highest α known material is TbPO_4 with a value of $\sim 730 \text{ ps}/\text{m}$ but at very low temperature of 2.38 K [12].

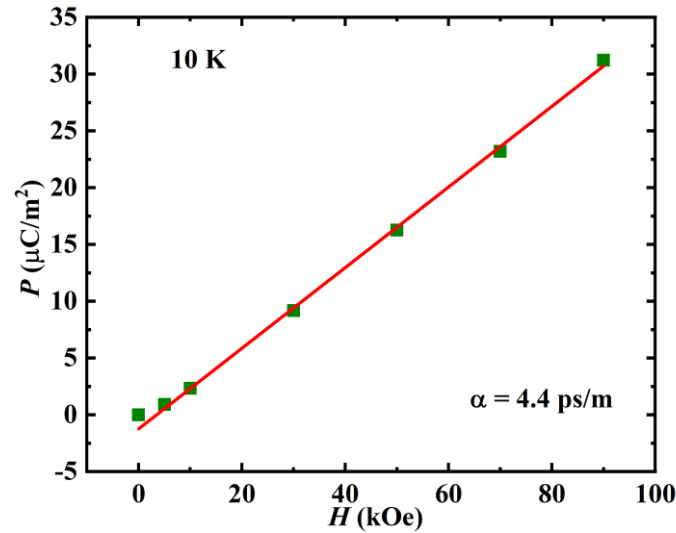


Figure 3.9 Polarization as a function of magnetic field measured at 10 K and the red line is linear fit.

3.3.4.2 Ferroelectric switching and DC bias measurements

To confirm the magnetoelectric effect further, we have carried out the switching of polarization and dc bias measurements [13]. As shown in Figure 3.10(a), the sign of the pyrocurrent and polarization switches simultaneously with the direction of poling electric field. Moreover, we observed a strong dc bias signal with positive polarization and negative depolarization peaks under applied magnetic field at the copper ordering temperature, as shown in Figure 3.10(b). The absence of dc bias signal around 15 K reveals the broad pyrocurrent is due to leakage contribution. Overall, these observations confirm that this transition is associated with magnetoelectric effect. To explain the microscopic mechanism responsible for ferroelectricity, we need to know the magnetic structure of this compound.

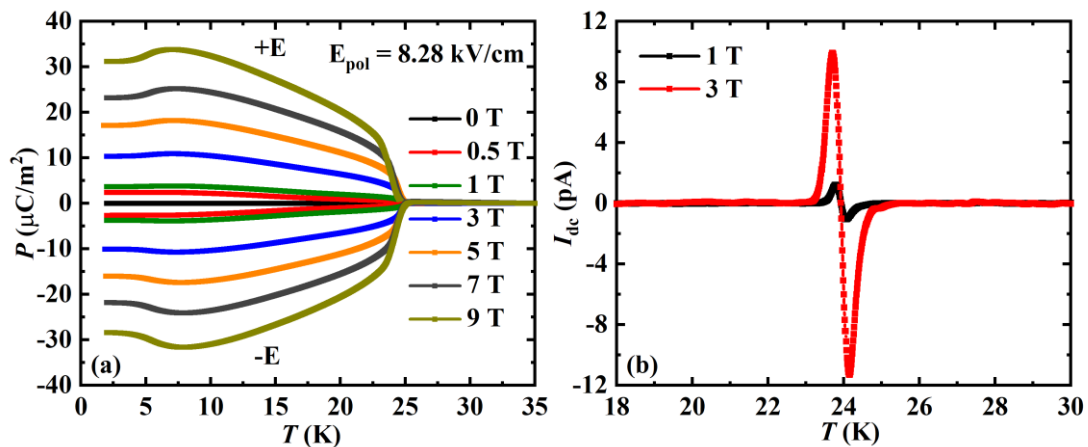


Figure 3.10 (a & b) Electric field switching of electric polarization and dc bias signal recorded at different magnetic fields under poling electric field $E = 8.28$ kV/cm, respectively.

3.3.5 Neutron diffraction and symmetry approach

As samarium is a strong absorbent of neutrons with neutron absorption cross-section $5922 \times 10^{-24} \text{ cm}^2$ (NIST), it is difficult to perform a reliable neutron diffraction measurement. Hence, we have used ^{154}Sm isotope with neutron absorption cross-section $8.4 \times 10^{-24} \text{ cm}^2$ (NIST) and prepared the sample for neutron diffraction measurements. We performed the experiments on GEM, ISIS at temperatures 2 and 40 K. Unfortunately, these data are exactly same, with a glimpse of intensity increase of some of the nuclear peaks indicating the possible \mathbf{k} -vector $(0, 0, 0)$. This can be due to the low moment of Cu^{2+} -ions ($\sim 1 \mu_B$) and poor resolution of GEM diffractometer. However, extracting the magnetic information from this data is difficult. Also, one must perform neutron diffraction on this sample to analyse the magnetic structure using high resolution diffractometer like WISH, ISIS.

In the absence of knowledge about magnetic structure, here we present the possible reasons for the linear magnetoelectric effect by using symmetry analysis along with theoretical calculations. The analysis of literature data on $R_2\text{BaCuO}_5$ shows that these compounds experience one or two magnetic phase transitions at low temperatures (below ~ 25 K) depending on the nature of rare earth and the strength of the interaction between the rare-earth and Cu-sublattices [3,4]. Neutron diffraction data reveal that various magnetic ordering wave vectors are found in the green phases, including, e.g., $\mathbf{k} = (0, \frac{1}{2}, 0)$ in $R = \text{Dy, Ho, Er}$, $\mathbf{k} = (0, \frac{1}{2}, \frac{1}{2})$ in $R = \text{Yb, Y}$, and $\mathbf{k} = (0, 0, \frac{1}{2})$ in $R = \text{Gd}$ [14–16]. Furthermore, incommensurate magnetic structure is found in $\text{Gd}_2\text{BaCuO}_5$, [16] whereas a $\vec{k} = 0$ magnetic structure is found in the ground state of $\text{Dy}_2\text{BaCuO}_5$ [14]. The variety of magnetic ordering wave vectors can be arguably explained by the presence of three different magnetic sublattices and a multitude of exchange constants because simple geometrical calculation reveals that within a distance of, e.g., 5 \AA , there exist up to eleven different exchange paths. Our experimental results unambiguously show that $\text{Sm}_2\text{BaCuO}_5$ is a linear magnetoelectric below T_{N1} , which, together with the temperature dependence of electric polarization around T_{N1} , supports the appearance of magnetic ordering with $\vec{k} = 0$ below T_{N1} because of the following. According to the phenomenological theory of phase transitions, linear magnetoelectric effect induced by a magnetic structure with nonzero wave vector $\vec{k} \neq 0$ would be treated by the terms of the form $\xi_i^n MP$ in the thermodynamic potential, where ξ_i is a (generally multicomponent) order parameter describing the antiferromagnetic structure, M

is magnetization, and P is electric polarization. Due to nonzero wave vector, one has $n > 1$, whereas the product $\xi_i^n M$ should be of even power with respect to magnetic order parameters because of time reversal symmetry. This gives the minimal value $n = 3$. In this case, however, the electric polarization at constant magnetic field will be proportional to $P \sim (T_{N1} - T)^\gamma$ with $\gamma = \frac{n}{2} > 1$ below the magnetic phase transition temperature, which contradicts the experimentally observed value $\gamma \approx 0.5$. Thus, one can conclude that the appearing magnetic structure is described by $\vec{k} = 0$ and induces linear magnetoelectric effect due to interaction of the form ξMP , which results in $P \sim (T_{N1} - T)^\gamma$ with $\gamma \approx 0.5$ below T_{N1} . It has to be noted that under applied magnetic field (i.e., when $M \neq 0$) the phase transition at T_{N1} becomes a proper ferroelectric phase transition, because the order parameters ξ and P have the same symmetry if $M \neq 0$. This explains the magnetic field-induced dielectric anomaly at T_{N1} .

Given the absence of neutron diffraction data on $\text{Sm}_2\text{BaCuO}_5$, one can tentatively assume the same relative spin arrangement as found in the low temperature magnetic structure of $\text{Dy}_2\text{BaCuO}_5$. In the $Pnma$ crystal structure of the green phase, the copper ions as well as both inequivalent rare-earths are located in positions $4c$ with coordinates: 1 $(x, \frac{1}{4}, z)$, 2 $(\frac{1}{2} - x, \frac{3}{4}, \frac{1}{2} + z)$, 3 $(-x, \frac{3}{4}, -z)$, and 4 $(\frac{1}{2} + x, \frac{1}{4}, \frac{1}{2} - z)$. For each magnetic sublattice, one can define the basis vectors $\vec{F} = \vec{S}_1 + \vec{S}_2 + \vec{S}_3 + \vec{S}_4$, $\vec{G} = \vec{S}_1 - \vec{S}_2 + \vec{S}_3 - \vec{S}_4$, $\vec{C} = \vec{S}_1 + \vec{S}_2 - \vec{S}_3 - \vec{S}_4$, and $\vec{A} = \vec{S}_1 - \vec{S}_2 - \vec{S}_3 + \vec{S}_4$, where \vec{S}_i is the spin of atom i . Thus, \vec{F} is a ferromagnetic order parameter, whereas \vec{G} , \vec{C} , and \vec{A} describe antiferromagnetic structures. In $\text{Dy}_2\text{BaCuO}_5$, the low temperature magnetic structure is described by the order parameters C_x and A_z transforming according to irreducible representation Γ^{4-} . It can be found that such relative spin arrangement breaks inversion symmetry because the pairs of atoms 1 and 3, as well as 2 and 4, which are connected by spatial inversion, have oppositely directed magnetic moments. Thus, this magnetic structure allows linear magnetoelectric effect with magnetoelectric interactions of the form,

$$C_x F_x P_z,$$

$$C_x F_z P_x,$$

$$A_z F_x P_z,$$

$$A_z F_z P_x.$$

In our measurements of electric polarization, we employed parallel $H \parallel E$ geometry; however, similar results were obtained for $H \perp E$ due to the ceramic nature of the samples. It has to be noted that the same relative spin arrangement as in the low temperature phase of $\text{Dy}_2\text{BaCuO}_5$ is found in $\text{Yb}_2\text{BaCoO}_5$ below $T_N \approx 9.4$ K, which means that $\text{Yb}_2\text{BaCoO}_5$ should also experience linear magnetoelectric effect below this temperature [17]. Neutron diffraction experiments or single crystal magnetoelectric measurements in different geometries are required to confirm the suggested magnetic structure of $\text{Sm}_2\text{BaCuO}_5$. Alternative magnetic structures allowing linear magnetoelectric effect include those, which are described by inversion-odd irreducible representations in the Brillouin zone center, i.e., $\Gamma^{1-}(A_x C_z)$, $\Gamma^{2-}(A_y)$, and $\Gamma^{3-}(C_y)$, however the symmetry analysis above will remain qualitatively the same.

As noted above, according to our experimental results, $\text{Sm}_2\text{BaCuO}_5$ exhibits a considerable magnetoelectric effect. From our point of view, the high value of magnetoelectric coefficient can be related to the presence of rare-earth ions, which introduce strong spin-lattice coupling due to high spin-orbit interaction. From the analysis of literature, one can conclude that rare-earth-containing magnetoelectrics generally show high magnetically induced electric polarization [18]. Furthermore, the green phase compounds often develop strongly non-collinear magnetic ordering with magnetic moments lying predominantly in the \mathbf{ac} -plane [14]. In fact, both the Cu^{2+} and Sm^{3+} ions are located at positions with σ_y symmetry (mirror plane perpendicular to the \mathbf{b} -axis), which implies for all magnetic ions the existence of local electric dipole moments lying in the \mathbf{ac} -plane. Thus, the single-ion contribution to the magnetoelectric effect is allowed by symmetry and can be large for the rare-earth ions, as is the case in rare-earth manganites $R\text{MnO}_3$ [5]. The strong influence of rare-earth ions on magnetic field-induced electric polarization is further confirmed by strong dielectric anomaly at Sm^{3+} ordering temperature T_{N2} even in zero magnetic field.

Contrary to our results of linear magnetoelectric effect in $\text{Sm}_2\text{BaCuO}_5$ at low temperature, the recent report on $R_2\text{BaCuO}_5$ ($R = \text{Er}, \text{Dy}, \text{and Sm}$) claims that all the three compounds undergo ferroelectric transitions at high temperatures, ~ 235 , ~ 232 , and ~ 184 K, respectively, which have been attributed to structural transition from non-polar ($Pnma$) to polar ($Pna2_1$) space group as inferred from synchrotron powder diffraction [19]. However, earlier neutron diffraction studies on $R_2\text{BaCuO}_5$ family of compounds strongly suggest that the structure remains non-polar ($Pnma$) down to the lowest temperature measured [14–16].

Further, the authors have attributed the symmetric and broad pyrocurrent peaks at high temperature to ferroelectricity. In the case of $\text{Sm}_2\text{BaCuO}_5$, we observe two peak-like features in the pyrocurrent data at a lower temperature, which shifts to high temperature with different warming rates, indicating the extrinsic origin of this peak as shown in Figure 3.11(a). Furthermore, the extrinsic origin of polarization is confirmed by the dc bias measurement in which the pyrocurrent increases continuously as shown in Figure 3.11(b), indicating the absence of ferroelectric behavior.

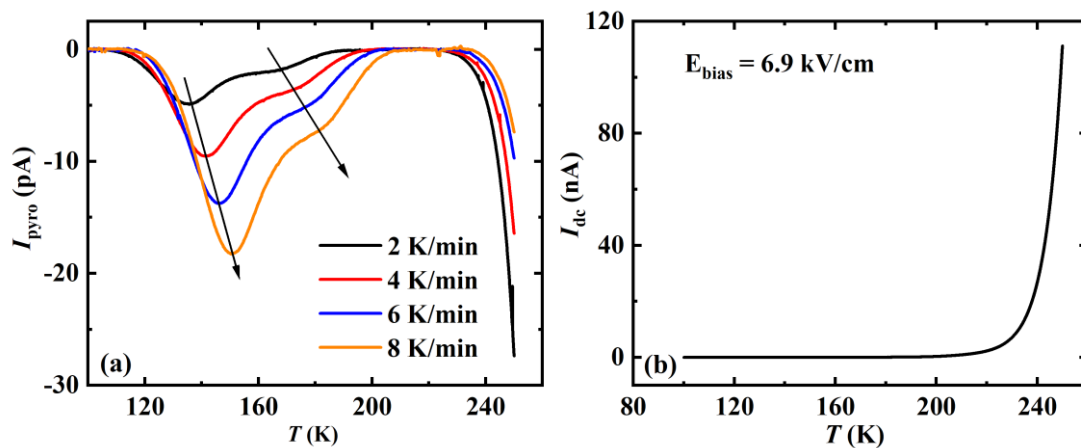


Figure 3.11 (a) Temperature-dependent pyrocurrent recorded with different warming rates after poling the sample under electric field of 6.9 kV/cm. (b) Monotonous increasing behavior of DC bias current.

3.4 Conclusion

We systematically investigated the linear magnetoelectric effect in the well-known green phase $\text{Sm}_2\text{BaCuO}_5$ by using magnetic, specific heat, dielectric, and pyrocurrent measurements. This compound exhibits antiferromagnetic ordering at 23 K where we observed the appearance of electric polarization under applied magnetic field. $\text{Sm}_2\text{BaCuO}_5$ shows a considerable linear magnetoelectric effect with strong coupling coefficient. Further single crystal studies are required to better understand the observed magnetoelectric effect.

References

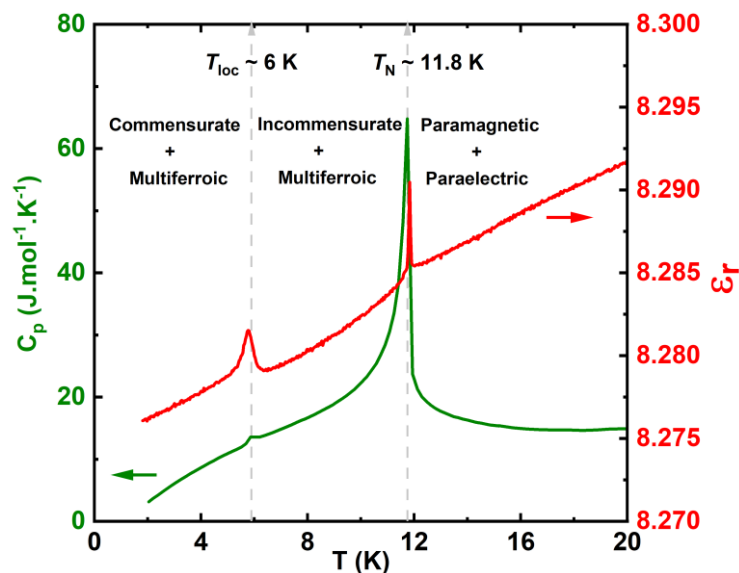
- [1] C. Michel and B. Raveau, *J. Solid State Chem.* **43**, 73 (1982).
- [2] A. Salinas-Sanchez, J. L. Garcia-Muñoz, J. Rodriguez-Carvajal, R. Saez-Puche, and J. L. Martinez, *J. Solid State Chem.* **100**, 201 (1992).
- [3] R. Z. Levitin, B. V. Mill, V. V. Moshchalkov, N. A. Samarin, V. V. Snegirev, and J. Zoubkova, *J. Magn. Magn. Mater.* **90**, 536 (1990).
- [4] V. V. Moshchalkov, N. A. Samarin, I. O. Grishchenko, B. V. Mill, and Z. J., *Solid State Commun.* **78**, 879 (1991).
- [5] V. P. Sakhnenko and N. V Ter-Oganessian, *J. Phys. Condens. Matter* **24**, 266002 (2012).
- [6] J. Rodriguez-Carvajal, in *Satell. Meet. Powder Diffr. XV Congr. IUCr* (Toulouse, France:[sn], 1990).
- [7] L. Baum, Thesis, Facultad de Ciencias Exactas (2003), <http://sedici.unlp.edu.ar/handle/10915/2114>.
- [8] Y. Fang, Y. Q. Song, W. P. Zhou, R. Zhao, R. J. Tang, H. Yang, L. Y. Lv, S. G. Yang, D. H. Wang, and Y. W. Du, *Sci. Rep.* **4**, 3860 (2014).
- [9] J. Hwang, E. S. Choi, H. D. Zhou, J. Lu, and P. Schlottmann, *Phys. Rev. B* **85**, 024415 (2012).
- [10] N. Mufti, G. R. Blake, M. Mostovoy, S. Riyadi, A. A. Nugroho, and T. T. M. Palstra, *Phys. Rev. B - Condens. Mater. Phys.* **83**, 104416 (2011).
- [11] R. Saha, S. Ghara, E. Suard, D. H. Jang, K. H. Kim, N. V Ter-Oganessian, and A. Sundaresan, *Phys. Rev. B* **94**, 014428 (2016).
- [12] J. P. Rivera, *Eur. Phys. J. B* **71**, 299 (2009).
- [13] C. De, S. Ghara, and A. Sundaresan, *Solid State Commun.* **205**, 61 (2015).
- [14] I. V. Golosovsky, V. P. Plakhtii, V. P. Kharchenkov, J. Zoubkova, B. V Mill, M. Bonnet, and E. Roudeau, *Fiz. Tve. Tela.* **34**, 1483 (1992).
- [15] I. V Golosovsky, P. Böni, and P. Fischer, *Solid State Commun.* **87**, 1035 (1993).
- [16] A. K. Ovsyanikov, I. V Golosovsky, I. A. Zobkalo, and I. Mirebeau, *J. Magn. Magn. Mater.* **353**, 71 (2014).
- [17] J. Hernández-Velasco, R. Sáez-Puche, and J. Rodríguez-Carvajal, *J. Alloys Compd.* **275**, 651 (1998).
- [18] T. Kimura, G. Lawes, T. Goto, Y. Tokura, and A. P. Ramirez, *Phys. Rev. B* **71**, 224425 (2005).
- [19] A. Indra, S. Mukherjee, S. Majumdar, O. Gutowski, M. v. Zimmermann, and S. Giri, *Phys. Rev. B* **100**, 014413 (2019).

Chapter 4

Elliptical cycloidal phase and spin-driven multiferroicity in $\text{Gd}_2\text{BaCuO}_5$ *

Summary

We have shown the ferroelectricity induced by polar incommensurate and commensurate spin orders in the well-known green phase compound $\text{Gd}_2\text{BaCuO}_5$, which crystallizes in a centrosymmetric orthorhombic structure ($Pnma$). This compound undergoes a long-range antiferromagnetic ordering at $T_N = 11.8$ K, where both Gd^{3+} and Cu^{2+} spins order in an elliptical cycloidal configuration with magnetic super space group $P2_1ma1'(0,0,g)0s0s$ associated to incommensurate modulation vector $(0, 0, g)$, which is accompanied by the emergence of ferroelectric polarization. With decreasing temperature, it undergoes a lock-in transition at $T_{\text{loc}} \sim 6$ K, below which the magnetic structure becomes commensurate with $\mathbf{k}_c = (0, 0, \frac{1}{2})$ and strongly noncollinear, which causes an additional contribution to the electric polarization resulting from the polar magnetic space group ($P_{\text{a}}ca2_1$). Based on the symmetry analysis of magnetoelectric interactions, we suggest that the ferroelectricity in both commensurate and incommensurate phases is driven by a complex interplay of two spins and single-spin contributions from magnetic ions located in noncentrosymmetric environments.



*This work is appeared in Phys. Rev. Research, 2, 023271 (2020), © 2020 by the American Physical Society.

4.1 Introduction

Spin-induced multiferroics, in which specific magnetic orders break inversion symmetry and thus induce electric polarization, attracted much attention because of strong coupling between electric and magnetic orders as discussed in Chapter 1. For example, the well-known rare-earth manganites $RMnO_3$, RMn_2O_5 , Ca_3CoMnO_6 , $MnWO_4$, $CoCr_2O_4$, and delafossites, etc. are known to exhibit spin induced multiferroicity [1–3]. While the layered copper oxides were known for the high temperature superconductivity, several complex copper oxides such as $LiCu_2O_2$, $LiCuVO_4$, CuO , Bi_2CuO_4 , $GeCu_2O_4$, and $CuFeO_2$ have been reported to exhibit multiferroic properties [3–5]. In all these materials, the microscopic mechanisms responsible for ferroelectricity are the exchange striction, the spin-current or the inverse Dzyaloshinskii-Moriya interaction, and in some cases p - d hybridization [1,3].

As we know, green phase compounds R_2BaCuO_5 , where $R = Sm$ – Lu and Y , having a centrosymmetric ($Pnma$) crystal structure exhibit a wide range of magnetism and ground state spin structures due to strong $4f$ and $3d$ interactions [6–8]. In these compounds, the magnetic interactions between Cu^{2+} ions occur through $Cu^{2+}-O^{2-}-R^{3+}-O^{2-}-Cu^{2+}$ super exchange path and therefore the magnetic interactions between $Cu^{2+}:3d$ and $R^{3+}:4f$ sublattice moments are important in understanding their magnetic properties. In general, the Cu and R sublattice moments in these compounds undergo long range antiferromagnetic ordering at different temperatures except Gd_2BaCuO_5 where the Cu^{2+} and Gd^{3+} moments order simultaneously around 12 K [8–11]. Previous neutron diffraction study on Gd_2BaCuO_5 reveals that this compound exhibits incommensurate magnetic structure with a modulation vector $\mathbf{k} = (0, 0, g)$ below 12 K and undergoes lock-in transition at 5 K to a commensurate magnetic structure with $\mathbf{k}_c = (0, 0, \frac{1}{2})$ [12]. In previous chapter, it is showed that Sm_2BaCuO_5 exhibits linear magnetoelectric effect at Cu ordering and which is affected by Sm ordering.

In this chapter, we demonstrate the observation of ferroelectricity in both commensurate and incommensurate spin states of the compound Gd_2BaCuO_5 . Reinvestigation of the previous neutron diffraction data [12] reveals that the incommensurate ordering corresponds to elliptical cycloidal structure with the polar magnetic point group $P2_1ma1'(0,0,g)0s0s$, and the low temperature commensurate phase is strongly noncollinear with the polar magnetic space group $Pc2_1ca$ (point group $2mm1'$). We suggest that a complex interplay of two spins and single-spin contributions from ions located in noncentrosymmetric environments are responsible for multiferroicity.

4.2 Experimental section

Polycrystalline sample of $\text{Gd}_2\text{BaCuO}_5$ was prepared by heating the stoichiometric mixture of high purity Gd_2O_3 (preheated), BaCO_3 , and CuO at $950\text{ }^\circ\text{C}$ in the air. Characterization and physical properties of this sample were done similar to that mentioned for $\text{Sm}_2\text{BaCuO}_5$ in Chapter 3. We have used a 0.46 mm thickness hardened pellet of polycrystalline $\text{Gd}_2\text{BaCuO}_5$ sample covered an area of 25 mm^2 with a silver paste to measure the electrical properties. Low temperature neutron diffraction data collected at the G61 diffractometer ($\lambda = 4.76\text{ \AA}$) in the Laboratory Léon Brillouin (Saclay) were used to analyse the magnetic structure [12].

4.3 Results and discussion

4.3.1 Crystal structure

Figure 4.1 shows the Rietveld refined X-ray diffraction data collected at room temperature and complete structural parameters are provided in Table 4.1. The refinement confirmed that this compound crystallizes in a centrosymmetric orthorhombic structure with space group $Pnma$, isostructural to $\text{Sm}_2\text{BaCuO}_5$. Figure 4.2(a) depicts the crystal structure of $\text{Gd}_2\text{BaCuO}_5$ viewed along the \mathbf{b} -axis. As can be seen from the figure, the Cu square pyramids are isolated, and the possible interaction path is $\text{Cu}^{2+}-\text{O}^{2-}-\text{Gd}^{3+}-\text{O}^{2-}-\text{Cu}^{2+}$. In this structure, the oxygen coordination polyhedrons of two Gd^{3+} sites differ slightly but the local environments differ significantly. The Gd2 ion is bonded to six nearby copper ions through oxygens, five of the six Gd2-O-Cu bond angles being close to 180° , whereas Gd1 is bonded to only three copper ions at bond angles close to 90° .

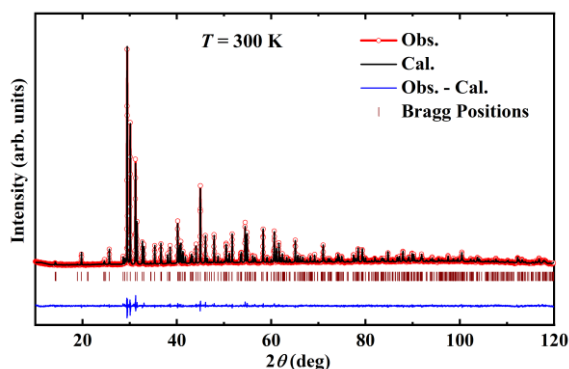


Figure 4.1 Rietveld refinement fit to room temperature powder X-ray diffraction data of $\text{Gd}_2\text{BaCuO}_5$

Table 4.1 Structural parameters of $\text{Gd}_2\text{BaCuO}_5$ obtained from Rietveld refinement. Space group: $Pnma$; $a = 12.3239$ (1) Å, $b = 5.7252$ (2) Å, $c = 7.2261$ (3) Å, $V = 509.858$ (4) Å³; $\chi^2 = 2.07$; Bragg R -factor = 6.86 (%), R_f -factor = 7.72 (%).

Atom	Wyckoff position	x	y	z	B_{iso} (Å ²)	Occ.
Gd1	4c	0.2886 (2)	0.250	0.1156 (3)	0.27 (6)	0.50
Gd2	4c	0.0738 (2)	0.250	0.3954 (3)	0.41 (6)	0.50
Ba	4c	0.9056 (2)	0.250	0.9313 (3)	0.64 (6)	0.50
Cu	4c	0.6592 (4)	0.250	0.7129 (7)	0.43 (1)	0.50
O	8d	0.4325 (15)	-0.012 (2)	0.1705 (16)	1.000	1.00
O	8d	0.2251 (12)	0.505 (3)	0.345 (2)	1.000	1.00
O	4c	0.094 (2)	0.250	0.069 (2)	1.000	0.50

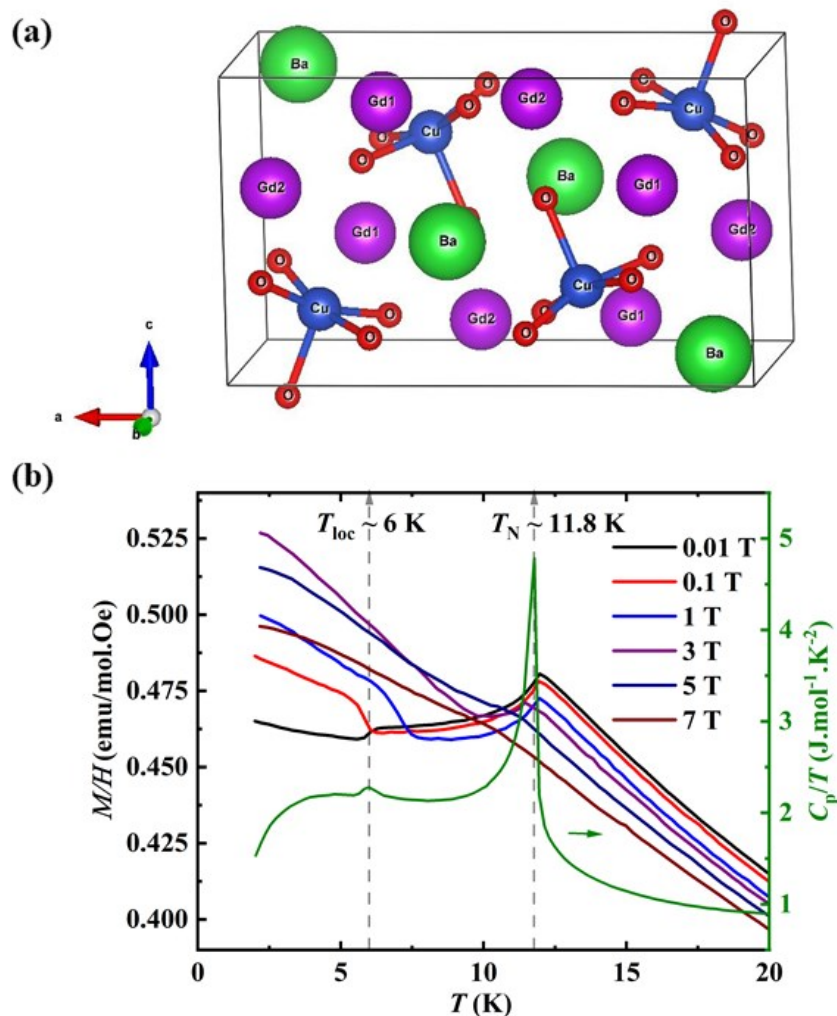


Figure 4.2 (a) Schematic of the crystal structure of $\text{Gd}_2\text{BaCuO}_5$ viewed along the b -axis. (b) Left. Temperature-dependent dc magnetization measured under various magnetic fields in field cooled sequence. Right. Specific heat data measured under zero magnetic field.

4.3.2 DC magnetization and heat capacity

Temperature dependence of magnetization of $\text{Gd}_2\text{BaCuO}_5$ measured under various magnetic fields is shown in Figure 4.2(b). The peak of magnetization at 11.8 K at magnetic field of 0.01 T confirms the long-range antiferromagnetic ordering of Cu^{2+} and Gd^{3+} moments, which is suppressed under applied magnetic fields indicating a possible change in the magnetic structure. Upon further cooling, we observe a small anomaly at $T_{\text{loc}} \sim 6$ K which is consistent with the lock-in transition [12]. This anomaly shifts to high temperatures with applied magnetic fields. As revealed by the neutron diffraction study, the Gd^{3+} spins are ordered at the Cu ordering temperature due to strong $4f-3d$ coupling. Magnetic structure locks to commensurate wave vector when the anisotropic energy terms become significant and external magnetic field adds to this anisotropy which increases the T_{loc} . The long-range order is further confirmed by λ -transition at 11.8 K in heat capacity, as seen in Figure 4.2(b), where a small anomaly at 6 K indicates the lock-in transition. The Curie-Weiss fit and field-dependent magnetization are presented in Figure 4.3. The effective magnetic moment obtained from the fit is $\mu_{\text{eff}} = 11.56 \mu_{\text{B}}/\text{f.u.}$, which is close to the theoretical value of $11.36 \mu_{\text{B}}/\text{f.u.}$. The negative value of the Curie-Weiss constant ($\theta_{\text{CW}} = -4$ K) indicating that dominant interaction is antiferromagnetic. The behavior of $M(H)$ data is consistent with the antiferromagnetic ordering.

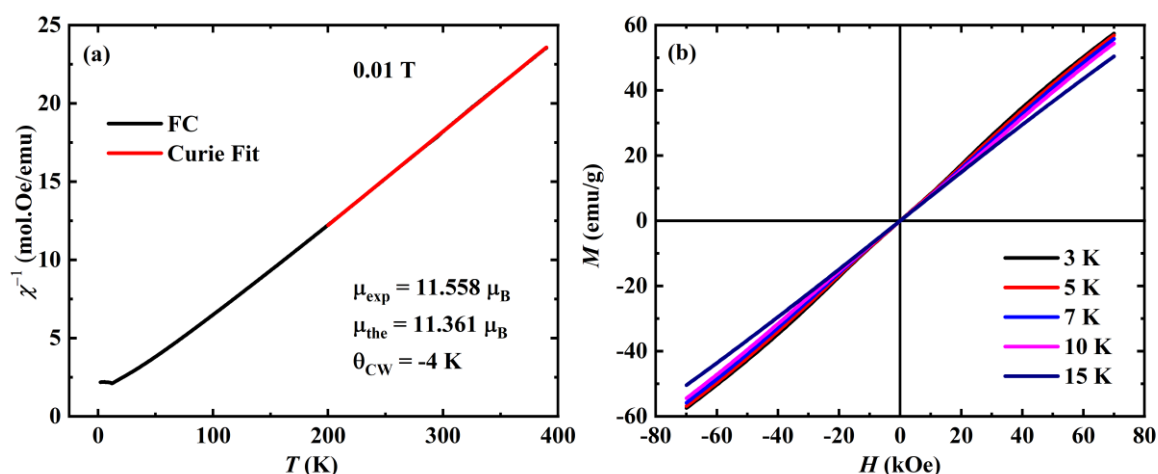


Figure 4.3 (a) Linear fit to inverse molar susceptibility of $\text{Gd}_2\text{BaCuO}_5$. (b) M vs H curves were measured at different temperatures.

4.3.3 Dielectric and pyrocurrent measurements

We observe dielectric anomalies at both the T_N and T_{loc} temperatures under zero magnetic field as shown in Figure 4.4(a). The low temperature anomaly at T_{loc} is suppressed gradually with applied magnetic field and disappears above 0.7 T. On the other hand, the high temperature anomaly shows a small shift to low temperature and becomes broad. To explore whether the dielectric peaks are associated with ferroelectricity, we have recorded temperature dependent pyroelectric current under different magnetic fields which are shown in Figure 4.4(b). Prior to the measurement, we have poled the sample where a magnetic field was applied parallel to the poling electric field. A clear asymmetric peak is seen at the $T_N = 11.8$ K under zero magnetic field, indicating the emergence of spontaneous electric polarization. At T_{loc} , another pyrocurrent peak appears in the same direction, indicating the appearance of a new ferroelectric state below T_{loc} with an additional polarization. The corresponding polarization is shown in Figure 4.4(c), where the appearance of spontaneous polarization at the onset of magnetic ordering and the enhanced polarization at T_{loc} demonstrate the type-II multiferroic nature of Gd_2BaCuO_5 . The value of polarization is $5.5 \mu C/m^2$ at 2 K under zero magnetic field. This value is comparable to that observed in spin-induced multiferroics. We did not observe any significant change when the magnetic field was applied perpendicular to the poling electric field. Interestingly, under applied magnetic fields, the pyrocurrent peaks at T_{loc} are opposite to that at T_N . This is reflected as a dip in polarization and shifts towards T_N consistent with the magnetization behavior [Figure 4.4(b)]. We performed switching and dc-bias current measurements to verify the switchable nature of electric polarization and confirm the intrinsic nature of ferroelectricity. It can be seen from Figure 4.4(d) that the polarization is switched by changing the direction of poling electric field which is the intrinsic behavior of ferroelectric material. From Figure 4.5(b), the dc bias signals further confirm that both the magnetic transitions are associated with ferroelectricity. Hence, our experimental results demonstrate the spin-induced multiferroicity in Gd_2BaCuO_5 . It is worth pointing out that the isostructural compound Sm_2BaCuO_5 exhibits polarization only under magnetic field, as shown in Chapter 3, typical of linear magnetoelectric effect [13]. In addition, a notable magnetodielectric effect is observed below magnetic ordering temperature with the value of ~ 0.05 % on an average as can be seen from Figure 4.5(a). The isothermal dielectric constant curve at 11 K shows anomalous behavior around 4 T indicating the change in magnetic structure under magnetic field.

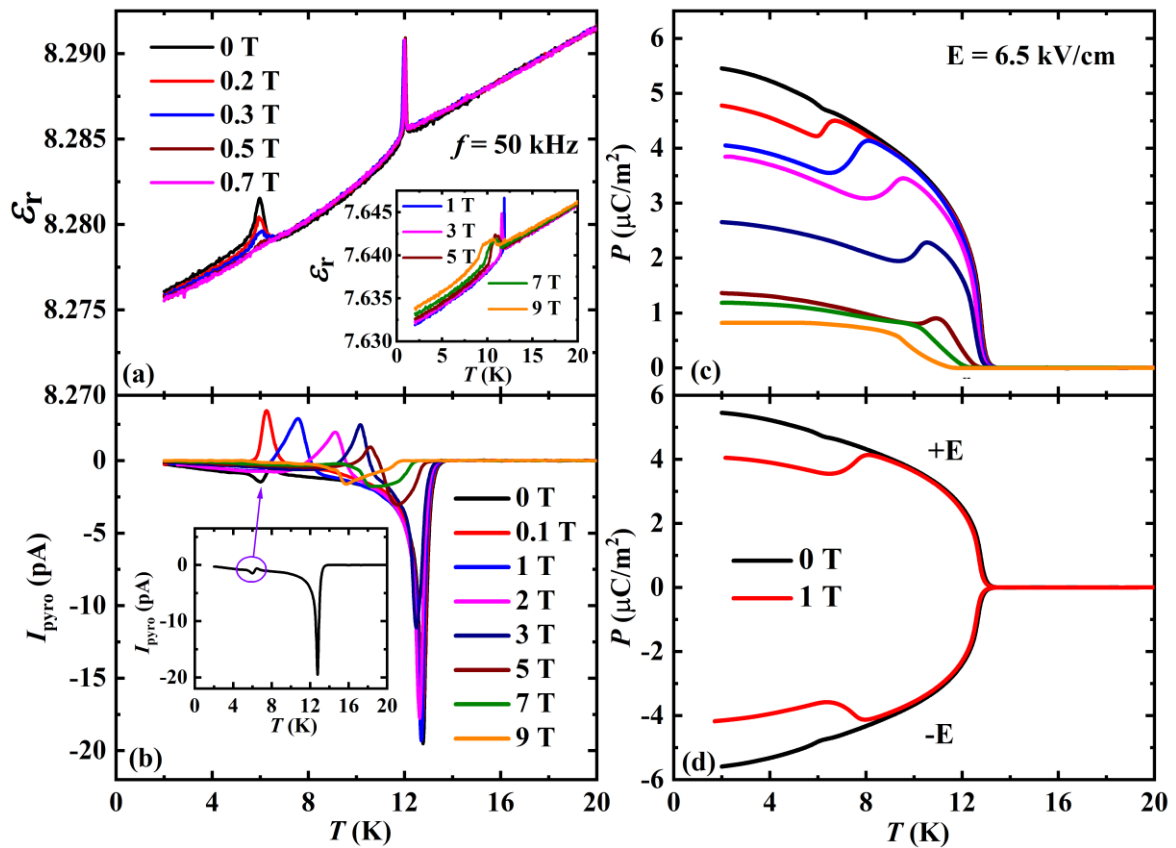


Figure 4.4 (a) Dielectric constant (ϵ_r) as a function of temperature measured under various magnetic fields at the frequency $f = 50$ kHz. (b) Pyrocurrent as a function of temperature and magnetic field. Inset shows pyrocurrent under zero magnetic field (c) Polarization obtained by integrating the pyrocurrent with respect to time. (d) Polarization is measured with positive and negative poling electric fields.

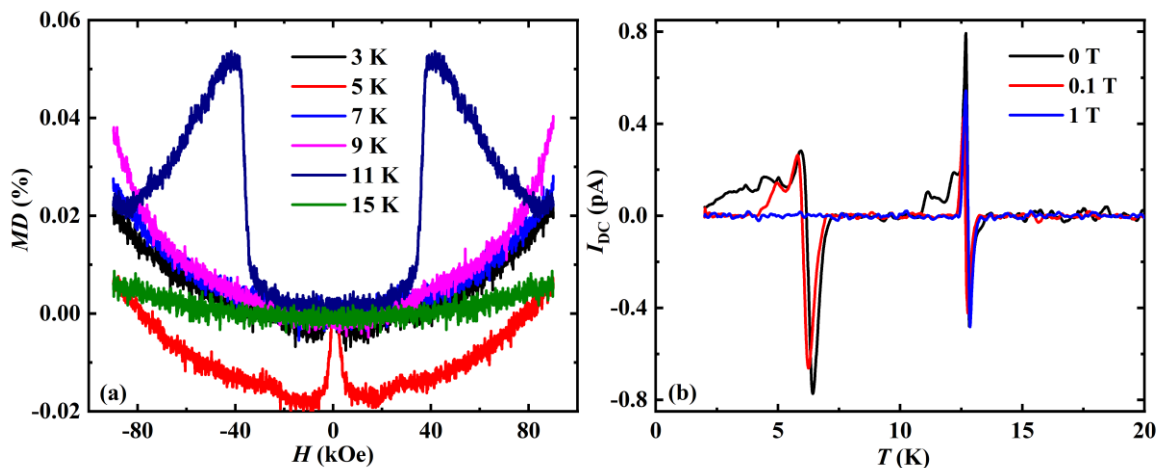


Figure 4.5 (a) Change in dielectric constant measured against magnetic field at different temperatures. (b) DC bias current measured under various magnetic fields.

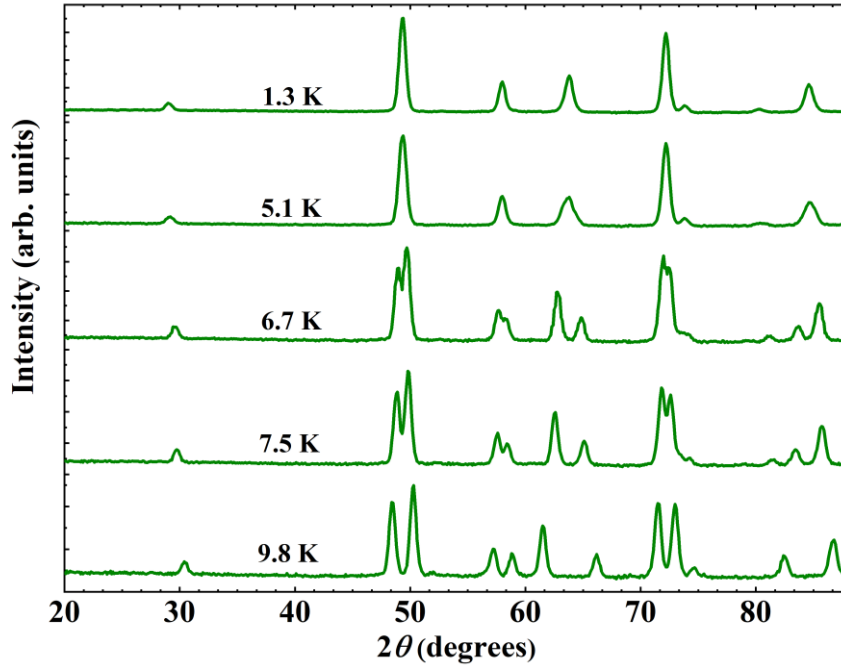


Figure 4.6 Temperature evolution of the magnetic contribution in the neutron diffraction pattern of $\text{Gd}_2\text{BaCuO}_5$ (difference pattern – pattern measured at T -pattern measured at $T = 12.1$ K).

4.3.4 Neutron diffraction study

The observation of multiferroicity in $\text{Gd}_2\text{BaCuO}_5$ is not consistent with the reported ground state magnetic structure with magnetic space group $P5\bar{1}$ which is centrosymmetric and therefore cannot induce ferroelectricity [12]. To unravel the nature of the magnetic ordering, which causes the polarization in $\text{Gd}_2\text{BaCuO}_5$, we have reinvestigated the magnetic structure by analysing low temperature neutron powder diffraction (NPD) data in more detail using the magnetic space group formalism. Figure 4.6 shows magnetic contribution – *i.e.*, the difference pattern of neutron diffraction data recorded at different temperatures below magnetic ordering to the same recorded at 12.1 K in the paramagnetic region. Firstly, we have refined the neutron data at 1.3 K by Rietveld method with the magnetic structural model consistent with the wave vector $\mathbf{k}_c = (0, 0, \frac{1}{2})$ and paramagnetic space group $Pnma1'$. There are six magnetic models corresponding to irreducible representations (*irreps*), namely mZ1 and mZ2, as shown below:

mZ1_P($a, 0$)	11.55	P_a2_1/m	mZ2_P($a, 0$)	14.82	P_c2_1/c
mZ1_P(a, a)	26.72	P_bmc2_1	mZ2_P(a, a)	29.104	$P_a ca2_1$
mZ1_C(a, b)	6.21	$P_a m$	mZ2_C(a, b)	7.28	$P_c c$

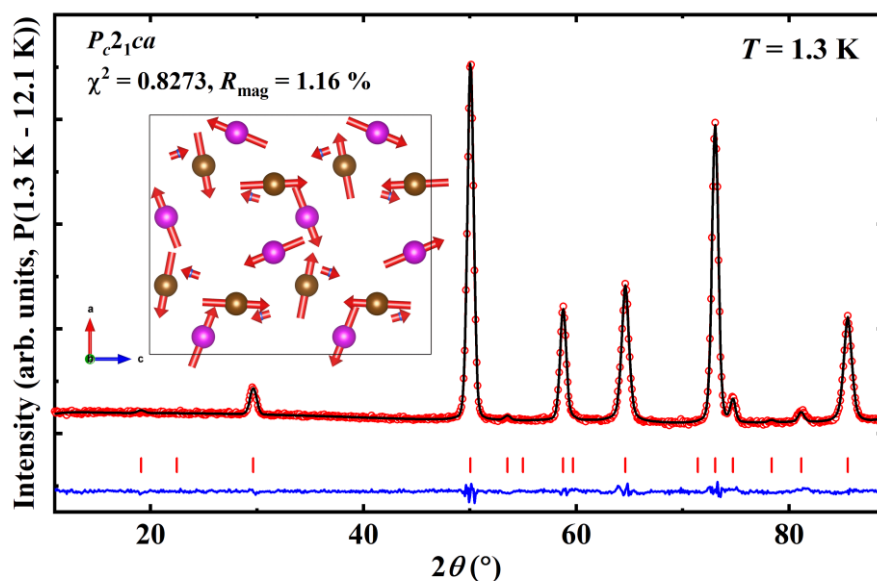


Figure 4.7 Refined neutron diffraction data recorded at 1.3 K. Inset shows the noncollinear commensurate magnetic structure of $\text{Gd}_2\text{BaCuO}_5$ at 1.3 K in the magnetic unit cell viewed along the **b**-axis. (Gd1 – Purple, Gd2 – Orange, Cu – Blue)

Table 4.2 Relevant parameters by Rietveld refinement for the six magnetic sites in the asymmetric unit of $Pc2_1ca$. The atom positions have been fixed and the value of the moments of atoms originally in Gd1, Gd2, and Cu sites of the paramagnetic structure have been constrained to be the same.

Generators of the magnetic group $Pc2_1ca$:

$$(0, 0, \frac{1}{2})' \quad x, y, z+1/2, -1$$

$$c \quad x, -y+1/2, z+1/2, +1$$

$$a \quad x+1/2, y, -z+3/4, +1$$

Atom	Mom (μB)	Phi ($^\circ$)	Theta ($^\circ$)	M_x (μB)	M_y (μB)	M_z (μB)
Gd1_1	6.874 (82)	0.00	259 (2)	-6.75 (8)	0.00	-1.30 (24)
Gd1_2	6.874 (82)	0.00	-2.9 (7)	-0.34 (8)	0.00	6.87 (8)
Gd2_1	6.611 (93)	0.00	69 (2)	6.17 (6)	0.00	2.37 (22)
Gd2_2	6.611 (93)	0.00	203 (2)	-2.56 (21)	0.00	-6.10 (8)
Cu_1	1.01 (1)	0.00	164 (4)	0.27 (7)	0.00	-0.97 (2)
Cu_2	1.01 (1)	0.00	199 (5)	-0.34 (9)	0.00	-0.95 (4)

Propagation vector: (0, 0, 1/2)

$\chi^2 = 0.8273$ and Magnetic R -factor = 1.14 %

From the refinement, the correct solution found to be $P_a c a 2_1$ which belongs to the irrep $mZ2$ as shown in Figure 4.7. The structural parameters obtained from the refinement are given in Table 4.2. The low temperature magnetic structure obtained from the refinement is commensurate and strongly noncollinear as illustrated in the inset of Figure 4.7. The obtained orthorhombic magnetic structure associated with cell doubling along **c**-axis can be described by magnetic space group $Pc2_1ca$ [Belov-Neronova-Smirnova (BNS) setting related to the

parent $Pnma1'$ and conserving the same origin $\mathbf{a}, \mathbf{b}, 2\mathbf{c}; 0, 0, 0$. The transformation to the standard setting P_6ca2_1 is performed by $\mathbf{c}, \mathbf{b}, -\mathbf{a}; 0, 1/4, 1/8$. The refined magnetic moment is $6.73(3) \mu_B/\text{Gd}^{3+}$ and $1.02(2) \mu_B/\text{Cu}^{2+}$ which are comparable to the theoretical values of $7.0 \mu_B/\text{Gd}^{3+}$ and $1 \mu_B/\text{Cu}^{2+}$ for fully localized electronic states, respectively. It is important to note that the new magnetic space group P_6ca2_1 is polar and thus breaks the inversion symmetry of the parent group $Pnma1'$ and induces electric polarization of the form $\mathbf{P}_m = (p_x, 0, 0)$ in the parent setting.

On the other hand, for $T_{\text{loc}} \leq T \leq T_N$, the magnetic structure is incommensurate with propagation vector $(0, 0, g)$, with g evolving with decreasing temperature and locking to $g = 1/2$ at 6 K. The symmetry analysis performed with BASIREPS for $Pnma$ and with the incommensurate wave vector, using the extended little group, provides four two-dimensional irreducible representations (*irreps*). The main characteristic of all the basis vectors for position $4c$ is that the corresponding magnetic moments are either along the \mathbf{b} -axis or perpendicular to it.

Single irreducible representations

We have used ISODISTORT for determining the possible magnetic modes and the corresponding magnetic super space groups of the incommensurate magnetic structure. The \mathbf{k} -vector corresponds to the point LD in the Brillouin zone, and four magnetic *irreps* are labeled as $mLD1$, $mLD2$, $mLD3$, and $mLD4$. The symmetry modes and the corresponding super space groups for each direction of the order parameters in the representation space give rise (using the notation of ISODISTORT) to the following table:

Irrep Label	Magnetic super space group Label	Magnetic super space group (MSSG)	Basis and Origin	Third component of k-vector
$mLD1_P(a, 0)$	62.1.9.1.m442.2	$Pnma1'(0,0,g)000s$	$\mathbf{a}_1, \mathbf{a}_2, \mathbf{a}_3, \mathbf{a}_4; 0, 0, 0, 0$	g
$mLD2_P(a, 0)$	62.1.9.2.m442.2	$Pnma1'(0,0,g)0s0s$	$\mathbf{a}_1, \mathbf{a}_2, \mathbf{a}_3 + \mathbf{a}_4, \mathbf{a}_4; 0, 0, 0, 1/4$	$-1+g$
$mLD3_P(a, 0)$	62.1.9.2.m442.2	$Pnma1'(0,0,g)0s0s$	$\mathbf{a}_1, \mathbf{a}_2, \mathbf{a}_3, \mathbf{a}_4; 0, 0, 0, 0$	g
$mLD4_P(a, 0)$	62.1.9.1.m442.2	$Pnma1'(0,0,g)000s$	$\mathbf{a}_1, \mathbf{a}_2, \mathbf{a}_3 + \mathbf{a}_4, \mathbf{a}_4; 0, 0, 0, 1/4$	$-1+g$
$mLD1_C(a, b)$	31.1.9.1.m124.2	$Pmn2_11'(0,0,g)000s$	$\mathbf{a}_2, -\mathbf{a}_1, \mathbf{a}_3, \mathbf{a}_4; 1/4, 3/4, 0, 0$	g
$mLD2_C(a, b)$	31.1.9.2.m124.2	$Pmn2_11'(0,0,g)s0ss$	$\mathbf{a}_2, -\mathbf{a}_1, \mathbf{a}_3 + \mathbf{a}_4, \mathbf{a}_4; 1/4, 3/4, 0, 0$	$-1+g$
$mLD3_C(a, b)$	31.1.9.2.m124.2	$Pmn2_11'(0,0,g)s0ss$	$\mathbf{a}_2, -\mathbf{a}_1, \mathbf{a}_3, \mathbf{a}_4; 1/4, 3/4, 0, 0$	g
$mLD4_C(a, b)$	31.1.9.1.m124.2	$Pmn2_11'(0,0,g)000s$	$\mathbf{a}_2, -\mathbf{a}_1, \mathbf{a}_3 + \mathbf{a}_4, \mathbf{a}_4; 1/4, 3/4, 0, 0$	$-1+g$

Notice that there are super space groups with the same symbol and number but the position of the origin or the component of the wave vector are different. ISODISTORT can export a CIF (Crystallographic Information File) file for each possible case and the utility *mCIF_to_PCR*, existing in the *FullProf Suite*, converts those CIF files to PCR template files that can be used, after the appropriate changes adapted to the neutron experiment, for calculating and comparing with the experimental data [14,15]. If we want to conserve the setting directly related to the parent paramagnetic space group, it is possible, within ISODISTORT, to export the CIF file in this setting. The user should select the option “Use alternate (possibly nonstandard) setting”, tick the radio button “Basis vectors of subgroup lattice relative to parent” and fill the matrix with the identity and zeros for the change of origin. This provides the super space symmetry operators having 3x3 submatrices and 3D translations identical to those of the parent crystallographic group. However, the symbols of the super space groups in this setting are not the same as those provided as standard.

Performing this procedure (the setting with respect to the parent is, in this case, always $\mathbf{a}_1, \mathbf{a}_2, \mathbf{a}_3, \mathbf{a}_4; 0, 0, 0, 0$, and the third component of the wave vector is always g), the above table is converted as:

Irrep Label	Magnetic super space group Label	Magnetic super space group (MSSG)	MSSG in standard setting
<i>mLD1_P(a, 0)</i>	62.1.9.1.m442.2	<i>Pnma1'(0,0,g)000s</i>	<i>Pnma1'(0,0,g)000s</i>
<i>mLD2_P(a, 0)</i>	62.1.9.2.m442.2	<i>Pnma1'(0,0,g)0s0s</i>	<i>Pnma1'(0,0,g)ssss</i>
<i>mLD3_P(a, 0)</i>	62.1.9.2.m442.2	<i>Pnma1'(0,0,g)0s0s</i>	<i>Pnma1'(0,0,g)0sss</i>
<i>mLD4_P(a, 0)</i>	62.1.9.1.m442.2	<i>Pnma1'(0,0,g)000s</i>	<i>Pnma1'(0,0,g)s00s</i>
<i>mLD1_C(a, b)</i>	31.1.9.1.m124.2	<i>Pmn2₁1'(0,0,g)000s</i>	<i>Pmn2₁1'(0,0,g)000s</i>
<i>mLD2_C(a, b)</i>	31.1.9.2.m124.2	<i>Pmn2₁1'(0,0,g)s0ss</i>	<i>Pmn2₁1'(0,0,g)ss0s</i>
<i>mLD3_C(a, b)</i>	31.1.9.2.m124.2	<i>Pmn2₁1'(0,0,g)s0ss</i>	<i>Pmn2₁1'(0,0,g)0sss</i>
<i>mLD4_C(a, b)</i>	31.1.9.1.m124.2	<i>Pmn2₁1'(0,0,g)000s</i>	<i>Pmn2₁1'(0,0,g)s0ss</i>

With these changes, we can simplify the comparisons and describe the symmetry constraints in a uniform way. All magnetic atoms are within the mirror plane common to all the groups forming an orbit or four equivalent atoms in the paramagnetic space group *Pnma1'*. In this group, there are 3 Wyckoff sites labeled Gd1, Gd2, and Cu. For each of these sites, four equivalent atoms exist within the unit cell, and this is also the case for the *P(a, 0)*

groups. If the center of symmetry is lost in the magnetic ordering, we have a splitting of the sites, so the number of atoms in the asymmetric unit rises from 3 to 6 which is the case for all the $C(a, b)$ groups. Let us use the following notation for the cosine and sine amplitudes of the magnetic moment modulations: a six-dimensional vector (u, v, w, p, q, r) formed by $\mathbf{M}_{\cos} = (u, v, w)$ and $\mathbf{M}_{\sin} = (p, q, r)$, with components along the 3D crystallographic axes, represents the general unconstrained case for the amplitudes. For $4c$ sites in paramagnetic $Pnma1'$, for $P(a, 0)$ groups, having in common the first part of the symbol $Pnma1'$, we have the following constraints and free parameters:

$mLD1_P(a, 0):$	$Pnma1'(0,0,g)000s$	$(0, v, 0, 0, q, 0)$	3 sites: 6 free parameters
$mLD2_P(a, 0):$	$Pnma1'(0,0,g)ssss$	$(u, 0, w, p, 0, r)$	3 sites: 12 free parameters
$mLD3_P(a, 0):$	$Pnma1'(0,0,g)0sss$	$(u, 0, w, p, 0, r)$	3 sites: 12 free parameters
$mLD4_P(a, 0):$	$Pnma1'(0,0,g)s00s$	$(0, v, 0, 0, q, 0)$	3 sites: 6 free parameters

For split sites in $C(a, b)$ groups having in common the first part of the symbol $Pnm2_11'$, we have the following constraints and free parameters:

$mLD1_C(a, b):$	$Pnm2_11'(0,0,g)000s$	$(0, v, 0, 0, q, 0)$	6 sites: 12 free parameters
$mLD2_C(a, b):$	$Pnm2_11'(0,0,g)ss0s$	$(u, 0, w, p, 0, r)$	6 sites: 24 free parameters
$mLD3_C(a, b):$	$Pnm2_11'(0,0,g)0sss$	$(u, 0, w, p, 0, r)$	6 sites: 24 free parameters
$mLD4_C(a, b):$	$Pnm2_11'(0,0,g)s0ss$	$(0, v, 0, 0, q, 0)$	6 sites: 12 free parameters

We have done systematic tests of all possible single *irrep* solutions using simulated annealing. From these tests, we concentrated on the groups coming from the *irreps* $mLD2_P(a, 0): Pnma1'(0,0,g)0s0s$ and $mLD2_C(a, b): Pnm2_11'(0,0,g)0s0s$. We have mainly worked on the data at 9.8 K because that corresponds to the highest departure from the commensurate $g = \frac{1}{2}$ value. The amplitude vectors of the magnetic moments are constrained to be in the **ac**-plane in both cases. A fit to the experimental data can be obtained using the centrosymmetric $Pnma1'(0,0,g)ssss$. However, we know that an electrical polarization is observed below the magnetic ordering temperature, so the noncentrosymmetric group (or a subgroup) should be the correct one. Unfortunately, the quality of the data (relatively small Q-range) we dispose of is not enough to refine the noncentrosymmetric structure with all free parameters by using the Rietveld method. Using least squares, it is impossible to refine all the

modulation amplitudes of the noncentrosymmetric group because we double the number of parameters (from 12 to 24, 23 in this case because an arbitrary phase can be fixed for an atom) and the number of independent magnetic reflections is 24 in the angular range. Using the recently implemented spherical components of the amplitudes and simulated annealing on the full profile within *FullProf*, we were able to refine all the possible noncentrosymmetric magnetic structures. A simulated annealing refinement corresponds to a classical simulated annealing run in which the cost function is the reduced chi-square of the full profile, a higher than usual number of Monte Carlo cycles per temperature is performed (typically 20 times the number of free parameters) and a convergence criterion based on a user-prescribed minimal global average step. The algorithm starts with a random set of parameters within the boundary conditions and finishes when the maximum number of temperatures is reached or when the average global step and chi-square simultaneously, in two consecutive temperatures, vary and amount less than 10^{-4} . The standard deviations of parameters provided in the tables below do not have the same meaning as those of least squares (Rietveld) refinement. They correspond to the average steps of the moves for each parameter during the Monte Carlo cycles in the last simulated annealing temperature.

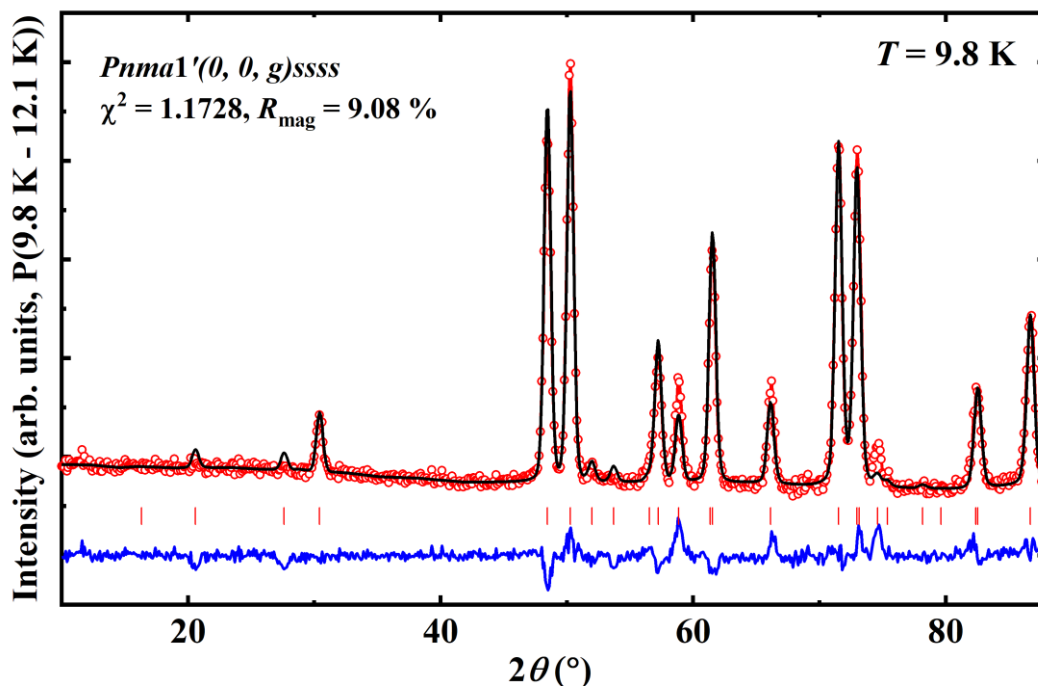


Figure 4.8 Simulated annealing refinement of the difference pattern (9.8 K – 12.1 K) in $Pnma1'(0,0,g)ssss$ at $T = 9.8$ K. The atom positions have been fixed and the modulus of the Gd and Cu modulated moment amplitudes have been constrained to be 8 and 1 μ_B , respectively.

Table 4.3 Relevant parameters obtained from Simulated annealing refinement, shown in Figure 4.8, for the three magnetic atoms in the asymmetric unit of $Pnma1'(0,0,g)ssss$. For each atom, the three components in the first line refer to *cosine* terms and those of the second line to *sine* terms of the modulation amplitudes.

Generators of the magnetic super space group $Pnma1'(0,0,g)ssss$:						
n	$-x_1+1/2, x_2+1/2, x_3+1/2, x_4+1/2, 1$					
m	$x_1, -x_2+1/2, x_3, x_4+1/2, 1$					
a	$x_1+1/2, x_2, -x_3+1/2, -x_4+1/2, 1$					
$1'$	$x_1, x_2, x_3, x_4+1/2, -1$					
Atom	Mom (μ_B)	Phi ($^\circ$)	Theta ($^\circ$)	M_x (μ_B)	M_y (μ_B)	M_z (μ_B)
Gd1	5.23 (12)	0.00	284 (16)	-5.07 (12)	0.00	1.30 (4)
	3.89 (15)	0.00	12.8 (6)	0.86 (3)	0.00	3.79 (16)
Gd2	5.23 (14)	0.00	46 (3)	3.73 (10)	0.00	3.70 (2)
	5.86 (14)	0.00	151 (6)	2.88 (7)	0.00	-5.10 (6)
Cu	0.48 (3)	0.00	258 (18)	-0.47 (3)	0.00	-0.10 (3)
	0.71 (2)	0.00	196 (14)	-0.195 (6)	0.00	-0.68 (17)

Cell Parameters: $a = 12.2266$ (3) Å, $b = 5.6784$ (2) Å, $c = 7.1673$ (2) Å
 Propagation vector: [0, 0, 0.44445 (4)]
 $\chi^2 = 1.1728$ and Magnetic R -factor = 9.0776 %

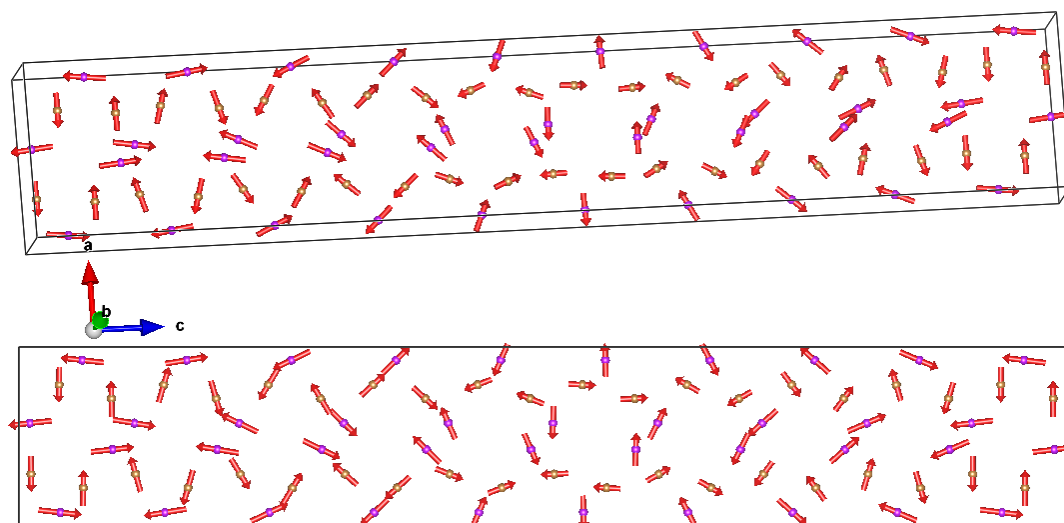


Figure 4.9 Magnetic structure model of Gd_2BaCuO_5 at 9.8 K viewed along the b -axis (Bottom) and a general orientation (Top) described in $Pnma1'(0,0,g)ssss$. The shown box is constituted by $1 \times 1 \times 10$ unit cells of the paramagnetic structure. The non-magnetic atoms as well as the Cu atoms have been removed for the sake of clarity.

The refinement of the magnetic structure using $Pnma1'(0,0,g)ssss$ is shown in Figure 4.8 and the values of the cosine and sine amplitudes for the three magnetic atoms in the asymmetric unit are gathered in Table 4.3. The value of the χ^2 is quite low because the standard deviations of the input data are not available and they are assumed to be the square

root of the intensities, which is clearly an overestimation. In forthcoming refinements, χ^2 is even lower than 1. The corresponding magnetic structure is shown in Figure 4.9. Visualization of the magnetic structures are done with VESTA [16]. As this program is unable to treat incommensurate structures, *FullProf* generates mCIF files in a supercell in which the magnetic moments are treated in *P1*. This helps to visualize the magnetic structures but an interactive option using the program Jmol [17], or its web version MVISUALIZE in the Bilbao Crystallographic Server [18], is better for capturing the features of incommensurate structures.

As an example of refinement using this approach, we have plotted the diffraction pattern corresponding to the first run of the simulated annealing in the noncentrosymmetric $Pnm2_11'(0,0,g)ss0s$ super space group at 9.8 K in Figure 4.10. A summary of the simulated annealing refined parameters related to Figure 4.10 is given in Table 4.4. We have shown the magnetic parameters in spherical coordinates and the corresponding magnetic moment components along each direction. The obtained magnetic structure is depicted in Figure 4.11. Even if the overall fit in both cases looks reasonable, it is important to notice a few regions in the diffraction pattern where a clear disagreement between the observed and calculated patterns for both models is observed. So, none of the maximal isotropy groups derived directly from a single representation adequately fit the experimental data.

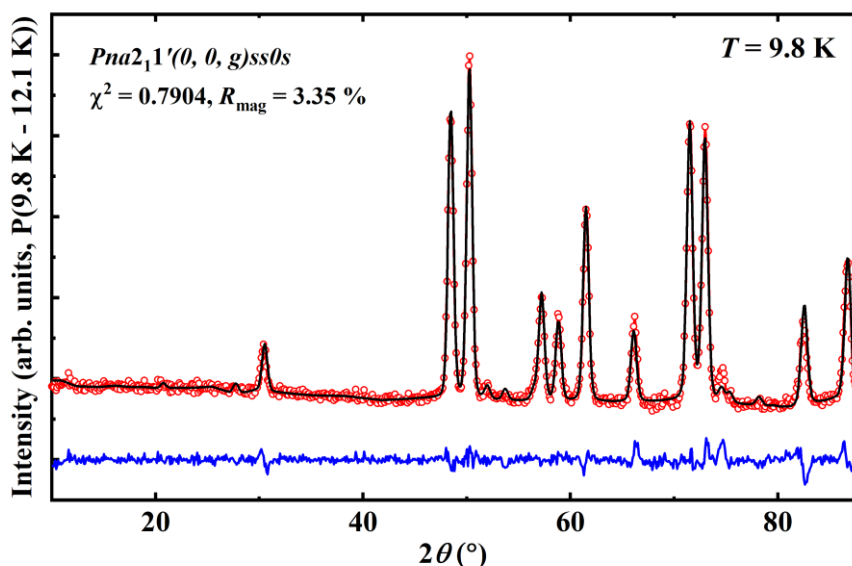


Figure 4.10 Simulated annealing refinement in $Pnm2_11'(0,0,g)ss0s$. The obtained structure has been fixed and pasted in a new PCR file to make a least squares refinement of background and other parameters. The values of χ^2 and R_{mag} are lower than those obtained for the centrosymmetric case. Notice that there are still major differences around $2\theta \approx 54.2^\circ$, and $2\theta \approx 75.1^\circ$.

Table 4.4 Relevant parameters from simulated annealing refinement, shown in Figure 4.10, for the six magnetic atoms in the asymmetric unit of $Pnm2_11'(0,0,g)ss0s$. The atom positions have been fixed and the value of the polar angle (*sine* term) of the atom Gd1_1 in the reference cell has been fixed to zero. For each atom, the three components in the first line refer to *cosine* terms and those of the second line to *sine* terms of the modulation amplitudes.

Generators of the magnetic super space group $Pnm2_11'(0,0,g)ss0s$:

$$n \quad -x_1+1/2, x_2+1/2, x_3+1/2, x_4+1/2, 1$$

$$m \quad x_1, -x_2+1/2, x_3, x_4+1/2, 1$$

$$2_1 \quad -x_1+1/2, -x_2, x_3+1/2, x_4, 1$$

$$1' \quad x_1, x_2, x_3, x_4+1/2, -1$$

Atom	Mom (μ_B)	Phi ($^\circ$)	Theta ($^\circ$)	M_x (μ_B)	M_y (μ_B)	M_z (μ_B)
Gd1_1	7.40 (2)	0.00	315 (19)	-5.26 (15)	0.00	5.20 (17)
	4.00 (15)	0.00	0.00	0.00	0.00	4.00 (15)
Gd1_2	4.57 (13)	0.00	86 (7)	4.56 (13)	0.00	0.320 (13)
	2.53 (9)	0.00	59 (3)	2.17 (8)	0.00	1.30 (9)
Gd2_1	3.81 (14)	0.00	63 (3)	3.38 (12)	0.00	1.76 (14)
	6.90 (16)	0.00	151 (12)	3.29 (10)	0.00	-6.00 (12)
Gd2_2	6.42 (16)	0.00	224 (14)	-4.43 (11)	0.00	-4.70 (12)
	4.80 (11)	0.00	143 (6)	2.86 (7)	0.00	-3.90 (4)
Cu_1	0.71 (2)	0.00	9 (2)	0.111 (4)	0.00	0.70 (4)
	0.98 (3)	0.00	252 (17)	-0.940 (3)	0.00	-0.30 (9)
Cu_2	1.00 (3)	0.00	174 (13)	0.110 (8)	0.00	-1.00 (2)
	1.00 (4)	0.00	188 (11)	-0.134 (7)	0.00	-0.99 (20)

$$\chi^2 = 0.7906 \text{ and Magnetic } R\text{-factor} = 3.35 \%$$

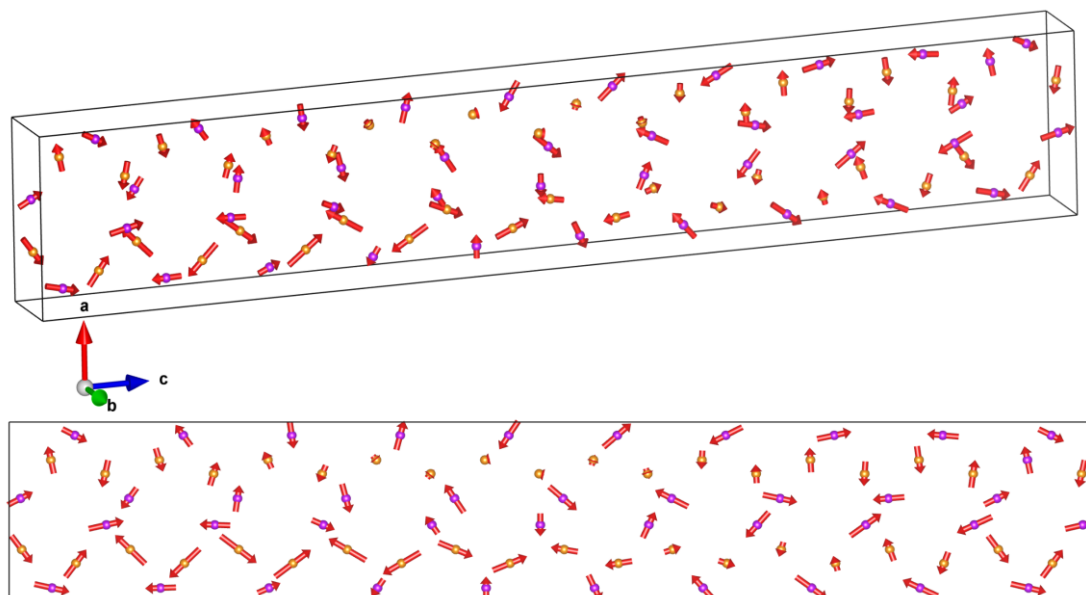


Figure 4.11 Magnetic structure of Gd_2BaCuO_5 at 9.8 K viewed along the **b**-axis (Bottom) and a general orientation (Top) described in $Pnm2_11'(0,0,g)ss0s$. The shown box is constituted by $1 \times 1 \times 10$ unit cells of the paramagnetic structure. The non-magnetic atoms as well as the Cu atoms have been removed for the sake of clarity.

Going down in symmetry, there is only the subgroup $Pm1'(\alpha,0,g)ss$ as the next candidate for a single representation if we want to comply with the fact that the moments mainly lie in the mirror plane. We have also changed the setting of the monoclinic group to have the atom positions within the crystallographic unit cell identical to those of the paramagnetic group $Pnma1'$. The generators of the super space group $Pm1'(\alpha,0,g)ss$ are $(x_1, -x_2+1/2, x_3, x_4+1/2)$ and $(x_1, x_2, x_3, x_4+1/2)'$. The number of independent reflections rises now to 48 but they are strongly overlapped. In this case, the number of free parameters is equal to $12 \times 4 = 48$ (less for fixing the phase, see Appendix). We have explored simulated annealing runs using this low symmetry super space group and successfully refined the powder diffraction pattern using several additional constraints reducing the number of free parameters to 32 instead of 48. An example of the plot corresponding to the simulated annealing refinement in this case is provided in Figure 4.12. However, there is another option by mixing representations that gives a similar fit as that of Figure 4.11 with a lower number of free parameters.

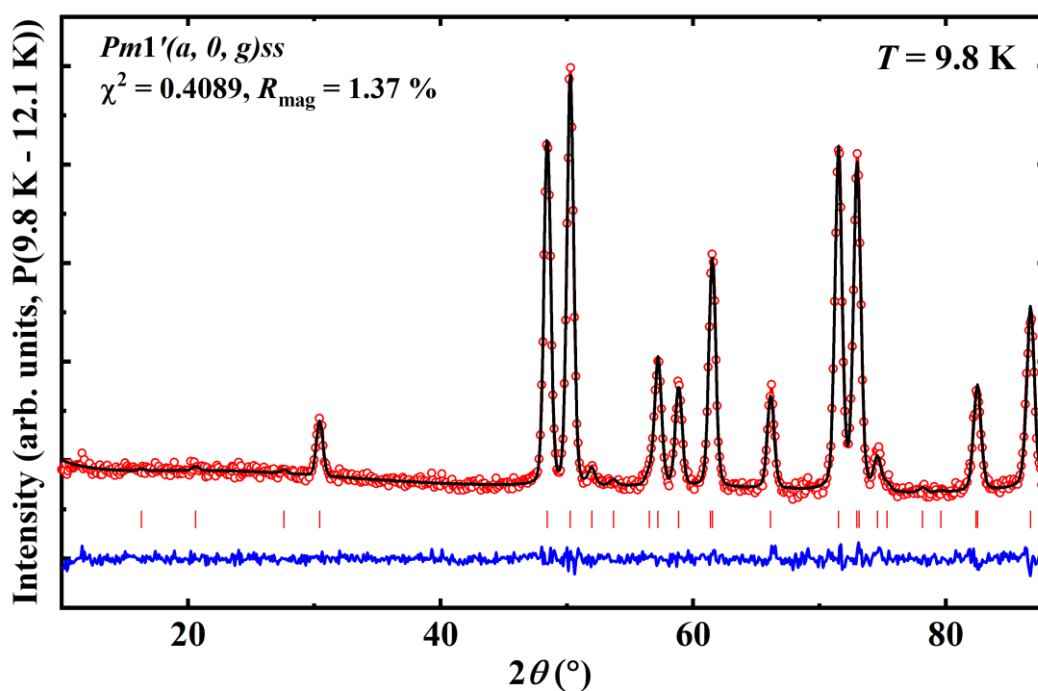


Figure 4.12 Simulated annealing refinement in $Pm1'(\alpha,0,g)ss$. The obtained structure has been fixed and pasted in a new PCR file to refine background and other profile parameters. The values of χ^2 and R_{mag} are lower than those obtained for the previous cases.

Mixing of irreducible representations

Another option that we must explore is the possibility of mixing two *irreps* to verify if we can obtain another super space group of orthorhombic symmetry like in the ground state lock-in case. This can be accomplished using ISODISTORT where one can select mixing of representations by putting two times the same information in the selection of \mathbf{k} -points. Doing that work, we obtain all the possible combinations of $mLD1$, $mLD2$, $mLD3$, and $mLD4$. From the previous work and continuity with the ground state *irrep* $mZ2$ (as mentioned earlier), we can see that the good representations to be combined are $mLD2$ and $mLD3$. The group that was obtained with the representation $mLD2 \oplus mLD3$ in the parent setting giving rise to the best results is $P2_1ma1'(0,0,g)0s0s$ corresponding to the order parameter $PP(a,0|b,0)$ in the notation of ISODISTORT. This group gives a total of 24 degrees of freedom as is the case of the noncentrosymmetric group $Pnm2_11'(0,0,g)ss0s$. An example of simulated annealing refinement using this group is given in Figure 4.13, and the refined parameters are provided in Table 4.5. The scheme of the magnetic structure is illustrated in Figure 4.14. Due to its small value, orientation of the magnetic moments of Cu atoms is weakly reliable. In fact, we can apply extra constraints that do not change the reliability factors.

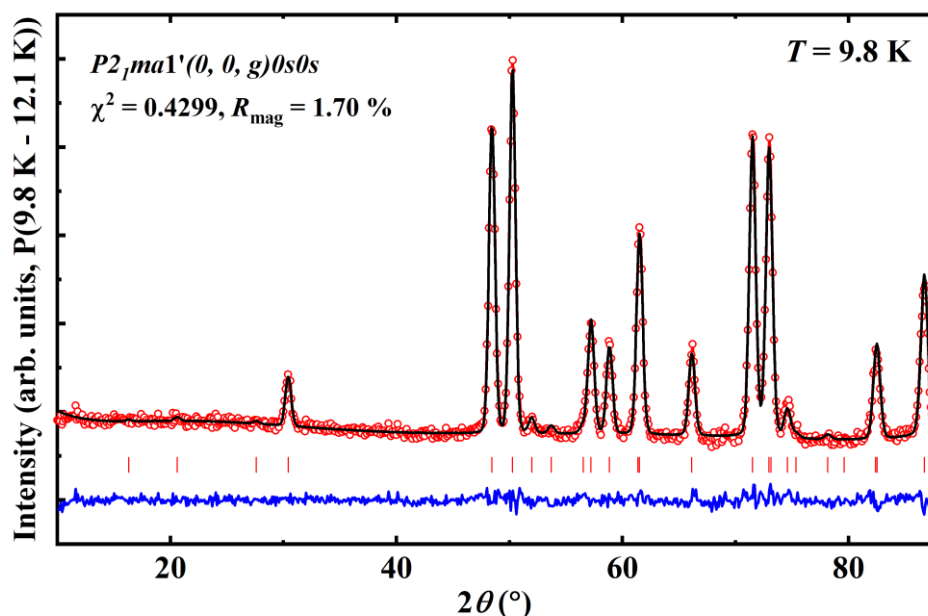


Figure 4.13 Simulated Annealing refinement in $P2_1ma1'(0,0,g)0s0s$. The number of free parameters reduced to 22 instead of 24 for the six sites because amplitudes of Cu atoms were constrained to be same. The obtained structure has been fixed and pasted in a new PCR file to refine background and other profile parameters. The value of χ^2 and R_{mag} are slightly higher than those of $Pm1'(0,0,g)ss$, but very close and with much smaller number of degrees of freedom, so this symmetry seems to be plausible.

Table 4.5 Relevant parameters used in the simulated annealing refinement, shown in Figure 4.13, for the six magnetic atoms in the asymmetric unit of $P2_1ma1'(0,0,g)0s0s$. For each atom, the three components in the first line refer to *cosine* terms and those of the second line to *sine* terms of the modulation amplitudes.

Generators of the magnetic super space group $P2_1ma1'(0,0,g)0s0s$:						
2_1	$x_1+1/2, -x_2+1/2, -x_3+1/2, -x_4, +1$					
m	$x_1, -x_2+1/2, x_3, x_4+1/2, +1$					
a	$x_1+1/2, x_2, -x_3+1/2, -x_4+1/2, +1$					
$1'$	$x_1, x_2, x_3, x_4+1/2, -1$					
Atom	Mom (μ_B)	Phi ($^\circ$)	Theta ($^\circ$)	M_x (μ_B)	M_y (μ_B)	M_z (μ_B)
Gd1_1	5.22 (16)	0.00	325 (19)	-2.99 (9)	0.00	4.28 (13)
	5.45 (13)	0.00	3.90 (4)	0.368 (9)	0.00	5.44 (13)
Gd1_2	6.37 (14)	0.00	63 (5)	5.69 (13)	0.00	2.87 (7)
	1.07 (3)	0.00	100 (7)	1.06 (3)	0.00	-0.178 (5)
Gd2_1	2.72 (9)	0.00	21.9 (14)	1.01 (4)	0.00	2.52 (9)
	7.80 (3)	0.00	164 (13)	2.20 (8)	0.00	-7.50 (3)
Gd2_2	5.35 (15)	0.00	258 (12)	-5.23 (14)	0.00	-1.11 (4)
	2.70 (6)	0.00	55 (2)	2.20 (5)	0.00	1.56 (4)
Cu_1	1.05 (3)	0.00	10.5 (11)	0.191 (6)	0.00	1.03 (3)
	1.05 (3)	0.00	321 (22)	-0.660 (2)	0.00	0.82 (3)
Cu_2	1.05 (3)	0.00	50 (3)	-0.800 (2)	0.00	0.680 (17)
	1.05 (3)	0.00	147 (11)	-0.578 (15)	0.00	-0.88 (2)
$\chi^2 = 0.4299$ and Magnetic R -factor = 1.70 %						

It is important to emphasize that, despite the limited information contained in the powder diffraction pattern, we can clearly distinguish between the centrosymmetric and noncentrosymmetric models able to fit the observed diffraction pattern globally. The deduced magnetic structure is polar $P2_1ma1'(0,0,g)0s0s$ (point group $2mm1'$, polarization within the **ac**-plane) which is in complete agreement with the observed spontaneous electric polarization below the Néel temperature. As seen from Figure 4.14, the magnetic structure of Gd_2BaCuO_5 is a non-constant moment cycloidal structure because the propagation vector is within the **ac**-plane where moments are lying. For different simulated annealing runs, there are differences in the amplitudes within the zero-cell in spite of fixing a polar angle for the first atom. This means that some other magnetic structures seem to fit the experimental data but the difference between them is only a phase between the different sites. The incommensurate structure corresponds to cycloidal structures with elliptical envelopes, so the magnetic moments are not constant. Only the ground state magnetic structure has constant moments. It is difficult to compare the magnetic structures at different temperatures by looking at the pictures due to the long period of modulation in the visualization box, and we see only a part

of the global magnetic structure. A global view of the magnetic structure of $\text{Gd}_2\text{BaCuO}_5$ at different temperatures is shown in Figure 4.15.

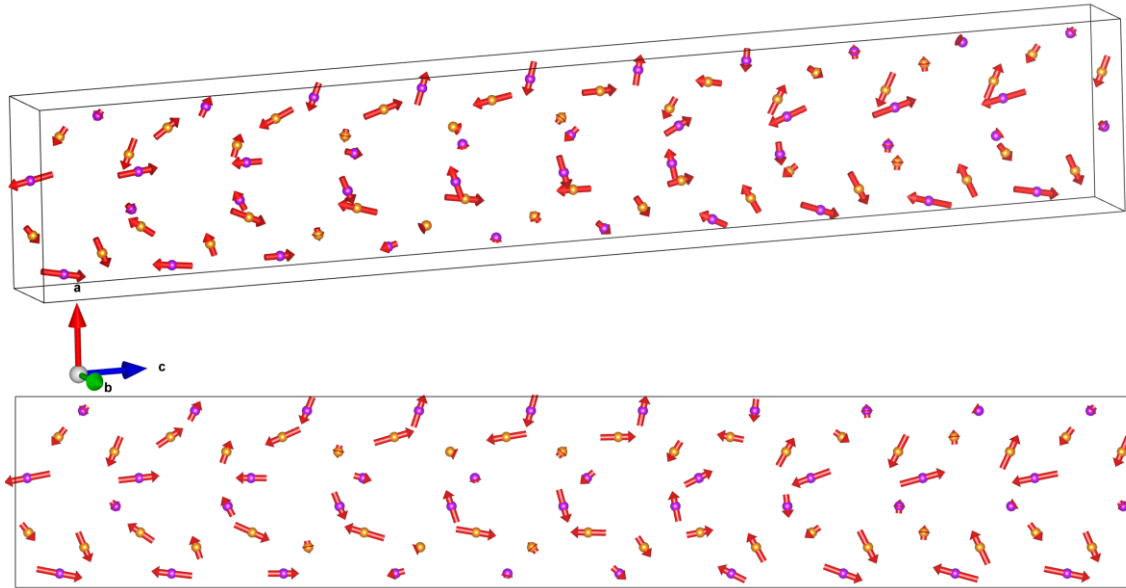


Figure 4.14 Magnetic structure of $\text{Gd}_2\text{BaCuO}_5$ at 9.8 K viewed along the **b**-axis (Bottom) and a general orientation (Top) described in $P2_1ma1'(0,0,g)0s0s$. The shown box is constituted by $1 \times 1 \times 10$ unit cells of the paramagnetic structure. The non-magnetic atoms as well as the Cu-atoms have been removed for the sake of clarity.

4.3.5 Theoretical approach

We discuss below the theoretical understanding of our experimental results using the symmetry analysis of magnetoelectric interactions. The low temperature commensurate magnetic structure doubles the crystallographic unit cell along the **c**-axis, whereas the incommensurate magnetic structure possesses the wave vector $\mathbf{k} = (0, 0, g)$ with g continuously varying from ≈ 0.4449 at temperature T_N to $\frac{1}{2}$ at T_{loc} . Thus, the magnetic phase transitions in $\text{Gd}_2\text{BaCuO}_5$ are due to the instability at the \mathbf{k}_c point of the Brillouin zone, whereas the phase transition at T_{loc} can arguably be considered as a lock-in phase transition. At the \mathbf{k}_c point of the Brillouin zone, the paramagnetic space group $Pnma1'$ has two two-dimensional irreducible representations (IR) Z_1 and Z_2 . The magnetic representation for each crystallographically different magnetic position (Cu, Gd1, and Gd2) splits into $2Z_1 \oplus 4Z_2$ with the x and z spin components transforming according to Z_2 and the y components according to Z_1 . According to our neutron diffraction data, in the commensurate phase, the spins are confined to the **ac**-plane. The symmetry analysis shows that the magnetic structure can, thus, be described by the phase state (c, c) of IR Z_2 .

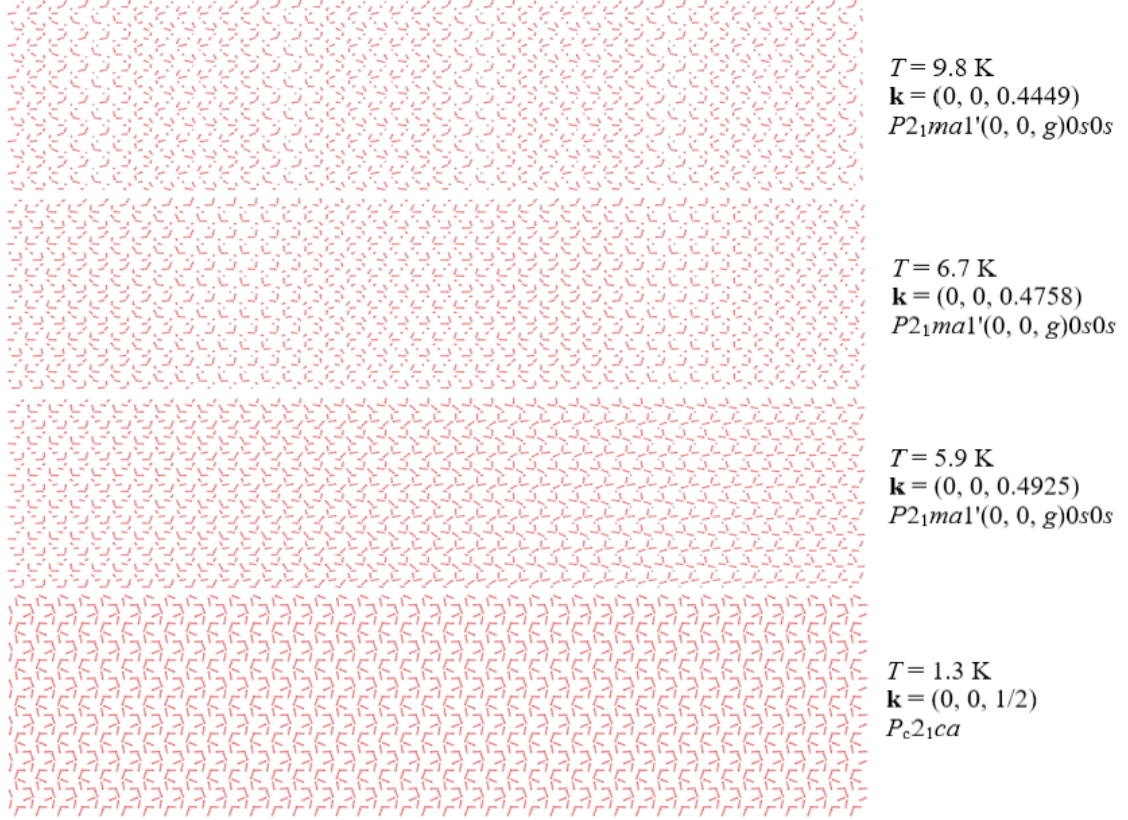


Figure 4.15 Global aspect of the magnetic structures at four temperatures viewed along the \mathbf{b} -axis. We can see that some motifs appearing in the incommensurate magnetic structures are reminiscent of those in the commensurate structure at 1.3 K.

Further, we use the magnetic order parameters (OP) (a_1, a_2) and (c_1, c_2) , which transform according to Z_2 and may describe the spin components along the \mathbf{a} and \mathbf{c} -axes, respectively, and (b_1, b_2) , which transforms according to Z_1 and describes the spin component along the \mathbf{b} -axis. The OP's (a_1, a_2) and (c_1, c_2) are only two of the twelve possible OP's transforming according to Z_2 , because this IR enters 12 times into the full magnetic representation of $\text{Gd}_2\text{BaCuO}_5$ at \mathbf{k}_c , whereas (b_1, b_2) is one out of six OP's transforming according to Z_1 .

The incommensurate modulation of the high temperature phase along the z -axis is due to the existence of Lifshitz invariants;

$$a_1 \frac{\partial a_2}{\partial z} - a_2 \frac{\partial a_1}{\partial z}, \quad b_1 \frac{\partial b_2}{\partial z} - b_2 \frac{\partial b_1}{\partial z}, \quad c_1 \frac{\partial c_2}{\partial z} - c_2 \frac{\partial c_1}{\partial z},$$

which prevent a direct phase transition to the commensurate phase.

The magnetoelectric interactions, constituting the relevant terms of the Landau free energy polynomial expression, are

$$a_1 a_2 P_x, \quad c_1 c_2 P_x, \quad b_1 b_2 P_x, \quad (1)$$

$$(a_1 c_2 + a_2 c_1) P_x, \quad (2)$$

$$(a_1 c_2 - a_2 c_1) P_z, \quad (3)$$

$$(a_1 b_1 - a_2 b_2) P_y, \quad (b_1 c_1 - b_2 c_2) P_y. \quad (4)$$

According to the neutron diffraction data in both the incommensurate and commensurate phases, the spins are confined to the **ac**-plane and the modulated phase is an elliptical cycloidal phase. Therefore, the OP (b_1, b_2) is zero and the magnetic phases are described by a single IR Z_2 . Our results indicate that electric polarization appears below T_N and experiences a small anomaly at T_{loc} becoming a more pronounced jump in applied magnetic field. In the modulated phase, the magnetoelectric interactions in terms (1) average out to zero and do not contribute to the macroscopic polarization. In turn, depending on the phase shift between the OP's (a_1, a_2) and (c_1, c_2) magnetoelectric interactions in term (2) and (3) can give rise to macroscopic electric polarization. However, according to neutron diffraction, in the elliptical cycloidal phase, the spins continuously rotate in the **ac**-plane and the phase shift is such that only term (2) is not zero, whereas term (3) is zero. Therefore, in the modulated phase the electric polarization is directed along the x -axis. In the commensurate phase, which is described by the OP's of the form (a, a) and (c, c) , additional contribution from the magnetoelectric interactions term (1) appears, which explains the anomaly of polarization at T_{loc} . Thus, electric polarization in both magnetically ordered phases has the form $(P_x, 0, 0)$.

In order to understand the microscopic origins of spin-induced electric polarization, one can rewrite the magnetoelectric interactions terms (1) and (2) through spins. Since in both the modulated and commensurate phases, all the twelve two-component OP's come into play, it appears that magnetoelectric interactions are numerous and are extremely difficult to analyse, however, general conclusions can still be made. All three magnetic ions Cu, Gd1, and Gd2 are located in local polar environments with local electric dipoles confined to the **ac**-plane. Therefore, the magnetoelectric interactions have single-spin contributions from all spins [19]. However, two-spin contributions to the magnetoelectric interactions are also present and the analysis reveals that they consist of exchange striction terms with $\mathbf{P} \sim \mathbf{P}_{ij}(\mathbf{S}_i \cdot \mathbf{S}_j)$ and general contributions from interactions of two canted spins. It has to be noted that the latter are not of the commonly assumed form $\mathbf{P} \sim [\mathbf{S}_i \times \mathbf{S}_j]$ though. Indeed, according to

results of neutron diffraction and symmetry analysis, the spins are confined to the **ac**-plane whereas electric polarization is directed along the **a**-axis, i.e., lies in the spin rotation plane. The facts that (i) the values of electric polarization are similar in incommensurate and commensurate phases and that (ii) upon approaching the lock-in phase transition the modulated magnetic structure continuously changes to the commensurate state suggest that the microscopic origin of spin-induced electric polarization is the same in both phases. Therefore, we conclude that both single-ion and two-ions interactions with general expressions for electric dipole moment induced by two canted spins [20] as well as exchange striction mechanisms are responsible for magnetoelectric effect in $\text{Gd}_2\text{BaCuO}_5$.

The occurrence of linear magnetoelectric effect is already shown in $\text{Sm}_2\text{BaCuO}_5$, whereas in this work multiferroic properties of $\text{Gd}_2\text{BaCuO}_5$ are found in accordance with Lifshitz criterion for IRs in $\mathbf{k}_c = (0, 0, \frac{1}{2})$. This explains the important role of the $4f$ - $3d$ magnetic coupling in determining the magnetic ground state of these compounds and thereby magnetoelectric or multiferroic properties. However, $\text{Gd}_2\text{BaCuO}_5$ is similar to $R\text{FeO}_3$ ($R = \text{Gd}$ and Dy) where the $4f$ - $3d$ interactions determine the magnetic structure and the ferroelectricity is induced by the exchange striction between the R and Fe sublattices [21,22]. Our results indicate that external magnetic field has strong influence on electric polarization, T_{loc} , and T_{N} . However, thorough, and substantiated description of the magnetic field effect on magnetic structure and electric polarization requires single crystal studies and possibly single crystal neutron diffraction under magnetic field, which will help to study different mutual geometries of magnetic field, electric polarization, and crystal lattice. The polycrystalline nature of the studied samples allows only for a general conclusion that external magnetic field alters the magnetic anisotropy of the system, which is responsible for the lock-in phase transition and affects the directions of noncollinear magnetic moments, which are responsible for emergence of electric polarization.

4.4 Conclusion

In conclusion, we have discovered multiferroicity in $\text{Gd}_2\text{BaCuO}_5$ which belongs to well-known green phases. In both the incommensurate and commensurate magnetic phases, spontaneous electric polarization is induced by magnetic ordering. According to the neutron diffraction data, the polar elliptical cycloidal and the low temperature commensurate magnetic structures break the inversion symmetry and induce ferroelectricity. We find that

$\text{Gd}_2\text{BaCuO}_5$ is a type-II multiferroic, in which both single-spin and general two-spin interactions are responsible for the observed multiferroicity.

Appendix

In the case of an incommensurate modulated magnetic structure with a single propagation vector ($\mathbf{k}, -\mathbf{k}$), in which we neglect the atomic displacements, the calculation of the magnetic moment of atom j at position \mathbf{r}_{jl} in the crystal is done by applying the simple formula (single harmonic):

$$\mathbf{m}_j(\bar{x}_4) = \mathbf{M}_{\cos j} \cos[2\pi\bar{x}_4] + \mathbf{M}_{\sin j} \sin[2\pi\bar{x}_4]$$

where we have defined the *fourth-dimension* variable as:

$$\bar{x}_4 = t + \mathbf{k}\mathbf{r}_{jl} = t + \mathbf{k}(\mathbf{R}_l + \mathbf{r}_j)$$

The value of the propagation vector components as well as the cosine and sine amplitudes ($\mathbf{M}_{\cos j}$ and $\mathbf{M}_{\sin j}$) for all the atoms in the asymmetric unit of the (3+1)D magnetic superspace group (MSSG) determines the magnetic structure. Notice that the phase factor t is arbitrary, so the values of the amplitudes are normally given for $t = 0$. Depending on the MSSG, even selecting $t = 0$, the complex vector $\mathbf{T}_j = \frac{1}{2}(\mathbf{M}_{\cos j} + i\mathbf{M}_{\sin j})$ is defined except for an arbitrary phase factor. As in conventional crystal structures, this is the case for noncentrosymmetric MSSGs where the origin is not fixed. In the least squares refinements, some components of the amplitudes should be fixed; otherwise, this floating phase prevents the refinement from converging. In treating the diffraction data using simulated annealing, this is not needed; so, one can obtain different sets of amplitudes in the reference cell, giving rise to the same magnetic structure.

References

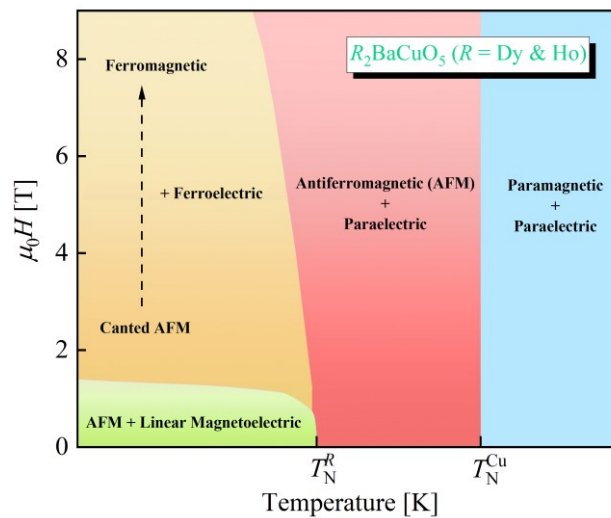
- [1] S. W. Cheong and M. Mostovoy, *Nat Mater* **6**, 13 (2007).
- [2] Y. Tokura and S. Seki, *Adv. Mater.* **22**, 1554 (2010).
- [3] Y. Tokura, S. Seki, and N. Nagaosa, *Rep. Prog. Phys.* **77**, 076501 (2014).
- [4] L. Zhao, H. Guo, W. Schmidt, K. Nemkovski, M. Mostovoy, and A. C. Komarek, *Phys. Rev. B* **96**, 054424 (2017).
- [5] P. Yanda, S. Ghara, and A. Sundaresan, *Solid State Commun.* **272**, 53 (2018).
- [6] C. Michel and B. Raveau, *J. Solid State Chem.* **43**, 73 (1982).
- [7] R. Z. Levitin, B. V Mill, V. V Moshchalkov, N. A. Samarin, V. V Snegirev, and J. Zoubkova, *J. Magn. Magn. Mater.* **90**, 536 (1990).
- [8] V. V Moshchalkov, N. A. Samarin, I. O. Grishchenko, B. V Mill, and Z. J., *Solid State Commun.* **78**, 879 (1991).
- [9] M. Strecker, P. Hettkamp, G. Wortmann, and G. Stewart, *J. Magn. Magn. Mater.* **177–181**, 1095 (1998).
- [10] G. A. Stewart, I. M. McPherson, P. C. M. Gubbens, C. T. Kaiser, P. D. de Reotier, A. Yaouanc, and S. P. Cottrell, *J. Alloys Compd.* **358**, 7 (2003).
- [11] G. F. Goya, R. C. Mercader, L. B. Steren, R. D. Sánchez, M. T. Causa, and M. Tovar, *J. Phys. Condens. Matter* **8**, 4529 (1996).
- [12] A. K. Ovsyanikov, I. V Golosovsky, I. A. Zobkalo, and I. Mirebeau, *J. Magn. Magn. Mater.* **353**, 71 (2014).
- [13] P. Yanda, N. V Ter-Oganessian, and A. Sundaresan, *Phys. Rev. B* **100**, 104417 (2019).
- [14] H. T. Stokes, D. M. Hatch, B. J. Campbell, and D. E. Tanner, *J. Appl. Crystallogr.* **39**, 607 (2006).
- [15] J. Rodriguez-Carvajal, in *Satell. Meet. Powder Diffr. XV Congr. IUCr* (Toulouse, France:[sn], 1990).
- [16] K. Momma and F. Izumi, *J. Appl. Crystallogr.* **44**, 1272 (2011).
- [17] J. M. Perez-Mato, S. V Gallego, E. S. Tasci, and L. Elcoro, *Annu. Rev. Mater. Res* **45**, 217 (2015).
- [18] Bilbao Crystallographic Server, <http://www.cryst.ehu.es>.
- [19] V. P. Sakhnenko and N. V Ter-Oganessian, *J. Phys. Condens. Matter* **24**, 266002 (2012).
- [20] T. A. Kaplan and S. D. Mahanti, *Phys. Rev. B* **83**, 174432 (2011).
- [21] Y. Tokunaga, S. Iguchi, T. Arima, and Y. Tokura, *Phys. Rev. Lett.* **101**, 097205 (2008).
- [22] Y. Tokunaga, N. Furukawa, H. Sakai, Y. Taguchi, T. Arima, and Y. Tokura, *Nat. Mater.* **8**, 558 (2009).

Chapter 5

Linear magnetoelectric effect and magnetic field-induced ferroelectricity in $R_2\text{BaCuO}_5$ ($R = \text{Dy}$, and Ho)*

Summary

The occurrence of a linear magnetoelectric effect and magnetic field-induced ferromagnetism and ferroelectricity below T_N^R in the orthorhombic green phases $R_2\text{BaCuO}_5$ ($R = \text{Dy}$ and Ho) are demonstrated. They undergo a long-range antiferromagnetic ordering of Cu^{2+} ($T_N^{\text{Cu}} = 18.5$ K and $T_N^{\text{Cu}} = 17.5$ K) and R^{3+} ions ($T_N^{\text{Dy}} = 10.7$ K and $T_N^{\text{Ho}} = 8$ K) for Dy and Ho compounds, respectively. Neutron diffraction study reveals that these compounds undergo a first-order magnetic transition from the high temperature centrosymmetric antiferromagnetic phase (P_b2_1/n) to the low-temperature noncentrosymmetric phases, $Pnm'a$ (Dy) and $P112'_1/a$ (Ho), which allows linear magnetoelectric coupling. This is consistent with field-induced electric polarization, below T_N^R , which varies linearly up to ~ 1.2 T. Above a critical field ($H_c > 1.2$ T), both compounds exhibit metamagnetic transitions with magnetization close to the saturation value, $M_s \sim 10.1 \mu_B/\text{f.u.}$ (Dy) and $\sim 11.8 \mu_B/\text{f.u.}$ (Ho) at 7 T. Above the metamagnetic transition, a new polar state appears with large electric polarization indicating field-induced ferroelectricity. We discuss the important role of $4f-3d$ coupling in determining the ground state magnetic structure responsible for the magnetoelectric coupling in both compounds.



*This work is appeared in Phys. Rev. B, **104**, 144401 (2021), © 2021 by the American Physical Society.

5.1 Introduction

The magnetic interaction between $4f$ - $3d$ electrons has been a key research topic in condensed matter physics. It plays a pivotal role in deciding the materials' properties, such as magnetoresistance, superconductivity, magnetoelectricity, and, most importantly, a wide variety of magnetic orderings. It is known that the interplay of $4f$ and $3d$ electrons of rare-earth (R) and transition metals (TM), respectively, play a crucial role in the magnetic properties and associated magnetoelectric coupling [1–5]. Several materials have been reported to be linear magnetoelectric or multiferroic where TM or R ions are solely responsible for the magnetoelectric effect [6,7]. However, not many materials are known where the linear magnetoelectric effect or ferroelectricity arises due to $4f$ - $3d$ coupling [3–5].

The $R_2\text{BaCuO}_5$ ($R = \text{Dy}$, and Ho) exhibit two magnetic transitions for Cu (T_{N1}) and R (T_{N2}) ions, $T_{\text{N1}} = 18$ - 20 K, and $T_{\text{N2}} = 9$ - 11 K for Dy and $T_{\text{N1}} = 17$ K, and $T_{\text{N2}} = 7$ - 8 K for Ho, as confirmed various experiments like magnetic, heat capacity, young's modulus, and spectral studies [8–13]. Later, these were reported to be strong anisotropic antiferromagnets based on magnetic and spectral studies of single crystals [14]. The ground state magnetic structures possess different propagation vectors $\mathbf{k} = (0, 0, 0)$ for $\text{Dy}_2\text{BaCuO}_5$ and $\mathbf{k}_{\text{C1}} = (0, \frac{1}{2}, 0) + \mathbf{k}_{\text{C2}} = (0, 0, 0)$ for $\text{Ho}_2\text{BaCuO}_5$ [15]. As seen in Chapter 3, $\text{Sm}_2\text{BaCuO}_5$ evidence linear magnetoelectric effect below $T_{\text{N}}^{\text{Cu}} = 23$ K [17]. The scenario is completely different in $\text{Gd}_2\text{BaCuO}_5$, where both copper and Gd moments order at the same temperature ($T_{\text{N}} = 11.8$ K). It exhibits an incommensurate magnetic structure (elliptical interpenetrated cycloids) possessing a modulation vector $\mathbf{k} = (0, 0, g)$, with $g = 0.4446$ below $T_{\text{N}} = 11.8$ K and undergoes lock-in transition at $T_{\text{loc}} = 6$ K to a commensurate structure with $\mathbf{k}_{\text{c}} = (0, 0, \frac{1}{2})$ as discussed earlier in Chapter 4 [18]. Therefore, we have investigated the magnetoelectric properties of $R_2\text{BaCuO}_5$ ($R = \text{Dy}$, and Ho).

In this chapter, we show the observation of a linear magnetoelectric effect, magnetic field-induced ferromagnetism, and ferroelectricity in the compounds $R_2\text{BaCuO}_5$ ($R = \text{Dy}$ and Ho). These isostructural compounds crystallize in the centrosymmetric orthorhombic structure ($Pnma$), containing an unusual distorted CuO_5 square pyramid. $\text{Dy}_2\text{BaCuO}_5$ and $\text{Ho}_2\text{BaCuO}_5$ show long-range antiferromagnetic ordering of copper ions at 18.5 K and 17.5 K, whereas Dy^{3+} and Ho^{3+} moments order at 10.7 K and 8 K, respectively. The applied magnetic field induces electric polarization at the $\text{Dy}^{3+}/\text{Ho}^{3+}$ ordering temperatures. Both compounds exhibit metamagnetic transitions above a critical field with a large magnetization

and electric polarization. Our results demonstrate that the $R_2\text{BaCuO}_5$ ($R = \text{Dy}$ and Ho) compounds represent new magnetoelectric materials where the $4f$ - $3d$ interactions play a crucial role.

5.2 Experimental section

Polycrystalline samples of $R_2\text{BaCuO}_5$ ($R = \text{Dy}$ and Ho) were prepared by heating a stoichiometric mixture of high purity $R_2\text{O}_3$ (preheated), BaCO_3 , and CuO at 950°C in air. Structural characterization and physical properties of these samples were done similar to that mentioned for $\text{Sm}_2\text{BaCuO}_5$ in Chapter 3. The dimensions of the pellets used for electrical measurements are $t = 0.279$ mm and $A = 20$ mm² for $\text{Dy}_2\text{BaCuO}_5$ and $t = 0.33$ mm & $A = 50$ mm² for $\text{Ho}_2\text{BaCuO}_5$. Neutron diffraction measurements on $\text{Dy}_2\text{BaCuO}_5$ were carried on the WISH instrument at ISIS [19]. We have used two different samples of $\text{Ho}_2\text{BaCuO}_5$ for neutron diffraction measurements. The sample used on D1B, ILL was free of impurities and was synthesized and measured a long time ago (1993) using thermal scans between 2 and 32 K. Another sample containing less than 1% of cubic Ho_2O_3 was measured with the WISH instrument, ISIS.

5.3 Results and discussion

5.3.1 Crystal structure

Rietveld refinement of room temperature X-ray (see Figure 5.1) diffraction data confirmed that the $R_2\text{BaCuO}_5$ ($R = \text{Dy}$ and Ho) crystallizes in orthorhombic non-polar structure (Space group: $Pnma$). The corresponding structural parameters are provided in Tables 5.1(a & b). To check whether these compounds undergo any phase transition, we have carried neutron diffraction at low temperatures. A careful analysis of these data (see Figure 5.2) confirmed that the centrosymmetric crystal structure ($Pnma1'$) is stable down to the lowest temperature measured. The corresponding structural parameters are provided in Tables 5.2(a & b). The crystal structure obtained from the refinement of neutron data (WISH) of $\text{Dy}_2\text{BaCuO}_5$ at 25 K is shown in Figure 5.3(a). The crystal structure (except the change of cell parameters with temperature) is close to the room temperature data published earlier.

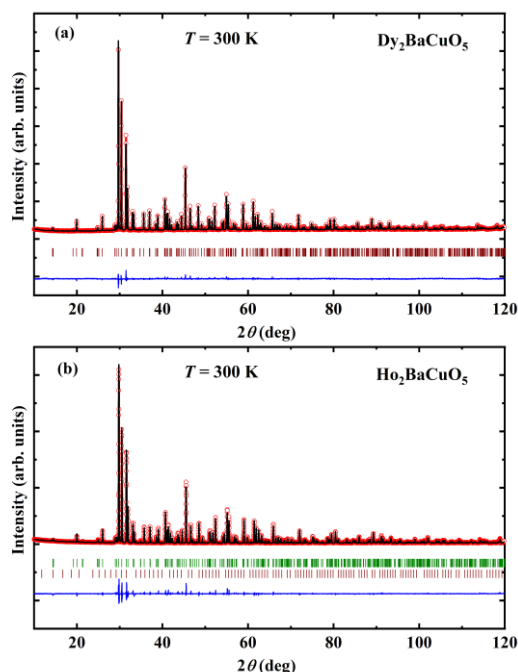


Figure 5.1 Rietveld refined powder X-ray diffraction patterns of $\text{Dy}_2\text{BaCuO}_5$ and $\text{Ho}_2\text{BaCuO}_5$ at room temperature.

Table 5.1-a Structural parameters of $\text{Dy}_2\text{BaCuO}_5$ obtained from Rietveld refinement of X-ray diffraction data. Space group: $Pnma1'$; $a = 12.2277$ (1) Å, $b = 5.6827$ (1) Å, $c = 7.1563$ (1) Å, $V = 497.264$ (3) Å³; global- $\chi^2 = 2.37$; Bragg R -factor = 7.36 (%), and R_F -factor = 8.68 (%).

Atom	Site	x	y	z	B_{iso} (Å ²)
Dy1	4c	0.2886 (2)	0.2500	0.1166 (4)	0.449 (58)
Dy2	4c	0.0741 (2)	0.2500	0.3962 (3)	0.620 (55)
Ba	4c	0.9051 (2)	0.2500	0.9297 (3)	0.705 (58)
Cu	4c	0.6590 (5)	0.2500	0.7125 (8)	0.384 (128)
O1	8d	0.4347 (16)	-0.0124 (29)	0.1732 (19)	1
O2	8d	0.2262 (14)	0.5079 (32)	0.3546 (26)	1
O3	4c	0.0951 (21)	0.2500	0.0731 (32)	1

Table 5.1-b Structural parameters of $\text{Ho}_2\text{BaCuO}_5$ obtained from Rietveld refinement of X-ray diffraction data. S.G: $Pnma1'$; $a = 12.1857$ (1) Å, $b = 5.6644$ (1) Å, $c = 7.1348$ (1) Å, $V = 492.48$ (1) Å³; global- $\chi^2 = 4.24$, Bragg R -factor = 5.22 (%), and R_F -factor = 4.58 (%).

Atom	Site	x	y	z	B_{iso} (Å ²)
Ho1	4c	0.2883 (2)	0.2500	0.1162 (4)	1.289 (59)
Ho2	4c	0.0742 (2)	0.2500	0.3963 (3)	1.315 (57)
Ba	4c	0.9049 (1)	0.2500	0.9301 (3)	0.482 (41)
Cu	4c	0.6594 (4)	0.2500	0.7134 (7)	0.324 (103)
O1	8d	0.4333 (14)	-0.0113 (28)	0.1713 (20)	1
O2	8d	0.2268 (13)	0.5060 (30)	0.3553 (24)	1
O3	4c	0.0995 (19)	0.2500	0.0772 (31)	1

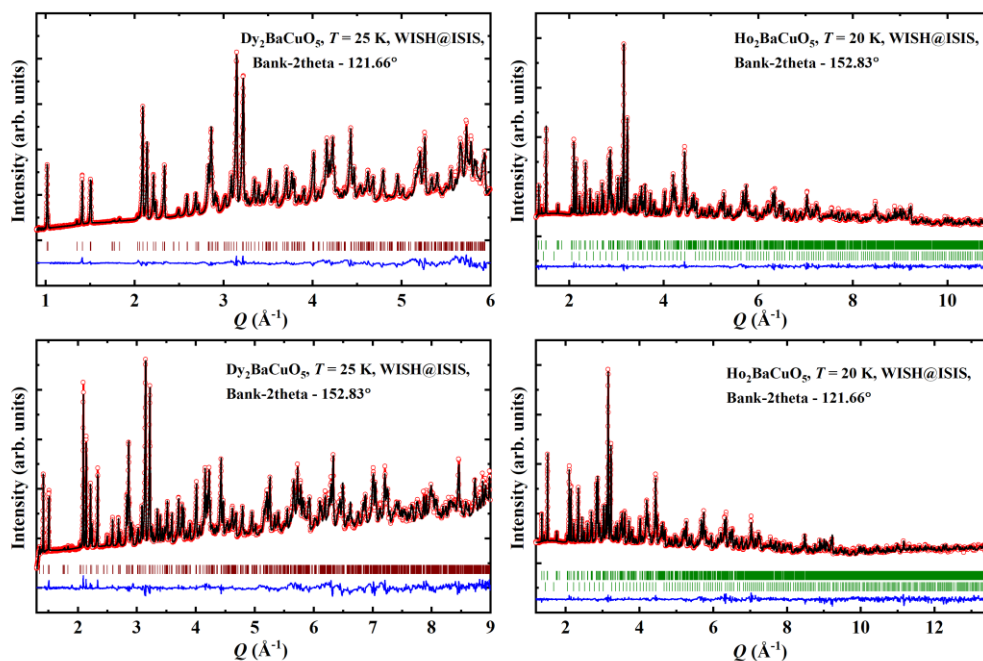


Figure 5.2 Rietveld refined neutron powder diffraction patterns at 25 K for $\text{Dy}_2\text{BaCuO}_5$ and at 20 K for $\text{Ho}_2\text{BaCuO}_5$ collected on different banks of WISH. The second row of tick marks corresponds to the impurity of cubic Ho_2O_3 ($\approx 0.5\%$).

Table 5.2-a Structural parameters of $\text{Dy}_2\text{BaCuO}_5$ obtained from Rietveld refinement of neutron data collected at 25 K. Space group: $Pnma1'$; $a = 12.2025$ (2) Å, $b = 5.6733$ (1) Å, $c = 7.1379$ (1) Å, $V = 494.14$ (1) Å³; global- $\chi^2 = 5.64$; $R_p = 1.90$ (%), $wR_p = 2.25$ (%).

Atom	Site	x	y	z	B_{iso} (Å ²)
Dy1	4c	0.2889 (1)	0.2500	0.1172 (1)	0.047 (8)
Dy2	4c	0.0743 (1)	0.2500	0.3968 (1)	0.047 (8)
Ba	4c	0.9075 (2)	0.2500	0.9288 (3)	0.230 (5)
Cu	4c	0.6600 (1)	0.2500	0.7115 (2)	0.790 (1)
O1	8d	0.4332 (2)	-0.0082 (2)	0.1686 (2)	0.490 (2)
O2	8d	0.2282 (1)	0.5057 (3)	0.3552 (3)	0.490 (2)
O3	4c	0.1005 (2)	0.2500	0.0837 (3)	0.490 (2)

Table 5.2-b Structural parameters of $\text{Ho}_2\text{BaCuO}_5$ obtained from Rietveld refinement of neutron data collected at 20 K. Space group: $Pnma1'$; $a = 12.1668$ (5) Å, $b = 5.6553$ (2) Å, $c = 7.1135$ (3) Å, $V = 489.46$ (4) Å³; $\chi^2 = 9.99$; Bragg R -factor = 2.32 (152°) and 3.11 (121°).

Atom	Site	x	y	z	B_{iso} (Å ²)
Ho1	4c	0.2880 (1)	0.2500	0.1152 (2)	0.34 (4)
Ho2	4c	0.0740 (1)	0.2500	0.3952 (2)	0.50 (4)
Cu	4c	0.6601 (1)	0.2500	0.7110 (2)	0.77 (4)
Ba	4c	0.9057 (2)	0.2500	0.9286 (3)	0.34 (5)
O1	8d	0.4324 (1)	-0.0076 (3)	0.1670 (1)	0.93 (4)
O2	8d	0.2278 (1)	0.5061 (3)	0.3557 (2)	0.85 (4)
O3	4c	0.1011 (2)	0.250	0.0811 (3)	0.79 (5)

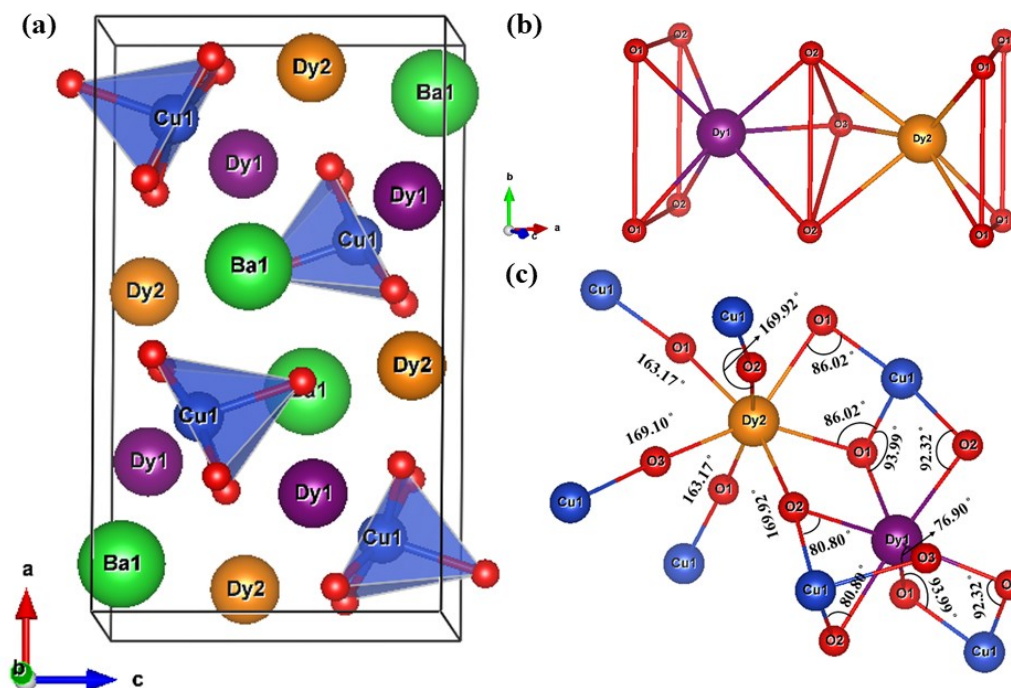


Figure 5.3 (a) Crystal structure of Dy₂BaCuO₅ at 25 K. (b) Dy₂O₁₁ blocks are formed by triangular face shared DyO₇ polyhedrons. (c) Inequivalent Dy sites with Dy–O–Cu bond angles. This structure is equally valid for all R₂BaCuO₅ (R = Sm–Lu, Y) compounds.

The crystal structure of Dy₂BaCuO₅ given in Figure 5.3(a) is equally valid for R₂BaCuO₅ (R = Sm – Lu and Y). The structure consists of monocapped trigonal prisms RO₇ connected by trigonal faces to form R₂O₁₁ blocks, whose cavities are occupied by Cu²⁺ and Ba²⁺ ions. The Cu²⁺ ions are in isolated square pyramids CuO₅ and Ba²⁺ ions found in BaO₁₁ polyhedrons. It is important to note that all the cations occupy the fourfold sites (Wyckoff positions 4c in *Pnma*) with mirror symmetry, and there are two inequivalent sites for rare earth R³⁺ ions as shown in Figure 5.3(b). The oxygen coordination polyhedrons of R³⁺ in both sites differ slightly, but the local environment varies significantly. The R³⁺ ions at the R₂ site are connected through oxygen atoms to six nearby Cu²⁺ ions, and five of six R₂-O-Cu bond angles are being close to 180°, while the R³⁺ ions in the R₁ site are connected only to three Cu²⁺ ions with R₁-O-Cu bond angles close to 90° as shown in Figure 5.3(c).

5.3.2 DC magnetization and specific heat

The temperature dependence of magnetization of R₂BaCuO₅ (R = Dy & Ho), measured under different magnetic fields, and specific heat measured under zero magnetic field are displayed in Figure 5.4. As seen in Figure 5.4(a), Dy₂BaCuO₅ exhibits long-range

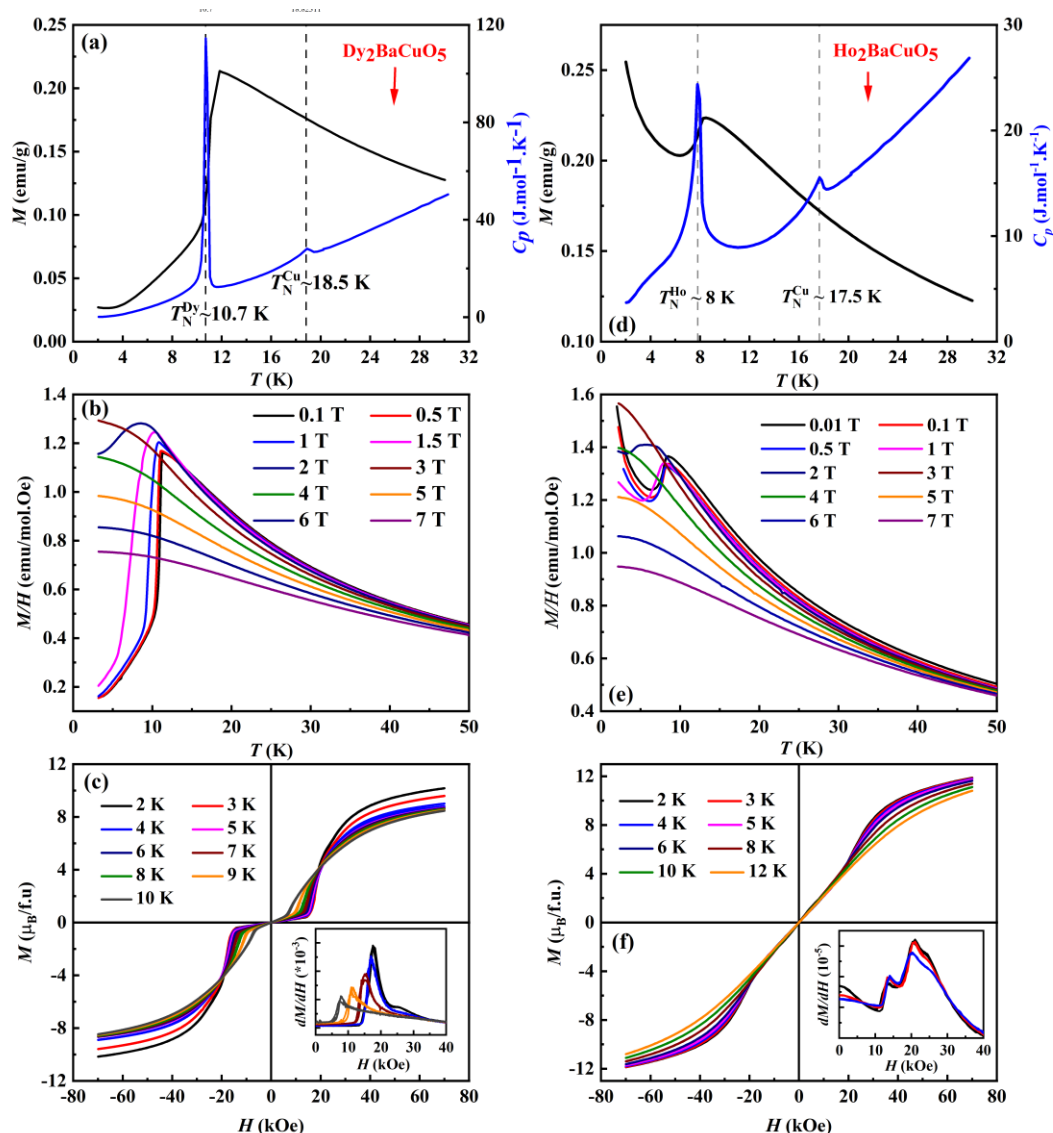


Figure 5.4 (a & d) Left axis. Temperature-dependent DC magnetization measured under 100 Oe in field-cooled (FC) condition. Right axis. Specific heat measured under zero magnetic field. (b & e) DC magnetization measured under different magnetic fields. (c & f) Isothermal $M(H)$ curves and insets show dM/dH vs H ; for $\text{Dy}_2\text{BaCuO}_5$ and $\text{Ho}_2\text{BaCuO}_5$, respectively.

magnetic ordering of Cu^{2+} and Dy^{3+} moments at $T_N^{\text{Cu}} = 18.5$ K and $T_N^{\text{Dy}} = 10.7$ K, respectively. At the same time, the Ho compound exhibits long-range magnetic ordering at $T_N^{\text{Cu}} = 17.5$ K and $T_N^{\text{Ho}} = 8$ K as seen in Figure 5.4(d). In DC magnetization, we do not observe any anomaly at T_N^{Cu} due to the high paramagnetic moment of Dy^{3+} and Ho^{3+} ions. The possible magnetic interaction path in these compounds is $\text{Cu}^{2+}-\text{O}^{2-}-\text{Dy}^{3+}-\text{O}^{2-}-\text{Cu}^{2+}$ because each copper ion is isolated, and there are no Cu–O–Cu bonds. The effective magnetic moment is in good agreement with the theoretical value of the R^{3+} and Cu^{2+} ions, as shown in Figure 5.5. The negative sign of the Curie-Weiss constant indicating the dominating antiferromagnetic interactions in these compounds. Upon increasing the applied magnetic

field, the anomaly at $T_N^{\text{Dy}} = 10.7$ K and $T_N^{\text{Ho}} = 8$ K in DC magnetization (M/H vs T) is suppressed, indicating possible metamagnetic transitions or changes in magnetic structure [Figure 5.4(b & e)]. Indeed, below T_N^R , the isothermal $M(H)$ curves exhibit field-induced steps, which is the signature of the metamagnetic nature of the phase transitions, as shown in Figure 5.4(c & f). This behavior can be seen from the dM/dH curves, given in the insets of Figure 5.4(c & f). These data show an initial linear behavior below a critical field ($H_c \sim 1.2$ T) due to the antiferromagnetic ordering. Above the critical field, both compounds show field-induced metamagnetic transitions leading to large magnetization with values up to ~ 10.1 $\mu_B/\text{f.u.}$ (Dy) and ~ 11.8 $\mu_B/\text{f.u.}$ (Ho) at 7 T and 2 K. Upon increasing the temperature, the metamagnetic transitions shift to lower fields.

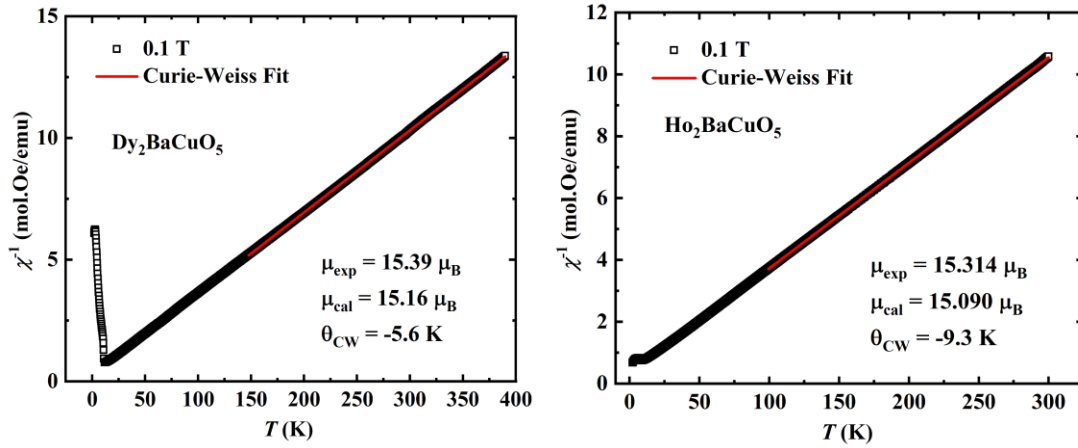


Figure 5.5 Inverse susceptibility data of $\text{Dy}_2\text{BaCuO}_5$ and $\text{Ho}_2\text{BaCuO}_5$ along with Curie-Weiss fit (solid line).

5.3.3 Dielectric constant and electric polarization

To check the possibility of linear magnetoelectric effect, we have carried the electrical measurements on both compounds in $E \perp H$ and $E \parallel H$ configurations [20]. Figure 5.6(a & b) shows the temperature-dependent dielectric constant at different magnetic fields for $\text{Dy}_2\text{BaCuO}_5$ and the corresponding dissipation factor measured under $E \perp H$ configuration, respectively. An apparent dielectric anomaly is seen at T_N^{Dy} under zero magnetic field, but there is no noticeable feature at copper ordering temperature. With an increasing magnetic field, the dielectric anomaly develops into a peak-like feature. In addition, a small dielectric peak appears around 4.5 K above the magnetic field of 2 T, which is suppressed above 3 T. A notable magnetodielectric (MD) effect is observed around T_N^{Dy} with the value of 0.16 %. The appearance of the dielectric peak at the Dy magnetic ordering indicates a possible

ferroelectric transition. To check this, we have recorded the pyroelectric current as a function of temperature and magnetic field after magnetoelectric poling in $E \perp H$ configuration, which is shown in Figure 5.6(c). We have not observed the pyrocurrent anomaly under a zero magnetic field. However, a clear asymmetric pyrocurrent peak appears at T_N^{Dy} under applied magnetic fields. At magnetic fields larger than ~ 1.2 T, the pyrocurrent peaks continue to be present. However, the pyrocurrent peaks start decreasing with further increasing the field. In addition to this, we have observed another pyrocurrent peak at 4.5 K between 2-3 T as observed in dielectric data, indicating another field-induced change in magnetic structure.

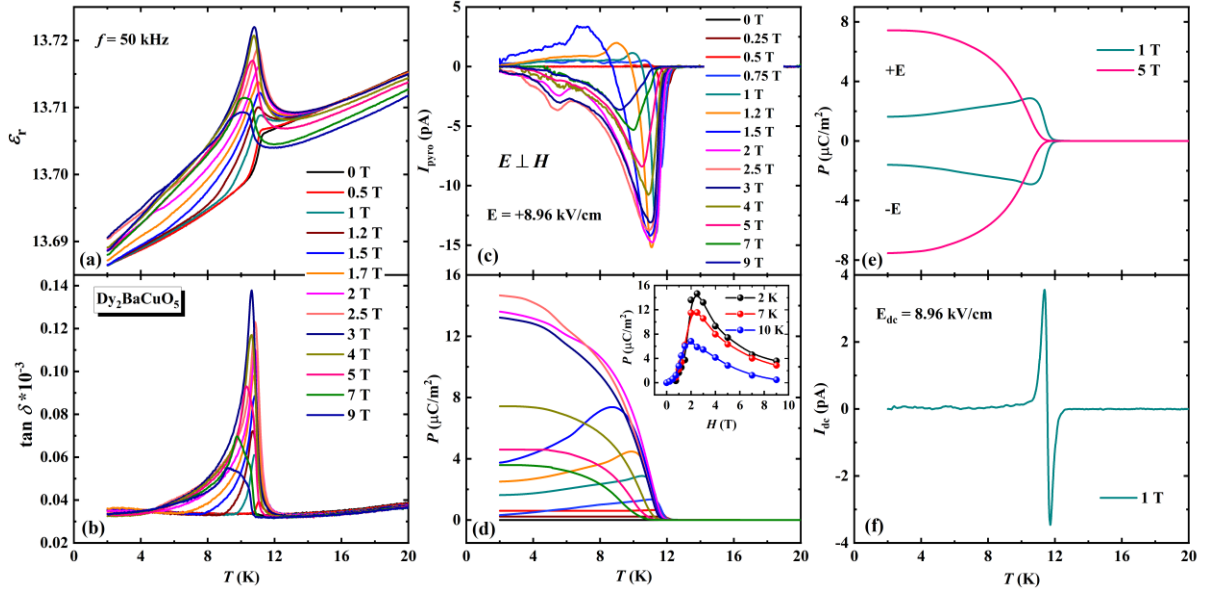


Figure 5.6 (a & b) Temperature-dependent dielectric constant and corresponding loss measured under different magnetic fields and frequency $f = 50$ kHz, respectively. (c) T -dependence of pyrocurrent recorded for different magnetic fields with the poling electric field $E = +8.96$ kV/cm. (d) The corresponding polarization and the inset shows magnetic field-dependent polarization. (e) Switching of polarization by changing the direction of the poling electric field measured under 1 and 5 T magnetic fields. (f) DC bias current; for $\text{Dy}_2\text{BaCuO}_5$.

The corresponding electric polarization is shown in Figure 5.6(d). Surprisingly, unlike $\text{Sm}_2\text{BaCuO}_5$, where the polarization appears at the copper ordering temperature, $\text{Dy}_2\text{BaCuO}_5$ shows the polarization at dysprosium ordering T_N^{Dy} under magnetic field [17]. With increasing magnetic field, electric polarization increases linearly up to metamagnetic transitions, demonstrating the linear magnetoelectric effect. Above this transition, electric polarization becomes nonlinear and finally suppressed at high fields, as seen from the inset of Figure 5.6(d). The nonlinear behavior indicates the symmetry of the new magnetic phase above the metamagnetic transition might be polar. Similar linear magnetoelectric effect and

field-induced magnetoelectric coupling is reported in DyCrO_4 , where the presence of polar symmetry above the metamagnetic transition is confirmed by neutron diffraction [5]. As indicated by the pyrocurrent peak, there is an additional polarization between 2-3 T at 4.5 K [see Figure 5.6(c & d)]. However, one must perform neutron diffraction experiments under magnetic fields to understand the nature of the field-induced magnetic structures. The maximum polarization observed is $\sim 14.6 \mu\text{C}/\text{m}^2$ at magnetic field $H = 2.5$ T and 2 K. The intrinsic nature of the linear magnetoelectric effect and field-induced ferroelectric transitions is further supported by switching polarization and dc bias measurements, as depicted in Figure 5.6(e & f). The calculated magnetoelectric coefficient α of $\text{Dy}_2\text{BaCuO}_5$ is 3.47 ps/m (1 T & 10 K) and 7.37 ps/m (2.5 T & 2 K), which is higher than that of the isostructural compound $\text{Sm}_2\text{BaCuO}_5$ [17].

The outcome of the electrical measurements done in the $E \perp H$ configuration for $\text{Ho}_2\text{BaCuO}_5$ is provided in Figure 5.7. Unlike the $\text{Dy}_2\text{BaCuO}_5$, this compound exhibits multiple metamagnetic transitions and associated dielectric properties under applied magnetic fields. The temperature-dependent dielectric constant and the corresponding dissipation factor for $\text{Ho}_2\text{BaCuO}_5$ are shown in Figure 5.7(a & b). From the figure, there is no dielectric anomaly at T_N^{Cu} but there is an anomaly at T_N^{Ho} in the absence of a magnetic field. Under applied magnetic fields, the anomaly at T_N^{Ho} increases and finally disappeared above 3 T. Moreover, we have observed a second dielectric anomaly below T_N^{Ho} at 1 T, which shifts to low temperatures with further increasing the magnetic field. In addition, there are new anomalies at high fields ($H > 5$ T) at very low temperatures. Temperature-dependent pyrocurrent measured at selected magnetic fields and related electric polarization are shown in Figures 5.7(c) and 5.7(d), respectively. No significant polarization is observed at $H = 0$ T at temperatures down to 2 K. However, the external magnetic field induces electric polarization at T_N^{Ho} which varies linearly up to 1 T, as seen from the inset of Figure 5.7(d), demonstrating the linear magnetoelectric effect. Also, it is clear from the pyrocurrent data [see Figure 5.7(c)] that there is a broad anomaly around 4 K under the magnetic field. At $H \geq 1$ T, pyrocurrent anomalies near T_N^{Ho} show two peak features indicating that the second dielectric anomaly is associated with ferroelectricity. This second transition can be due to the metamagnetic transition. A maximum polarization of $32.9 \mu\text{C}/\text{m}^2$ is observed at 2 K and 1 T. The calculated magnetoelectric coefficient α of $\text{Ho}_2\text{BaCuO}_5$ at 5 K is 41.4 ps/m for ~ 1 T, higher than that of the isostructural compounds $\text{Sm}_2\text{BaCuO}_5$, $\text{Dy}_2\text{BaCuO}_5$, and most of the known magnetoelectrics. Further, dc bias measurement and switching nature of electric

polarization, as seen from Figure 5.7(e & f), confirm the intrinsic nature of electric polarization. Further, it demonstrates the two transitions discussed above.

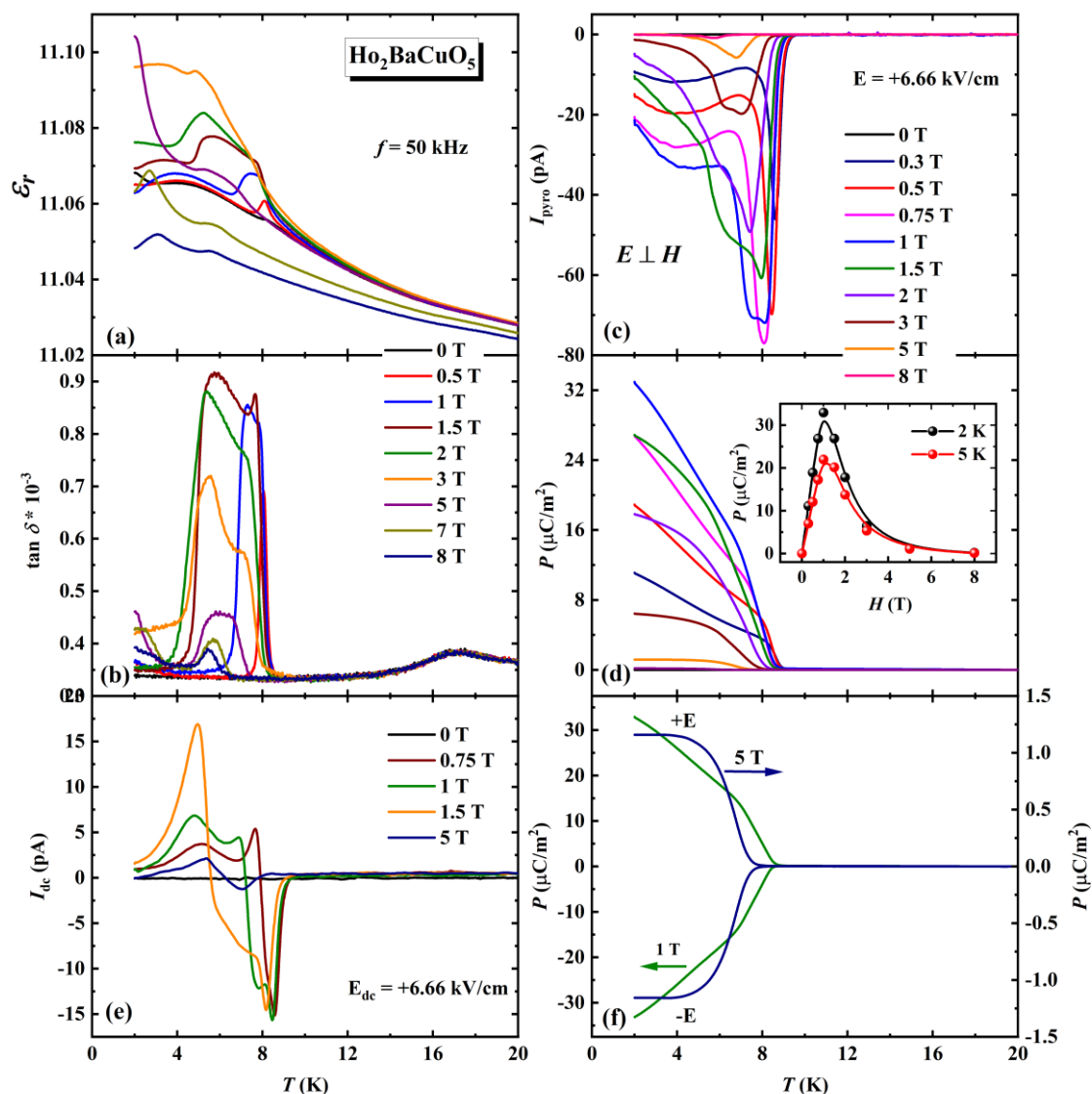


Figure 5.7 (a & b) Dielectric constant and dissipation factor against temperature measured with frequency $f = 50$ kHz and under different magnetic fields, respectively. (c) T - H dependent pyrocurrent measured after magnetoelectric poling in $E \perp H$ configuration. (d) The corresponding electric polarization and the inset shows P vs H . (e & f) DC bias signals and switching under different magnetic fields; for $\text{Ho}_2\text{BaCuO}_5$.

The results obtained under $E \parallel H$ configuration for $\text{Dy}_2\text{BaCuO}_5$ and $\text{Ho}_2\text{BaCuO}_5$ are shown in Figure 5.8. The dielectric constant for both compounds is decreased as compared to the $E \perp H$ configuration. Moreover, The observed electric polarization in $E \perp H$ configuration is higher than that of $E \parallel H$ configuration, indicating nonzero off-diagonal magnetoelectric tensors for both compounds [20].

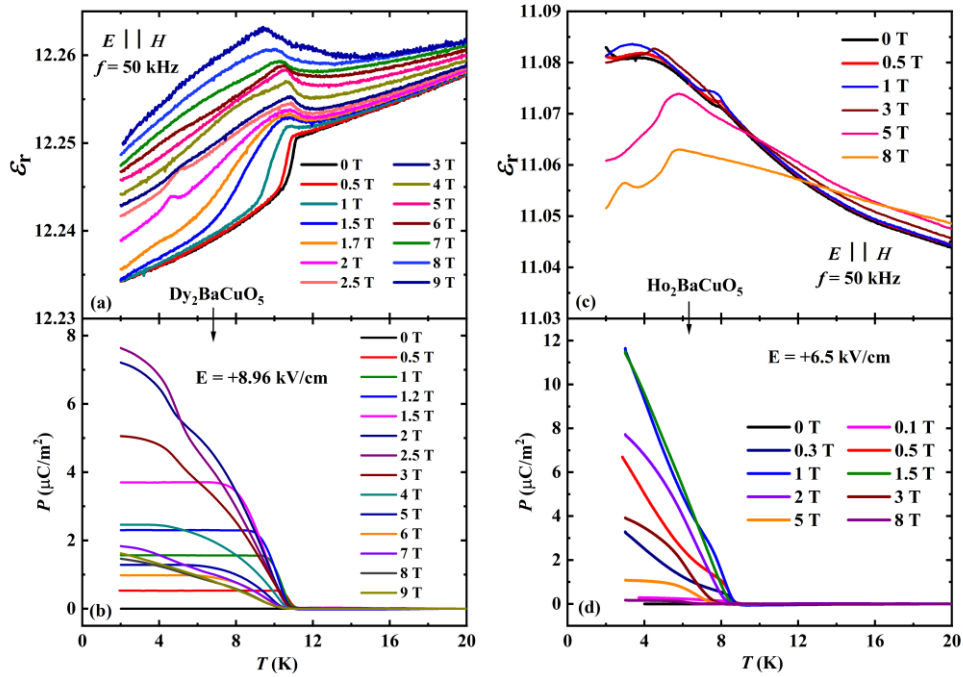


Figure 5.8 Temperature-dependent dielectric constant and electric polarization for (a & b) $\text{Dy}_2\text{BaCuO}_5$ (c & d) $\text{Ho}_2\text{BaCuO}_5$; measured in $E \parallel H$ configuration.

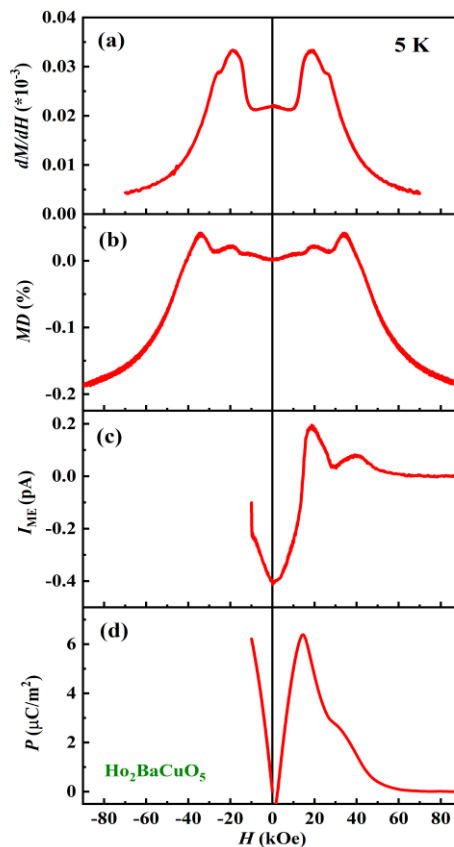


Figure 5.9 Magnetic field-dependent (a) derivative of magnetization at 2 K (b) relative dielectric constant measured at $f = 50$ kHz (c) magneto-electric current recorded after poling the sample under electric and magnetic fields. (d) Electric polarization is obtained by integrating the magneto-electric current; for $\text{Ho}_2\text{BaCuO}_5$.

The magnetic field dependence of magnetization, relative dielectric constant, magnetoelectric current, and electric polarization at 5 K for polycrystalline $\text{Ho}_2\text{BaCuO}_5$ is shown in Figure 5.9. The first derivative of the magnetization [Figure 5.9(a)] shows an anomalous behavior that indicates field-induced metamagnetic transitions under applied magnetic fields. Similarly, the dielectric constant displays an anomalous behavior with the magnetic field, as seen from Figure 5.9(b). The magnetoelectric current [Figure 5.9(c)] was recorded from -1 T to 9 T at 5 K, after poling the sample with 6.7 kV/cm and magnetic field of -1 T, and the corresponding polarization is given in Figure 5.9(d). As seen from the figure, there is no polarization at zero magnetic field. Upon increasing the magnetic field, electric polarization appears with a linear increase up to ~ 1 T and reaches a maximum at ~ 1.3 T. With further increase of the magnetic field, polarization shows anomalous behavior and finally vanishes above ~ 7 T. These results demonstrate that $\text{Ho}_2\text{BaCuO}_5$ exhibits linear magnetoelectric effect and field-induced ferroelectric transitions.

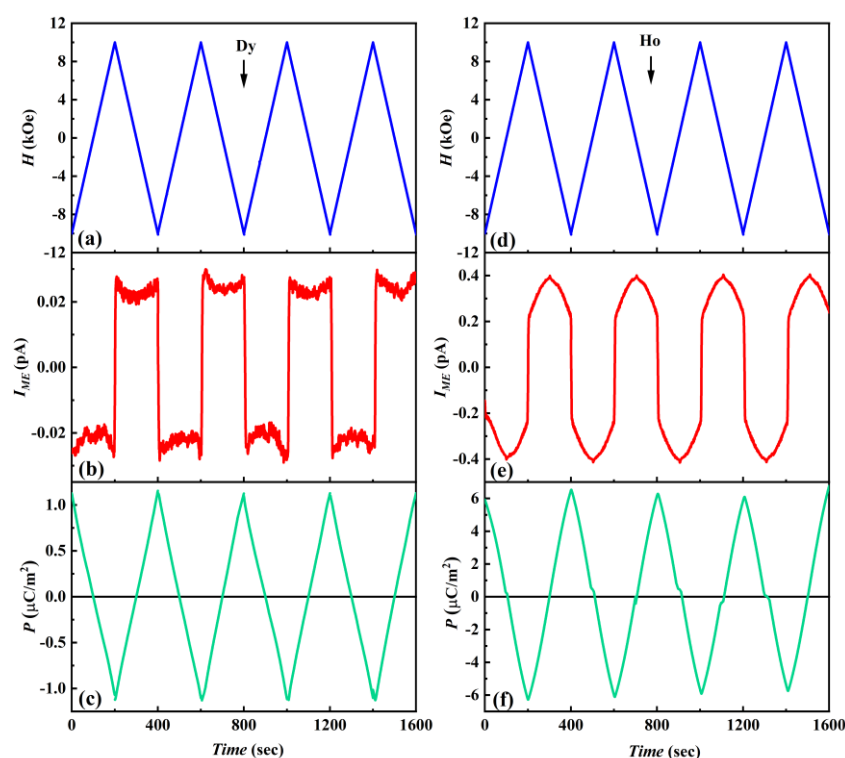


Figure 5.10 Magnetoelectric current measured against the magnetic field for both compounds. Left panel: $\text{Dy}_2\text{BaCuO}_5$ and Right panel: $\text{Ho}_2\text{BaCuO}_5$.

To examine further the linear magnetoelectric effect in both compounds, we carried out magnetic field-dependent magnetoelectric current measurements in the linear magnetoelectric region (< 1 T). In this measurement, we have poled the sample in the presence of an electric field and magnetic field (-1 T) across T_N^R to 2 K and 5 K for

Dy₂BaCuO₅ and Ho₂BaCuO₅, respectively. Subsequently, we have recorded the current in response to the sweeping of the magnetic field from -1 T to +1 T at fixed temperatures and presented in Figure 5.10. As seen from the figure, the magnetoelectric current changes periodically with the applied magnetic field. However, the corresponding polarization oscillates linearly with the magnetic field providing evidence of the linear magnetoelectric effect.

5.3.4 Magnetic structure of Dy₂BaCuO₅

We have carried the neutron diffraction measurements below and above the magnetic ordering temperatures on both compounds to understand the observed linear magnetoelectric effect. From our neutron data (WISH) of Dy₂BaCuO₅, we obtain the **k**-vectors (0, ½, 0) at $T_N^{\text{Dy}} < T \leq T_N^{\text{Cu}}$ and (0, 0, 0) at $T \leq T_N^{\text{Dy}}$ by using the `k_SEARCH` program in the `FULLPROF SUITE` [21]. Knowing the crystal structure (*Pnma*1') and **k**-vector, we have used `ISODISTORT` to find out the possible magnetic modes and associated magnetic space groups [22]. We found six possible magnetic models, which correspond to two two-dimensional irreducible representations (*irreps*) with different order parameters. In the temperature interval $T_N^{\text{Dy}} < T \leq T_N^{\text{Cu}}$, the correct solution is found to be centrosymmetric with the magnetic space group symbol P_b112_1/n (transformation to standard-setting P_a2_1/c can be performed by **b**, **a**, **-b-c**; 0, 0, 0) which represents *irrep* mY1: (*a*, *a*). The Rietveld refinement patterns and the related structural parameters along with the magnetic parameters at 13 K, are shown in 5.11 and Table 5.3(a). The equivalent Hall symbol [23] is $\bar{P}2_n1'_b$ in which the presence of a center of symmetry is explicit by the bar on top of the primitive lattice symbol. From the symmetry, it is evident that the corresponding point group (*2/m1*') imposes a null magnetoelectric tensor consistent with the absence of the magnetoelectric effect. The obtained magnetic structure is commensurate but noncollinear, as illustrated in Figure 5.12(a). We have fixed the *z*-component of the Dy1 moment to zero because there are correlations between the *z*-components of Dy1 and Cu in the refinement, resulting in high errors, and the Dy1 moment was close to zero. From Figure 5.12(a), the Cu and Dy2 moments lie in the **ac**-plane, and Dy1 moments are pointed along the **a**-axis. The moment of the Dy2 is considerably high as compared to Dy1 on account of the high molecular field on Dy2, which is surrounded by 6 Cu²⁺ ions, whereas Dy1 is surrounded by three Cu²⁺ ions. The Dy1 moments are aligned along the Dy1-O3 bond, and this is not the case for Dy2. This different behavior is due to the different single-ion anisotropy of both sites.

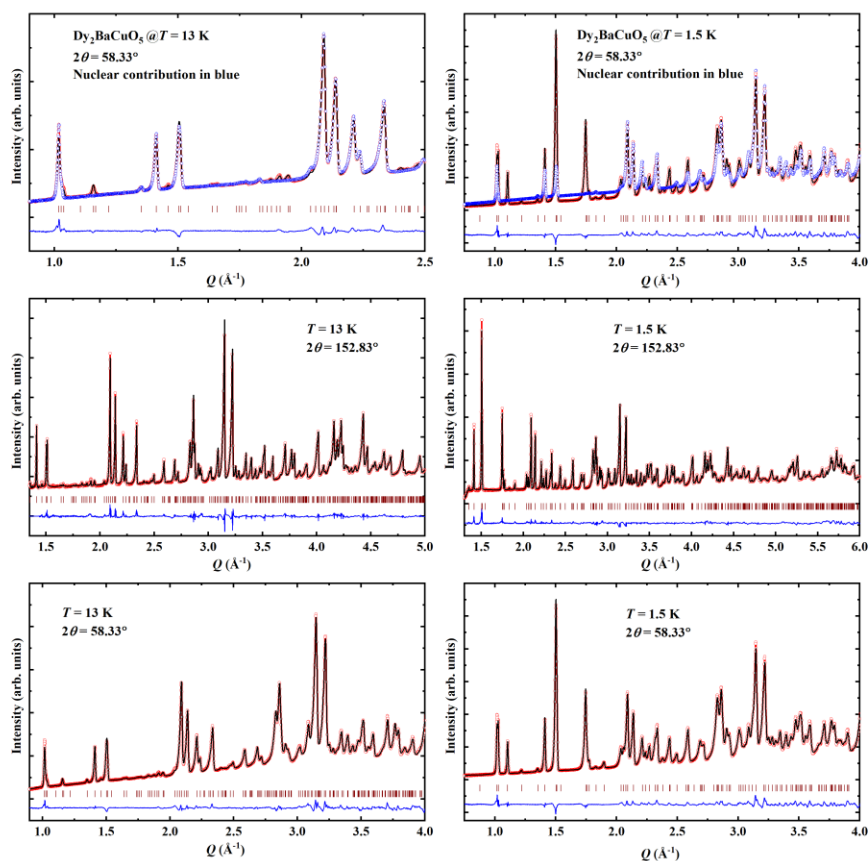


Figure 5.11 Refinement of the WISH data at 13 K and 1.5 K of $\text{Dy}_2\text{BaCuO}_5$ using the magnetic space groups $P112_1/n$ and $Pnm'a$, respectively. The nuclear contribution (25 K) is superimposed in blue. Rietveld refined neutron diffraction patterns at 13 K and 1.5 K for crystal and magnetic structures of $\text{Dy}_2\text{BaCuO}_5$. We have shown the data collected on two different banks of the WISH diffractometer. The tick marks include both the nuclear and magnetic contributions.

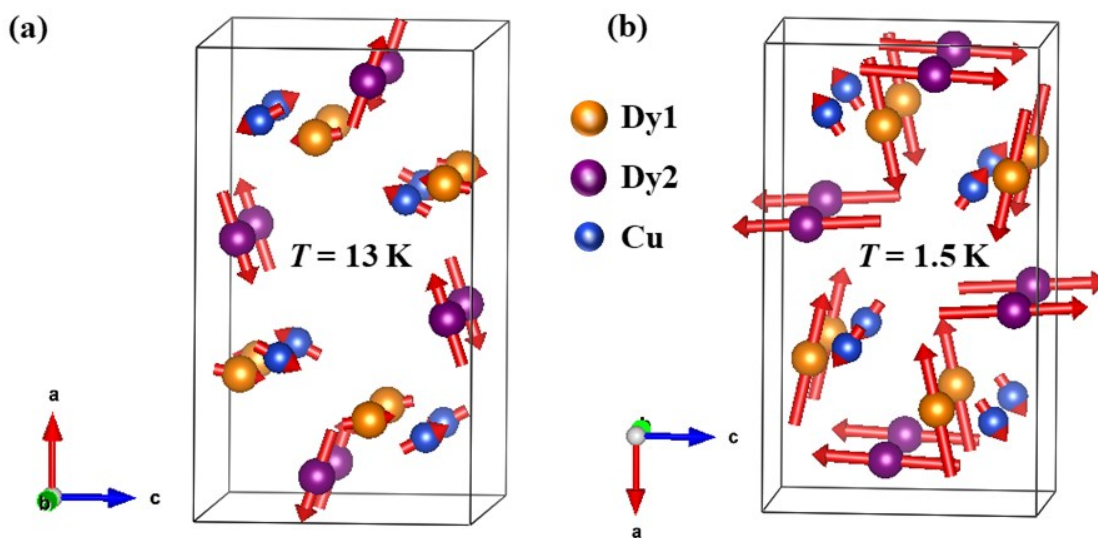


Figure 5.12 Representation of magnetic structure of $\text{Dy}_2\text{BaCuO}_5$ at (a) 13 K and (b) 1.5 K (Orange – Dy1, Purple – Dy2, and Blue – Cu). The magnetic moments of Dy1 and Cu atoms for 13 K and Cu for 1.5 K have been multiplied by 3 for display purposes.

Table 5.3-a Structural parameters obtained from the refinement of neutron data collected at 13 K by using the magnetic space group P_b112_1/n for $\text{Dy}_2\text{BaCuO}_5$.

Atom	x	y	z	$B_{\text{iso}} (\text{\AA}^2)$
Dy1	0.2889	0.1250	0.1172	0.047 (8)
Dy2	0.0743	0.1250	0.3968	0.047 (8)
Ba	0.9075	0.1250	0.9288	0.230 (5)
Cu	0.6600	0.1250	0.7115	0.790 (1)
O1	0.4332	0.9959	0.1686	0.490 (2)
O2	0.7282	0.4972	0.1448	0.490 (2)
O3	0.1005	0.1250	0.0837	0.490 (2)
Atom	$M_{\text{tot}} (\mu\text{B})$	$M_x (\mu\text{B})$	$M_y (\mu\text{B})$	$M_z (\mu\text{B})$
Dy1	0.104 (29)	0.104 (29)	0.000	0.000
Dy2	3.004 (54)	2.692 (24)	0.000	1.332 (49)
Cu	0.560 (72)	-0.419 (31)	0.000	0.372 (65)

Table 5.3-b Structural parameters obtained from the refinement of neutron data collected at 1.5 K by using the magnetic space group $Pnm'a$ for $\text{Dy}_2\text{BaCuO}_5$.

Atom	x	y	z	$B_{\text{iso}} (\text{\AA}^2)$
Dy1	0.2888 (1)	0.2500	0.1174 (2)	0.056 (13)
Dy2	0.0747 (1)	0.2500	0.3972 (1)	0.056 (13)
Ba	0.9085 (3)	0.2500	0.9273 (4)	0.324 (66)
Cu	0.6599 (2)	0.2500	0.7112 (3)	0.588 (45)
O1	0.4342 (2)	0.9902 (3)	0.1674 (2)	0.549 (24)
O2	0.2286 (1)	0.5054 (4)	0.3536 (3)	0.549 (24)
O3	0.1014 (2)	0.2500	0.0842 (4)	0.549 (24)
Atom	$M_{\text{tot}} (\mu\text{B})$	$M_x (\mu\text{B})$	$M_y (\mu\text{B})$	$M_z (\mu\text{B})$
Dy1	8.834 (20)	-8.622 (15)	0.000	-1.922 (13)
Dy2	9.686 (22)	-0.559 (15)	0.000	9.669 (16)
Cu	0.641 (22)	-0.528 (17)	0.000	-0.363 (22)

We have solved the ground state structure from the data (WISH) collected at 1.5 K (below $T < T_N^{\text{Dy}}$) with the $\mathbf{k} = (0, 0, 0)$. Eight possible solutions are possible, which corresponds to eight one-dimensional *irreps*. Out of which, the following four *irreps* $m\text{GM}_1^-$ ($Pn'm'a'$), $m\text{GM}_2^-$ ($Pnma'$), $m\text{GM}_3^-$ ($Pn'ma$), and $m\text{GM}_4^-$ ($Pnm'a$) allow the linear magnetoelectric effect. We have systematically tested all eight possible solutions, and the preferred solution is $Pnm'a$ which belongs to irrep $m\text{GM}_4^-$. The obtained pattern of

refinement and crystallographic parameters are shown in Figure 5.11 and Table 5.3(b), respectively. The corresponding magnetic structure is illustrated in Figure 5.12(b). In this structure, Cu moments lie in the **ac**-plane, whereas Dy1 and Dy2 moments are preferentially oriented along the **a**-axis and **c**-axis. Thus, there are small components of the magnetic moment along the **c**-axis for Dy1 and along the **a**-axis for Dy2. The moment projections with respect to temperature for all three magnetic cations, Dy1, Dy2, and Cu, are presented in Figure 5.13. At T_N^{Cu} , there is an induced moment in Dy sublattices which indicates the importance of exchange paths of type $\text{Cu}^{2+}\text{-O}^{2-}\text{-Dy}^{3+}\text{-O}^{2-}\text{-Cu}^{2+}$ and the strong $4f\text{-}3d$ coupling present in this compound. The deduced magnetic symmetry $mm'm$ which, breaks the inversion symmetry with respect to spin and allows the linear magnetoelectric effect.

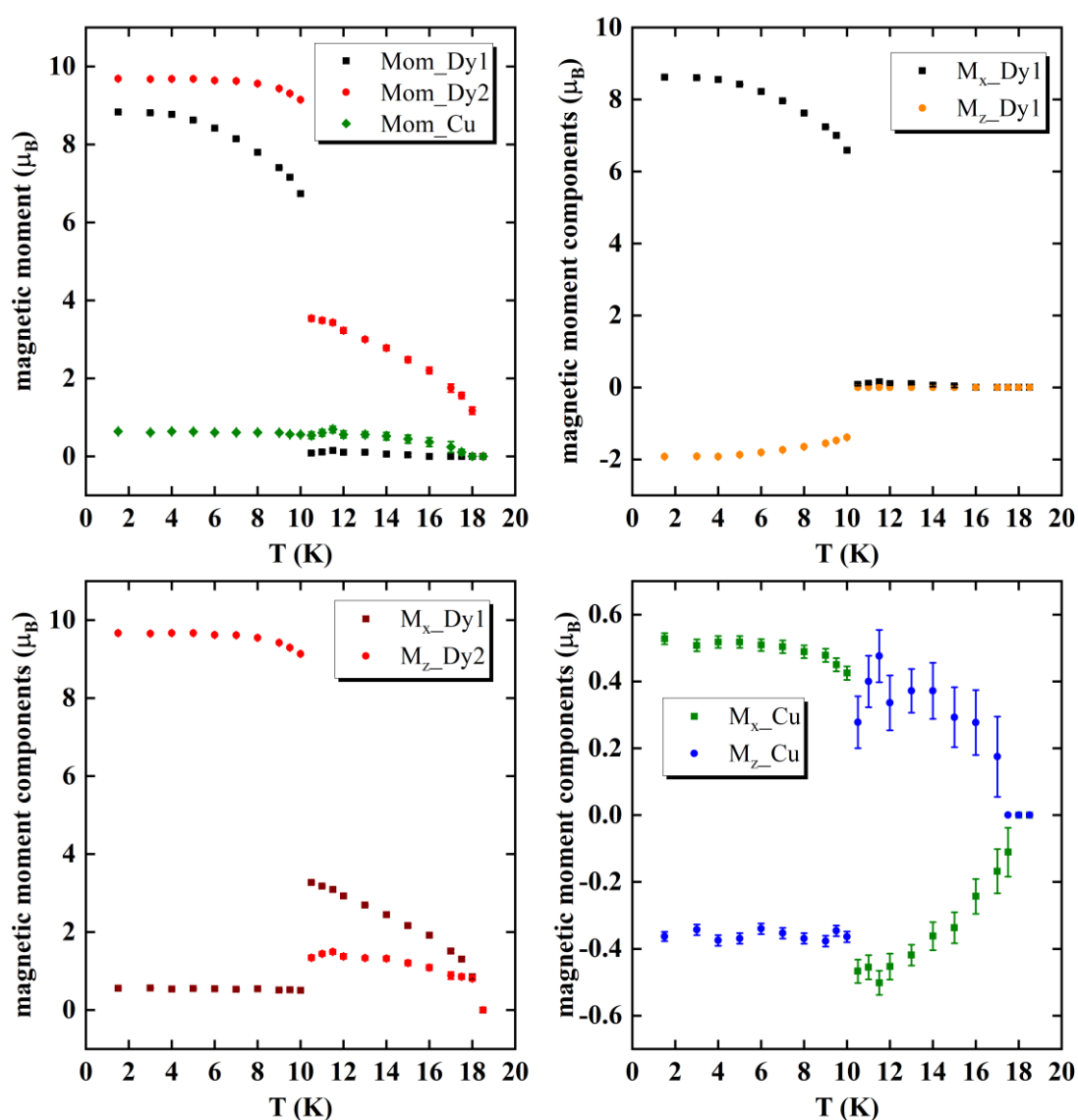


Figure 5.13 The ordered magnetic moments and their components for Dy1, Dy2, and Cu as a function of temperature for Dy₂BaCuO₅.

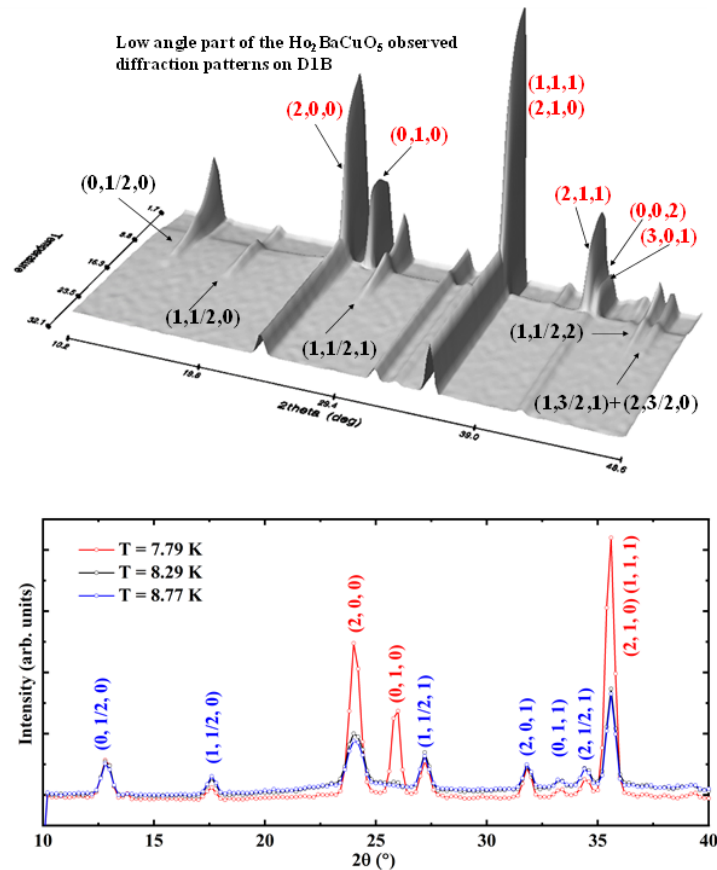


Figure 5.14 (Upper panel) 3D visualization of the low angle part of diffraction patterns taken on D1B ($\lambda = 2.52 \text{ \AA}$). The abrupt change of background and the simultaneous appearance of the $\mathbf{k}_{C2} = (0, 0, 0)$ magnetic peaks indicate a first-order magnetic transition. (Bottom panel) Details of the evolution of diffraction patterns of $\text{Ho}_2\text{BaCuO}_5$ around the transition at $T_N^{\text{Ho}} \approx 8 \text{ K}$. The indexing of peaks [blue for $\mathbf{k}_{C1} = (0, \frac{1}{2}, 0)$, and red for $\mathbf{k}_{C2} = (0, 0, 0)$] is given with respect to the paramagnetic unit cell.

5.3.5 Magnetic structure of $\text{Ho}_2\text{BaCuO}_5$

The magnetic phase transitions in $\text{Ho}_2\text{BaCuO}_5$ are similar to those of the $\text{Dy}_2\text{BaCuO}_5$ compound. However, the ground state of the Ho compound conserves the two propagation vectors $\mathbf{k}_{C1} = (0, \frac{1}{2}, 0)$ and $\mathbf{k}_{C2} = (0, 0, 0)$ as it is seen in the diffraction patterns (see the upper panel of Figure 5.14). The first transition, on cooling, takes place at $T_N^{\text{Cu}} = 17.5 \text{ K}$; similar to $\text{Dy}_2\text{BaCuO}_5$, the propagation vector is $\mathbf{k}_{C1} = (0, \frac{1}{2}, 0)$ and the magnetic space group is monoclinic P_b112_1/n which is allowed by the *irrep* $mY1(a, a)$. From the symmetry, it is evident that the point group $(2/m 1')$ impose a null magnetoelectric tensor, which is consistent with our electrical measurements. The refined diffraction patterns at 8.29 K (D1B) and 12 K (WISH) are given in Figure 5.15, and the results of these refinements are provided in Tables 5.4-a and 5.4-b. The magnetic structures obtained from the refinement at 12 K

(WISH) and 8.3 K (D1B), displaying only magnetic atoms, are depicted in Figure 5.15. The observed magnetic structure below Cu ordering is similar to that of $\text{Dy}_2\text{BaCuO}_5$.

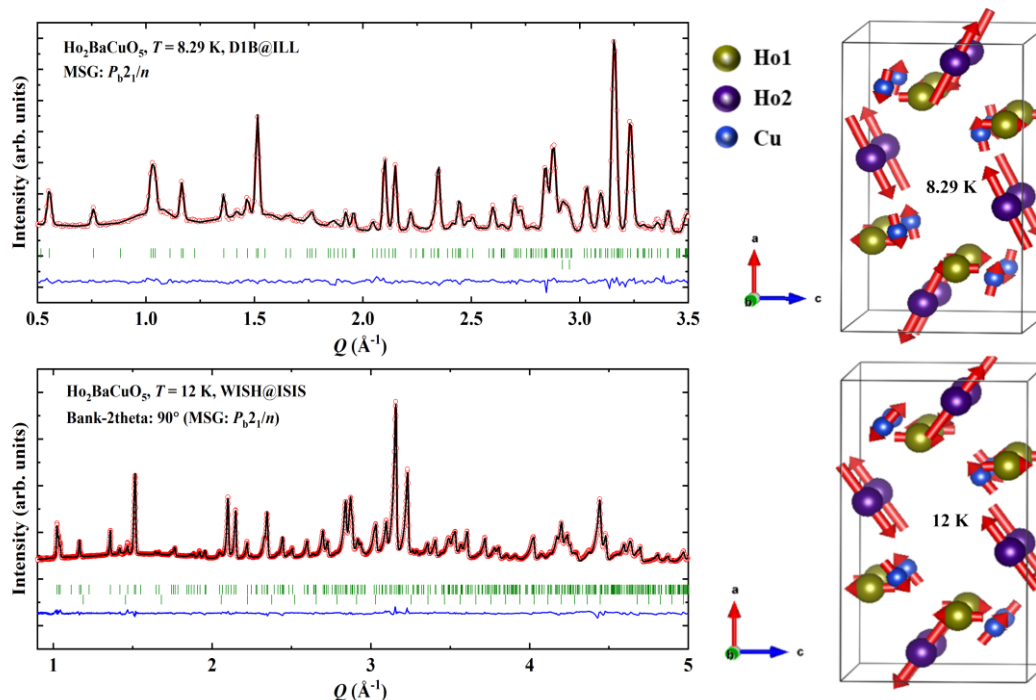


Figure 5.15 Left. Refinement of the crystal and magnetic structure of $\text{Ho}_2\text{BaCuO}_5$ at $T = 8.29$ K (D1B) and $T = 12$ K (WISH). We have used a single-phase described in the magnetic space group P_b112_1/n (standard setting P_a2_1/c) using symmetry modes and refining the amplitudes of the modes. The second-row tick marks in D1B data correspond to two small peaks coming from the cryostat vanadium screens, and the second phase in WISH data is an impurity of cubic Ho_2O_3 . Right. Representation of the magnetic structures of $\text{Ho}_2\text{BaCuO}_5$ at $T = 8.29$ K (D1B) and 12 K (WISH). The magnetic moments of Ho1 and Cu atoms are multiplied by 3 for display purposes.

Table 5.4-a Crystal structure parameters of $\text{Ho}_2\text{BaCuO}_5$ at 12 K, described in the Shubnikov group P_b112_1/n and using symmetry modes. The constraints of the paramagnetic group, $Pnma1'$, have been applied by refining only displacive amplitudes (with respect to the paramagnetic structure at 20 K) corresponding to the identical representation GM_1^+ . $a = 12.1663$ (6) Å, $b = 11.3106$ (6) Å, $c = 7.1137$ (4) Å, $\langle R\text{-Bragg} \rangle = 3.45$ %.

Atom	x	y	z	B_{iso} (Å ²)
Ho1_1	0.2878 (1)	0.1250	0.1159 (2)	0.490 (30)
Ho2_1	0.0743 (1)	0.1250	0.3957 (2)	0.490 (30)
Ba_1	0.9051 (2)	0.1250	0.9280 (3)	0.470 (60)
Cu_1	0.6604 (2)	0.1250	0.7115 (2)	1.070 (50)
O1_1	0.4326 (1)	0.9966 (1)	0.1668 (2)	1.030 (40)
O1_2	0.9326 (1)	0.2534 (1)	0.3332 (2)	1.030 (40)
O2_1	0.2277 (1)	0.7530 (2)	0.3560 (2)	1.080 (50)
O2_2	0.7277 (1)	0.4970 (2)	0.1440 (2)	1.080 (50)
O3_1	0.1012 (2)	0.1250	0.0817 (3)	1.160 (50)

Table 5.4-b Magnetic data extracted from the summary file of *FullProf* after refinement of four banks of WISH data at 12 K and D1B data at 8.29 K using magnetic symmetry modes.WISH: $\langle R\text{-magnetic} \rangle = 7.56\%$

Atom	M_{tot} (μB)	M_x (μB)	M_y (μB)	M_z (μB)
Ho1_1	0.493 (9)	0.020 (30)	0.000	0.492 (64)
Ho2_1	2.268 (10)	1.843 (67)	0.000	1.322 (61)
Cu_1	0.440 (6)	-0.335 (35)	0.000	0.284 (39)
Symmetry Modes		Amplitude	Sigma	
A1_mY1		0.000000	0.000000	
A2_mY1		0.020087	0.030303	
A3_mY1		0.492324	0.063647	
A4_mY1		0.000000	0.000000	
A5_mY1		1.842855	0.066926	
A6_mY1		1.321918	0.061218	
A7_mY1		0.000000	0.000000	
A8_mY1		-0.335422	0.034964	
A9_mY1		0.283906	0.039153	

D1B: $\langle R\text{-magnetic} \rangle = 11.56\%$

Atom	M_{tot} (μB)	M_x (μB)	M_y (μB)	M_z (μB)
Ho1_1	0.424 (30)	-0.011(59)	0.000	0.424 (213)
Ho2_1	3.219 (23)	2.891 (63)	0.000	1.417 (161)
Cu_1	0.641 (19)	-0.624 (59)	0.000	0.150 (134)
Symmetry Modes		Amplitude	Sigma	
A1_mY1		0.000000	0.000000	
A2_mY1		-0.010916	0.059066	
A3_mY1		0.423782	0.212654	
A4_mY1		0.000000	0.000000	
A5_mY1		2.888924	0.062531	
A6_mY1		1.415972	0.160938	
A7_mY1		0.000000	0.000000	
A8_mY1		-0.623342	0.059284	
A9_mY1		0.149515	0.133703	

Below $T_N^{\text{Ho}} = 8$ K, the magnetic structure possesses two propagation vectors, namely, $\mathbf{k}_{C1} = (0, \frac{1}{2}, 0)$ and $\mathbf{k}_{C2} = (0, 0, 0)$ as can be seen from the bottom panel of Figure 5.14. The magnetic structure can be analyzed in two ways; one way is to consider two magnetic phases corresponding to the two propagation vectors and another with a single magnetic phase which can be obtained by studying the isotropy subgroups associated with the mixture of irreps of the two propagation vectors. In general, the magnetic structure can be described as a Fourier series of the form:

$$\mathbf{m}_{jL} = \sum_{n=1}^{n=n_k} \mathbf{S}_{\mathbf{k}_n}^j e^{-2\pi i \mathbf{k}_n \mathbf{R}_L}$$

where \mathbf{m}_{jL} is the magnetic moment of atom j in the unit cell with the origin at \mathbf{R}_L , n_k is the number of \mathbf{k} -vectors, and $\mathbf{S}_{\mathbf{k}_n}^j$ is the Fourier component of atom j for the \mathbf{k} -vector \mathbf{k}_n in reference zero, $\mathbf{R}_L = (0, 0, 0)$ in the unit cell. In our case, the Fourier components are real vectors (magnetic moments), and the form adopted by the Fourier series is:

$$\mathbf{m}_{jL} = \mathbf{S}_{(0,0,0)}^j + \mathbf{S}_{(0,1/2,0)}^j e^{-\pi i L_y}$$

The L_y is integers obtained by the scalar product of the propagation vector \mathbf{k}_{C1} and the paramagnetic unit cell lattice vectors \mathbf{R}_L . The exponential factor is either 1 or -1, depending on if L_y is even or odd, respectively. The magnetic structure factor of a particular reflection indexed as $\mathbf{h} = \mathbf{H} + \mathbf{k}_n$ depends only on the Fourier coefficients $\mathbf{S}_{\mathbf{k}_n}^j$. So, there is no interference between the reflections corresponding to different propagation vectors. A refinement of the structure considering the two propagation vectors (two magnetic phases) independently and putting the symmetry constraints of the P_b112_1/n (\mathbf{k}_{C1}) and $Pnm'a$ (\mathbf{k}_{C2}) groups (essentially no component along the \mathbf{b} -axis for all atoms: $\mathbf{S}_{\mathbf{k}_n}^j = (m_{nx}^j, 0, m_{nz}^j)$, with $j = 1, 2, 3$ and $n = 1, 2$), give an excellent fit to the experimental data [see Figure 5.16(a)].

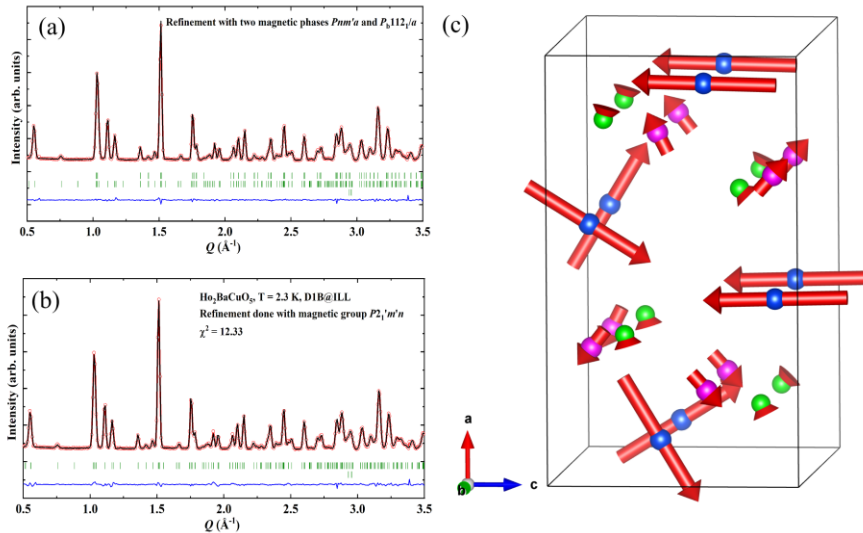


Figure 5.16 Left. (Upper panel) Refinement with two magnetic phases corresponding to two \mathbf{k} -vectors of D1B data at 2.3 K. The Fourier components verifying the symmetry of $Pnm'a$ $\{\mathbf{k} = (0, 0, 0)\}$ and P_b112_1/a $\{\mathbf{k} = (0, \frac{1}{2}, 0)\}$; $\chi^2 = 9.02$ and $R_{\text{mag}} = 1.88$. (Bottom panel) Refinement of D1B data at 2.3 K using the magnetic space group $P2_1'm'n$. Right. Scheme of the magnetic structure of $\text{Ho}_2\text{BaCuO}_5$ at $T = 2.3$ K using the orthorhombic space group $P2_1'm'n$; $\chi^2 = 12.3$ and $R_{\text{mag}} = 2.85$.

In a single magnetic phase model, two possibilities (type-3 orthorhombic and monoclinic magnetic groups) are close to explaining the experimental results. The orthorhombic group $P2'_1m'n$ (standard setting $Pm'n2'_1$, No. 31.125, $1D - \mathbf{k}_{C2}$ irreps: mGM_4^- , and $2D - \mathbf{k}_{C1}$ irreps: $mY_1: (a, 0)$) gives a relatively good refinement of D1B data at 2.3 K as shown in Figure 5.16(b). The corresponding magnetic structure is presented in Figure 5.16(c). The group allows a linear magnetoelectric effect with a magnetoelectric tensor like that of the group $Pnm'a$. However, the fit is worse than that of the two magnetic phases case, and then, it corresponds to a false minimum.

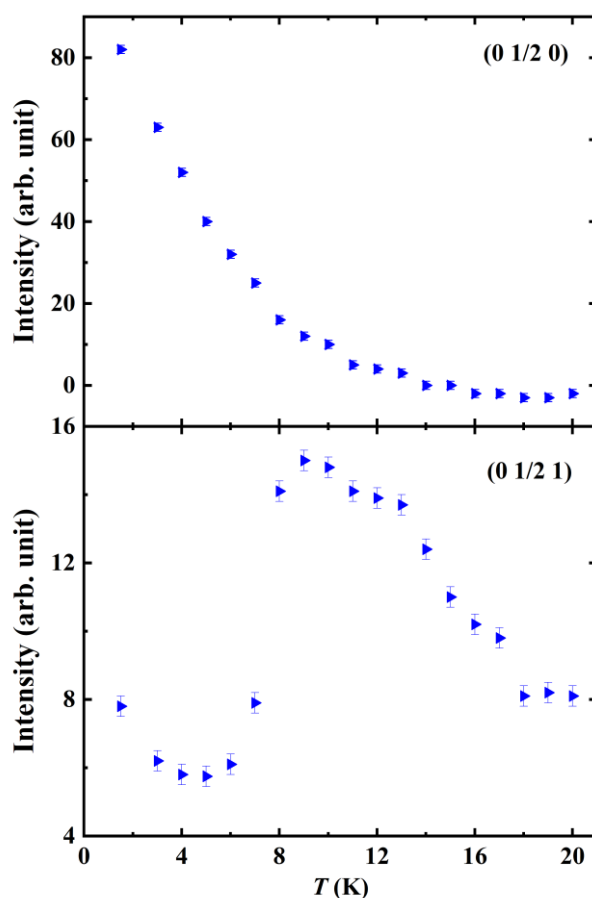


Figure 5.17 T -evolution of the Bragg reflections $(0 \frac{1}{2} 0)$ and $(0 \frac{1}{2} 1)$ of $\text{Ho}_2\text{BaCuO}_5$ obtained from WISH data.

Whereas the refinement with monoclinic magnetic group $P112'_1/a$, which we discuss later, gives an excellent fit comparable to that of two magnetic phases refinement and thus making it difficult to distinguish between these two solutions. However, the temperature evolution of $(0 \frac{1}{2} 0)$ and $(0 \frac{1}{2} 1)$ reflections (see Figure 5.17) suggests that the single magnetic phase with the monoclinic magnetic structure be the plausible model. The reflection $(0 \frac{1}{2} 0)$ behaves like an induced moment, and $(0 \frac{1}{2} 1)$ that relates primarily to Cu positions

clearly shows a jump at T_N^{Ho} . In phase coexistence (two magnetic phases), such a different behavior between reflections belonging to the same propagation vector is unlikely. Therefore, the coherent superposition of the modes (single magnetic phase) with monoclinic $P112'_1/a$ is the correct solution [24].

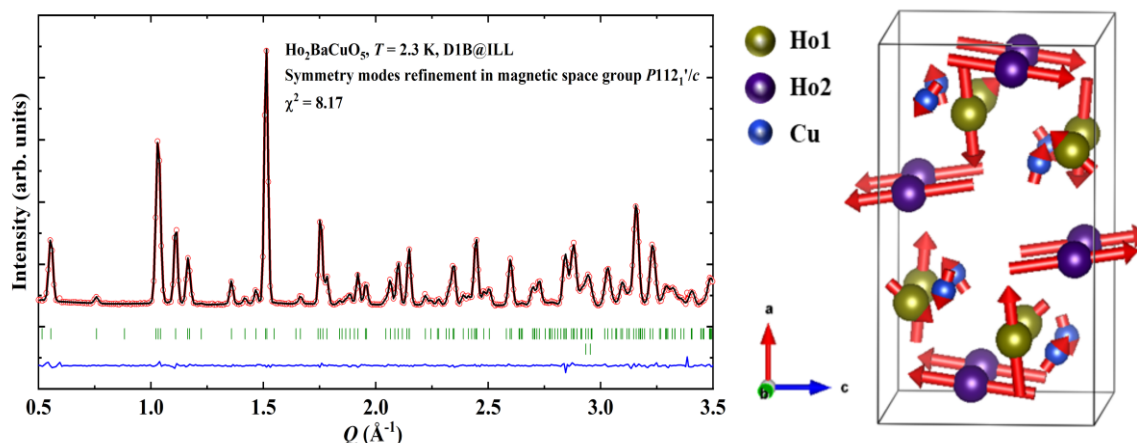


Figure 5.18 Left. Refinement (with single magnetic phase) of D1B data at 2.3 K using the magnetic space group $P112'_1/a$. The second-row tick marks correspond to two small peaks coming from the vanadium screens of the cryostat. Right. Representation of the magnetic structure at $T = 2.3$ K (D1B) for $\text{Ho}_2\text{BaCuO}_5$. The magnetic moments of Ho1_2 and Cu atoms have been multiplied by 3 for display purposes.

Table 5.5-a Crystal structure parameters of $\text{Ho}_2\text{BaCuO}_5$ at 1.5 K, described in the Shubnikov group $P112'_1/a$ and using symmetry modes. $a = 12.1613$ (6) Å, $b = 11.3081$ (5) Å, $c = 7.1130$ (3) Å, $\langle R\text{-Bragg} \rangle = 2.70$ %.

Atom	x	y	z	B_{iso} (Å ²)
Ho1_1	0.2869 (2)	0.12500	0.1168 (3)	0.57 (6)
Ho1_2	0.2869 (2)	0.62500	0.1168 (3)	0.57 (6)
Ho2_1	0.0746 (1)	0.12500	0.3963 (2)	0.95 (6)
Ho2_2	0.0746 (1)	0.62500	0.3963 (2)	0.95 (6)
Ba_1	0.6599 (2)	0.12500	0.7105 (4)	1.16 (7)
Ba_2	0.6599 (2)	0.62500	0.7105 (4)	1.16 (7)
Cu_1	0.9062 (4)	0.12500	0.9274 (5)	0.64 (9)
Cu_2	0.9062 (4)	0.62500	0.9274 (5)	0.64 (9)
O1_1	0.4334 (2)	0.9958 (3)	0.1663 (2)	1.23 (6)
O1_2	0.4334 (2)	0.4958 (3)	0.1663 (2)	1.23 (6)
O1_3	0.9334 (2)	0.2542 (3)	0.3337 (2)	1.23 (6)
O1_4	0.9334 (2)	0.7542 (3)	0.3337 (2)	1.23 (6)
O2_1	0.2274 (2)	0.7528 (3)	0.3556 (4)	1.29 (7)
O2_2	0.2274 (2)	0.2528 (3)	0.3556 (4)	1.29 (7)
O2_3	0.7274 (2)	0.4972 (3)	0.1444 (4)	1.29 (7)
O2_4	0.7274 (2)	0.9972 (3)	0.1444 (4)	1.29 (7)
O3_1	0.1020 (3)	0.1250	0.0815 (5)	1.21 (9)
O3_2	0.1020 (3)	0.6250	0.0815 (5)	1.21 (9)

Table 5.5-b Magnetic data extracted from the summary file of *FullProf* after refinement of D1B data at 2.3 K. $\langle R\text{-magnetic} \rangle = 1.73\%$

Atom	M_{tot} (μB)	M_x (μB)	M_y (μB)	M_z (μB)
Ho1_1	7.212 (22)	7.165 (121)	0.000	0.816 (141)
Ho1_2	3.858 (22)	-2.593 (121)	0.000	2.857 (141)
Ho2_1	8.522 (26)	1.052 (117)	0.000	-8.457 (168)
Ho2_2	8.401 (26)	1.170 (117)	0.000	-8.319 (168)
Cu_1	1.011 (20)	-0.772 (108)	0.000	0.653 (129)
Cu_2	0.707 (20)	0.687 (108)	0.000	0.167 (129)
Symmetry Modes	Amplitude	Sigma		
A1_mY1	0.000000	0.000000		
A2_mY1	4.874680	0.052245		
A3_mY1	-1.019091	0.131627		
A4_mY1	0.000000	0.000000		
A5_mY1	-0.059403	0.060102		
A6_mY1	-0.068837	0.143512		
A7_mY1	0.000000	0.000000		
A8_mY1	-0.728523	0.053872		
A9_mY1	0.242409	0.120353		
A10_mGM3-	0.000000	0.000000		
A11_mGM3-	0.000000	0.000000		
A12_mGM3-	0.000000	0.000000		
A13_mGM4-	2.284233	0.109372		
A14_mGM4-	1.833950	0.049805		
A15_mGM4-	1.109978	0.100385		
A16_mGM4-	-8.377424	0.086828		
A17_mGM4-	-0.042449	0.093628		
A18_mGM4-	0.409514	0.046660		

The monoclinic magnetic group $P112'_1/a$ (standard setting $P2'_1/c$, No. 14.77, $1D - k_{C2}$ *irreps*: mGM_4^- , and $2D - k_{C1}$ *irreps*: mY_1 : (a, a)) gives a splitting into two sites for each one of the initial three sites ($4c$) in the paramagnetic state. This splitting has been previously observed from spectroscopic studies [14]. The number of magnetic free parameters for this group is $3 \times (3 + 3) = 18$. Nullifying the \mathbf{b} -axis components (close to zero) of the magnetic moments corresponding to the secondary mGM_3^- *irrep* contribution, one obtains the 12 free parameters. We have performed a symmetry mode refinement in $P112'_1/a$ (primary order parameter constituted by the *irreps* mY_1 and mGM_4^-) as described in the literature using the most recent version of *FullProf* [25]. The results of the refinement are given in Figure 5.18 and Table 5.5, respectively. In Figure 5.19, we show the magnetic moments and their components, deduced from the values of the amplitudes of symmetry modes, as a function of

temperature, for the case in which we consider that there is no contribution to the mGM_3^- *irrep* (moment along \mathbf{b} are set to zero). Notice that the magnetic moment of Ho1, contrary to Ho2, in the region $T > 8$ K, is relatively small, this is because the molecular field at the Ho2 site (surrounded by 6 Cu^{2+} ions) is higher than that of the Ho1 site (surrounded by 3 Cu^{2+} ions) similar to $\text{Dy}_2\text{BaCuO}_5$. The scheme of the magnetic structure with all magnetic free parameters can be seen in Figure 5.18. The magnetic structure of $\text{Ho}_2\text{BaCuO}_5$ differs from that of $\text{Dy}_2\text{BaCuO}_5$ at low temperatures. The presence of the two propagation vectors in the former case and the strong reorientations of magnetic moments as a function of temperature makes $\text{Ho}_2\text{BaCuO}_5$ possess a relatively labile magnetic structure sensitive to magnetic and thermal perturbations. As in the case of Dy-compound, the magnetic moments of Ho2 sites experiment a drastic reorientation making the coupling along \mathbf{b} -axis ferromagnetic below T_N^R . The Ho1 site, which interacts weakly with the surrounding magnetic atoms, experiments with the more significant changes with temperature.

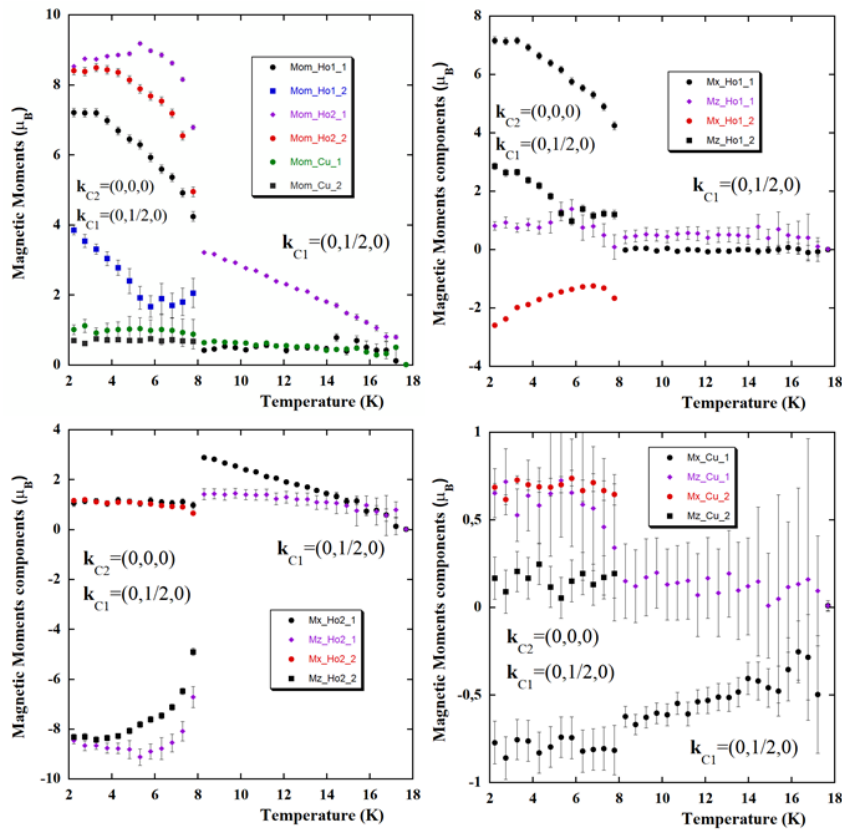


Figure 5.19 Magnetic moments and their components for atoms Ho1, Ho2, and Cu as a function of temperature for $\text{Ho}_2\text{BaCuO}_5$. The refinements have been performed with no contribution of mGM_3^- (no y-components). In the region of \mathbf{k}_{C1} ($T > 8$ K), there are single sites (Ho1_1, Ho2_1, and Cu_1), and in the region of two propagation vectors $\mathbf{k}_{C1} + \mathbf{k}_{C2}$ ($T < 8$ K), the sites of magnetic atoms split into two inequivalent positions (Ho1_1, Ho1_2, Ho2_1, Ho2_2, Cu_1, Cu_2).

The magnetic structures of $\text{Dy}_2\text{BaCuO}_5$ and $\text{Ho}_2\text{BaCuO}_5$ are unusual and complicated. The presence of two magnetic sublattices formed by Cu^{2+} and R^{3+} ions and two different sites for the R^{3+} ions are responsible for this behavior. At T_N^{Cu} , spin ordering occurs with $\mathbf{k} = (0, \frac{1}{2}, 0)$ under the influence of Cu-Cu exchange interaction through the path $\text{Cu}^{2+}-\text{O}^{2-}-\text{Dy}^{3+}-\text{O}^{2-}-\text{Cu}^{2+}$ in both compounds. The Dy and Ho magnetic moments become weakly polarized by Cu^{2+} moments below T_N^{Cu} . Upon lowering the temperature, independent ordering of Dy and Ho-spins occurs with different k-vectors as mentioned earlier. The $R1$ magnetic moments are pointing along the R -O bonds in both compounds due to a strong single-ion anisotropy together with isotropic and anisotropic exchanges [14]. However, theoretical calculations on crystal field splitting of R^{3+} ions and single-crystal study would help understand the role of anisotropy and the unusual magnetic structures of $R_2\text{BaCuO}_5$ ($R = \text{Dy}$ and Ho).

Finally, below T_N^{Cu} , the P_b112_1/n spin structure preserves the inversion center in both compounds and does not allow a magnetoelectric effect. Whereas below the T_N^R , the observed magnetic symmetry $Pnm'a$ (magnetic point group $mm'm$) for Dy and $P112'_1/a$ (magnetic point group $2'/m$) for Ho allow the linear magnetoelectric effect because the inversion center of the paramagnetic group $Pnma1'$ become now associated with time inversion ($-1'$), so the magnetic groups are noncentrosymmetric. The respective magnetoelectric tensors, in the standard setting, are given by [26]

$$\alpha = \begin{pmatrix} 0 & 0 & \alpha_{13} \\ 0 & 0 & 0 \\ \alpha_{31} & 0 & 0 \end{pmatrix} \text{ and } \begin{pmatrix} 0 & \alpha_{12} & 0 \\ \alpha_{21} & 0 & \alpha_{23} \\ 0 & \alpha_{32} & 0 \end{pmatrix}$$

The presence of nonzero off-diagonal magnetoelectric coefficients allows the magnetoelectric terms corresponding to $P \perp H$ [20]. The large value of polarization in the $E \perp H$ configuration confirms this fact. However, the nonzero polarization was observed in $E \parallel H$ due to the polycrystalline nature of the samples. The presence of R ions with high spin-orbit interaction can introduce strong spin-lattice coupling in both compounds. Therefore, the observed magnetoelectric effect can be significantly large for these compounds. Also, the magnetic Cu^{2+} and R^{3+} ions are located at the noncentrosymmetric sites, and their spins predominantly lie in the \mathbf{ac} -plane as confirmed by the neutron diffraction. This implies that local electric dipole moments exist for all the magnetic ions lying in the \mathbf{ac} -plane. Thus, magnetic symmetries in both cases allow the single-ion contributions to the magnetoelectric effect with large polarization due to rare-earth ions [16,17]. However, it requires theoretical work to understand the microscopic mechanism of the magnetoelectric effect.

In these compounds, there are no direct Cu-Cu, Cu-O-Cu, or Cu-O-O-Cu bonds. So, the possible magnetic exchange path is Cu-O-*R*-O-Cu. Due to this, rare-earth Cu interaction (*4f-3d* coupling) plays a crucial role in green phase compounds. However, *R* ion magnetic anisotropy, crystal field effects, and strength of *4f-3d* interaction decide the ordering of *R* ion along with the Cu spins. In the green phase compounds, only Gd orders along with Cu since there are no crystal field effects due to the ground S-state term of Gd ion. From our neutron diffraction measurements, it was clear that the Dy and Ho spin partially polarized by Cu-moments below T_N^{Cu} . The spin structure changes upon Dy and Ho ordering due to strong rare-earth and Cu interaction and allows the linear magnetoelectric effect. Also, the absence of *R*-ion magnetic ordering in isostructural compounds $R_2\text{BaZnO}_5$ suggests the importance of the magnetic exchange path (Cu-O-*R*-O-Cu) in the green phase family [27]. Moreover, this behavior is different in $\text{Sm}_2\text{BaCuO}_5$ and $\text{Gd}_2\text{BaCuO}_5$, where linear magnetoelectric effect and multiferroicity are observed at Cu ordering temperature as we have seen in previous Chapters [17,18]. Therefore, we believe that the *4f-3d* interaction plays a pivotal role in determining the magnetic structure and the associated magnetoelectric coupling in this family of compounds.

Under applied magnetic fields, both compounds exhibit field-induced metamagnetic transitions below T_N^R . Due to the remarkable magnetic anisotropy, applied magnetic fields can change the *R*-sublattices spin structure and affect the Cu-spin structure due to strong *4f-3d* interaction, resulting in metamagnetic transitions. The resulting new spin states should be associated with nonlinear electric polarization with a magnetic field indicating the ferroelectric nature at high magnetic fields ($H > 1.2$ T). At fields (~ 7 T), though the polarization decreased, there is a finite ferroelectric polarization. This allows the magnetization (polarization) control by using an electric field (magnetic field), which is essential for the applications. Neutron diffraction and single-crystal studies are required for a better understanding of the magnetoelectric coupling in these compounds.

5.4 Conclusion

In conclusion, we have systematically investigated the linear magnetoelectric effect and field-induced ferromagnetism and ferroelectricity in the well-known green phase compounds $R_2\text{BaCuO}_5$ ($R = \text{Dy}$, and Ho). Both exhibit long-range antiferromagnetic ordering of Cu^{2+} ($T_N^{\text{Cu}} = 18.5$ K and $T_N^{\text{Cu}} = 17.5$ K) and R^{3+} ions ($T_N^{\text{Dy}} = 10.7$ K and $T_N^{\text{Ho}} = 8$ K) for Dy

and Ho compounds, respectively. The applied magnetic field induces electric polarization at T_N^R , which varies linearly up to a critical field of ~ 1.2 T confirming the linear magnetoelectric effect. The observed linear magnetoelectric effect is consistent with the magnetic symmetry. Under applied magnetic fields > 1.2 T, they show field-induced metamagnetic transitions with a large magnetization and ferroelectric polarization. The $4f$ - $3d$ interaction plays a vital role in governing the magnetic structure and associated magnetoelectric properties.

References

- [1] T. Kimura, T. Goto, H. Shintani, K. Ishizaka, T. Arima, and Y. Tokura, *Nature* **426**, 55 (2003).
- [2] N. Hur, S. Park, P. A. Sharma, J. S. Ahn, S. Guha, and S. W. Cheong, *Nature* **429**, 392 (2004).
- [3] Y. Tokunaga, S. Iguchi, T. Arima, and Y. Tokura, *Phys. Rev. Lett.* **101**, 097205 (2008).
- [4] Y. Tokunaga, N. Furukawa, H. Sakai, Y. Taguchi, T. Arima, and Y. Tokura, *Nat. Mater.* **8**, 558 (2009).
- [5] X. Shen, L. Zhou, Y. Chai, Y. Wu, Z. Liu, Y. Yin, H. Cao, C. Dela Cruz, Y. Sun, C. Jin, A. Muñoz, J. A. Alonso, and Y. Long, *NPG Asia Mater.* **11**, 50 (2019).
- [6] M. Fiebig, *J. Phys. D. Appl. Phys.* **38**, R123 (2005).
- [7] P. Yanda and A. Sundaresan, in *Adv. Chem. Phys. Mater. Overv. Sel. Top.* (World Scientific, 2020), pp. 224–248.
- [8] R. Z. Levitin, B. V Mill, V. V. Moshchalkov, N. A. Samarin, V. V. Snegirev, and J. Zoubkova, *J. Magn. Magn. Mater.* **90**, 536 (1990).
- [9] R. Z. Levitin, B. V. Mill, V. V. Moshchalkov, N. A. Samarin, V. V. Snegirev, and Y. Zoubkova, *Solid State Commun.* **73**, 443 (1990).
- [10] V. V Moshchalkov, N. A. Samarin, I. O. Grishchenko, B. V Mill, and Z. J., *Solid State Commun.* **78**, 879 (1991).
- [11] M. N. Popova and G. G. Chepurko, *Sov. J. Exp. Theor. Phys. Lett.* **52**, 562 (1990).
- [12] I. V Paukov, M. N. Popova, and B. V Mill, *Phys. Lett. A* **169**, 301 (1992).
- [13] R. Burriel, M. Castro, C. Piqué, A. Salinas-Sánchez, and R. Sáez-Puche, *J. Magn. Magn. Mater.* **104**, 627 (1992).
- [14] M. Baran, H. Szymczak, S. A. Klimin, M. N. Popova, and R. Z. Levitin, *J. Exp. Theor. Phys.* **84**, 175 (1997).
- [15] I. V. Golosovsky, V. P. Plakhtii, V. P. Kharchenkov, J. Zoubkova, B. V. Mill, M. Bonnet, and E. Roudeau, *Fiz. Tve. Tela.* **34**, 1483 (1992).
- [16] V. P. Sakhnenko and N. V Ter-Oganessian, *J. Phys. Condens. Matter* **24**, 266002 (2012).
- [17] P. Yanda, N. V Ter-Oganessian, and A. Sundaresan, *Phys. Rev. B* **100**, 104417 (2019).
- [18] P. Yanda, I. V Golosovsky, I. Mirebeau, N. V Ter-Oganessian, J. Rodríguez-Carvajal, and A. Sundaresan, *Phys. Rev. Res.* **2**, 023271 (2020).
- [19] L. C. Chapon, P. Manuel, P. G. Radaelli, C. Benson, L. Perrott, S. Ansell, N. J. Rhodes, D. Raspino, D. Duxbury, and E. Spill, *Neutron News* **22**, 22 (2011).
- [20] S. Shtrikman and D. Treves, *Phys. Rev.* **130**, 986 (1963).
- [21] J. Rodriguez-Carvajal, in *Satell. Meet. Powder Diffr. XV Congr. IUCr* (Toulouse,

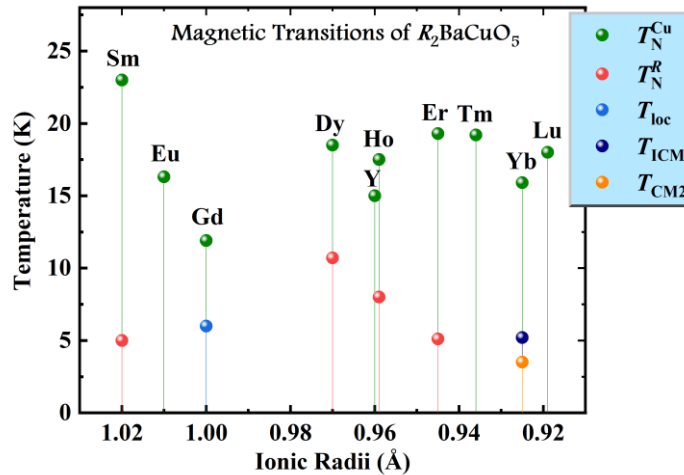
- France:[sn], 1990).
- [22] H. T. Stokes, D. M. Hatch, B. J. Campbell, and D. E. Tanner, *J. Appl. Crystallogr.* **39**, 607 (2006).
 - [23] J. González-Platas, N. A. Katcho, and J. Rodríguez-Carvajal, *J. Appl. Crystallogr.* (2021).
 - [24] J. Rodríguez-Carvajal and F. Bourée, *EPJ Web Conf.* **22**, (2012).
 - [25] S. Ghara, E. Suard, F. Fauth, T. T. Tran, P. S. Halasyamani, A. Iyo, J. Rodríguez-Carvajal, and A. Sundaresan, *Phys. Rev. B* **95**, 224416 (2017).
 - [26] R. E. Newnham, *Properties of Materials: Anisotropy, Symmetry, Structure* (Oxford University Press on Demand, 2005).
 - [27] G. F. Goya, R. C. Mercader, M. T. Causa, and M. Tovar, *J. Phys. Condens. Matter* **8**, 8607 (1996).

Chapter 6

Role of $4f$ - $3d$ coupling on magnetic and multiferroic properties of $R_2\text{BaCuO}_5$ ($R = \text{Er}, \text{Eu}, \text{Y}, \text{Tm}, \text{Yb}, \text{and Lu}$)*

Summary

We present the systematic investigation of magnetic and multiferroic properties of green phase compounds $R_2\text{BaCuO}_5$ ($R = \text{Er}, \text{Eu}, \text{Y}, \text{Tm}, \text{Yb}, \text{and Lu}$) by DC magnetization, specific heat, dielectric, pyrocurrent, and neutron diffraction measurements. All the compounds exhibit antiferromagnetic ordering of Cu^{2+} ions in the range $T_N^{\text{Cu}} = 15$ -20 K. The magnetic Er^{3+} ions order antiferromagnetically at $T_N^{\text{Er}} = 5.1$ K. Surprisingly, we did not observe the independent ordering of magnetic Tm^{3+} and Yb^{3+} ions. Isothermal magnetization curves of $\text{Er}_2\text{BaCuO}_5$ confirm the metamagnetic transition at a critical field of $H_c = 0.9$ T. Further, it shows the field-induced pyrocurrent anomalies above metamagnetic transition and near T_N^{Er} indicating the strong magnetoelectric coupling. At high magnetic fields ~ 7 T, Er compound exhibits ferromagnetism with a large magnetization value of $9 \mu_B/\text{f.u.}$ We did not observe the magnetoelectric coupling in $R_2\text{BaCuO}_5$ ($R = \text{Eu}, \text{Y}, \text{Tm}, \text{and Lu}$). The absence of this coupling is consistent with the magnetic symmetry obtained from the neutron diffraction. Moreover, $\text{Yb}_2\text{BaCuO}_5$ exhibits commensurate to incommensurate to commensurate magnetic phase transitions along with the multiferroic properties. Our results demonstrate that $4f$ - $3d$ coupling determines the ground state magnetic structure and hence, the magnetoelectric and multiferroic properties of the green phase compounds.



*Manuscript based on this work is under preparation

6.1 Introduction

The magnetic properties of $R_2\text{BaCuO}_5$ ($R = \text{Eu}, \text{Er-Lu}, \text{Y}$) compounds are well studied by different techniques such as magnetic measurements, specific heat, Young's modulus, spectral studies, and neutron diffraction experiments [1–10]. For example, all these compounds exhibit antiferromagnetic ordering of Cu^{2+} spins in the range of 15-20 K. $\text{Er}_2\text{BaCuO}_5$ evidence the metamagnetic transition at low temperatures associated with the Er^{3+} moments [2]. Interestingly, the magnetic rare-earth ions Tm^{3+} and Yb^{3+} ions did not order down to 0.5 K but there is an induced moment at these sites due to Cu- R interaction [8,11,12]. Moreover, it has been shown from spectral studies that $\text{Yb}_2\text{BaCuO}_5$ exhibits spin reorientation at 5.5 K and the origin of this is not known [8].

In earlier chapters, some of this family of compounds were shown to exhibit strong magnetoelectric coupling, mainly due to the interplay of $4f$ - $3d$ coupling. For example, $\text{Sm}_2\text{BaCuO}_5$ exhibit a linear magnetoelectric effect below the Cu^{2+} spins ordering temperature $T_N^{\text{Cu}} = 23$ K [13]. This coupling is further affected by the Sm^{3+} spins ordering at $T_N^{\text{Sm}} = 5$ K. Interestingly, isostructural compound $\text{Gd}_2\text{BaCuO}_5$ shown to exhibit multiferroic properties below $T_N = 11.9$ K where Cu^{2+} and Gd^{3+} spins order simultaneously [14]. Further, this compound shows lock-in phase transition from incommensurate to commensurate with additional polarization at $T_{\text{loc}} = 6$ K [14,15]. Neutron diffraction study reveals the elliptical cycloidal magnetic structure with magnetic symmetry $P2mm1'$ below T_N , which is responsible for the multiferroicity. Further, $\text{Dy}_2\text{BaCuO}_5$ and $\text{Ho}_2\text{BaCuO}_5$ compounds evidence the linear magnetoelectric effect and field-induced multiferroicity. In this sense, it will be fascinating to study the other family members, including nonmagnetic R ions, to understand the role of $4f$ - $3d$ coupling on magnetoelectric properties in more detail.

This chapter presents the magnetic and magnetoelectric properties of centrosymmetric $R_2\text{BaCuO}_5$ with $R = \text{Er}, \text{Eu}, \text{Y}, \text{Tm}, \text{Yb},$ and Lu . All these compounds develop antiferromagnetic ordering of Cu^{2+} ions in the range $T_N^{\text{Cu}} \sim 15$ -20 K. Surprisingly, magnetic Tm^{3+} and Yb^{3+} ions did not order down to 2 K. Er^{3+} ions in $\text{Er}_2\text{BaCuO}_5$ undergo magnetic ordering at $T_N^{\text{Er}} = 5.1$ K and a metamagnetic transition is observed above the critical field of $H_c \sim 0.9$ T. Above H_c , we observed field-induced electric polarization around $T_N^{\text{Er}} = 5.1$ K indicating coupling between magnetic and electric orders. Whereas $R_2\text{BaCuO}_5$ ($R = \text{Eu}, \text{Y}, \text{Tm},$ and Lu) did not show magnetoelectric properties. Neutron diffraction measurements on Y_2BaCuO_5 and $\text{Lu}_2\text{BaCuO}_5$ reveal the collinear magnetic structure (P_a2_1/c) with propagation

vector $(0, \frac{1}{2}, \frac{1}{2})$, which is centrosymmetric and does not allow the magnetoelectric coupling. $\text{Er}_2\text{BaCuO}_5$ exhibit noncollinear magnetic order (P_b2_1/n) with \mathbf{k} -vector $(0, \frac{1}{2}, 0)$. Whereas $\text{Yb}_2\text{BaCuO}_5$ shows commensurate $(0, \frac{1}{2}, 0)$ to incommensurate $(0, \frac{1}{2}, g)$ to a commensurate $(0, \frac{1}{2}, \frac{1}{2})$ magnetic transitions. This compound exhibits strong magnetodielectric coupling below incommensurate ordering, indicating the presence of multiferroicity.

6.2 Experimental section

Polycrystalline samples of $R_2\text{BaCuO}_5$ ($R = \text{Er, Eu, Y, Tm, Yb, and Lu}$) were made under the conventional solid-state route. Stoichiometric amounts of $R_2\text{O}_3$, BaCO_3 , and CuO were mixed homogeneously and heated at 950°C for 12 hrs. Our attempts to make $\text{Tb}_2\text{BaCuO}_5$ are not successful due to the formation of the stable phase BaTbO_3 . Phase purity was checked by using a PANalytical Empyrean X-ray diffractometer with monochromatic $\text{Cu K}\alpha 1$ radiation. Neutron diffraction experiments were carried on the D1B diffractometer at ILL with wavelength 2.52 \AA . Diffuse reflectance spectra of powder samples were recorded using a Perkin–Elmer Lambda 900 spectrometer. Background correction was performed by subtracting pre-recorded reflectance spectra of a BaSO_4 disc from the compound spectra. Crystal, magnetic structure analysis, and physical property measurements were performed as mentioned in previous chapters.

6.3 Results and discussion

6.3.1 Crystal structure and UV-Vis spectra

The Rietveld refined X-ray diffraction data and the obtained structural parameters for $R_2\text{BaCuO}_5$ ($R = \text{Er, Eu, Y, Tm, Yb, and Lu}$) at room temperature are shown in Figure 6.1 and Tables 6.1-6.6. The titled compounds crystallize in orthorhombic structure with space group (S.G) $Pnma$, as reported earlier [16,17]. This structure is centrosymmetric and does not allow the ferroelectric properties. Figure 6.2 shows the variation of lattice parameters of all the green phase compounds with R ion ionic radii. Going from Sm to Lu, the ionic radii decrease (Lanthanide Contraction), and the lattice parameters also decrease. As mentioned in previous chapters, R ions have two non-equivalent sites ($R1$ and $R2$) with the same site symmetry ($mm2$) with seven coordination in this structure. The $R1\text{O}_7$ and $R2\text{O}_7$ capped prisms connected by common trigonal face into $R1R2\text{O}_{11}$ units, which share edges to form a three-dimensional network. The Cu^{2+} ions are in unusual oxygen square pyramids. These pyramids are isolated

from each other so that there are no direct Cu-O-Cu bonds. The $R1$ ion is connected to three copper ions through oxygen with bond angles close to 90° . Whereas $R2$ ion surrounded by six copper ions through oxygen and five out six bonds are close 180° . Thus, copper molecular field at both R sites is different and making the compound highly anisotropic. Figure 6.3 shows the UV-Vis spectra of all the compounds which are collected in reflectance mode. All these compounds give a strong reflectance peak in the green range of 519-542 nm, which belongs to the strong $d-d$ transition of the CuO_5 square pyramid. Therefore, these samples are green in color and thus, called “green phases”. The maxima decrease to the lower wavelength side as going from Sm to Lu. The corresponding bandgap ranges from 2.2–2.4 eV, which is semiconducting.

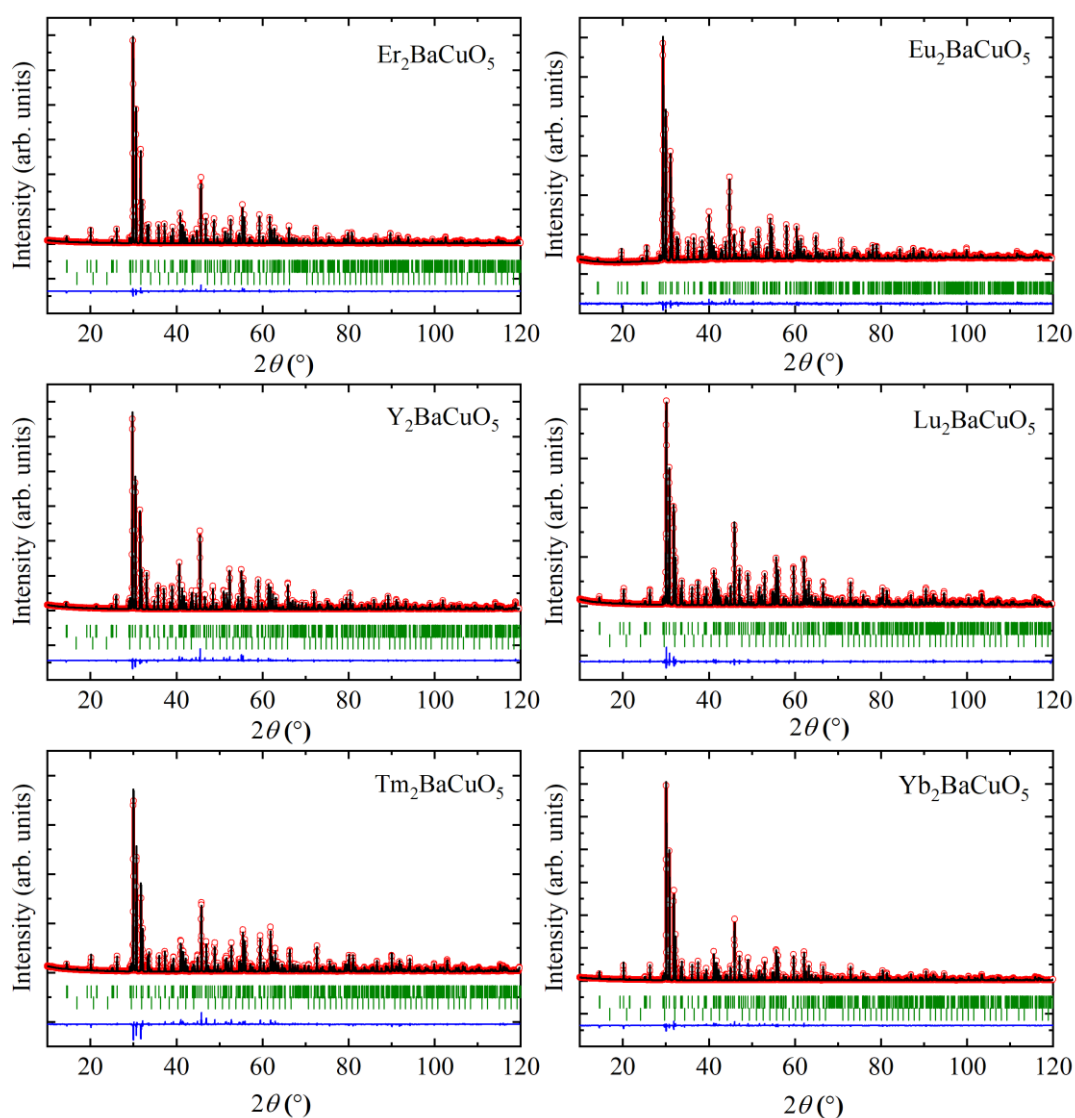


Figure 6.1 Rietveld refined X-ray diffraction patterns at room temperature for $R_2\text{BaCuO}_5$ ($R = \text{Er, Eu, Y, Lu, Tm, and Yb}$).

Table 6.1 Structural parameters of Er₂BaCuO₅ obtained from Rietveld refinement of X-ray data collected at room temperature. S.G: *Pnma*; $a = 12.1411$ (1) Å, $b = 5.6456$ (1) Å, $c = 7.1069$ (1) Å, $V = 487.133$ (5) Å³; global- $\chi^2 = 5.55$, Bragg R -factor = 3.79 (%), R_F -factor = 2.30 (%).

Atom	Site	x	y	z	B_{iso} (Å ²)
Er1	4c	0.2884 (1)	0.2500	0.1167 (2)	0.146 (31)
Er2	4c	0.0740 (1)	0.2500	0.3963 (2)	0.177 (31)
Ba	4c	0.9046 (1)	0.2500	0.9296 (2)	0.291 (32)
Cu	4c	0.6588 (3)	0.2500	0.7122 (5)	0.126 (72)
O1	8d	0.4333 (10)	-0.0108 (19)	0.1719 (14)	1
O2	8d	0.2277 (9)	0.5060 (20)	0.3562 (17)	1
O3	4c	0.0972 (13)	0.2500	0.0769 (21)	1

Table 6.2 Structural parameters of Eu₂BaCuO₅ obtained from Rietveld refinement of X-ray data collected at room temperature. S.G: *Pnma*; $a = 12.3717$ (2) Å, $b = 5.7449$ (1) Å, $c = 7.2485$ (1) Å, $V = 515.48$ (2) Å³; global- $\chi^2 = 1.73$; Bragg R -factor = 6.05 (%), R_F -factor = 6.03 (%).

Atom	Site	x	y	z	B_{iso} (Å ²)
Eu1	4c	0.2888 (2)	0.2500	0.1150 (4)	0.462 (61)
Eu2	4c	0.0738 (2)	0.2500	0.3948 (3)	0.696 (60)
Ba	4c	0.9061 (2)	0.2500	0.9305 (3)	0.588 (60)
Cu	4c	0.6592 (5)	0.2500	0.7134 (8)	0.110 (131)
O1	8d	0.4358 (16)	-0.0148 (30)	0.1770 (19)	1
O2	8d	0.2257 (13)	0.5080 (33)	0.3496 (27)	1
O3	4c	0.0927 (21)	0.2500	0.0704 (32)	1

Table 6.3 Structural parameters of Y₂BaCuO₅ obtained from Rietveld refinement of X-ray data collected at room temperature. S.G: *Pnma*; $a = 12.1947$ (1) Å, $b = 5.6663$ (1) Å, $c = 7.1413$ (1) Å, $V = 439.449$ (9) Å³; global- $\chi^2 = 5.04$, Bragg R -factor = 5.30 (%), R_F -factor = 3.08 (%).

Atom	Site	x	y	z	B_{iso} (Å ²)
Y1	4c	0.2884 (2)	0.2500	0.1167 (3)	0.141 (46)
Y2	4c	0.0738 (2)	0.2500	0.3959 (3)	0.235 (44)
Ba	4c	0.9048 (1)	0.2500	0.9301 (2)	0.411 (31)
Cu	4c	0.6589 (3)	0.2500	0.7131 (5)	0.305 (78)
O1	8d	0.4353 (10)	-0.0062 (23)	0.1650 (15)	1
O2	8d	0.2259 (10)	0.5023 (23)	0.3577 (18)	1
O3	4c	0.0981 (14)	0.2500	0.0811 (23)	1

Table 6.4 Structural parameters of $\text{Lu}_2\text{BaCuO}_5$ obtained from Rietveld refinement of X-ray data collected at room temperature. S.G: $Pnma$; $a = 12.0684$ (2) Å, $b = 5.6169$ (1) Å, $c = 7.0586$ (10) Å, $V = 478.48$ (1) Å³; global- $\chi^2 = 6.39$, Bragg R -factor = 5.93 (%), R_f -factor = 3.30 (%).

Atom	Site	x	y	z	B_{iso} (Å ²)
Lu1	4c	0.2884 (2)	0.2500	0.1179 (4)	0.346 (56)
Lu2	4c	0.0740 (2)	0.2500	0.3974 (4)	0.486 (56)
Ba	4c	0.9046 (2)	0.2500	0.9283 (4)	0.390 (67)
Cu	4c	0.6598 (6)	0.2500	0.7122 (10)	0.135 (143)
O1	8d	0.4368 (22)	-0.0148 (39)	0.1740 (29)	1
O2	8d	0.2283 (19)	0.5068 (40)	0.3570 (35)	1
O3	4c	0.0939 (28)	0.2500	0.0751 (44)	1

Table 6.5 Structural parameters of $\text{Tm}_2\text{BaCuO}_5$ obtained from Rietveld refinement of X-ray data collected at room temperature. S.G: $Pnma$; $a = 12.1090$ (2) Å, $b = 5.6320$ (1) Å, $c = 7.0838$ (1) Å, $V = 483.102$ (2) Å³; global- $\chi^2 = 6.33$, Bragg R -factor = 7.63 (%), R_f -factor = 3.44 (%).

Atom	Site	x	y	z	B_{iso} (Å ²)
Tm1	4c	0.2885 (2)	0.2500	0.1174 (4)	0.028 (58)
Tm2	4c	0.0741 (2)	0.2500	0.3969 (4)	0.191 (60)
Ba	4c	0.9044 (3)	0.2500	0.9293 (5)	0.281 (65)
Cu	4c	0.6590 (7)	0.2500	0.7136 (11)	0.171 (155)
O1	8d	0.4351 (24)	-0.0102 (44)	0.1682 (33)	1
O2	8d	0.2260 (22)	0.4990 (47)	0.3555 (39)	1
O3	4c	0.0955 (31)	0.2500	0.0779 (50)	1

Table 6.6 Structural parameters of $\text{Yb}_2\text{BaCuO}_5$ obtained from Rietveld refinement of X-ray data collected at room temperature. S.G: $Pnma$; $a = 12.0657$ (1) Å, $b = 5.6156$ (1) Å, $c = 7.0572$ (1) Å, $V = 478.167$ (6) Å³; global- $\chi^2 = 8.0$, Bragg R -factor = 4.12 (%), R_f -factor = 2.33 (%).

Atom	Site	x	y	z	B_{iso} (Å ²)
Yb1	4c	0.2884 (2)	0.2500	0.1179 (3)	0.132 (44)
Yb2	4c	0.0741 (2)	0.2500	0.3971 (3)	0.195 (42)
Ba	4c	0.9044 (2)	0.2500	0.9283 (3)	0.298 (50)
Cu	4c	0.6593 (4)	0.2500	0.7122 (7)	0.120 (112)
O1	8d	0.4335 (16)	-0.0131 (29)	0.1752 (21)	1
O2	8d	0.2286 (14)	0.5075 (30)	0.3592 (25)	1
O3	4c	0.0950 (20)	0.2500	0.0750 (33)	1

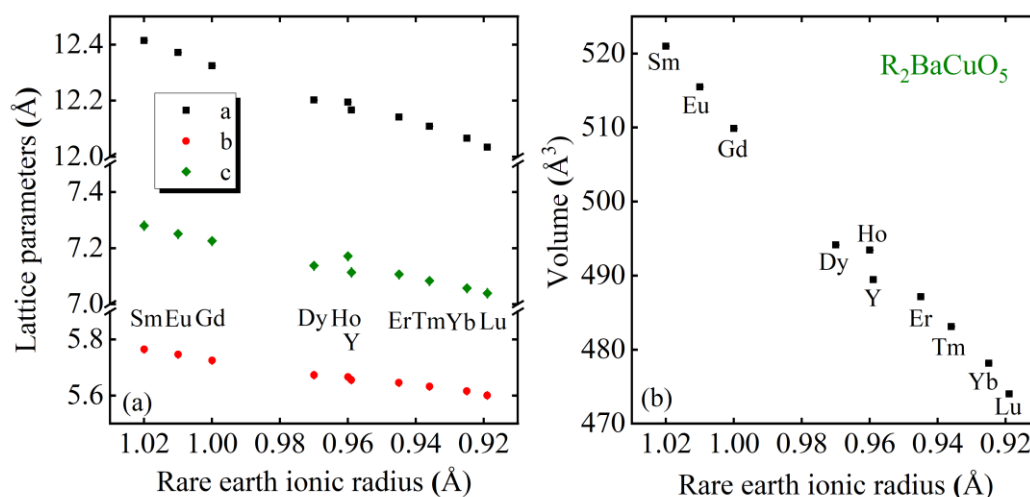


Figure 6.2 (a) Lattice parameters and (b) volume with respect to rare-earth ionic radius.

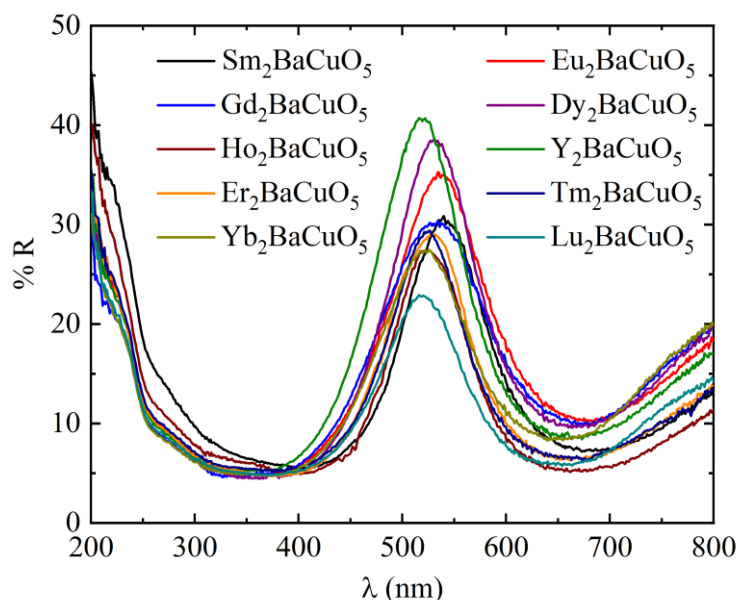


Figure 6.3 UV-Vis spectra of $R_2\text{BaCuO}_5$ ($R = \text{Sm–Lu}$, and Y) were measured in the range of 200–800 nm in the reflectance mode.

6.3.2 Field-induced ferroelectricity in $\text{Er}_2\text{BaCuO}_5$

6.3.2.1 Magnetic properties

DC magnetization and specific measurements on $\text{Er}_2\text{BaCuO}_5$ are shown in Figure 6.4. From Figure 6.4(a), the magnetic susceptibility shows an anomaly around 5.1 K which can be due to the independent ordering of Er^{3+} ions. However, we did not observe any anomaly for Cu^{2+} ordering, which can be due to the high paramagnetic moment of Er^{3+} . The effective magnetic moment obtained from the Curie-Weiss fit to inverse susceptibility data in the high-temperature region [Figure 6.4(b)] is $13.97 \mu_B/\text{f.u.}$ which agrees with the spin-only value 13.66

$\mu_B/\text{f.u.}$ for both Er^{3+} and Cu^{2+} ions. The negative sign of the Curie-Weiss temperature $\theta_{\text{CW}} = -7.35$ K indicates the dominant antiferromagnetic interactions. As the magnetic field increases, the magnetic anomaly became broad and suppressed, suggesting the possible change in magnetic structure. Moreover, isothermal magnetization curves are shown in Figure 6.4(c) reveals the metamagnetic transition at a critical field $H_c = 0.9$ T and below T_N^{Er} . Below H_c , curves are linear as expected for the antiferromagnetic ordering. The metamagnetic transition can be a first-order transition from antiferromagnetic to ferromagnetic. At high magnetic fields ~ 7 T, this compound exhibit ferromagnetic behavior with large magnetization with a value $\sim 9 \mu_B/\text{f.u.}$ which is close to saturation. Further, the long-range magnetic ordering is confirmed by specific heat measurements shown in Figure 6.4(d). As seen from the figure, it exhibits an antiferromagnetic arrangement of Cu^{2+} spins at $T_N^{\text{Cu}} = 19.3$ K and Er^{3+} moments at $T_N^{\text{Er}} = 5.1$ K. The Schottky type anomaly is observed at T_N^{Er} . However, under applied magnetic fields, the spin structure below T_N^{Cu} looks insensitive to the field, but the structure below T_N^{Er} shows significant change.

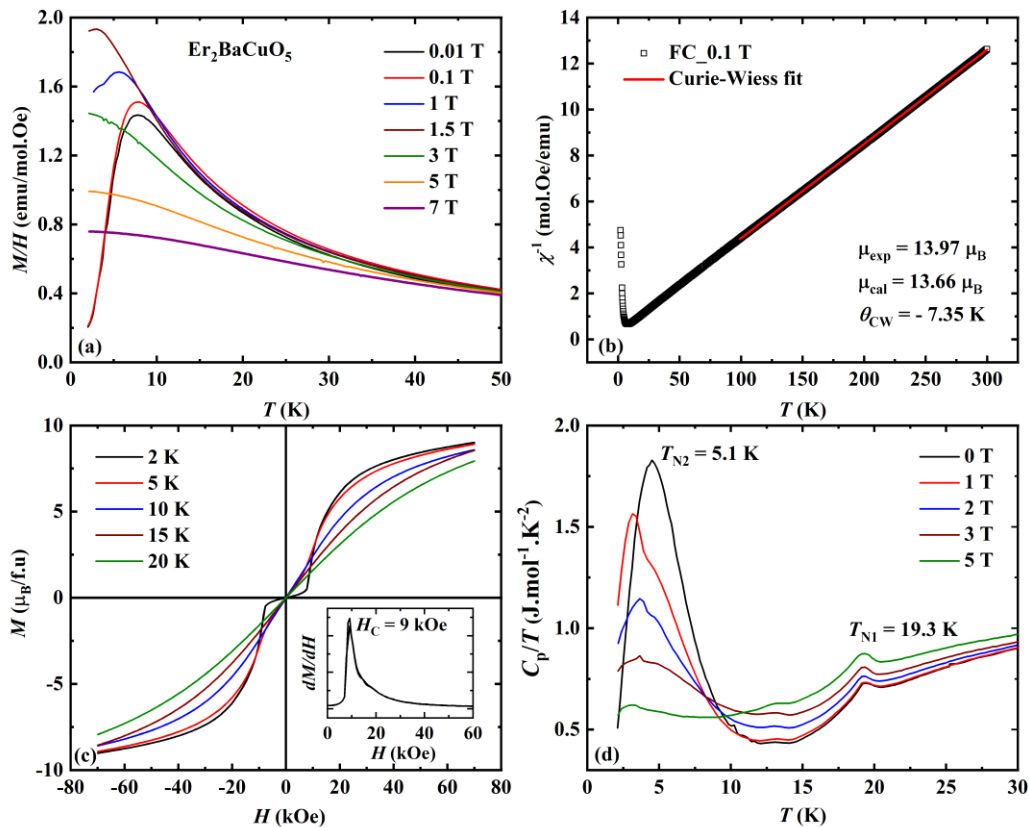


Figure 6.4 (a) Temperature-dependent magnetization of measured under different magnetic fields in field cooled sequence. (b) Inverse susceptibility data for magnetic field 0.1 T along with Curie-Weiss fitting. (c) Isothermal magnetization curves are recorded at different temperatures. Inset shows the dM/dH curve at 2 K. (d) Specific heat data measured at various magnetic fields; for $\text{Er}_2\text{BaCuO}_5$.

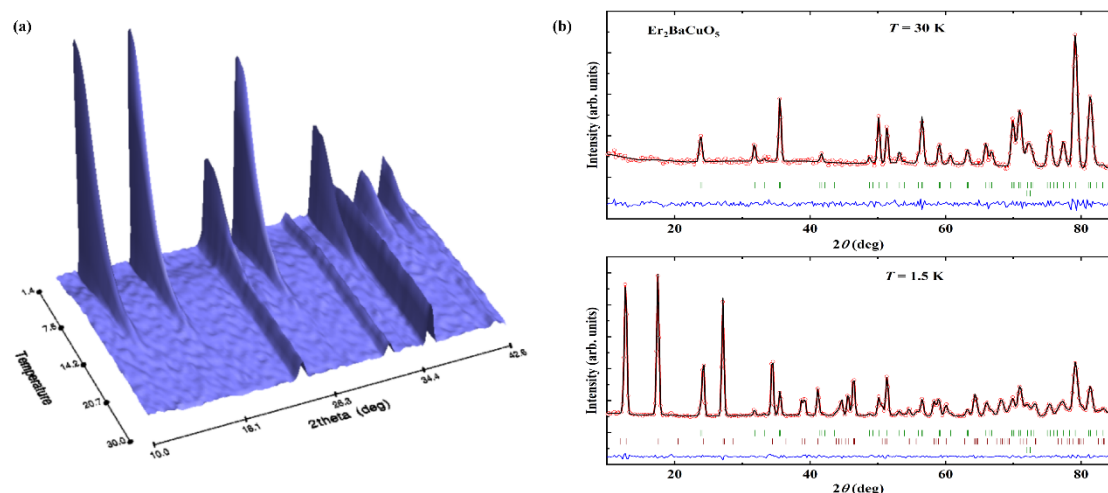


Figure 6.5 (a) Temperature evolution of neutron diffraction data for $\text{Er}_2\text{BaCuO}_5$. (b) Rietveld refined neutron diffraction data at 30 K and 1.5 K. The data at 1.5 K is solved with magnetic space group P_b2_1/n .

6.3.2.2 Neutron diffraction

To know the ground state magnetic structure, we have carried the neutron diffraction measurements on polycrystalline samples of $\text{Er}_2\text{BaCuO}_5$. As can be seen from Figure 6.5(a), the temperature evolution of neutron diffraction data evidence the new magnetic reflections below T_N^{Cu} . We have found that the \mathbf{k} -vector is $(0, \frac{1}{2}, 0)$ below T_N^{Cu} and this is stable down to 1.5 K. The observed \mathbf{k} -vector is same as that of the high-temperature phase of $\text{Dy}_2\text{BaCuO}_5$ and $\text{Ho}_2\text{BaCuO}_5$. We have used ISODISTORT to find out the possible magnetic solutions. There are two irreps, namely mY1 and mY2, which give the six possible magnetic solutions for the \mathbf{k} -vector $(0, \frac{1}{2}, 0)$ and the paramagnetic space group $Pnma1'$. We have tried each solution to fit our experimental data and found that P_b2_1/n is the correct solution obtained for the irrep mY1(a, a). The refinement patterns are shown in Figure 6.5(b). The corresponding magnetic structure at 1.5 K is shown in Figure 6.6(a), and the structure is strongly noncollinear. Figures 6.6(b-d) show the temperature evolution of magnetic moments of all three ions and their magnetic moment components, respectively. It is clear from Figure 6.6(b) that the Er moments in the range $T_N^{\text{Er}} \leq T \leq T_N^{\text{Cu}}$ behave like an induced moment by Cu spins. Below T_N^{Er} , the Er moment saturated where Er^{3+} moments order independently. In contrast to Dy and Ho compounds, the \mathbf{k} -vector is stable down 1.5 K indicates the role of single-ion rare-earth anisotropy and $4f$ - $3d$ coupling in deciding the magnetic ground state. The observed magnetic symmetry $2/m$ is centrosymmetric and induces the null magnetoelectric tensor.

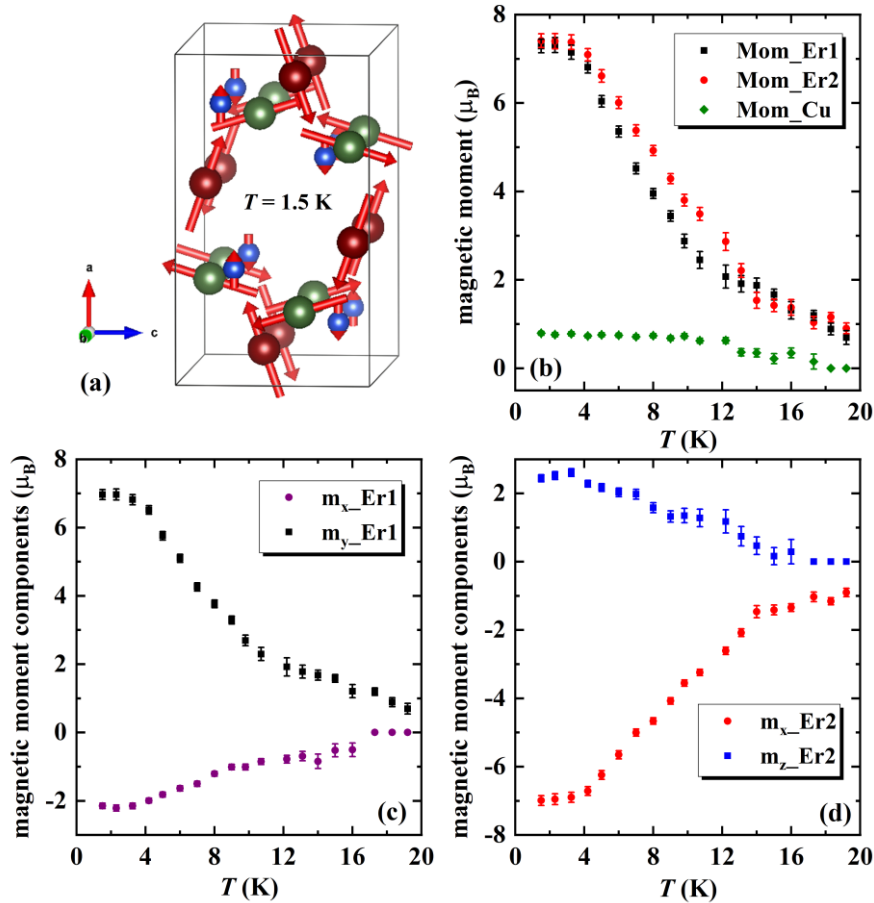


Figure 6.6 (a) Magnetic structure of $\text{Er}_2\text{BaCuO}_5$ at 1.5 K. Er1 (Green), Er2 (Wine), and Cu (Blue). (b) Temperature evolution of magnetic moments of Er1, Er2, and Cu. (c & d) Magnetic moment components behavior with the temperature of the Er1 and Er2 atoms.

6.3.2.3 Electrical properties

We have carried dielectric and pyrocurrent measurements to check the possibility of magnetodielectric effect or multiferroicity. The obtained dielectric measurements results are displayed in Figure 6.7(a). We did not observe any dielectric anomaly at both Cu and Er ordering temperatures. Interestingly, we have observed dielectric anomaly near to T_N^{Er} under applied magnetic fields above $H_c > 0.9$ T. This compound exhibits a magnetodielectric effect of 0.12 % at 2 K and 9 T, as seen from Figure 6.7(b). The isothermal magnetodielectric curves show anomalies as that of magnetic data indicating the metamagnetic transitions. We have carried the pyrocurrent measurements to check whether the field-induced dielectric anomaly is associated with magnetoelectric or not. Temperature and magnetic field variation of pyrocurrent data is shown in Figure 6.7(c). In accordance with the neutron diffraction, we did not observe the polarization at 0 T. Interestingly, this compound exhibits a pyrocurrent anomaly at T_N^{Er} above 0.9 T. Upon further increasing the magnetic field, we have observed pyrocurrent

anomalies at different temperatures around T_N^{Er} . These anomalies are suppressed at high magnetic fields. The corresponding polarization is shown in Figure 6.7(d). The appearance of electric polarization above $H_c \sim 0.9$ T indicates polar state and change of magnetic structures. The maximum polarization of $4.7 \mu\text{C}/\text{m}^2$ is observed at 1.25 T and 2 K. Under magnetic field, the appearance of pyrocurrent anomalies at different temperatures reveal that this compound may undergo different magnetic phase transitions with different magnetic symmetries. These magnetic symmetries, in turn, allows magnetoelectric coupling. These results demonstrate that $\text{Er}_2\text{BaCuO}_5$ shows magnetic field-induced ferroelectric properties. Further, the DC bias measurements confirmed the intrinsic nature of ferroelectricity, which is shown in the inset of Figure 6.7(d). To understand the possible mechanism responsible for the field-induced magnetoelectric coupling, one must perform the neutron diffraction under magnetic fields.

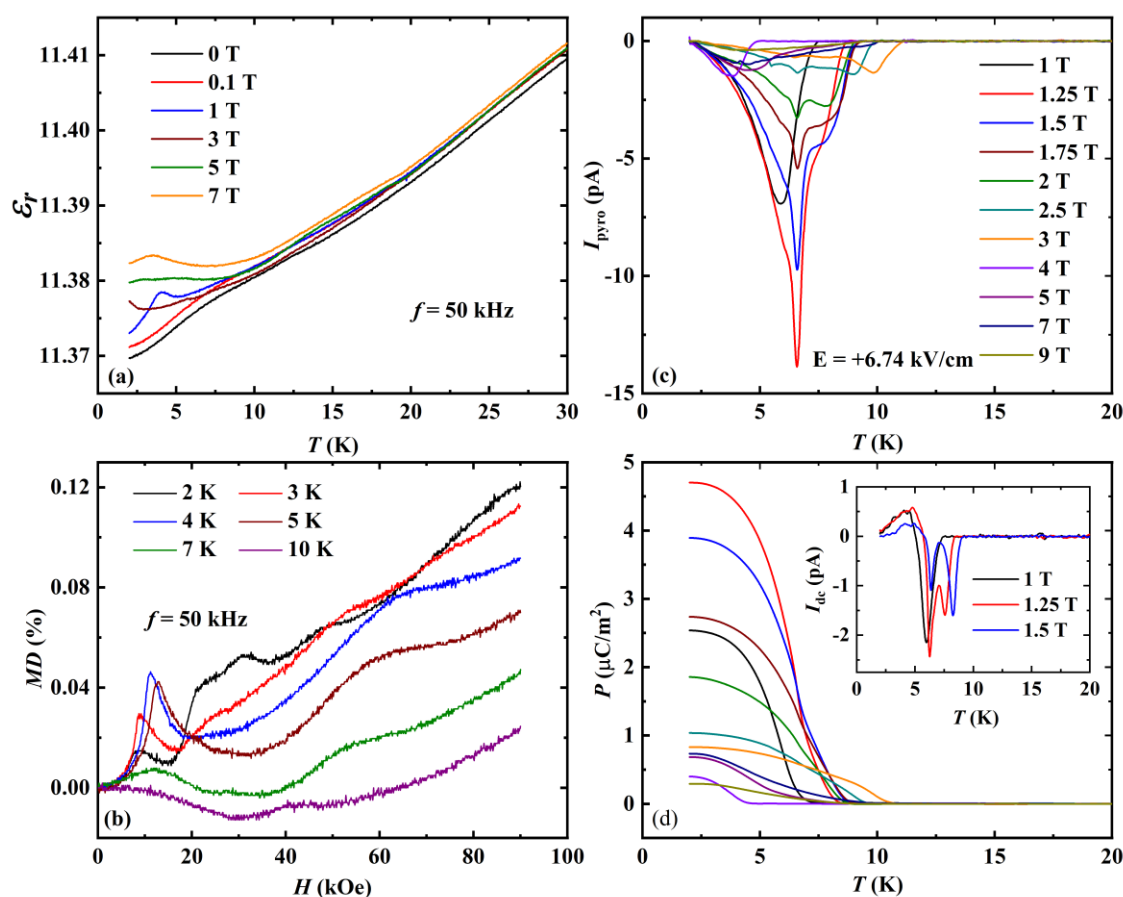


Figure 6.7 (a) Dielectric constant variation with temperature measured under different magnetic fields and frequency $f = 50$ kHz. (b) Isothermal magnetodielectric curves [$MD = \frac{\varepsilon(H) - \varepsilon(0)}{\varepsilon(0)}$ in %] at different temperatures. (c) Temperature-dependent pyrocurrent recorded under different magnetic fields with the poling electric field of $E_{\text{pol}} = 6.74$ kV/cm. (d) The corresponding electric polarization. Inset shows the DC bias measurement under a magnetic field of 1, 1.25, and 1.5 T; for $\text{Er}_2\text{BaCuO}_5$.

6.3.3 Absence of magnetoelectric coupling in $R_2\text{BaCuO}_5$ ($R = \text{Eu}, \text{Y}, \text{Lu},$ and Tm)

As we learned, green phase compounds with each R ion exhibit a wide variety of magnetic properties. This is mainly because the single-ion anisotropy associated with each rare earth and its interaction with crystal fields are different. Therefore, the interaction between R and Cu plays a crucial role in deciding the magnetic ground state. In view of this, it will be interesting to study the magnetic properties of $R_2\text{BaCuO}_5$ compounds where R is nonmagnetic to understand the role of $4f-3d$ coupling on magnetoelectric properties. In this section, we will present the results of $R_2\text{BaCuO}_5$ ($R = \text{Eu}, \text{Y}, \text{Lu}$) along with $\text{Tm}_2\text{BaCuO}_5$ where Tm is magnetic.

6.3.3.1 $\text{Eu}_2\text{BaCuO}_5$

$\text{Eu}_2\text{BaCuO}_5$ exhibits a broad anomaly around 25 K in magnetization data, as shown in Figure 6.8(a). Specific heat data [see Figure 6.8(b)] shows a sharp λ -type anomaly at $T_N^{\text{Cu}} = 16.3$ K revealing the long-range magnetic ordering. Therefore, this compound exhibits an antiferromagnetic arrangement of Cu^{2+} moments at $T_N^{\text{Cu}} = 16.3$ K. The isothermal magnetization curves show linear behavior indicating the antiferromagnetic coupling. The broad anomaly in magnetization data is possibly associated with the low dimensional correlations between the Cu spins. This might be present in previously shown green phase compounds, but it is not apparent due to the high paramagnetic moment of the R ion. However, this compound does not exhibit magnetoelectric coupling.

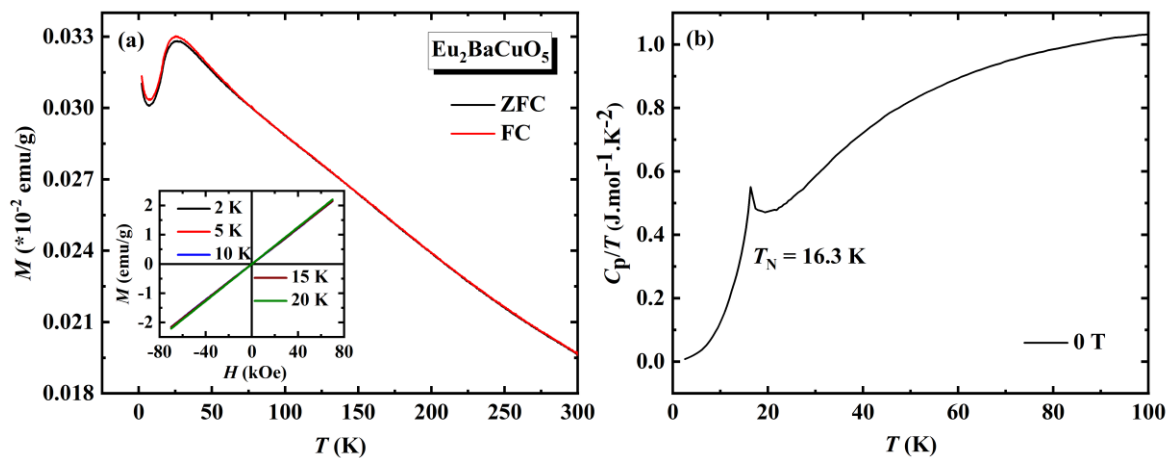


Figure 6.8 (a) DC magnetization measured under 0.01 T in zero field-cooled (ZFC) and field-cooled (FC). Inset shows the M vs H curves. (b) Specific heat data is collected at 0 T: for $\text{Eu}_2\text{BaCuO}_5$.

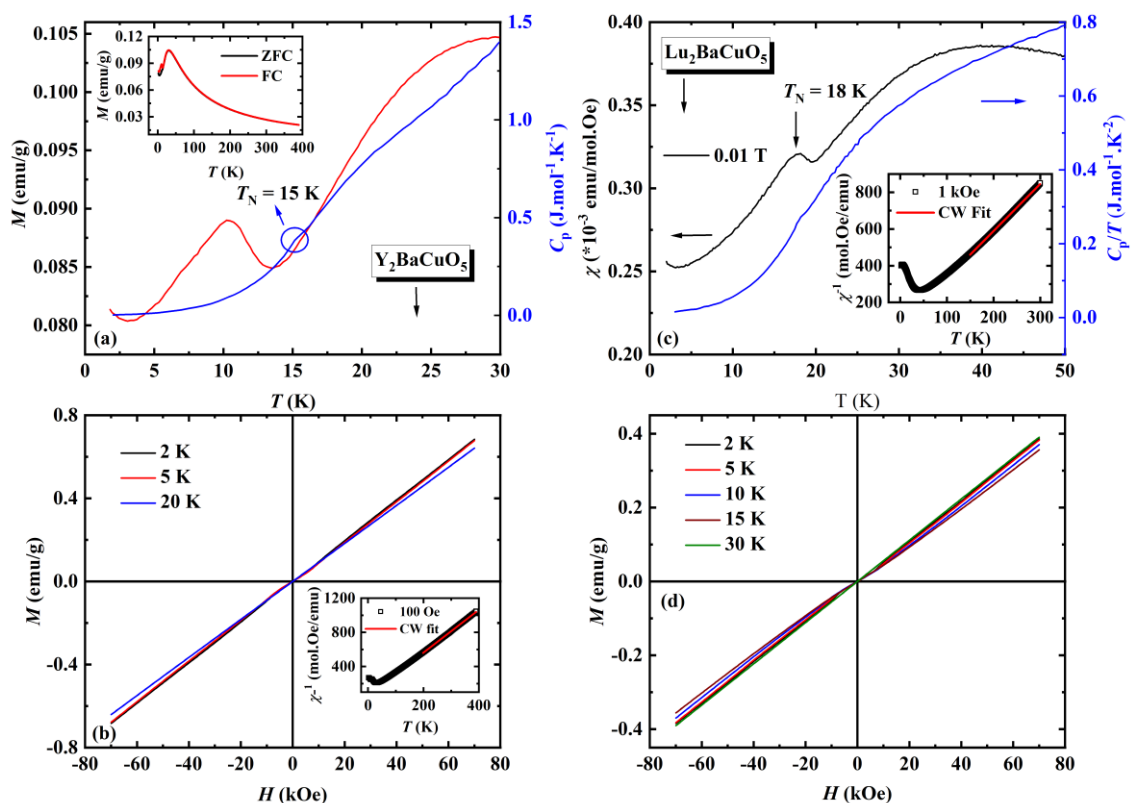


Figure 6.9 (a) Temperature dependence of magnetization (under 0.01 T) and specific heat (at 0 T). Inset shows the ZFC and FC magnetizations in the temperature range 2–390 K. (b) Isothermal magnetization curves, and the inset shows the inverse susceptibility; for Y_2BaCuO_5 . (c) Left. M vs T is measured under a magnetic field of 0.01 T in the field-cooled protocol. Right. Heat capacity data. Inset shows the inverse susceptibility with Curie-Weiss fit. (d) M vs H data. Inset. dM/dH vs H ; for Lu_2BaCuO_5 .

6.3.3.2 R_2BaCuO_5 ($R = Y$, and Lu)

Y_2BaCuO_5 exhibits magnetic order of Cu^{2+} spins at $T_N^{Cu} = 15$ K, which is further confirmed by the heat capacity as seen from Figure 6.9(a). The broad maximum at 30 K from the magnetic data [see inset of Figure 6.9(a)] is due to the presence of short-range correlations. The broad anomaly in magnetization below T_N^{Cu} might be due to spin reorientation of Cu spins. The linear behavior of the magnetic field-dependent magnetization shown in Figure 6.9(b) confirms the antiferromagnetic behavior. From the Curie-Weiss fit [inset of Figure 6.9(b)], the effective paramagnetic moment is $1.786 \mu_B/Cu^{2+}$ which is in good agreement with the theoretical value ($1.73 \mu_B$) of Cu^{2+} ions and the Curie-Weiss temperature $\theta_{CW} = -25.27$ K. Whereas Lu_2BaCuO_5 exhibits anomaly at $T_N^{Cu} = 18$ K in magnetic data [Figure 6.9(c)] where the Cu^{2+} spins order antiferromagnetically. Correspondingly, there is a small kink in specific heat data, revealing the long-range magnetic ordering. The broad peak around 35 K indicates short-range correlations between Cu spins like that observed for Eu and Y compounds. The

effective magnetic moment of $1.76 \mu_B/\text{f.u.}$ confirmed that the Cu indeed is in oxidation state +2. The negative value of $\theta_{CW} = -29.98 \text{ K}$ shows the presence of antiferromagnetic ordering. Further, the isothermal magnetization curves from Figure 6.9(d) suggest the antiferromagnetic interactions between the Cu^{2+} spins below T_N^{Cu} . Our dielectric and pyrocurrent measurements confirmed the absence of magnetoelectric coupling in all these compounds. Therefore, the lack of magnetoelectric effect in nonmagnetic R ions indicates the necessity of $4f$ - $3d$ coupling.

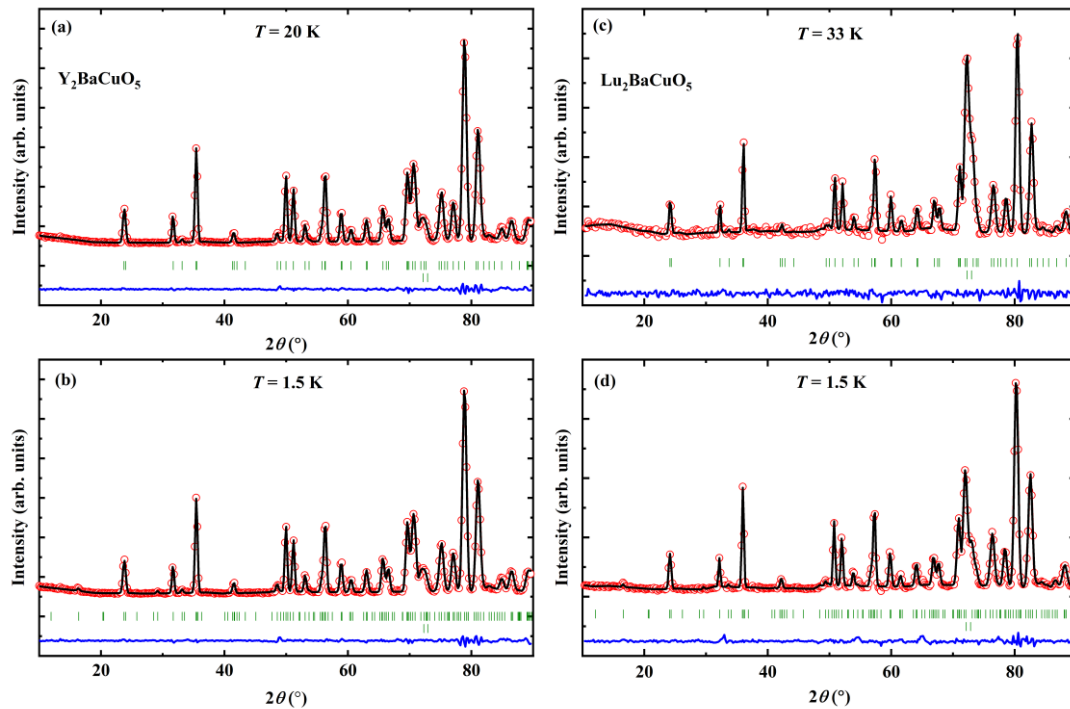


Figure 6.10 Rietveld refined neutron diffraction data above and below T_N for (a & b) Y_2BaCuO_5 and (c & d) $\text{Lu}_2\text{BaCuO}_5$.

Additionally, we have carried neutron diffraction measurements on Y_2BaCuO_5 and $\text{Lu}_2\text{BaCuO}_5$ compounds. Both compounds exhibit the same magnetic structure with propagation vector $\mathbf{k} = (0, \frac{1}{2}, \frac{1}{2})$. We have carried symmetry analysis using ISODISTORT for the \mathbf{k} -vector $(0, \frac{1}{2}, \frac{1}{2})$ and paramagnetic space group $Pnma1'$. There are six possible magnetic solutions (C_{2v} , P_{21}/c , and P_{21}) that belong to irreps mT1 and mT2. The correct solution is P_{21}/c which is defined from the irrep mT1(a, a). The Rietveld refined neutron data at 1.5 K and paramagnetic data for both compounds are shown in Figure 6.10. The obtained magnetic moments per Cu are $0.706(62) \mu_B$ for Y and $0.69(12) \mu_B$ for Lu compounds. The obtained magnetic structure is shown in Figure 6.11, which is equally valid for both compounds. The magnetic structure is commensurate and collinear, with spins oriented along the c -direction. Moreover, this structure is A-type antiferromagnetic, where it shows a parallel arrangement in

the layers and antiparallel coupling between these layers. This A-type spin structure has been predicted previously [9]. From these results, one can expect a similar magnetic structure for $\text{Eu}_2\text{BaCuO}_5$ in the absence of neutron data. In support of this, previous spectral studies suggested the same magnetic structures for all these three compounds [8]. Also, the A-type spin structure does not break the inversion symmetry to show a magnetoelectric effect.

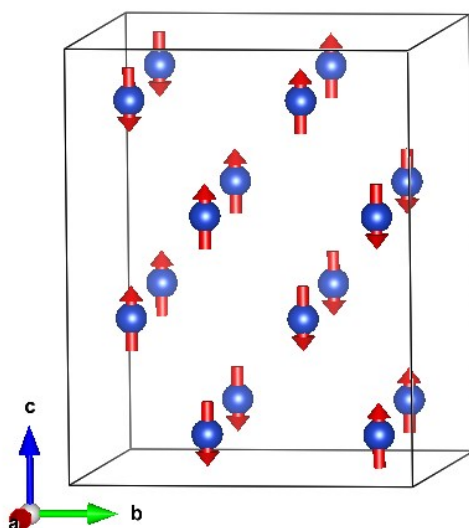


Figure 6.11 Schematic magnetic structure at 1.5 K for Y_2BaCuO_5 and $\text{Lu}_2\text{BaCuO}_5$.

6.3.3.3 $\text{Tm}_2\text{BaCuO}_5$

Finally, we have shown the results of $\text{Tm}_2\text{BaCuO}_5$ in Figure 6.12. From Figure 6.12(a), the magnetization did not show any anomaly till down to 2 K. However, heat capacity shows an apparent anomaly at $T_N^{\text{Cu}} = 19.2$ K where Cu^{2+} spins can be ordered antiferromagnetically. We did not see the corresponding anomaly in magnetic can be due to the high paramagnetic moment of Tm^{3+} ions. Unlike other compounds, the absence of an anomaly below T_N^{Cu} in magnetic data suggests that Tm^{3+} ions did not order till down to 2 K. This different behavior might be associated with Tm^{3+} ion magnetic anisotropy. Also, it can be possible that Cu spins would have polarized Tm^{3+} spins below T_N^{Cu} [11]. The M vs H curves [Figure 6.12(b)] are not exactly linear as expected for the antiferromagnetic behavior, which might be due to induced moment at Tm site or Tm orders independently below 2 K. There is no metamagnetic transition indicating the Tm^{3+} ions order is absent. The effective magnetic moment obtained from the Curie-Weiss fit is $10.414 \mu_B/\text{f.u.}$ which is consistent with the free ion value ($10.816 \mu_B$) of Tm^{3+} and Cu^{2+} ions. $\text{Tm}_2\text{BaCuO}_5$ did not show any multiferroic properties, further confirming the weak $4f-3d$ coupling and the absence of Tm ordering.

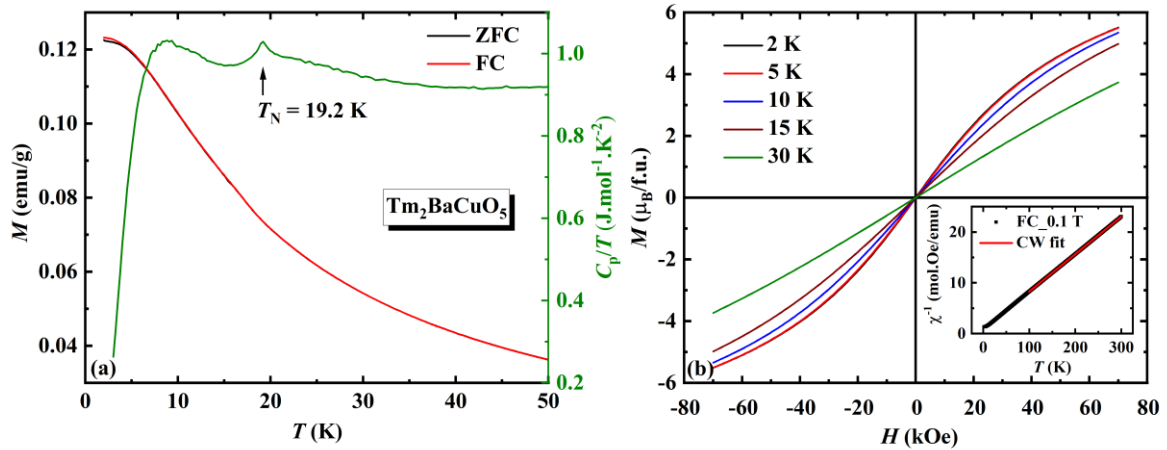


Figure 6.12 (a) Left. DC magnetization with respect to the temperature measured with 0.01 T under ZFC and FC conditions. Right. Specific heat at constant pressure is measured in the absence of a magnetic field. (b) M vs H curves are recorded at different temperatures. Inset shows the χ^{-1} vs T data; for Tm_2BaCuO_5 .

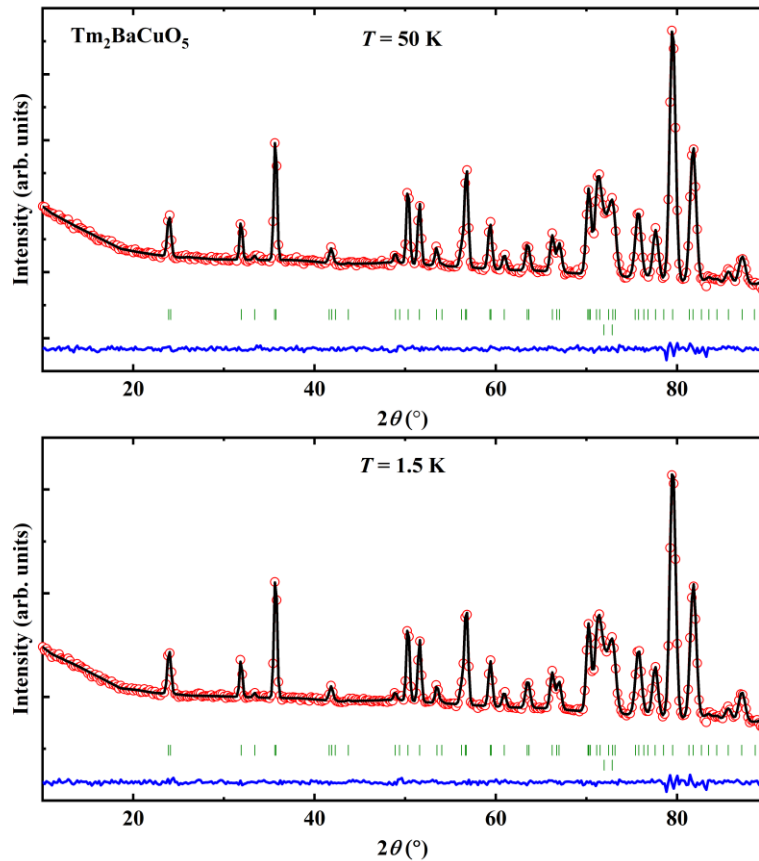


Figure 6.13 Neutron diffraction data for Tm_2BaCuO_5 at $T = 50$ and 1.5 K.

It is shown that this compound can have the \mathbf{k} -vector to be $(0, \frac{1}{2}, 0)$ like Er_2BaCuO_5 [10]. The neutron diffraction experiments in the paramagnetic region ($T = 50$ K) confirm the centrosymmetric $Pnma$ crystal structure (see Figure 6.13). Below T_N^{Cu} , down to 1.5 K, we did not observe any new peaks corresponding to magnetic ordering, which is because of

the low value of Cu moments and the amount of sample used in the experiment is less. Moreover, the absence of any new peaks confirms the non-appearance of the Tm^{3+} ions ordering. Further, the lack of ferroelectricity in this compound under null or finite magnetic fields suggests the absence of Tm ordering despite having the same spin structure as that of Er compound. It can be possible that the magnetic structure of $\text{Tm}_2\text{BaCuO}_5$ with \mathbf{k} -vector $(0, \frac{1}{2}, 0)$ is similar to that ($P_{621/n}$) of Dy, Ho, and Er, which is centrosymmetric and does not allow the magnetoelectric coupling.

6.3.4 Magnetic transitions and magnetodielectric effect in $\text{Yb}_2\text{BaCuO}_5$

6.3.4.1 DC magnetization and heat capacity

Figure 6.14(a) shows the DC magnetization of the $\text{Yb}_2\text{BaCuO}_5$. We did not observe any anomalies in this data. The Curie-Weiss fit [see Figure 6.14(a)] to the inverse susceptibility data results in an effective paramagnetic moment of $6.673 \mu_B/\text{f.u.}$, which is close to the spin only value of $6.65 \mu_B$ for Yb^{3+} and Cu^{2+} ions. However, from Figure 6.14(b), heat capacity shows three different anomalies at 15.9, 5.2, and 2.4 K indicating the distinct magnetic phase transitions. The M vs H curves below these temperatures show linear behavior suggests the antiferromagnetic coupling. Based on previous reports, Cu^{2+} spins order at 15.9 K and induce moment at both Yb sites. Also, it can be possible that the anomaly at 2.4 K can be of Schottky type associated with the splitting of crystal field levels of Yb^{3+} ions. Other transitions can be changes in the magnetic structure of $\text{Yb}_2\text{BaCuO}_5$ upon decreasing the temperature.

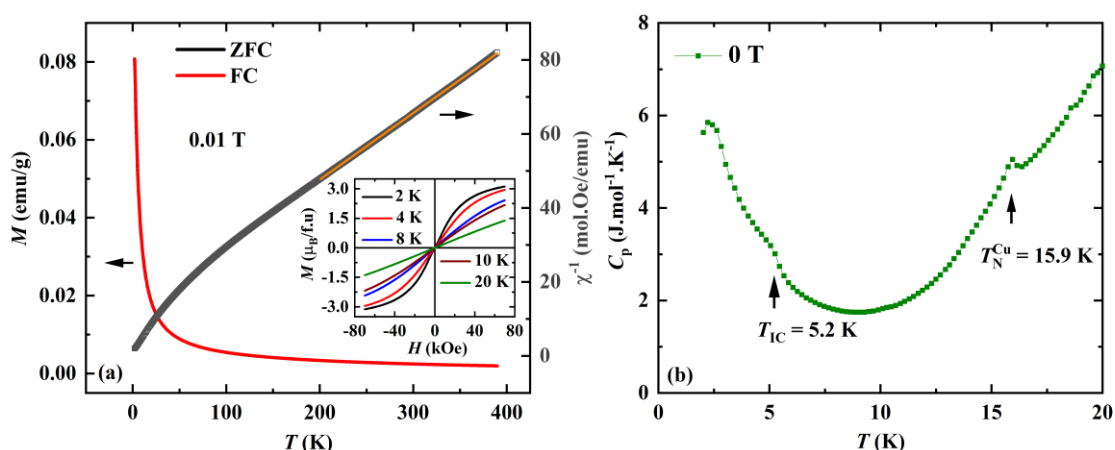


Figure 6.14 (a) Left axis. DC magnetization measured with respect to temperature under 100 Oe in zero field-cooled (ZFC) and field-cooled (FC) conditions. Right axis. Inverse susceptibility data obtained from magnetization measured under 100 Oe in FC mode. Inset shows the isothermal M - H curves. (b) Heat capacity measured under zero magnetic field.

6.3.4.2 Elastic neutron scattering

To get more insight into these magnetic transitions, we have performed neutron powder diffraction on this sample. As can be seen from Figure 6.15(a), there is a clear appearance of magnetic reflections at low 2θ below T_N^{Cu} and they change with further cooling down. From the analysis of this data, we found the \mathbf{k} -vector $(0, \frac{1}{2}, 0)$ below $T_N^{\text{Cu}} = 15.9$ K like that observed for Dy, Ho, and Er. Interestingly, it exhibits commensurate (CM) to incommensurate (ICM) magnetic transition at $T_{\text{ICM}} = 5.2$ K with modulation vector $\mathbf{k}_{\text{IC}} = (0, \frac{1}{2}, g)$. Further, it shows ICM to CM ground state with $\mathbf{k} = (0, \frac{1}{2}, \frac{1}{2})$ below 3.5 K. We have used ISODISTORT to explore possible magnetic solutions correspond to these \mathbf{k} -vectors and paramagnetic space group $Pnma1'$. Firstly, we have refined the data at 9 K, shown in Figure 6.15(b). There are six possible solutions that are defined from the two irreps mY1 and mY2. The correct solution is P_a2_1/c (standard setting) with the irrep mY1(a, a). The obtained magnetic moment is 0.65(21) μ_B per Cu, 0.38(19) μ_B per Yb2, and 0 μ_B for Yb1. The observed values are relatively low which is because of the poor data quality. The observed magnetic point group $2/m1'$ is centrosymmetric and imposes a null magnetoelectric tensor. Figure 6.15(c) shows the LeBail fit using the incommensurate \mathbf{k} -vector $(0, \frac{1}{2}, g)$ for the neutron data collected at the 4.1 K. The g -value is found to be ~ 0.19 . However, the complete data analysis of this data is not yet done.

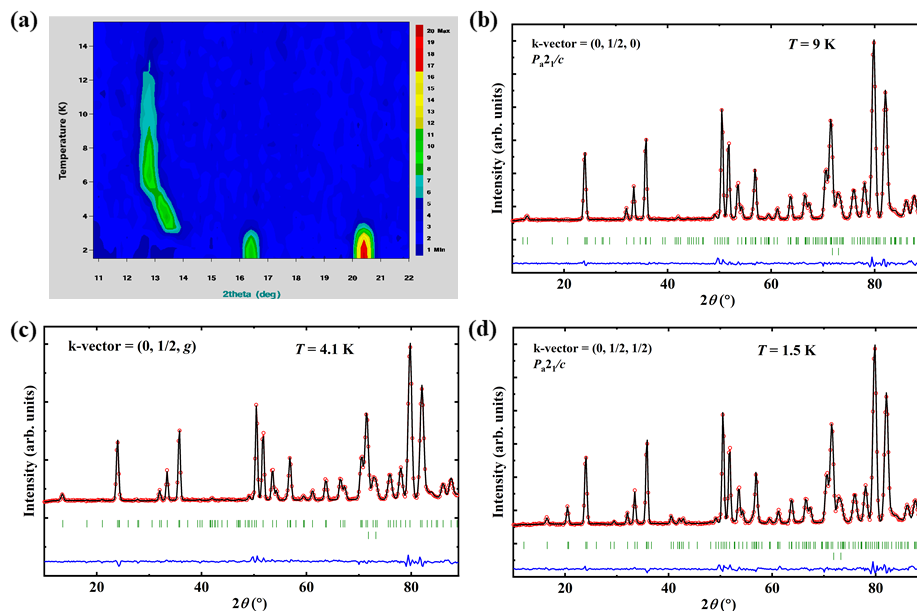


Figure 6.15 (a) Temperature-dependent neutron diffraction data of $\text{Yb}_2\text{BaCuO}_5$ at low angles shown in 2D logarithmic scale. (b) Rietveld refined neutron pattern at $T = 9$ K. The analysis is carried using P_a2_1/c with $(0, \frac{1}{2}, 0)$. (c) Le-Bail fit to the neutron data at $T = 4.1$ K using \mathbf{k} -vector $(0, \frac{1}{2}, g)$. (d) Rietveld refined neutron pattern at $T = 1.5$ K with the magnetic solution P_a2_1/c corresponds to $(0, \frac{1}{2}, \frac{1}{2})$.

The refinement of the neutron diffraction data is shown in Figure 6.15(d) with \mathbf{k} -vector $(0, \frac{1}{2}, \frac{1}{2})$. There are six plausible magnetic solutions ($C_{amc}2_1$, $P_{a2_1/c}$, and P_{a2_1}) that belong to irreps mT1 and mT2. The solution $P_{a2_1/c}$ defined from the irrep mT1(a, a) fit the experimental data very well. However, the obtained magnetic symmetry does not allow the magnetoelectric coupling since the inversion center did not break. The acquired magnetic moment is $0.65 \mu_B$ per Cu, $2.04(4) \mu_B$ per Yb2, and $0.14(1) \mu_B$ per Yb1. We have fixed the magnetic moment of the Cu during refinement to get stable refinement. We have illustrated the corresponding magnetic structures in Figure 6.16. From this figure, the spin structure is strongly noncollinear at $T = 9$ K like $\text{Er}_2\text{BaCuO}_5$ and collinear at $T = 1.5$ K, similar to that of the nonmagnetic case. Moreover, neutron experiments confirmed that Yb^{3+} moments did not order down to 1.5 K, and there is an induced moment at Yb sites by Cu spins. Therefore, this compound also may not show magnetoelectric coupling like $\text{Tm}_2\text{BaCuO}_5$. However, it will be interesting to check this possibility in the incommensurate phase.

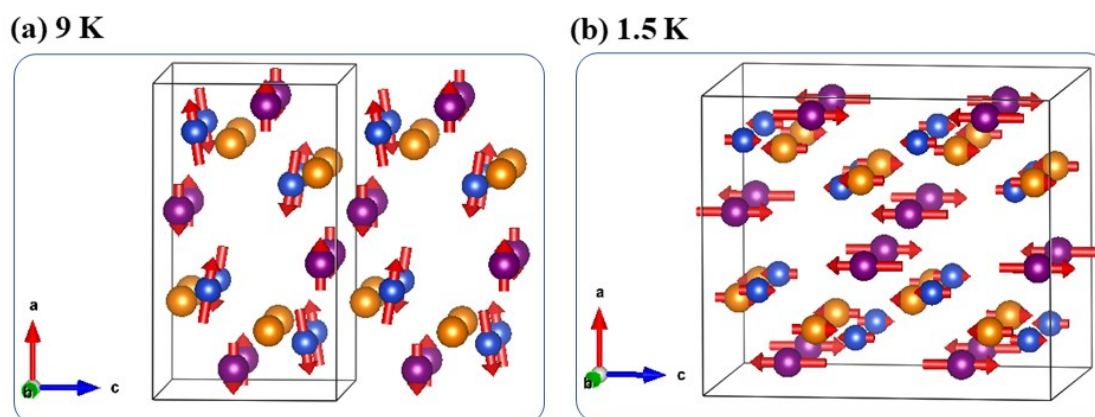


Figure 6.16 Illustration of magnetic structures of $\text{Yb}_2\text{BaCuO}_5$ at (a) 9 K and (b) 1.5 K.

6.3.4.3 Dielectric study

To check magnetodielectric or magnetoelectric coupling, we have carried the electrical measurements, and the results are displayed in Figure 6.17. It exhibits a strong upturn in dielectric constant data at $T_{IC} = 5.2$ K and increases down to 2 K, and corresponding loss shows broad anomaly. Further, the dielectric constant changes under magnetic fields. These results indicate the presence of strong magnetodielectric coupling in $\text{Yb}_2\text{BaCuO}_5$. Above T_{IC} , we did not observe any dielectric anomalies. The presence of magnetodielectric effect below T_{IC} suggests the possibility of multiferroicity. However, we did not observe any significant feature in pyrocurrent measurements in support of this. This might be due to the small temperature

range of the incommensurate phase. Finally, we have drawn the phase diagram for the $\text{Yb}_2\text{BaCuO}_5$ from the above results and displayed it in Figure 6.18.

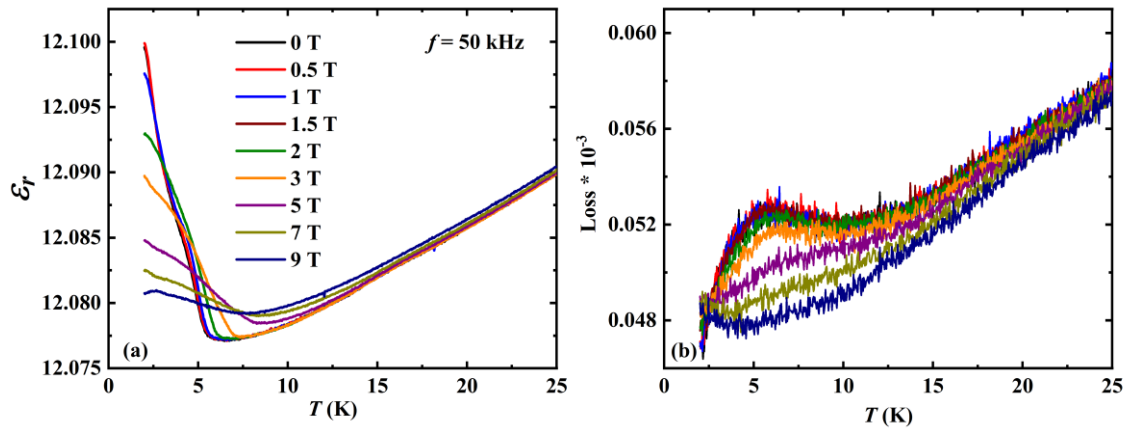


Figure 6.17 (a) Temperature-dependent dielectric constant under different magnetic fields recorded at frequency $f=50$ kHz. (b) corresponding loss.

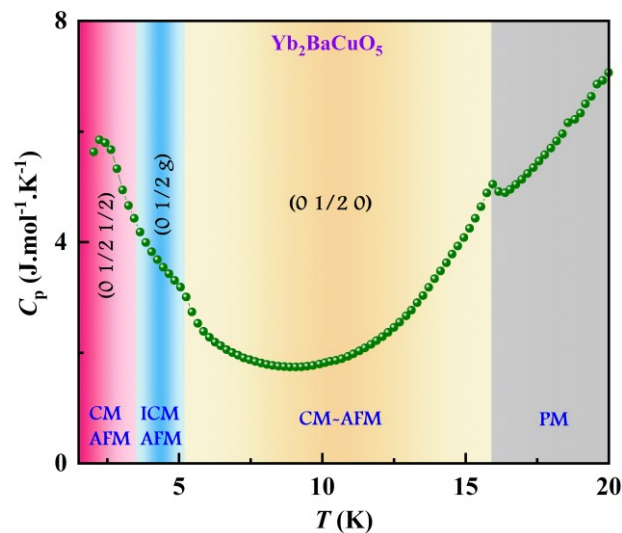


Figure 6.18 The phase diagram of $\text{Yb}_2\text{BaCuO}_5$ shows the different magnetic phase transitions.

We summarized all the magnetic and electrical properties of green phases in Table 6.7. From the Table, it can be noted that these compounds exhibit a wide variety of magnetic properties along with magnetoelectric coupling. Moreover, R ions did not order down to 2 K in isostructural compounds $R_2\text{BaZnO}_5$ [18]. This suggests the interaction between Cu and R ions is necessary for the ordering of R ions. In most of the green phases, ordering of the magnetic rare-earth ion, in turn, changes the magnetic symmetry and allows the magnetoelectric effect. However, the symmetry below T_N^{Cu} does not allow the coupling between magnetic and electric orders except for $\text{Sm}_2\text{BaCuO}_5$. Also, there is a quite difference in the ground states for the Dy, Ho, and Er compounds. The low temperature structure changes

Table 6.7 Summary of magnetic and magnetoelectric properties of $R_2\text{BaCuO}_5$ ($R = \text{Sm-Lu}$, and Y).

Rare earth (R)	T_N^{Cu} (K)	T_N^R (K)	k-vectors $T_N^{\text{Cu}} \leq T \leq T_N^R$ $T < T_N^R$	Magnetic structure	Mag. Symm.	Property	Ref.
Sm	23	5	(0, 0, 0)	-	-	Linear magnetoelectric (LME)	[13], Chapter 3
Eu	16.3	-	(0, $\frac{1}{2}$, $\frac{1}{2}$)	-	-	Not ME	This work
Gd	11.8	6	(0, 0, g) (0, 0, $\frac{1}{2}$)	Cycloidal Noncollinear	$2mm$	Multiferroic	[14], Chapter 4
Dy	18.5	10.7	(0, $\frac{1}{2}$, 0) (0, 0, 0)	Noncollinear Noncollinear	$2/m$ $mm'm$	LME + Field-Induced Ferroelectric	Chapter 5
Ho	17.5	8	(0, $\frac{1}{2}$, 0) (0, 0, 0) + (0, $\frac{1}{2}$, 0)	Noncollinear Noncollinear	$2/m$ $2'/m$	LME + Field-Induced Ferroelectric	Chapter 5
Y	15	-	(0, $\frac{1}{2}$, $\frac{1}{2}$)	Collinear	$2/m$	Not ME	This work
Er	19.3	5.1	(0, $\frac{1}{2}$, 0) (0, $\frac{1}{2}$, 0)	Noncollinear Noncollinear	$2/m$	Field Induced Ferroelectric	This work
Tm	19.2	-	(0, $\frac{1}{2}$, 0)	-	-	Not ME	[10], This work
Yb	15.9	-	(0, $\frac{1}{2}$, 0)	Noncollinear	$2/m$	Multiferroic	This work
	5.2		(0, $\frac{1}{2}$, g)	Cycloidal	-		
	3.5		(0, $\frac{1}{2}$, $\frac{1}{2}$)	Collinear	$2/m$		
Lu	18	-	(0, $\frac{1}{2}$, $\frac{1}{2}$)	Collinear	$2/m$	Not ME	This work

to (0, 0, 0) for Dy and (0, 0, 0) + (0, $\frac{1}{2}$, 0) for Ho from high temperature structure with **k**-vector (0, $\frac{1}{2}$, 0) upon R ion ordering. Both compounds exhibit linear magnetoelectric effect up to a magnetic field of ~ 1 T and ferroelectricity above their respective metamagnetic transitions. Whereas the structure with (0, $\frac{1}{2}$, 0) is same across the Er ordering till down to 1.5 K. This compound shows the magnetoelectric coupling only above $H_c = 0.9$ T. Surprisingly, Tm and Yb ions did not order down to 2 K. However, there is an induced moment at these sites by Cu spins. Though the magnetic structure of $\text{Tm}_2\text{BaCuO}_5$ is similar to Er, it did not show

magnetoelectric properties, which might be due to the absence of Tm order. Whereas $\text{Yb}_2\text{BaCuO}_5$ shows different magnetic phase transitions with the temperature and might be multiferroic in the incommensurate phase, consistent with the magnetic symmetry. This indicates the importance of R ion and its ordering. Unlike these compounds, the $\text{Gd}_2\text{BaCuO}_5$ case is completely different where it shows the simultaneous ordering of Gd and Cu ions. This is because Gd ground state is S -state and the crystalline electric field effects are negligible for this. These compounds have two different sites for R ions, and the crystalline electric fields at both sites are different. Each R ion has significant crystal field splitting, which can lead to different magnetic structures. The variation of the number of electrons in the $4f$ shell for different R ions leads to a suppression of interactions and ordering in some cases. Therefore, these results suggest the important role of $4f$ - $3d$ coupling and single-ion anisotropy of R ions in determining the magnetic properties and hence, observation of magnetoelectric effect.

6.4 Conclusion

In conclusion, we have systematically investigated the magnetic and magnetoelectric properties of $R_2\text{BaCuO}_5$ ($R = \text{Er, Eu, Y, Tm, Yb, and Lu}$). $\text{Er}_2\text{BaCuO}_5$ exhibits metamagnetic transition at a critical field of $H_c \sim 0.9$ T and a large magnetization of $9 \mu_B/\text{f.u.}$ at 7 T and 2 K. Moreover, above H_c , it shows field-induced electric polarization indicating the presence of magnetoelectric coupling. In all other compounds, Cu^{2+} ordered antiferromagnetically at $T_N^{\text{Cu}} = 15\text{-}20$ K. Neutron diffraction measurements revealed a strongly noncollinear magnetic structure obtained from \mathbf{k} -vector $(0, \frac{1}{2}, 0)$, with magnetic symmetry P_b2_1/n for Er and collinear structure obtained from $(0, \frac{1}{2}, \frac{1}{2})$, with magnetic symmetry P_a2_1/c for Y and Lu compounds. $\text{Yb}_2\text{BaCuO}_5$ exhibits three different magnetic phase transitions including the incommensurate magnetic phase, where it might be multiferroic. Unlike Er and Yb, magnetoelectric coupling is absent in other compounds. Our results suggest that $4f$ - $3d$ coupling is necessary to observe the magnetoelectric coupling in these green phase family compounds. This work opens a pathway to design new magnetoelectric materials based on f - d coupling. Also, the wide variety of magnetic structures in isostructural compounds makes the green phase family as interesting as famous manganites.

References

- [1] K. Kanoda, T. Takahashi, T. Kawagoe, T. Mizoguchi, S. Kagoshima, and M. Hasumi, *Jpn. J. Appl. Phys.* **26**, L2018 (1987).
- [2] R. Z. Levitin, B. V. Mill, V. V. Moshchalkov, N. A. Samarin, V. V. Snegirev, and J. Zoubkova, *J. Magn. Magn. Mater.* **90**, 536 (1990).
- [3] V. V. Moshchalkov, N. A. Samarin, I. O. Grishchenko, B. V. Mill, and Z. J., *Solid State Commun.* **78**, 879 (1991).
- [4] A. Salinas-Sánchez, R. Sáez-Puche, and M. A. Alario-Franco, *J. Solid State Chem.* **89**, 361 (1990).
- [5] K. Tagaya, *J. Magn. Magn. Mater.* **104**, 561 (1992).
- [6] T. Kobayashi, H. Katsuda, K. Hayashi, M. Tokumoto, and H. Ihara, *Jpn. J. Appl. Phys.* **27**, L670 (1988).
- [7] R. Burriel, M. Castro, C. Piqué, A. Salinas-Sánchez, and R. Sáez-Puche, *J. Magn. Magn. Mater.* **104**, 627 (1992).
- [8] I. V. Paukov, M. N. Popova, and B. V. Mill, *Phys. Lett. A* **169**, 301 (1992).
- [9] I. V Golosovsky, P. Böni, and P. Fischer, *Solid State Commun.* **87**, 1035 (1993).
- [10] I. V Golosovsky, V. P. Plakhtii, V. P. Kharchenkov, J. Zoubkova, B. V Mill, M. Bonnet, and E. Roudeau, *Fiz. Tve. Tela.* **34**, 1483 (1992).
- [11] G. A. Stewart and P. C. M. Gubbens, *J. Magn. Magn. Mater.* **206**, 17 (1999).
- [12] J. A. Hodges and J. P. Sanchez, *J. Magn. Magn. Mater.* **92**, 201 (1990).
- [13] P. Yanda, N. V. Ter-Oganessian, and A. Sundaresan, *Phys. Rev. B* **100**, 104417 (2019).
- [14] P. Yanda, I. V. Golosovsky, I. Mirebeau, N. V. Ter-Oganessian, J. Rodríguez-Carvajal, and A. Sundaresan, *Phys. Rev. Res.* **2**, 023271 (2020).
- [15] A. K. Ovsyanikov, I. V. Golosovsky, I. A. Zobkalo, and I. Mirebeau, *J. Magn. Magn. Mater.* **353**, 71 (2014).
- [16] C. Michel and B. Raveau, *J. Solid State Chem.* **43**, 73 (1982).
- [17] A. Salinas-Sanchez, J. L. Garcia-Muñoz, J. Rodriguez-Carvajal, R. Saez-Puche, and J. L. Martinez, *J. Solid State Chem.* **100**, 201 (1992).
- [18] G. F. Goya, R. C. Mercader, M. T. Causa, and M. Tovar, *J. Phys. Condens. Matter* **8**, 8607 (1996).

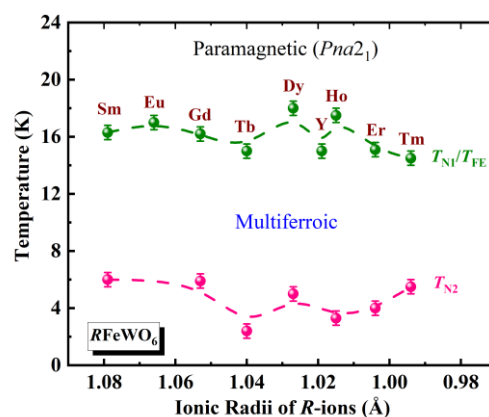
PART B

Chapter 7

Magnetic order-induced change in ferroelectric polarization in aeschynites $R\text{FeWO}_6$ ($R = \text{Sm, Gd, Ho, Er, and Tm}$)*

Summary

We have shown the synthesis, structure, and magnetism-induced multiferroic properties of the polar magnets $R\text{FeWO}_6$ ($R = \text{Tm, Sm, Gd, Ho, and Er}$). All these compounds crystallize in the orthorhombic structure with the polar symmetry $Pna2_1$ which results from the ordering of Fe^{3+} and W^{6+} ions at different crystallographic sites. DC magnetization and specific heat measurements confirm the antiferromagnetic order of Fe^{3+} spins at $T_{N1} = 14 - 18$ K and magnetic ordering of R ions at low temperatures. The magnetic ordering of Fe^{3+} ions in these compounds is accompanied by a dielectric anomaly and a change in electric polarization. Intriguingly, a second ferroelectric transition occurs at the magnetic ordering temperature ($T_{N2} = 5.5$ K) of Tm^{3+} ions in TmFeWO_6 . The magnetic field dependent behaviour of electric polarization varies with R ion, indicating the coupling between $4f - 3d$ electrons. The emergence of change in ferroelectric polarization at the magnetic ordering temperatures demonstrates the multiferroic nature of the polar magnets $R\text{FeWO}_6$ ($R = \text{Tm, Sm, Gd, Ho, and Er}$). Our study indicates that the aeschynite type family of compounds with polar symmetry can be an excellent platform to understand the role of $4f - 3d$ coupling on multiferroicity.



*This work is appeared in Phys. Rev. Material, **5**, 074406 (2021), © 2021 by the American Physical Society.

7.1 Introduction

Recently, polar magnets that possess polar crystal symmetry and exhibit magnetic ordering have drawn much attention to multiferroicity [1–8]. These materials can be classified as a new class of multiferroics since they differ from the type-I and type-II multiferroics as discussed in Chapter 1. Mainly, polar magnets do not need complicated spin structures to show the electric polarization, giving hope for room temperature multiferroics. There are few reports, and recently there is a perspective on polar magnets as multiferroics in the literature [1,6–8]. It appears that most of these compounds are stabilized in the polar structure by chemical ordering. There are quite a few polar magnetic materials reported to be multiferroics, for example, $\text{CaBaCo}_4\text{O}_7$, $M_2\text{Mo}_3\text{O}_8$ ($M = \text{Mn, Fe, and Co}$), Ni_3TeO_6 , corundum derivatives, and doubly ordered perovskites, etc [1,2,5,9–15]. Recently, another interesting family of compounds $R\text{FeWO}_6$ ($R = \text{Dy, Tb, Eu, and Y}$) reported to be polar magnets which are ordered derivatives of the centrosymmetric parent compound aeschynite- CaTa_2O_6 and show multiferroic properties [6,16,17]. We have illustrated the mechanism of chemical ordering for stabilizing the polar- $R\text{FeWO}_6$ compounds in Figure 7.1. As can be seen from figure, CaTa_2O_6 structure has edge shared TaO_6 octahedra pairs, and these pairs are connected by corners making the structure centrosymmetric [17]. The combination of transition metals with Fe^{3+} and W^{6+} charge at Ta^{5+} site and rare earth at Ca^{2+} site resulted in polar structure [6]. These compounds crystallize in the orthorhombic structure with polar space group $Pna2_1$. The polar nature is stabilized by the ordering of Fe^{3+} and W^{6+} ions at different crystallographic sites. They exhibit the antiferromagnetic order of Fe^{3+} ions at $T_{N1} = 15 - 18 \text{ K}$, where they show a change in switchable electric polarization, indicating that these compounds are multiferroics. From the neutron diffraction studies, the magnetic structure of DyFeWO_6 is reported to be (MSG: $C_a c$) a noncollinear and commensurate with the \mathbf{k} -vector $(0 \frac{1}{2} \frac{1}{2})$, which is compatible with observed polarization. Following this study, two other isostructural compounds, $R\text{CrWO}_6$ ($R = \text{Y, Ho, and Lu}$) and DyVWO_6 were reported to be polar magnets with a collinear magnetic structure of Cr^{3+} sublattice [18–22]. In contrast to $R\text{FeWO}_6$ ($R = \text{Dy, Tb, Eu, \& Y}$), Cr and V based compounds are not multiferroics which may be due to different spin structures that they adapt or the change in polarization is very small to be detected within the limit of our measurement ($\sim 0.01 \mu\text{C}/\text{m}^2$). Besides, the $4f - 3d$ interactions seem to play a role in the multiferroic properties like those observed in the manganites, orthoferrites, and green phase compounds [23–28]. Along this line, we have

studied the other members of this family to understand the effect of rare-earth on the multiferroic properties.

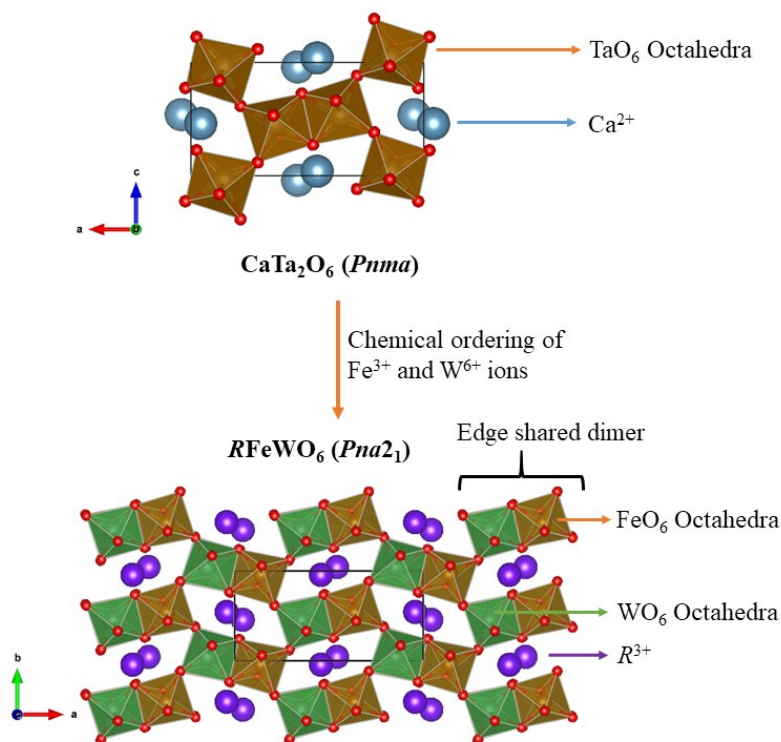


Figure 7.1 Schematic representation of how chemical ordering stabilizes the polar structure from centrosymmetric aeschynite- CaTa_2O_6 .

In this chapter, we show the synthesis and characterization of polar magnets $R\text{FeWO}_6$ ($R = \text{Tm}, \text{Sm}, \text{Gd}, \text{Ho}, \text{and Er}$) that are isostructural to DyFeWO_6 [6]. All these compounds crystallize in the orthorhombic $Pna2_1$ crystal structure which is ordered derivatives of centrosymmetric parent compound CaTa_2O_6 [17]. They exhibit an antiferromagnetic ordering of Fe^{3+} ions around $T_{N1} = 14 - 18$ K. Isothermal magnetization curves reveal the metamagnetic transitions at a critical field. We observe a change in polarization at the magnetic ordering temperature T_{N1} , demonstrating that these compounds are multiferroics. Interestingly, TmFeWO_6 shows a second ferroelectric transition below $T_{N2} = 5.5$ K where Tm^{3+} ions order independently. The ferroelectric polarization in these polar magnets is greatly affected by the applied magnetic field, demonstrating a strong magnetoelectric coupling.

7.2 Experimental section

We have prepared polycrystalline samples of $R\text{FeWO}_6$ ($R = \text{Tm}, \text{Sm}, \text{Gd}, \text{Ho}, \text{and Er}$) by a conventional solid-state reaction method. Stoichiometric amounts of $R\text{FeO}_3$ and WO_3

powders were mixed well and heated in the temperature range 1050-1100 °C for 24 hrs in evacuated and sealed quartz tubes with intermittent grindings. Powder X-ray diffraction data were collected at room temperature with a PANalytical Empyrean alpha-1 diffractometer using monochromatic Cu K α 1 radiation and analysis is carried out by using FULLPROF. DC magnetization measurements were carried out using a SQUID magnetometer (Quantum Design, USA). Specific heat measurements were performed in the Physical Property Measurement System (PPMS), Quantum Design, USA. Dielectric measurements were carried out on disc-shaped pellets with silver electrodes given on either side by using an Agilent E4980A LCR meter. The dimensions of each sample are provided in Table 7.1. Keithley electrometer is used to record the pyrocurrent, DC bias current, and the polarization was obtained by integrating pyrocurrent with respect to time. The details of all experimental techniques were discussed in Chapter 2.

Table 7.1 The dimensions of the pellets used for electrical measurements.

Compound	Thickness (in mm)	Area (in mm ²)
TmFeWO ₆	0.278	23
SmFeWO ₆	0.267	13
GdFeWO ₆	0.277	40
HoFeWO ₆	0.321	10
ErFeWO ₆	0.271	35

7.3 Results and discussion

7.3.1 Crystal structure

Figure 7.2(a) shows the Rietveld refined XRD pattern of TmFeWO₆ obtained at the final cycle of the refinement and the obtained structural parameters are provided in Table 7.2. The refinements of all other compounds and their structural parameters are provided in Figure 7.3 and Tables 7.3-7.6, respectively. These samples contain minor impurity phases, such as garnet, R₆WO₁₂, and Fe₃O₄. We have realized that it requires a synchrotron or neutron diffraction to get accurate positional parameters for all the compounds reported here. Our refinement confirms that all the four compounds crystallize in polar orthorhombic structure with space group *Pna*2₁, isostructural with DyFeWO₆ [6]. The chemical ordering of Fe³⁺ and W⁶⁺ ions from the parent aeschynite compound CaTa₂O₆ (space group: *Pnma*) breaks the

inversion centre and results in polar structure [17]. The schematic of the crystal structure of $R\text{FeWO}_6$ ($R = \text{Tm}, \text{Sm}, \text{Gd}, \text{Ho}, \text{and Er}$) is shown in Figure 7.2(b). It can be seen from this figure that the 3D structure formed by connecting the corners of FeO_6 and WO_6 edge shared octahedra dimers. The rare-earth ions are located in the tunnels to form RO_8 polyhedra. As shown in Figure 7.4, the lattice parameters b , c , and volume of unit cell decrease linearly as a function of the radius of lanthanide ion while going from Sm to Tm. The parameter a remains almost constant. We have collected the XRD data of GdFeWO_6 at 800°C which is not shown here, confirming that there is no structural transition, and the polar structure might be stable up to the decomposition temperatures of all these compounds. In the following sections, we will present the physical properties of all the compounds.

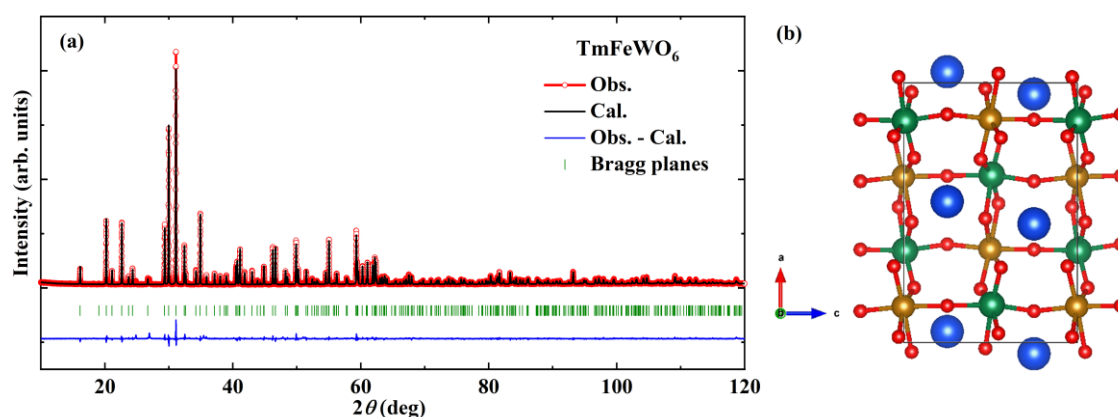


Figure 7.2 (a) Rietveld refinement of room temperature (RT) XRD data of TmFeWO_6 . (b) Schematic of the crystal structure of $R\text{FeWO}_6$ ($R = \text{Tm}, \text{Sm}, \text{Gd}, \text{Ho}, \text{and Er}$) viewed along the \mathbf{b} -direction. Rare earth (Blue), Iron (Brown), Tungsten (Green), and Oxygen (Red).

Table 7.2 Crystallographic structural parameters of TmFeWO_6 obtained from the refinement of room temperature XRD data. Space group: $Pna2_1$; $a = 10.9738(2) \text{ \AA}$, $b = 5.1371(1) \text{ \AA}$, $c = 7.3095(1) \text{ \AA}$, $\alpha = \beta = \gamma = 90^\circ$, $V = 412.063(11) \text{ \AA}^3$; $\chi^2 = 3.62$, $R_{\text{Bragg}}(\%) = 5.44$, $R_{\text{f}}(\%) = 4.72$.

Atom	Wyckoff Position	x	y	z	$B_{\text{iso}}(\text{\AA}^2)$	Occu.
Tm	$4a$	0.0435(2)	0.4575(6)	0.25	0.789(68)	1
Fe	$4a$	0.1387(9)	0.9659(15)	0.9870(32)	0.176(52)	1
W	$4a$	0.3532(3)	0.4503(6)	0.0046(12)	0.844(60)	1
O1	$4a$	0.9732(31)	0.7782(70)	0.0523(63)	1	1
O2	$4a$	0.5389(30)	0.2609(67)	0.9685(73)	1	1
O3	$4a$	0.2031(31)	0.6416(66)	0.0672(46)	1	1
O4	$4a$	0.2875(31)	0.1029(74)	0.9399(47)	1	1
O5	$4a$	0.1593(26)	0.0685(56)	0.2448(59)	1	1
O6	$4a$	0.1132(24)	0.8366(55)	0.7679(64)	1	1

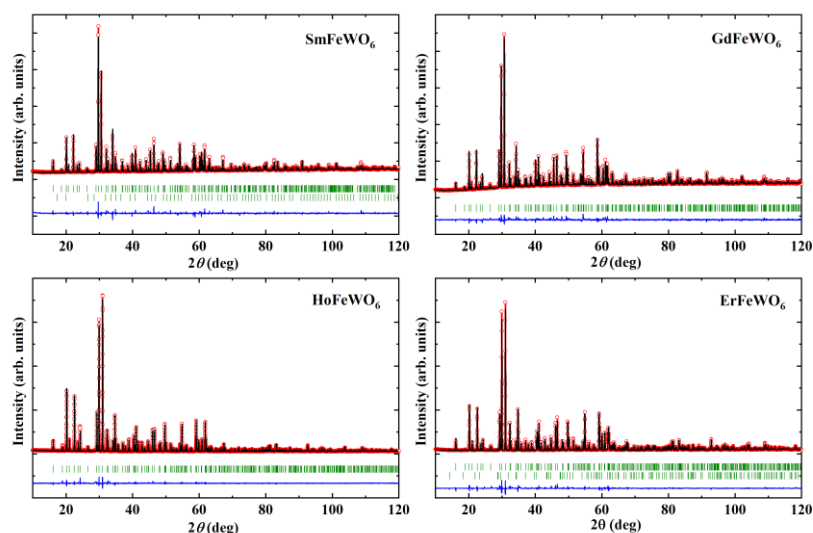


Figure 7.3 Rietveld refined XRD data of $R\text{FeWO}_6$ ($R = \text{Sm}, \text{Gd}, \text{Ho}, \text{and Er}$) collected at RT.

Table 7.3 Crystallographic structural parameters of SmFeWO_6 obtained from refinement of room temperature XRD data. Space group: $Pna2_1$; $a = 10.9788(2)$ Å, $b = 5.2672(1)$ Å, $c = 7.4151(1)$ Å, $\alpha = \beta = \gamma = 90^\circ$, $V = 428.791(11)$ Å³; $\chi^2 = 3.99$, $R_{\text{Bragg}}(\%) = 6.93$, $R_{\text{f}}(\%) = 5.24$.

Atom	Wyckoff Position	x	y	z	$B_{\text{iso}}(\text{Å}^2)$	Occu.
Sm	4a	0.0430(3)	0.4566(8)	0.25	0.397(85)	1
Fe	4a	0.1399(11)	0.9623(19)	0.9977(61)	1.224(230)	1
W	4a	0.3536(3)	0.4541(7)	0.0083(19)	0.188(76)	1
O1	4a	0.9824(33)	0.7587(73)	0.0512(89)	1	1
O2	4a	0.5472(32)	0.2604(72)	0.9842(110)	1	1
O3	4a	0.1990(37)	0.6520(63)	0.0778(70)	1	1
O4	4a	0.2883(38)	0.1394(71)	0.9627(80)	1	1
O5	4a	0.1462(34)	0.0921(65)	0.2761(71)	1	1
O6	4a	0.1296(32)	0.8353(62)	0.7857(78)	1	1

Table 7.4 Crystallographic structural parameters of GdFeWO_6 obtained from refinement of room temperature XRD data. Space group: $Pna2_1$; $a = 10.9775(2)$ Å, $b = 5.2325(1)$ Å, $c = 7.3874(1)$ Å, $\alpha = \beta = \gamma = 90^\circ$, $V = 424.328(20)$ Å³; $\chi^2 = 3.59$, $R_{\text{Bragg}}(\%) = 8.21$, $R_{\text{f}}(\%) = 5.32$.

Atom	Wyckoff Position	x	y	z	$B_{\text{iso}}(\text{Å}^2)$	Occu.
Gd	4a	0.0422(3)	0.4561(11)	0.25	0.176(103)	1
Fe	4a	0.1400(14)	0.9628(23)	0.9996(74)	1	1
W	4a	0.3535(4)	0.4532(8)	0.0050(23)	0.141(85)	1
O1	4a	0.9961(41)	0.7420(78)	0.0300(101)	1	1
O2	4a	0.5551(32)	0.2617(72)	0.9521(110)	1	1
O3	4a	0.1976(37)	0.6625(63)	0.0790(70)	1	1
O4	4a	0.2774(38)	0.0940(71)	0.9521(80)	1	1
O5	4a	0.1532(34)	0.0620(65)	0.2244(71)	1	1
O6	4a	0.1311(32)	0.8529(62)	0.7695(78)	1	1

Table 7.5 Crystallographic structural parameters of HoFeWO_6 obtained from refinement of room temperature XRD data. Space group: $Pna2_1$; $a = 10.9725(1)$ Å, $b = 5.1693(1)$ Å, $c = 7.3345(1)$ Å, $\alpha = \beta = \gamma = 90^\circ$, $V = 416.042(7)$ Å³; $\chi^2 = 3.04$, $R_{\text{Bragg}}(\%) = 5.68$, $R_{\text{f}}(\%) = 5.24$.

Atom	Wyckoff Position	x	y	z	$B_{\text{iso}}(\text{Å}^2)$	Occu.
Ho	4a	0.0430(2)	0.4568(7)	0.25	1.536(92)	1
Fe	4a	0.1390(8)	0.9633(14)	0.9959(43)	0.245(163)	1
W	4a	0.3541(2)	0.4516(5)	0.0063(15)	0.178(41)	1
O1	4a	0.9945(26)	0.7690(58)	0.0444(70)	1	1
O2	4a	0.5222(28)	0.2472(58)	0.9696(76)	1	1
O3	4a	0.2110(29)	0.6337(53)	0.0588(47)	1	1
O4	4a	0.2936(32)	0.1387(63)	0.9425(46)	1	1
O5	4a	0.1417(25)	0.0542(54)	0.2534(54)	1	1
O6	4a	0.1212(23)	0.8326(51)	0.7493(67)	1	1

Table 7.6 Crystallographic structural parameters of ErFeWO_6 obtained from refinement of room temperature XRD data. Space group: $Pna2_1$; $a = 10.9704(1)$ Å, $b = 5.1524(1)$ Å, $c = 7.3223(1)$ Å, $\alpha = \beta = \gamma = 90^\circ$, $V = 413.888(11)$ Å³; $\chi^2 = 6.42$, $R_{\text{Bragg}}(\%) = 4.82$, $R_{\text{f}}(\%) = 3.89$.

Atom	Wyckoff Position	x	y	z	$B_{\text{iso}}(\text{Å}^2)$	Occu.
Er	4a	0.0437(2)	0.4575(7)	0.25	0.610(80)	1
Fe	4a	0.1388(10)	0.9643(17)	0.9870(41)	0.358(211)	1
W	4a	0.3523(3)	0.4509(6)	0.0034(15)	0.600(69)	1
O1	4a	0.9781(31)	0.7550(73)	0.0441(79)	1	1
O2	4a	0.5453(31)	0.2588(71)	0.9601(86)	1	1
O3	4a	0.2008(34)	0.6614(66)	0.0723(54)	1	1
O4	4a	0.2902(33)	0.1040(75)	0.9403(53)	1	1
O5	4a	0.1592(29)	0.0787(63)	0.2500(68)	1	1
O6	4a	0.1177(27)	0.8415(61)	0.7618(79)	1	1

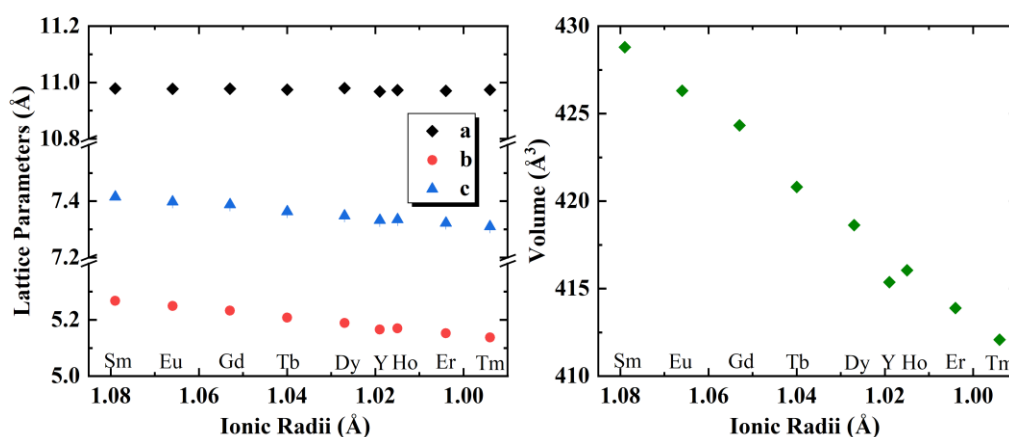


Figure 7.4 Variation of the lattice parameters a , b , and c vs ionic radii and the unit cell volume for different $R\text{FeWO}_6$ compounds. We have taken the Dy, Eu, Tb, Y values from Ref. [6].

7.3.2 TmFeWO₆

Temperature-dependent susceptibility and specific heat are given in Figure 7.5(a). It is apparent from the heat capacity figure that TmFeWO₆ exhibits anomalies corresponding to the magnetic ordering of Fe³⁺ ions at $T_{N1} = 14.5$ K and an independent ordering of Tm³⁺ ions at $T_{N2} = 5.5$ K. From the Curie-Weiss fit to inverse susceptibility [see Figure 7.5(b)], the obtained value of the effective paramagnetic moment is $9.965 \mu_B/\text{f.u.}$, which is in good agreement with the theoretical value $9.602 \mu_B$ for both Tm³⁺ and Fe³⁺ ions and the Curie-Weiss temperature $\theta_{CW} = -38.5$ K. The negative sign indicates that the dominant interactions are antiferromagnetic. The θ_{CW} is high as compared to the T_{N1} indicating that the system is moderately frustrated. We did not observe any signs of ordering in the magnetic susceptibility at T_{N1} because the susceptibility is dominated by the large paramagnetic moment of Tm³⁺ ions. From the inset of Figure 7.5(a), the linear behaviour of field-dependent isothermal magnetization at $T > T_{N2}$ is as expected for the antiferromagnetic ordering. Below T_{N2} , it exhibits a metamagnetic transition with a critical field of about 1 T. This field-induced transition develops with the hysteresis in isothermal magnetization, indicating the first-order nature of the metamagnetic transition below T_{N2} .

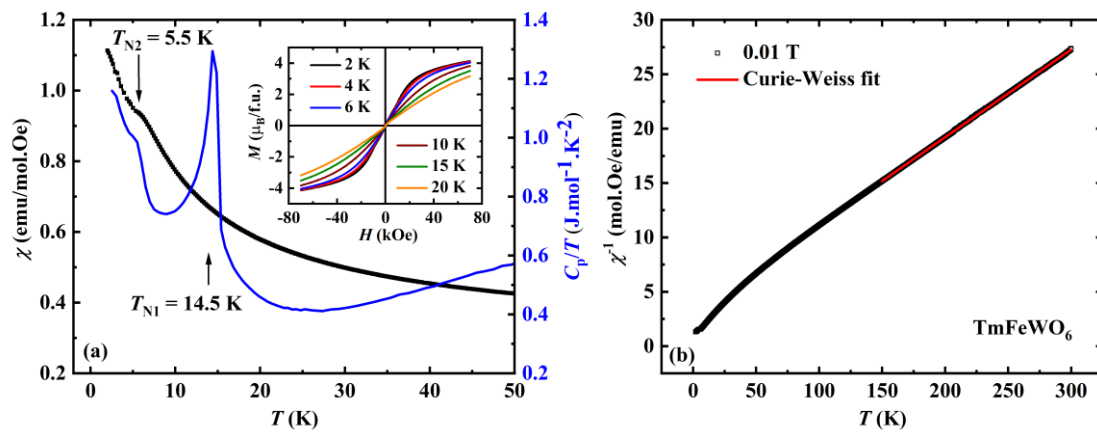


Figure 7.5 (a) Left. Variation of DC susceptibility with temperature in TmFeWO₆ measured under 0.01 T. Right. Heat capacity measured under 0 T. Inset shows the isothermal magnetization curves at different temperatures. (b) Inverse susceptibility under 0.01 T and field-cooled conditions. The red line indicates the Curie-Weiss fit.

The results of dielectric measurements are presented in Figure 7.6(a). The dielectric anomaly was observed at T_{N1} is nearly independent of applied magnetic fields and there is a broad anomaly around T_{N2} which starts well above the transition and is suppressed under applied magnetic fields, indicating the coupling between magnetic and dipole orders in this

compound. As shown in the inset of Figure 7.6(a), the dissipation factor shows similar behaviour as the dielectric constant. The observed dielectric anomalies did not shift with the frequency [Figure 7.6(b)], which excludes any extrinsic effects and confirms its magnetic origin. However, we have observed dispersion of dielectric curves in the measured temperature range, indicating the presence of dielectric relaxation that can be of the Maxwell-Wagner type.

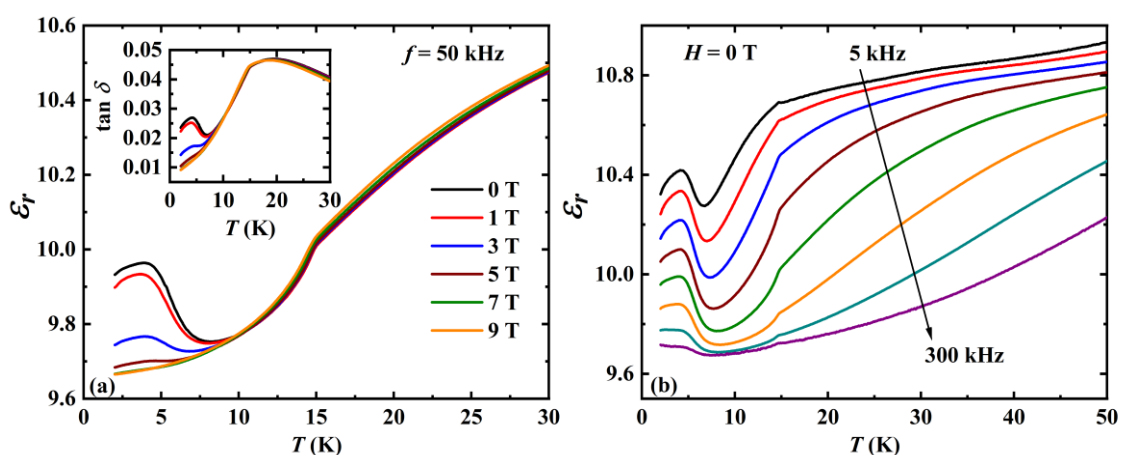


Figure 7.6 (a) Temperature-dependent dielectric constant measured under different magnetic fields at the frequency $f = 50$ kHz. Inset shows the corresponding loss behaviour. (b) Temperature variation of dielectric constant at different frequencies measured under 0 T; for TmFeWO_6 .

To examine whether these dielectric anomalies are associated with ferroelectricity or not, we have recorded the pyrocurrent behaviour across the magnetic ordering temperatures. In accordance with the observed dielectric anomalies, we observe two pyrocurrent anomalies in the same direction at both T_{N1} and T_{N2} , implying two ferroelectric (FE) transitions which can be seen in Figure 7.7(a). The second ferroelectric transition is absent in the isostructural compounds $R\text{FeWO}_6$ ($R = \text{Dy}, \text{Eu}, \text{Tb}, \text{and Y}$) [6]. The change in polarization (ΔP) below the magnetic ordering obtained by integrating the pyrocurrent with respect to time and its magnetic field dependence is shown in Figure 7.7(b). As can be seen from Figure 7.7(c), the change in polarization in the FE1 region is almost unchanged under the applied magnetic field. Whereas the change in polarization below FE2 is four times higher than that of FE1 under zero field and suppressed with the applied magnetic field. The maximum change in polarization (ΔP) is $\sim 0.4 \mu\text{C}/\text{m}^2$ in the FE1 region and $\sim 1.8 \mu\text{C}/\text{m}^2$ in the FE2 region at 2 K under zero magnetic field. Further, the ΔP is switched by changing the direction of the poling electric field as seen from Figure 7.7(b). It is known that DC bias measurement is a useful tool to find out the intrinsic nature of the ferroelectric polarization, as mentioned in Chapter

2. The intrinsic nature of the ferroelectricity is further supported by the DC bias measurement which is given in Figure 7.7(d). The presence of two DC bias signals at magnetic transitions evidencing the FE transitions. The change in polarization in the FE2 region is started well above the T_{N2} like dielectric behaviour. Later, we will discuss this behaviour in comparison with the other compounds. A schematic H - T phase diagram of TmFeWO_6 is shown in Figure 7.8 where we can see the two ferroelectric transitions and their field dependence.

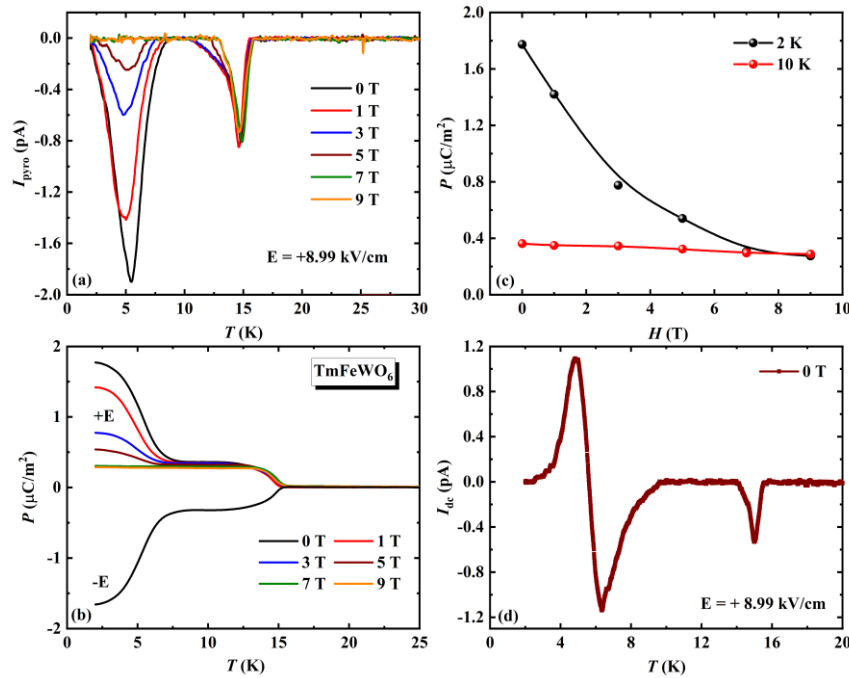


Figure 7.7 (a) Temperature and magnetic field-dependent pyrocurrent measured after electric poling. (b) The corresponding polarization and its switching. (c) ΔP vs H behaviour at 2 and 10 K. (d) DC bias signal recorded across the ferroelectric transition under 0 T; for TmFeWO_6 .

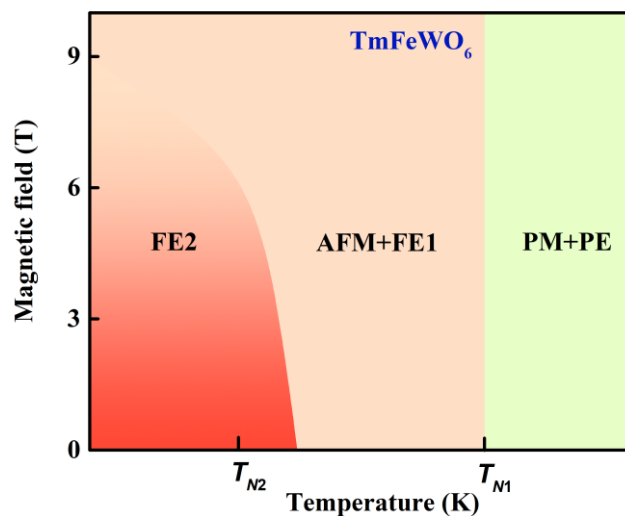


Figure 7.8 Schematic H - T phase diagram for TmFeWO_6 which shows two ferroelectric transitions.

7.3.3 SmFeWO₆

From Figure 7.9(a), the temperature-dependent susceptibility of SmFeWO₆ shows the anomaly around $T_{N1} = 16.3$ K indicating the antiferromagnetic ordering of Fe³⁺ ions. The susceptibility increases below T_{N1} due to the paramagnetic moment contribution of Sm³⁺ ions. The long-range magnetic ordering is confirmed by the λ -type anomaly in $C_p(T)$ as seen in the same figure. The broad hump around 6 K in heat capacity indicates a possible Schottky-type anomaly. It can be possible that Fe spins might polarize the Sm moments below T_{N1} and the independent magnetic ordering of Sm³⁺ ions can occur at $T_{N2} = 6$ K. However, this possibility can be confirmed from the neutron diffraction study. The magnetic field-dependent isothermal magnetization curves [inset of Figure 7.9(a)] are consistent with the antiferromagnetic ordering of SmFeWO₆. This compound exhibits dielectric anomaly at T_{N1} indicating the magnetodielectric effect as seen from Figure 7.9(b). This anomaly is nearly independent of the applied magnetic field but shifts towards lower temperatures as the field increases. Similar behaviour is observed for the loss factor which is shown in the inset of Figure 7.9(b). At low temperatures, the dielectric constant falls off and a broad anomaly is observed in the corresponding loss data around 6 K. This change may be due to the independent ordering of Sm³⁺ ions. Moreover, these results confirm the magnetodielectric coupling of SmFeWO₆.

The recorded pyrocurrent shows an asymmetric peak at T_{N1} indicating the appearance of polarization and suppresses under applied magnetic fields. The corresponding change in polarization and its magnetic field dependence are shown in Figure 7.9(c). The change in polarization (ΔP) is maximum with the value $\sim 1.5 \mu\text{C}/\text{m}^2$ at 2 K under zero magnetic field and suppressed with increasing applied magnetic fields. The applied magnetic fields can change the ground state magnetic structure and results in decreasing the change in polarization. Further, the electric polarization is switched by changing the direction of the poling electric field [Figure 7.9(c)] and DC bias measurement from Figure 7.9(d) confirms the intrinsic behaviour of ferroelectricity. These results demonstrate that SmFeWO₆ is multiferroic.

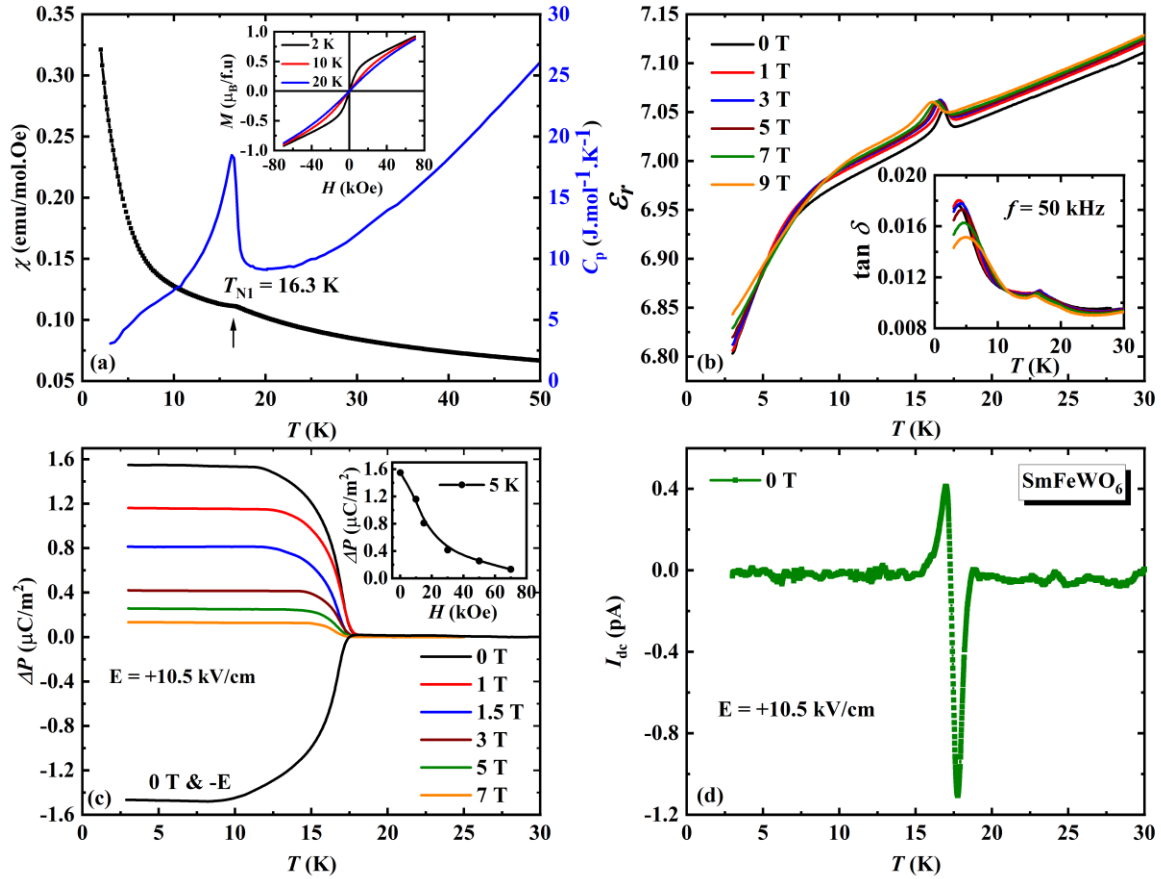


Figure 7.9 (a) Left. Temperature-dependent dc susceptibility measured under 0.01 T. Right. Specific heat obtained under 0 T. Inset shows M vs H curves at different temperatures. (b) Temperature evolution of dielectric constant measured under different magnetic fields with frequency $f = 50$ kHz. Inset shows the corresponding dissipation factor. (c) Temperature and magnetic field-dependent change in polarization and its switching behaviour obtained from pyrocurrent. Inset. ΔP vs H behaviour at 5 K. (d) DC bias signal; for SmFeWO_6 .

7.3.4 GdFeWO_6

GdFeWO_6 exhibits antiferromagnetic ordering of Fe^{3+} ions at $T_{N1} = 16.2$ K and Gd^{3+} ions ordering at $T_{N2} = 5.9$ K as shown in Figure 7.10(a). The effective magnetic moment $10.175 \mu_B/\text{f.u.}$ obtained from the Curie-Weiss fit is in good agreement with the free ion moment for Gd^{3+} and Fe^{3+} ions which is $9.904 \mu_B$. The Curie-Weiss temperature is $\theta_{\text{CW}} = -27.2$ K indicates the dominant antiferromagnetic interactions. We did not observe the peak at T_{N1} in susceptibility because of the large contribution from the paramagnetic moment of Gd^{3+} ions. Isothermal magnetization curves were given in the inset of Figure 7.10(a), show linear behaviour supporting the antiferromagnetic ordering below T_{N1} . The S-type behaviour below T_{N2} indicates the possible metamagnetic transition. The value of magnetization observed at 2 K and 7 T is $\sim 7.9 \mu_B/\text{f.u.}$, which is nearly equivalent to the saturated magnetization ~ 8.6

$\mu_B/f.u.$, of both Gd^{3+} and Fe^{3+} ions. Therefore, the metamagnetic transition associated with Gd^{3+} spins is antiferromagnetic to ferromagnetic.

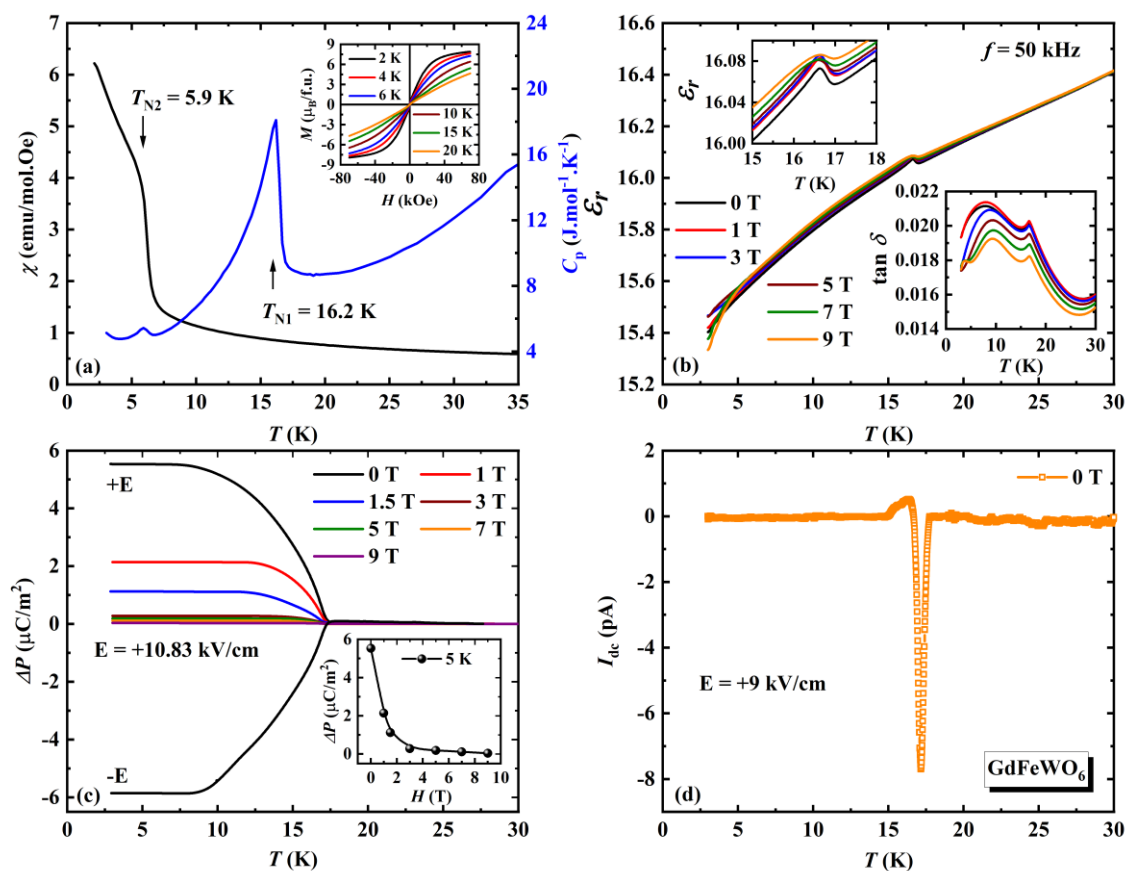


Figure 7.10 (a) Left. DC susceptibility against temperature measured under a magnetic field of 0.01 T. Right. C_p vs T . Inset. M vs H plots at different temperatures. (b) Dielectric constant with respect to the temperature recorded under different magnetic fields with frequency $f = 50$ kHz. Inset. Enlarged view of dielectric constant (Left) and loss data (Right). (c) Change in polarization under different magnetic fields and switching of polarization with the direction of the poling electric field. Inset shows ΔP vs H at 5 K. (d) DC bias measurement; for $GdFeWO_6$.

From Figure 7.10(b), $GdFeWO_6$ exhibits a dielectric anomaly at T_{N1} which became broad under the applied magnetic fields. This effect is very clear in loss data where a sharp anomaly is observed at T_{N1} [see inset of Figure 7.10(b)]. These anomalies did not shift with the frequency, which is not shown here, indicating the magnetic origin and cross-coupling between magnetic and dielectric orders. The emergence of polarization at T_{N1} as seen from Figure 7.10(c), confirm that this dielectric anomaly is associated with ferroelectricity. The maximum change in polarization (ΔP) is $5.5 \mu C/m^2$ at 2 K under zero magnetic field and ΔP is suppressed upon increasing the magnetic field. As can be seen from the inset of Figure 7.10(c), this compound shows strong magnetoelectric coupling. Further, the polarization is

switchable [Figure 7.10(c)], and DC bias measurements [Figure 7.10(d)] confirmed the intrinsic nature of ferroelectricity.

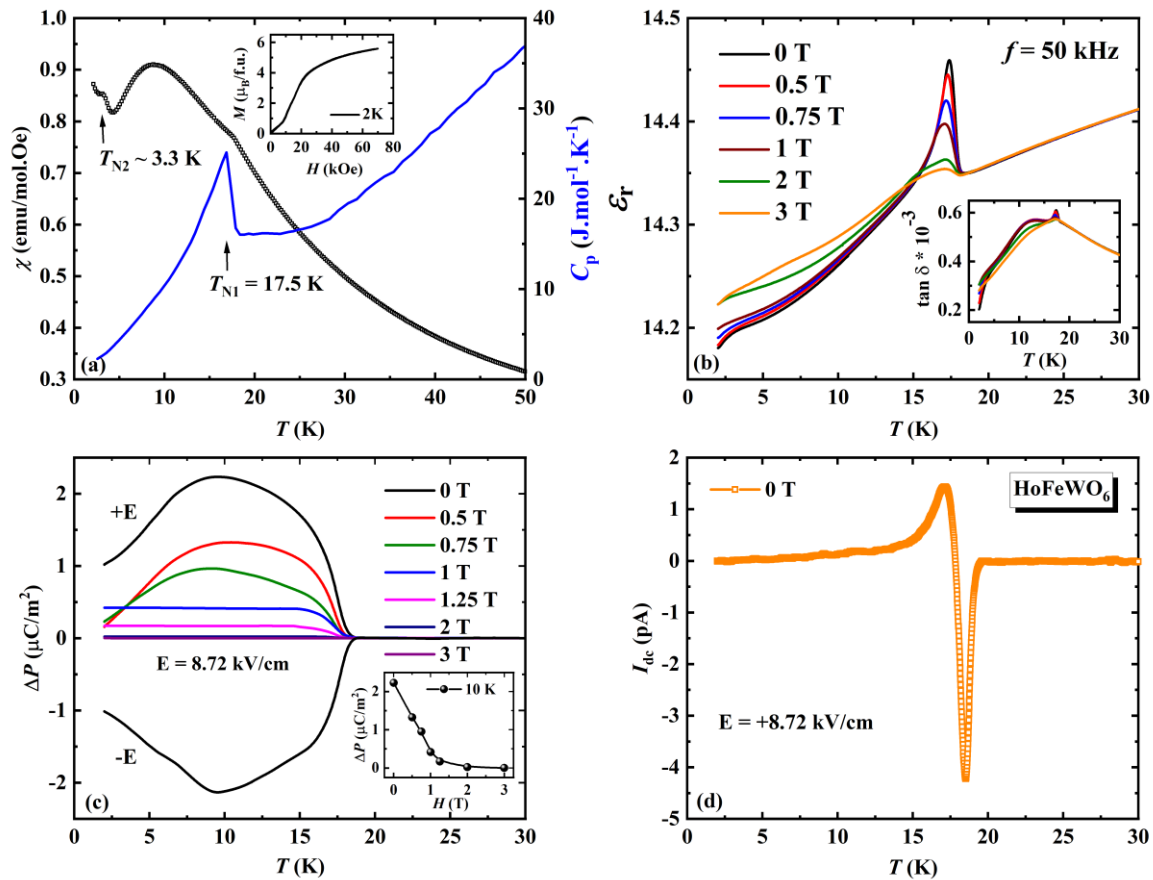


Figure 7.11 (a) Left. DC susceptibility as function of temperature measured under a magnetic field of 0.01 T. Right. Heat capacity obtained at 0 T. Inset. Isothermal magnetization curve at 2 K. (b) Dielectric constant measured while warming under different magnetic fields with frequency $f = 50$ kHz. Inset. Related loss data. (c) Change in polarization under different magnetic fields and its switching upon changing the direction of the poling electric field. Inset shows ΔP vs H at 10 K. (d) DC bias measurement under 0 T; for HoFeWO₆.

7.3.5 HoFeWO₆

The kink in DC magnetic susceptibility and λ -type anomaly in heat capacity at $T_{N1} = 17.5$ K, from Figure 7.11(a), indicate the second-order magnetic transition from paramagnetic to the long-range antiferromagnetic ordering of Fe³⁺ ($S = 5/2$) ions. This behavior is similar to that of DyFeWO₆, revealing the polarization of Ho³⁺ spins by Fe³⁺ moments at T_{N1} . Upon cooling, susceptibility shows a broad maximum at $T_{max} = 9$ K. This can be associated with low dimensional magnetic correlations between the Ho³⁺ spins. Further, it exhibits the long-range magnetic ordering of Ho³⁺ ions at $T_{N2} = 3.3$ K. The M vs H curve at 2 K, shown in the inset of Figure 7.11(a), evidence the presence of metamagnetic transition in this compound.

As shown in Figure 7.11(b), the AFM transition at $T_{N1} = 17.5$ K is accompanied by the dielectric anomaly in the absence of a magnetic field measured at frequency $f = 50$ kHz, indicating the possible ferroelectric transition. Under applied magnetic fields, the dielectric anomaly is suppressed at T_{N1} but increased at low temperatures with significant magnetodielectric coupling. The corresponding dissipation factor shows similar behavior as of dielectric constant. Indeed, the ferroelectric transition is further confirmed by the appearance of switchable polarization, as shown in Figure 7.11(c). The observed polarization is affected by the ordering of Ho^{3+} ions at T_{N2} . The polarization is suppressed by the magnetic field of 3 T [see inset of Figure 7.11(c)]. The spin induced multiferroicity is further supported by the DC bias signal, which is shown in Figure 7.11(d).

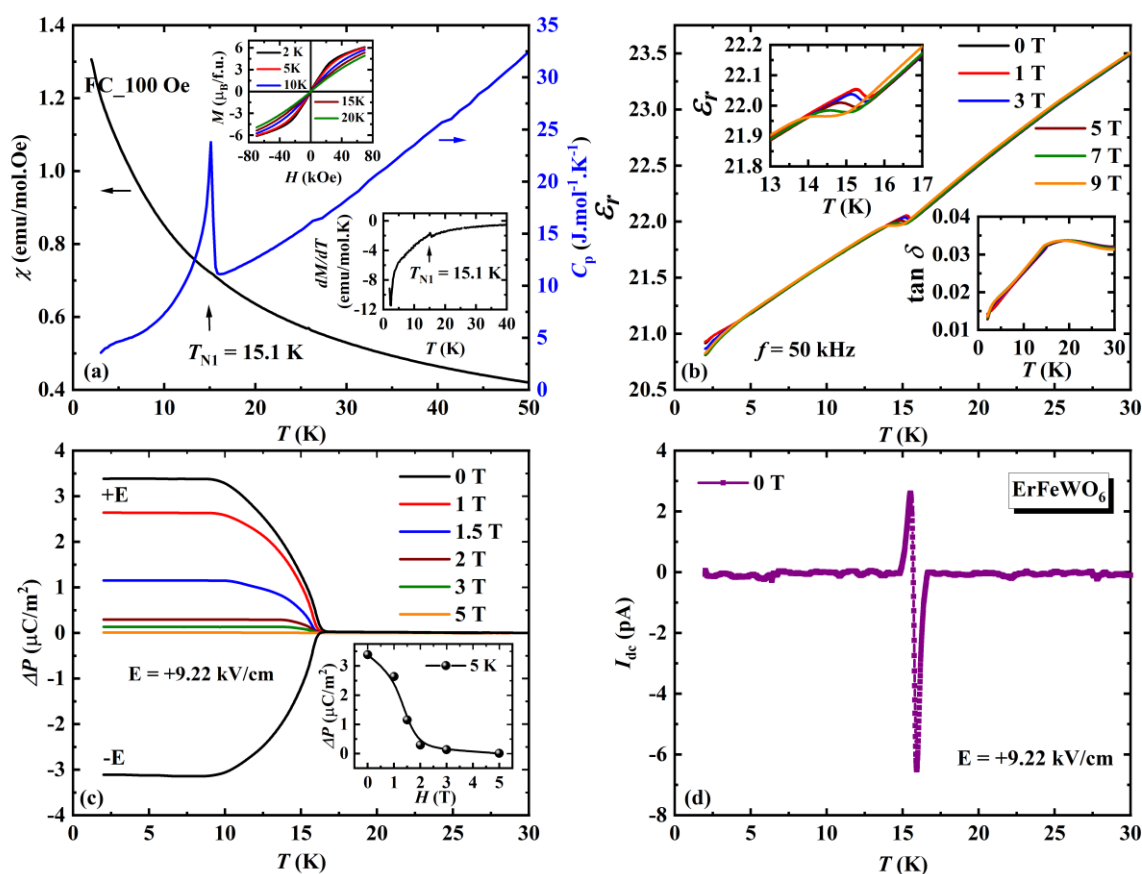


Figure 7.12 (a) Left. Temperature evolution of magnetic susceptibility measured under a magnetic field of 0.01 T. Right. Specific heat data obtained at 0 T. Inset. Isothermal magnetization curves at different temperatures (Top) and dM/dT vs T (Bottom). (b) Temperature-dependent dielectric constant recorded under different magnetic fields with frequency $f = 50$ kHz. Inset. Enlarged view of dielectric constant (Left) and dielectric loss (Right). (c) Temperature and magnetic field dependence of change in polarization and its switching. Inset shows ΔP vs H . (d) DC bias measurement in the absence of magnetic field; for ErFeWO_6 .

7.3.6 ErFeWO₆

The results of ErFeWO₆ are presented in Figure 7.12, where the antiferromagnetic order of Fe sublattice is seen at $T_{N1} = 15.1$ K [Figure 7.12(a)] which is further supported by the anomaly in dM/dT as shown in the bottom inset. A clear indication of the antiferromagnetic ordering of the Fe³⁺ ions is further confirmed by the heat capacity data given in Figure 7.12(a). Also, Schottky-type anomaly around $T_{N2} = 4$ K where Er³⁺ moments independent ordering might be possible. The Curie-Weiss fit to susceptibility also suggests the presence of Er³⁺ and Fe³⁺ oxidation states and the presence of antiferromagnetic interactions. Isothermal magnetization curves are linear as expected for the antiferromagnetic ordering and reveal the metamagnetic transition associated with the magnetic Er³⁺ ion below T_{N2} . ErFeWO₆ compound exhibits dielectric anomaly at T_{N1} which shifts to lower temperatures upon increasing the applied magnetic field as shown in Fig. 7.12(b), suggesting the strong magnetodielectric coupling. The corresponding loss data shows anomalous behaviour at T_{N1} . Pyroelectric measurements suggest a change in polarization that occurs below T_{N1} as depicted in Figure 7.12(c), demonstrating the multiferroic nature of ErFeWO₆. The maximum change in polarization is $3.5 \mu\text{C}/\text{m}^2$ at 2 K under zero magnetic fields. These results are further supported by switching and DC bias measurements which are given in Figure 7.12(c & d), respectively.

Finally, we have summarized the magnetic transition temperatures of aeschynite family of compounds along with the reported ones in Table 7.7. All these compounds exhibit the antiferromagnetic ordering of Fe³⁺ ions around $T_{N1} = 14 - 18$ K and rare-earth ions order at low temperatures. However, Fe³⁺ ions induce the moment at the rare-earth site indicating the $4f$ and $3d$ interactions. As shown earlier, isothermal magnetization measurements reveal the presence of metamagnetic transitions associated with the magnetic rare-earth ions. In the case of GdFeWO₆, the magnetization almost saturated at 7 T with a large magnetization value of $\sim 7.9 \mu_B/\text{f. u.}$, indicating the ferromagnetic behaviour. Whereas the magnetic moments do not saturate within the experimental limit of 7 T for other compounds suggesting that the role of magnetic anisotropy associated with each rare-earth ion. Owing to the rare-earth magnetic anisotropy, the applied magnetic field can change the magnetic state of the rare-earth and thus affect the polarization. The magnetic field-dependent change in polarization reveals the effect of strong $4f - 3d$ interaction in these compounds.

Nevertheless, this is not the case for TmFeWO_6 . From our understanding, there may be no induced moment at Tm site and Tm^{3+} ions order independently at $T_{N2} = 5.5$ K. The polarization in FE1 state is robust against a magnetic field which is similar to YFeWO_6 , whereas same in FE2 is highly affected by the applied magnetic field [6]. This can be due to the strong antiferromagnetic exchange interaction of Fe^{3+} ions, causing the polarization in FE1 state which is strong against the applied magnetic field. Unlike Fe^{3+} ordering, the Tm^{3+} magnetic ordering which is mainly contributing to the polarization in the FE2 state rather weak and changes easily by the magnetic field. This results in the suppression of polarization under the magnetic fields. Thus, these results indicate that the $4f - 3d$ interaction in TmFeWO_6 is absent or rather weak. Moreover, the polarization in the FE2 state appears well above the T_{N2} which might be due to the development of the antiferromagnetic ordering of Tm^{3+} ions at higher temperatures and orders completely at T_{N2} . In addition to this, the rare-earth cationic size also can be accountable for this behaviour. However, one needs to perform neutron diffraction measurements and a single crystal study to validate these arguments.

Table 7.7 The magnetic transition temperatures of $R\text{FeWO}_6$ compounds.

R	T_{N1} (K)	T_{N2} (K)	Ref.
Sm	16.3	6	Present work
Eu	17	-	[6]
Gd	16.2	5.9	Present work
Tb	15	2.4	[6]
Dy	18	5	[6]
Y	15	-	[6]
Ho	17.5	3.3	Present work
Er	15.1	4	Present work
Tm	14.5	5.5	Present work

The paramagnetic space group $Pna2_11'$ is polar and allows the spontaneous electric polarization along z -direction. However, our PE loop measurements down to liquid nitrogen temperature (77 K) indicates leaky nature of the samples as shown in Figure 7.13. Since the polar structure is stabilized by the cation ordering at the formation temperature, these compounds do not seem to undergo polar to nonpolar transition and thus, the polarization may not be switchable due to large energy barrier between two ferroic states. Nevertheless,

all compounds show change in electric polarization at the magnetic ordering temperature through magnetoelectric coupling.

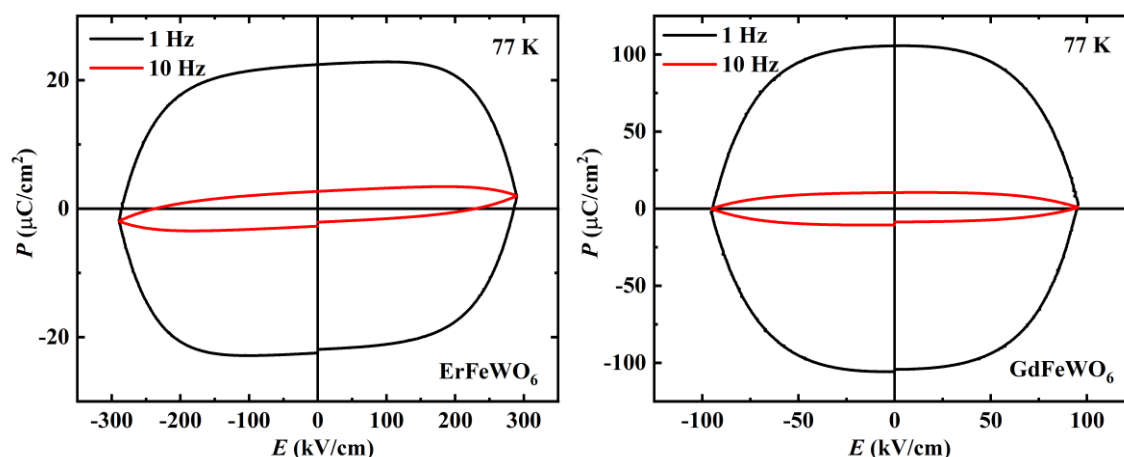


Figure 7.13 The results of PE loop measurements carried at 77 K for ErFeWO₆ (Left) and GdFeWO₆ (Right).

It should be mentioned here that the change in polarization is very less for all the compounds could be due to the polycrystalline nature of the samples measured. Although we did not determine the magnetic structure of these compounds, the emergence of polarization in all the four compounds below Fe-ordering indicates that these compounds should have a similar noncollinear magnetic structure of Fe spins as that of DyFeWO₆ [6]. The magnetic space group C_{2c} associated with the k -vector $(0, \frac{1}{2}, \frac{1}{2})$ allows additional polarization along x -direction with the form $(P_x, 0, P_z)$. As discussed earlier, there are two major structural distortions belong to irreps GM1 and GM4 which are responsible for the displacement of O3, O4, and O6 atoms, which split into two atoms each, with respect to paramagnetic structure. This results in polarization with strong magnetoelectric coupling. In the present compounds, the polarization below T_N could be enhanced by magnetic order through magnetoelastic coupling or the magnetic symmetry itself induces a new polarization. Also, the mechanism of inverse Dzyaloshinskii-Moriya interaction cannot be neglected since the magnetic structure is noncollinear. Hence, our detailed experimental study reveals that these compounds are magnetically induced multiferroics. The difference in multiferroic properties with each isostructural compound and the magnetic field effect demonstrates the role of $4f - 3d$ interaction along with the rare-earth magnetic anisotropy. Further, it requires single crystal and neutron diffraction studies to understand the magnetoelectric coupling in these compounds.

7.4 Conclusion

In conclusion, we have illustrated the magnetically induced multiferroicity in $R\text{FeWO}_6$ ($R = \text{Tm, Sm, Gd, Ho, and Er}$). All these compounds crystallize in polar orthorhombic structure due to the chemical ordering of Fe^{3+} and W^{6+} ions and exhibit antiferromagnetic ordering of Fe^{3+} ions between $T_{\text{N1}} = 14 - 18$ K. These oxides display the field-induced metamagnetic transitions below the rare-earth magnetic ordering temperatures. The dielectric anomalies accompanied by a change in polarization at T_{N1} , evidence the coupling between magnetism and ferroelectricity. Surprisingly, we have observed a second ferroelectric transition at T_{N2} for TmFeWO_6 . The influence of magnetic field on change in polarization indicating the role of $4f - 3d$ interaction. Hence, the whole aeschynite family of compounds may serve as a playground for studying the multiferroic phenomena and the important role of $4f - 3d$ interaction.

References

- [1] Y. Wang, G. L. Pascut, B. Gao, T. A. Tyson, K. Haule, V. Kiryukhin, and S. W. Cheong, *Sci. Rep.* **5**, 12268 (2015).
- [2] Y. S. Oh, S. Artyukhin, J. J. Yang, V. Zapf, J. W. Kim, D. Vanderbilt, and S. W. Cheong, *Nat. Commun.* **5**, 3201 (2014).
- [3] G. H. Cai, M. Greenblatt, and M. R. Li, *Chem. Mater.* **29**, 5447 (2017).
- [4] M. R. Li, P. W. Stephens, M. Retuerto, T. Sarkar, C. P. Grams, J. Hemberger, M. C. Croft, D. Walker, and M. Greenblatt, *J. Am. Chem. Soc.* **136**, 8508 (2014).
- [5] M. R. Li, E. E. McCabe, P. W. Stephens, M. Croft, L. Collins, S. V. Kalinin, Z. Deng, M. Retuerto, A. Sen Gupta, H. Padmanabhan, V. Gopalan, C. P. Grams, J. Hemberger, F. Orlandi, P. Manuel, W.-M. Li, C.-Q. Jin, D. Walker, and M. Greenblatt, *Nat. Commun.* **8**, 2037 (2017).
- [6] S. Ghara, E. Suard, F. Fauth, T. T. Tran, P. S. Halasyamani, A. Iyo, J. Rodríguez-Carvajal, and A. Sundaresan, *Phys. Rev. B* **95**, 224416 (2017).
- [7] R. Shankar P N, S. Mishra and S. Athinarayanan, *APL Mater.* **8**, 040906 (2020).
- [8] P. Yanda and A. Sundaresan, in *Adv. Chem. Phys. Mater.* (WORLD SCIENTIFIC, 2019), pp. 224–248.
- [9] V. Caignaert, A. Maignan, K. Singh, C. Simon, V. Pralong, B. Raveau, J. F. Mitchell, H. Zheng, A. Huq, and L. C. Chapon, *Phys. Rev. B* **88**, 174403 (2013).
- [10] T. Kurumaji, S. Ishiwata, and Y. Tokura, *Phys. Rev. X* **5**, 031034 (2015).
- [11] T. Kurumaji, S. Ishiwata, and Y. Tokura, *Phys. Rev. B* **95**, 045142 (2017).
- [12] Y. S. Tang, S. M. Wang, L. Lin, C. Li, S. H. Zheng, C. F. Li, J. H. Zhang, Z. B. Yan, X. P. Jiang, and J.-M. Liu, *Phys. Rev. B* **100**, 134112 (2019).
- [13] M. Li, D. Walker, M. Retuerto, T. Sarkar, J. Hadermann, P. W. Stephens, M. Croft, A. Ignatov, C. P. Grams, and J. Hemberger, *Angew. Chemie Int. Ed.* **52**, 8406 (2013).
- [14] C. De and A. Sundaresan, *Phys. Rev. B* **97**, 214418 (2018).
- [15] R. Shankar P N, F. Orlandi, P. Manuel, W. Zhang, P. S. Halasyamani, and A. Sundaresan, *Chem. Mater.* **32**, 5641-5649 (2020).
- [16] R. Salmon, H. Baudry, J. Grannec, G. Le Flem, and F. Sur, *Rev. Chim. Miner.* **11**, 71 (1974). [17] L. Jahnberg, *Acta Chem. Scand.* **71**, 2548 (1963).
- [18] S. W. Kim, T. J. Emge, Z. Deng, R. Uppuluri, L. Collins, S. H. Lapidus, C. U. Segre, M. Croft, C. Jin, and V. Gopalan, *Chem. Mater.* **30**, 1045 (2018).
- [19] S. Ghara, F. Fauth, E. Suard, J. Rodríguez-Carvajal, and A. Sundaresan, *Inorg. Chem.* **57**, 12827 (2018).
- [20] C. Dhital, D. Pham, T. Lawal, C. Bucholz, A. Poyraz, Q. Zhang, R. Nepal, R. Jin, and R. Rai, *J. Magn. Magn. Mater.* **514**, 167219 (2020).
- [21] S. W. Kim, X. Tan, C. E. Frank, Z. Deng, H. Wang, L. Collins, S. H. Lapidus, C. Jin,

- V. Gopalan, S. V Kalinin, D. Walker, and M. Greenblatt, *Inorg. Chem.* **59**, 3579 (2020).
- [22] P. Yanda and A. Sundaresan, *Mater. Res. Express* **6**, 124007 (2020).
- [23] T. Kimura, T. Goto, H. Shintani, K. Ishizaka, T. Arima, and Y. Tokura, *Nature* **426**, 55 (2003).
- [24] N. Hur, S. Park, P. A. Sharma, J. S. Ahn, S. Guha, and S.-W. Cheong, *Nature* **429**, 392 (2004).
- [25] Y. Tokunaga, S. Iguchi, T. Arima, and Y. Tokura, *Phys. Rev. Lett.* **101**, 097205 (2008).
- [26] Y. Tokunaga, N. Furukawa, H. Sakai, Y. Taguchi, T. Arima, and Y. Tokura, *Nat. Mater.* **8**, 558 (2009).
- [27] P. Yanda, N. V. Ter-Oganessian, and A. Sundaresan, *Phys. Rev. B* **100**, 104417 (2019).
- [28] P. Yanda, I. V. Golosovsky, I. Mirebeau, N. V Ter-Oganessian, J. Rodríguez-Carvajal, and A. Sundaresan, *Phys. Rev. Res.* **2**, 023271 (2020).

Summary of the thesis

In the past two decades, there were ground-breaking efforts to find new magnetoelectric and multiferroic materials and understand the mechanism of magnetoelectric coupling. Despite tremendous development, it is still challenging and fascinating to design a new magnetoelectric or multiferroic material. The critical theme of this thesis is to find new magnetoelectric or multiferroics with strong magnetoelectric coupling. Primarily, we have worked on well-known green phase compounds with the chemical formula $R_2\text{BaCuO}_5$, where R is a rare earth. These compounds exhibit a wide variety of magnetic structures depending on the particular R ion owing to the peculiar properties of $4f$ - $3d$ magnetic exchange coupling and local anisotropic properties of the rare-earth. We have discovered that these compounds exhibit interesting magnetoelectric and multiferroic properties. The compounds $R_2\text{BaCuO}_5$ ($R = \text{Sm}, \text{Dy}, \text{and Ho}$) exhibit a linear magnetoelectric effect whereas $R_2\text{BaCuO}_5$ ($R = \text{Gd}$ and Yb) show multiferroic properties. Besides, $R_2\text{BaCuO}_5$ ($R = \text{Er}, \text{Dy}, \text{and Ho}$) reveals field-induced multiferroic properties where a linear magnetoelectric effect is absent in the former compound. Therefore, the variety of magnetic structures suggests the diversity of multiferroic and magnetoelectric properties in the whole green phase family of compounds. Given this and the fact that solid solutions like $(R',R'')_2\text{BaCuO}_5$ (where R' and R'' are different rare earths) should have even more complex magnetic properties, one can conclude that the green phase family may serve as a playground for the studies of multiferroic and magnetoelectric phenomena. The importance of $4f$ - $3d$ interactions in determining the ground state magnetic structure suggests that the richness of such phenomena in this class of compounds will arguably become as famous as orthorhombic rare-earth manganites RMnO_3 and manganates RMn_2O_5 , including the diversity in electric polarization directions and its magnetic field induced reorientations.

Further, the multiferroics materials should exhibit a strong magnetoelectric coupling at accessible temperatures for practical applications. Though multiferroics (type-II) reveals strong coupling, they fail to show high transition temperatures due to complex magnetic structures which break the inversion symmetry. For this reason, polar magnets can be good candidates since they do not have complex spin structures. Along this line, we have prepared new polar magnets RFeWO_6 ($R = \text{Sm}, \text{Gd}, \text{Ho}, \text{Er}, \text{and Tm}$) which belong to the aeschynite family of compounds, and they exhibit interesting multiferroic properties below their antiferromagnetic ordering temperature. It will be interesting to explore spin-lattice coupling in these compounds for understanding the origin of ferroelectricity below magnetic ordering.